

University of Windsor

Scholarship at UWindor

Electronic Theses and Dissertations

Theses, Dissertations, and Major Papers

1995

Liquid prebreakdown phenomena and the associated involvement of electrohydrodynamic processes.

Diana Hua. Ren
University of Windsor

Follow this and additional works at: <https://scholar.uwindsor.ca/etd>

Recommended Citation

Ren, Diana Hua., "Liquid prebreakdown phenomena and the associated involvement of electrohydrodynamic processes." (1995). *Electronic Theses and Dissertations*. 2623.
<https://scholar.uwindsor.ca/etd/2623>

This online database contains the full-text of PhD dissertations and Masters' theses of University of Windsor students from 1954 forward. These documents are made available for personal study and research purposes only, in accordance with the Canadian Copyright Act and the Creative Commons license—CC BY-NC-ND (Attribution, Non-Commercial, No Derivative Works). Under this license, works must always be attributed to the copyright holder (original author), cannot be used for any commercial purposes, and may not be altered. Any other use would require the permission of the copyright holder. Students may inquire about withdrawing their dissertation and/or thesis from this database. For additional inquiries, please contact the repository administrator via email (scholarship@uwindsor.ca) or by telephone at 519-253-3000ext. 3208.



National Library
of Canada

Acquisitions and
Bibliographic Services Branch

395 Wellington Street
Ottawa, Ontario
K1A 0N4

Bibliothèque nationale
du Canada

Direction des acquisitions et
des services bibliographiques

395, rue Wellington
Ottawa (Ontario)
K1A 0N4

Your library - votre bibliothèque

Our name - notre référence

NOTICE

The quality of this microform is heavily dependent upon the quality of the original thesis submitted for microfilming. Every effort has been made to ensure the highest quality of reproduction possible.

If pages are missing, contact the university which granted the degree.

Some pages may have indistinct print especially if the original pages were typed with a poor typewriter ribbon or if the university sent us an inferior photocopy.

Reproduction in full or in part of this microform is governed by the Canadian Copyright Act, R.S.C. 1970, c. C-30, and subsequent amendments.

AVIS

La qualité de cette microforme dépend grandement de la qualité de la thèse soumise au microfilmage. Nous avons tout fait pour assurer une qualité supérieure de reproduction.

S'il manque des pages, veuillez communiquer avec l'université qui a conféré le grade.

La qualité d'impression de certaines pages peut laisser à désirer, surtout si les pages originales ont été dactylographiées à l'aide d'un ruban usé ou si l'université nous a fait parvenir une photocopie de qualité inférieure.

La reproduction, même partielle, de cette microforme est soumise à la Loi canadienne sur le droit d'auteur, SRC 1970, c. C-30, et ses amendements subséquents.

**LIQUID PREBREAKDOWN PHENOMENA AND THE
ASSOCIATED INVOLVEMENT OF
ELECTROHYDRODYNAMIC PROCESSES**

by

Diana Hua REN

**A Dissertation
Submitted to the Faculty of Graduate Studies and Research
Through the Department of Electrical Engineering
in Partial Fulfilment of the Requirements for
the Degree of Doctor of Philosophy at the
University of Windsor**

**Windsor, Ontario, Canada
1995**

(c) 1995 Diana Hua Ren



National Library
of Canada

Acquisitions and
Bibliographic Services Branch

395 Wellington Street
Ottawa, Ontario
K1A 0N4

Bibliothèque nationale
du Canada

Direction des acquisitions et
des services bibliographiques

395, rue Wellington
Ottawa (Ontario)
K1A 0N4

Vous êtes notre référence

Vous êtes notre référence

The author has granted an irrevocable non-exclusive licence allowing the National Library of Canada to reproduce, loan, distribute or sell copies of his/her thesis by any means and in any form or format, making this thesis available to interested persons.

L'auteur a accordé une licence irrévocable et non exclusive permettant à la Bibliothèque nationale du Canada de reproduire, prêter, distribuer ou vendre des copies de sa thèse de quelque manière et sous quelque forme que ce soit pour mettre des exemplaires de cette thèse à la disposition des personnes intéressées.

The author retains ownership of the copyright in his/her thesis. Neither the thesis nor substantial extracts from it may be printed or otherwise reproduced without his/her permission.

L'auteur conserve la propriété du droit d'auteur qui protège sa thèse. Ni la thèse ni des extraits substantiels de celle-ci ne doivent être imprimés ou autrement reproduits sans son autorisation.

ISBN 0-612-10955-0

Canada

ABSTRACT

Six dielectric liquids have been investigated for the confirmation of the EHD theory of current response to the application of ramped high voltage by using a prebreakdown technique. The conduction current and displacement current were measured and studied individually. Upon plotting conduction current as well as displacement current on a $\log V$ - $\log I$ scale, two linear portions of the current characteristics were observed in the high stress regime. Thus two separate regimes of the characteristic were found exhibiting current transport in direct proportion to a simple power of the applied voltage, $I \propto V^s$ (or $I \propto V^g$ with respect to displacement current), where s (or g) represented upper s_u (or g_u) and lower slope s_l (or g_l) values. The impact of the developments on the relationship between the maximum applied voltage and the power law is discussed. The relationship referred to is one involving both s values merging to $3/2$ when the electric field becomes large. A new approach using a computer modelling process for these EHD studies will be presented. Attention will also be given to the magnetic field effect observed from the final series of displacement current measurements. A turbulence phenomenon in dielectric liquids has been discovered from a special experiment performed in order to verify the nature of dielectric liquid behaviour under high applied electric field conditions.

DEDICATION

To my parents and to my husband

谨献给

父母，丈夫，及关怀和帮助过我的人们。

ACKNOWLEDGEMENTS

I wish to express deeply my gratitude to Dr. A. Watson for the guidance and encouragement I received under his supervision. I want to sincerely thank him for his continuous guidance, assistance and understanding. It has indeed been a privilege to work with him.

Special thanks to Dr. R. Hackam for his essential and valuable advice, his encouragement and help, which will long be remembered.

Members of my Ph.D program committee, Dr. G.R.G. Raju and Dr. D. Tuck, have provided useful criticisms and suggestions throughout the course of this work for which I am grateful.

I also thank Mr. A. Johns for his technical assistance, his advice, support and friendship during all these years.

I wish to thank Dr. J. Soltis for his assistance and help when it was needed.

I wish to thank Mr. D. Liebsch and Mr. G. Hamelin, from the Central Research Workshop, and Mr. A. Ditchburn in the Department of Chemistry for their assistance during this work.

Additionally, I wish to express my gratitude to the Delta Kappa Gamma Society International. They supported me with a Fellowship during my research work. Their members' kindness and friendship were and will always be invaluable to me.

Finally, I want to deeply thank Mr. and Mrs. Ed. Wagner for everything they did for me, for which I feel greatly indebted.

CONTENTS

ABSTRACT	iii
DEDICATION	iv
ACKNOWLEDGEMENTS	v
LIST OF FIGURES	ix
LIST OF TABLES	xix
LIST OF ILLUSTRATIONS	xx

CHAPTER

I.	INTRODUCTION	1
II.	REVIEW OF THE LITERATURE	4
2.1	Progress in dielectric liquids	4
2.2	Electrical conduction and mobility in dielectric liquids	8
2.3	Phenomena associated with the prebreakdown phase in dielectric liquids	13
2.3.1	The metal/dielectric interface-double layer phenomenon	13
2.3.2	Charge injection and charge carrier creation	17
2.3.3	Electrode processes	19
2.3.4	Space charge effects	26
2.3.5	Magnetic field effects	28
2.4	Electrohydrodynamic (EHD) phenomena	32
2.5	General background of breakdown phenomena in dielectric liquid	36
2.6	The ramped high voltage technique	39
III.	EXPERIMENTAL TECHNIQUE	43
3.1	The high voltage power supply system	43
3.2	The test chamber and the test cell	45
3.3	The measurement and protection system	49
3.4	The properties of liquid dielectrics and the electrode	

	materials	53
3.5	The magnetic field supply	59
3.6	Experimental processing procedure and data-gathering	61
3.7	Prebreakdown test conditions	68
3.7.1	Background noise effects on the experimental system .	68
3.7.2	Residual voltage, current and their corresponding ratio	70
3.7.3	Charge and discharge time effects of the test cell . . .	79
3.7.4	The stability and reproducibility of the experimental results	81
3.7.5	The test cell effect and the meniscus phenomenon . . .	84
IV.	EXPERIMENTAL INVESTIGATION	86
4.1	Dimethyl siloxane liquid (silicone oil)	86
4.1.1	Introduction	86
4.1.2	The average current variation with maximum applied voltage	89
4.1.3	The displacement current variation with maximum applied voltage	90
4.1.4	The displacement current variation with gap distance .	96
4.1.5	V-I threshold point	102
4.2	Voltesso 35 liquid (transformer oil)	126
4.2.1	V-I characteristics with maximum applied voltage . .	126
4.2.2	Current turnover phenomenon	136
4.2.3	V-I threshold point	137
4.2.4	V-I characteristics as a function of gap separation . .	148
4.2.5	Magnetic field effect	164
4.3	Di-iso-octyl-phthalate liquid (ester oil)	179
4.4	Castor oil, polybutene and dodecylbenzene liquids	193
4.4.1	Castor oil	193
4.4.2	Polybutene	194
4.4.3	Dodecylbenzene liquids	196
4.5	Summary and discussion of results	207
4.5.1	Conduction current	208
4.5.2	Displacement current	214
4.5.3	Magnetic field effects	227
V.	AN ELECTROHYDRODYNAMIC (EHD) MODEL FOR HIGH STRESS CONDUCTION IN DIELECTRIC LIQUID	238
5.1	Introduction	238
5.2	Experimental results and discussion	239
5.3	EHD theoretical model	256

5.3.1	Introduction	256
5.3.2	Basic EHD model theory	258
5.3.3	The solitary wave	264
5.4	Computer simulation	269
5.4.1	The iteration equation of the theoretical model	269
5.4.2	Computer-graphical methods	272
5.4.3	Comparison with experimental results	279
5.5	EHD turbulence and the α -effect	288
5.5.1	Experimental results	288
5.5.2	Theoretical considerations	289
VI.	CONCLUSION AND FUTURE WORK	300
	APPENDIX	303
A	Residual voltage and its response current	303
B	The field distribution of the test cell	313
B.1	Computation method and modelling	313
B.2	Calculations and comparison	315
C	The properties of force-free Beltrami flow fields	324
D	Gauge transformation	327
E	The derivation of an analogue to the electrodynamic body force . .	330
F	First and second viscosities	336
	BIBLIOGRAPHY	343
	VITA AUCTORIS	351

LIST OF FIGURES

Figure 2.1	Potential profile in the double-layer	14
Figure 2.2	Metal electrode and liquid interface	23
Figure 2.3	Neutralization of ionic impurities at electrodes under sufficient applied voltage	23
Figure 2.4	Energy states for an insulating micro-region on a metal cathode . . .	24
Figure 2.5	Energy states for an insulating micro-region on a metal anode	25
Figure 2.6	Space charge distortion of the electric field distribution between parallel plate electrodes	41
Figure 2.7	Flow pattern for the EHD phenomenon	42
Figure 3.1	Triangular ramp generator circuit	46
Figure 3.2	High voltage generator circuit	46
Figure 3.3	Sectional view of the test chamber	47
Figure 3.4	Sectional view of the test cell	48
Figure 3.5	Schematic diagram of measurement and protection systems	51
Figure 3.6	Waveform of ramp voltage and the response current as a function of time in silicone oil	52
Figure 3.7	Electromagnetic power supply circuit diagram	60
Figure 3.8	Variations in flux density between the magnetic poles	60
Figure 3.9	A V-I characteristic loop for silicone oil	65
Figure 3.10	A V-I characteristic loop for transformer oil at a relatively high electric field level without current turnover phenomenon	65
Figure 3.11	Applied voltage versus mean current response	67

Figure 3.12	Applied voltage versus displacement current response	67
Figure 3.13	The V-I characteristic loops without the test cell present	71
Figure 3.14	The residual resistance as a function of gap distance	75
Figure 3.15	The high voltage power supply equivalent circuit	76
Figure 3.16	The simplified RC circuit from Figure 3.15	76
Figure 3.17	The modelling of high voltage power supply input and output waveforms	78
Figure 3.18	The maximum applied voltage versus the residual voltage for the high voltage power supply	78
Figure 3.19	The calculated result of the response current	82
Figure 3.20	Charge/discharge time as a function of applied D.C.voltage	83
Figure 3.21	The applied voltage versus the recorded response voltage	83
Figure 4.1	The upper slope value of mean current as a function of maximum applied voltage in silicone oil	92
Figure 4.2	The lower slope value of mean current as a function of maximum applied voltage in silicone oil	93
Figure 4.3	The lower slope value of displacement current as a function of maximum applied voltage in silicone oil	94
Figure 4.4	The upper slope value of displacement current as a function of maximum applied voltage in silicone oil	95
Figure 4.5	Inverse lower slope value of displacement current as a function of gap distance in silicone oil at 20 kV	103
Figure 4.6	Inverse lower slope value of displacement current as a function of gap distance in silicone oil at 30 kV	104
Figure 4.7	Inverse lower slope value of displacement current as a function of gap distance in silicone oil at 40 kV	105

Figure 4.8	Inverse lower slope value of displacement current as a function of gap distance with Cu cathode at 40 kV	106
Figure 4.9	Inverse lower slope value of displacement current as a function of gap distance with Cu anode at 40 kV	107
Figure 4.10	Inverse lower slope value of displacement current as a function of gap distance with Al cathode at 40 kV	108
Figure 4.11	Inverse lower slope value of displacement current as a function of gap distance with Al anode at 40 kV	109
Figure 4.12	Inverse lower slope value of displacement current as a function of gap distance with Mg cathode at 40 kV	110
Figure 4.13	Inverse lower slope value of displacement current as a function of gap distance with Mg anode at 40 kV	111
Figure 4.14	Inverse lower slope value of displacement current as a function of gap distance with Zn cathode at 40 kV	112
Figure 4.15	Inverse lower slope value of displacement current as a function of gap distance with Zn anode at 40 kV	113
Figure 4.16	Inverse upper slope value of displacement current as a function of gap distance in silicone oil at 20 kV	114
Figure 4.17	Inverse upper slope value of displacement current as a function of gap distance in silicone oil at 30 kV	115
Figure 4.18	Inverse upper slope value of displacement current as a function of gap distance in silicone oil at 40 kV	116
Figure 4.19	Inverse upper slope value of displacement current as a function of gap distance with Cu cathode at 40 kV	117
Figure 4.20	Inverse upper slope value of displacement current as a function of gap distance with Cu anode at 40 kV	118
Figure 4.21	Inverse upper slope value of displacement current as a function of gap distance with Mg cathode at 40 kV	119
Figure 4.22	Inverse upper slope value of displacement current as a function of gap distance with Mg anode at 40 kV	120

Figure 4.23	Inverse upper slope value of displacement current as a function of gap distance with Al cathode at 40 kV	121
Figure 4.24	Inverse upper slope value of displacement current as a function of gap distance with Al anode at 40 kV	122
Figure 4.25	Inverse upper slope value of displacement current as a function of gap distance with Zn cathode at 40 kV	123
Figure 4.26	Inverse upper slope value of displacement current as a function of gap distance with Zn anode at 40 kV	124
Figure 4.27	The threshold voltage as a function of the threshold current in silicone oil	125
Figure 4.28	Current response loops with different maximum applied ramped voltage in insulating oil	129
Figure 4.29	The ramp voltage waveform and current response in transformer oil with a relatively low applied voltage (48 kV)	130
Figure 4.30	The ramp voltage waveform and current response in transformer oil with a relatively high applied voltage (65 kV)	131
Figure 4.31	Log V-log I of mean current with applied voltage in transformer oil and silicone oils	132
Figure 4.32	Log V-log I of mean current response with different voltage ramp rates for Cu electrodes	133
Figure 4.33	Log V-log I of mean current response with different voltage ramp rates for Al electrodes	134
Figure 4.34	Upper and lower slope value as a function of maximum applied voltage if transformer oil	135
Figure 4.35	The threshold voltage as a function of threshold current in transformer oil	142
Figure 4.36	The threshold voltage as a function of maximum applied voltage in transformer oil	142
Figure 4.37	The threshold current as a function of ramp rate in transformer oil	143

Figure 4.38	The threshold voltage as a function of ramp rate in transformer oil	144
Figure 4.39	The threshold voltage as a function of ramp rate in transformer oil with current turnover phenomenon	145
Figure 4.40	The threshold voltage as a function of ramp rate in transformer oil with/without current turnover phenomenon using Al electrodes . .	146
Figure 4.41	The threshold ratio (V_{th}/I_{th}) as a function of electrical field	147
Figure 4.42	The upper slope of mean current with different gap spacings in transformer oil	153
Figure 4.43	The lower slope of mean current with different gap spacings in transformer oil	154
Figure 4.44	The upper slope and lower slope values of mean current with gap spacings in transformer oil at 20 kV	155
Figure 4.45	The upper and lower slope values of mean current with different gap spacings in transformer oil at 50 kV	156
Figure 4.46	Log V-log I of displacement current after current turnover point at 1.5 mm gap space	157
Figure 4.47	The upper and lower values of displacement current at 3.1 mm gap spacing in transformer oil	158
Figure 4.48	The upper and lower slope values of displacement current at 6.2 mm gap spacing in transformer oil	159
Figure 4.49	The lower slope value of displacement current as a function of gap separation with differing maximum applied voltages	160
Figure 4.50	The lower slope value of displacement current as a function of maximum applied voltage with different gap separations	161
Figure 4.51	The upper slope value of displacement current as a function of gap separation with differing maximum applied voltages	162
Figure 4.52	The upper slope value of displacement current as a function of maximum applied voltage with different gap separations	163

Figure 4.53	The upper slope of mean current as a function of magnetic flux density with differing maximum applied voltages in transformer oil	168
Figure 4.54	The upper slope of mean current as a function of gap spacings at 100 Gauss with differing maximum applied voltages in transformer oil	169
Figure 4.55	The lower slope of mean current with different magnetic flux density and differing maximum applied voltages in transformer oil	170
Figure 4.56	The lower slope of mean current as a function of gap spacing at 100 Gauss with differing maximum applied voltages in transformer oil	171
Figure 4.57	The upper slope value of mean current with/without magnetic field in transformer oil at 20 kV	172
Figure 4.58	The lower slope value of mean current with/without magnetic field in transformer oil at 20 kV	172
Figure 4.59	The upper slope value of mean current with/without magnetic field in transformer oil at 50 kV	174
Figure 4.60	The lower slope value of mean current with/without magnetic field in transformer oil at 50 kV	175
Figure 4.61	The upper slope value of displacement current with differing magnetic fields in transformer oil	176
Figure 4.62	The lower slope value of displacement current with differing magnetic fields in transformer oil	177
Figure 4.63	The upper slope and lower slope values of displacement current as a function of maximum applied voltage with/without magnetic field in transformer oil	178
Figure 4.64	The waveform of voltage and current response as a function of time in ester oil	186
Figure 4.65	The current response loop with the ramped applied voltage in ester oil	187
Figure 4.66	Log V-log I of mean current characteristics with maximum applied voltage in ester oil	188

Figure 4.67	Log V-log I of mean current characteristics in ester oil	189
Figure 4.68	The resistance R of ester oil as a function of gap spacing	190
Figure 4.69	The displacement current as a function of applied voltage in ester oil	191
Figure 4.70	The current response loop with ramped applied voltage in ester oil at lower field stress	192
Figure 4.71	The current response loop with ramped applied voltage in castor oil	198
Figure 4.72	Upper and lower slope values of mean current as a function of maximum applied voltages in castor oil	199
Figure 4.73	Upper and lower slope values of displacement current as a function of maximum applied voltages in castor oil	200
Figure 4.74	The current response loop with ramped applied voltage in polybutene liquid	201
Figure 4.75	Upper and lower slope values of mean current as a function of maximum applied voltages in Polybutene liquid	202
Figure 4.76	Upper and lower slope values of displacement current as a function of maximum applied voltages in polybutene liquid	203
Figure 4.77	The current response loop with differing ramped applied voltages in DoDecylBenzene liquid	204
Figure 4.78	Log V-log I of mean current characteristics with differing maximum applied voltages in DoDecylBenzene liquid	205
Figure 4.79	Upper and lower slope values of mean current as a function of maximum applied voltages in DoDecylBenzene liquid	206
Figure 4.80	The upper slope values of mean current with maximum applied voltage in six oils	231
Figure 4.81	General relationship between current and field strength for liquid dielectrics.	232
Figure 4.82	The lateral-repulsion model for the capacitance-potential curve . . .	233

Figure 4.83	The flip-up orientation of a water molecule on an electrode	234
Figure 4.84	The flip-down orientation of a water molecule on an electrode . . .	234
Figure 4.85	The RC charge and discharge circuit	235
Figure 4.86	The upper slope of mean current as a function of gap spacings with/without magnetic flux density in silicone oil	236
Figure 4.87a	Effective capacitance as a function of cathode to anode gap voltage	237
Figure 4.87b	The differential capacitance of a semiconductor-electrolyte interface as a function of the potential	237
Figure 5.1	Inverse upper slope value of mean current as a function of gap spacing at 40 kV	245
Figure 5.2	Inverse upper slope value of mean current as a function of gap spacing at 30 kV	246
Figure 5.3	Inverse upper slope value of mean current as a function of gap spacing at 40 kV using same anode materials	247
Figure 5.4	Inverse upper slope value of mean current as a function of gap spacing at 40 kV using same cathode materials	248
Figure 5.5	Inverse upper slope value of mean current as a function of gap spacing at 30 kV using same anode materials	249
Figure 5.6	Inverse upper slope value of mean current as a function of gap spacing at 30 kV using same cathode material	250
Figure 5.7	Inverse upper slope value of mean current as a function of gap spacing at 40 kV using differing cathode materials	251
Figure 5.8	Inverse lower slope value of mean current as a function of gap spacing at 40 kV	252
Figure 5.9	Inverse lower slope value of mean current as a function of gap spacing at 30 kV	253
Figure 5.10	Inverse lower slope value of mean current as a function of gap spacing at 20 kV	254

Figure 5.11	Inverse upper slope value of mean current at 40 kV with differing cathode materials	255
Figure 5.12	The theoretical model for the iteration scheme for EHD Beltrami flows	273
Figure 5.13	The execution of the iteration scheme for EHD Beltrami flows . .	274
Figure 5.14	Simulation result of Y as a function of b after 5 iterations	280
Figure 5.15	Simulation result of Y as a function of b after 40 iterations	281
Figure 5.16	Simulation result of Y as a function of b after 70 iterations	282
Figure 5.17	Iteration process for Y as a function of x	283
Figure 5.18	Iteration process for Y as a function of x with bifurcation	284
Figure 5.19	Iteration process for Y as a function of x with double-bifurcation .	285
Figure 5.20	Iteration process for Y as a function of x in chaotic case	286
Figure 5.21	The experimental and iterated values of slope as a function of maximum applied voltage	287
Figure 5.22	Photographs of bubble movement in castor liquid at 55 kV maximum applied voltage	299
Figure A.1	The equivalent circuit of high voltage power supply system	310
Figure A.2	The simplified RC circuit from Figure A.1	311
Figure A.3	The calculated results of input and output voltages from the RC circuit	311
Figure A.4	The calculated result of response current	312
Figure B.1	Typical examples of oil surface displacement at different maximum applied voltages	319
Figure B.2	Matrix representation of equations for application to two dielectric systems	320
Figure B.3	The arrangement of the boundary condition	321

Figure B.4	The two-dimensional equipotential field plot	322
Figure B.5	The field distribution between the electrodes	323
Figure B.6	The field distribution along the upper electrode	323

LIST OF TABLES

Table 3.1	Insulating fluid properties	58
Table 3.2	The corresponding Resistance R^* for different maximum applied voltages	70
Table 3.3	The residual voltage versus maximum applied voltage	70
Table 3.4	The relationship between the corresponding resistance and distance	73
Table 3.5	The calculated results of the supplied voltage and corresponding current in the test sample	79
Table 5.1	Data after 5 iterations in EHD modeling	277
Table A.1	The calculated results of the supplied voltage and corresponding current in the test sample	309

LIST OF ILLUSTRATIONS

a	acceleration, m/s^2
A	area, m^2
A_z	constant
\mathbf{A}	vector potential, V
\mathbf{A}'	vector potential, V
b	mobility, $\text{m}^2/(\text{V.s})$
B	magnetic flux density, T
B_z	constant
c	constant
\mathbf{c}	fixed vector
C	capacitance, F
C_1	constant
C_2	constant
C_t	total capacitance, F
C_H	Helmholtz layer capacitance, F
C_D	diffuse layer capacitance, F
C_{sc}	capacitance of a semiconductor-electrolyte interface, F
d	gap distance, mm
D	charge diffusion coefficient
D_e	electron diffusion coefficient
E	electric field, V/m

E_l	localized energy, eV (J)
E_d	conductor band energy, eV
E_+	positive energy, eV
E_-	negative energy, eV
E_f	Fermi energy, eV
E_0	uniform electric field, V/m
E_{\max}	maximum electric field, V/m
E_c	characteristic field strength, V/m
E_1	spark gap 1
E_2	spark gap 2
f	renormalized factor
f_c	charge force per volume, N/m ³
f_p	polarization force per volume, N/m ³
f	total force, N
f_e	electrostatic force, N
F_m	magnetic force, N
g	slope value of displacement current
g_u	upper slope value of displacement current
g_l	lower slope value of displacement current
I	total current, A
I_c	mean (or conduction) current, A
I_d	displacement current, A

I_1	the current during voltage ramp up, A
I_2	the current during voltage fall down, A
I_t	total calculated current, A
I_{ct}	capacitance current, A
I_r	resistance current, A
I_{th}	threshold current, A
i_1	charge current, A
i_2	discharge current, A
J	current density, A/m ²
k	constant
k_m	constant
k_{th}	constant
k_{mt}	constant
k_1	constant
k_2	constant
k_3	constant
k'	constant
L_1	discharge solenoid
n_e	electron charge density
p	pressure, Pa
P_v	virtual polarization
q_{CA}	contact-adsorbed ionic charge, C

q_M	charge on electrode, C
q	charge, C
r	resistor, Ω ; radius of the electrode hemisphere, mm
R	resistor, Ω
R_{abo}	constant
R_o	constant
R_1	resistor, Ω
R_2	resistor, Ω
R_3	resistor, Ω
R^*	ratio of V_m and its corresponding residual current, Ω
R_t	total equivalent resistor, Ω
s	appropriate exponent, slope value of mean current
s_u	upper slope value of mean current
s_l	lower slope value of mean current
t	time, s
T	temperature, $^{\circ}\text{C}$
T^*	renormalized temperature, $^{\circ}\text{C}$
u'	apparent convection velocity, m/s
u	velocity, m/s
u_1	first solution of VHE, m/s
u_2	second solution of VHE, m/s
u_3	third solution of VHE, m/s

u_w	wave velocity, m/s
u_e	electron velocity, m/s
U	normalized wave velocity, m/s
U	ratio of temperature of energetic free electrons and normal temperature
V	voltage; electrostatic potential, V
V_c	characteristic potential, V
V'	composite potential, V
V_o	a band potential, V
V_{up}	voltage ramp up, V
V_{down}	voltage full down, V
V_{th}	threshold voltage, V
V_m	maximum voltage, V
V_1	input (source) voltage, V
V_2	out put voltage, V
V_{tho}	constant
V_t	current turnover potential, V
x	space, m
α	α - effect (not to be confused with fluid vector potential)
α	fluid vector potential
α'	fluid dynamic vector potential
σ	conductivity, S
τ	time characteristic, s

μ_-	negative carrier mobilities, $\text{m}^2/(\text{V}\cdot\text{s})$
μ_+	positive carrier mobilities, $\text{m}^2/(\text{V}\cdot\text{s})$
μ_e	quasifree electrons mobilities, $\text{m}^2/(\text{V}\cdot\text{s})$
ρ	mass density, kg/m^3
ρ_e	net space charge density, C/m^3
ρ_e'	electron dynamic charge density, C/m^3
ω	vorticity, rad/s
λ	characteristic length, m
λ_D	Debye length
λ_o	normalized factor
χ	function of space and time
ψ	phase
Ψ	potential velocity
ξ	dynamic potential, V
ν	viscosity, $\text{Pa}\cdot\text{s}$
ν^*	effective dynamic viscosity; second viscosity, $\text{Pa}\cdot\text{s}$
ϵ	dielectric constant
η	magnetic (eddy) viscosity
ϕ	scalar potential
ϕ'	scalar potential
\mathbf{E}'	electrodynamic field, V/m

CHAPTER I

INTRODUCTION

Prebreakdown phenomena studies in dielectric liquids have been extended through the use of different techniques [1]. A ramped high voltage test technique method had been developed by Brignell in 1963 [2]. The strongly non-linear nature of the prebreakdown current versus voltage characteristic in liquid dielectrics has been well known since its description in the early work of Nikuradse in 1932 as reviewed by Denat et al. [3]. A division of the voltage-current (V-I) characteristic is conveniently made into low, intermediate, and high field regions, the last region being attributed to the injection of charge carriers from the cathode into the liquid. This division is more clearly evident from the log-log plot of the characteristic in which the high field portion is linear. Analysis of the experimental results of several studies was made by Ostroumov [4]. He showed from theoretical considerations that when the liquid is in laminar electrohydrodynamic motion induced by charge injection the current should vary as the cube of the voltage [4].

Watson et al. developed this ramped high voltage test technique in recent years with which accurately reproducible current characteristics are obtainable. These tests were performed with different viscosities of silicone oils [5-12]. In the previous work, only one type of liquid has been tested. Those test methods moreover do not give any

information on the effects of varying the maximum applied voltage swing, or the effect of changes in the electrode gap distance while subjected to the same changes in the maximum applied voltages.

The purpose of this work is to understand the mechanism of prebreakdown phenomena in dielectric liquids in which a great number of variables affects prebreakdown current. These variables include the nature of the dielectric liquid, the material properties of the electrodes, and experimental conditions. The research procedure that has been followed can be divided into two main parts. The first part is mainly experimental. It examines the response current variation with the applied voltage. This is done through the experimental observation of a number of phenomena and parameters associated with the liquid conduction, space charge effects and the prebreakdown process. This is accomplished by careful choice of different types of insulating liquids, electrode gap separations, maximum applied voltage rates, the presence of weak magnetic fields, etc. From the experimental results, an attempt is made to identify the mechanisms responsible for different dielectric liquids. Moreover, the space charge and displacement current are also taken into account.

The second part of the research is theoretical. It was considered appropriate to attempt to describe the many factors that affect the electric conduction current and prebreakdown processes, and to investigate the electrohydrodynamic phenomenon in liquid insulation in general. The objective was also to include development of a

mathematical model which is substantiated by results obtained by computer simulation.

Finally, a conclusion and suggestions for further work are included in the final chapter of this thesis. The details of theoretical derivations, an explanation of referenced theories, and the calculation of the electric field distribution of the test chamber are undertaken in appendices.

Chapter II

REVIEW OF THE LITERATURE

2.1 PROGRESS IN DIELECTRIC LIQUIDS

Dielectric liquids have extensively served as insulators or dielectrics in electrical equipment for more than 100 years. The dielectric liquid served the purpose of providing superior insulation when paper or other solid dielectrics are impregnated with it. When used by themselves they provided an excellent heat transfer medium for removal of heat which is generated by electrical losses. Among the advantages of liquid insulators, in comparison to solids, is the ease by which they take the shape of their container and cover conductors and other oddly shaped parts. They have the ability to recover after a failure and to circulate, thus transferring the generated heat to the environment. When compared to gaseous dielectrics, liquid insulators exhibit a much higher dielectric strength and a much higher thermal capacity. Only pressurized gas insulation systems have all the advantages of liquid insulators, but the related technology is more expensive.

The properties of insulating liquids can be divided into physical, chemical and electrical properties. In general, the thermal and flow characteristics of a liquid are of greatest importance at the design stage of equipment. While chemical properties are

important during equipment operation, electrical properties are important for monitoring the condition of oils both before and in service. However, the most important property of a liquid insulator is the ability to maintain insulating properties and other desirable attributes in service. For example, oil-cooled power equipment such as transformers requires a medium which is fluid at all climatic and operating temperatures [13].

Historically, the standard fluids used in electrical apparatus were low-viscosity, petroleum-based oils. They were used as liquid dielectrics for transformers even before 1887. Since then, various synthetic liquids have also been used as insulating liquids such as: chlorinated aromatics, fluorocarbons and silicones, together with synthetic hydrocarbons similar to the natural ones. Each of these has found uses only in specific circumstances. As the least costly and most efficient insulation for high voltage apparatus, mineral oils are the most important and main insulator type for the power industry in the future.

Most often properties of a mineral oil are dependent upon its composition. General conclusions can be drawn from a knowledge of the hydrocarbon distribution [14]. The low viscosity petroleum oil is related to a particular family of hydrocarbons, and remains fluid at comparatively low temperatures such as - 50 °C [15]. This property was believed to be necessary to insure proper performance of transformers after they had been inactive under arctic weather conditions. As a consequence of shrinking crude oil

reserves, it became evident during the early seventies that the world supply of naphthanic crude oil was decreasing rapidly [1]. The aromatic content of an oil, on the other hand, increases its tendency to absorb oxygen when subjected to discharge, and was widely believed to increase its tendency to oxidation [16]. Paraffinic crude oil did not satisfy the low temperature requirements, in part because of the saturated (paraffinic) hydrocarbon composition of the crude oil. In the new products, these molecules were mainly linear hydrocarbons, whereas those derived from naphthenic sources contain branched molecules. Two solutions offered themselves. The first created more branched species from the linear ones, while the second one involved the use of special additives that retarded the onset of crystallization of the linear hydrocarbons and thus lowered the pour point of the oil. After extensive field testing, this approach gained approval and is now being used in northern climates [1].

One of the earliest concerns with mineral based insulating oil was its flammability or explosive hazards associated with it in particular conditions. Polychlorinated biphenyls (PCB), also known under their trade names "askarels", were recognised as meaning a non-flammable insulating liquid and became synonymous with chlorinated aromatic liquids later on. There were nonflammable fluids that were used in applications such as indoor sites where the flammable mineral oils were not acceptable. These fluids have good properties for transformer applications, but they are not suitable for circuit breakers because the presence of hydrogen and chlorine produces hydrogen chloride when an arc is drawn under the liquid. In the mid 1970s, it was determined that PCBs

were no longer environmentally acceptable. Certain isomers of PCB have a high resistance to biological degradation with the result that problems of toxicity are being encountered subsequent to environmental pollution from spillage and leakage [15].

Since then, significant research efforts have been directed toward the development of improved fire- and explosion-resistant fluid filled transformers. This effort led to the requirement that all new candidates for use in electrical apparatus be biodegradable, and be harmless to people upon contact with their skin or when ingested. In the search for a replacement, questions arose as to what permittivity level was desirable and what was to be done about flammability and related fire hazards. It became apparent that new materials had to be found that had properties similar to those of PCB. However, all candidates had some deficiency. For example, silicone oils were "flammable" but their permittivity was low and the cost was high. Others such as the phthalate ester were commercial, had reasonable permittivity, but they were flammable and their flash point was too low.

Recently, phenylxylene ethane (PXE) isopropyl biphenyl with good gas absorption characteristics and reasonably inexpensive, was found to be an acceptable replacement [1]. Another commercial alternative to PCB fluids was the so-called high temperature hydrocarbons (HTH) with high molecular weight. They have good electrical insulating and adequate heat-transfer properties. They also were flammable but with high fire points up to 312°C [17]. These fluids are chemically very similar to regular petroleum-

based mineral oils for transformers. Tetrachloroethylene (C_2Cl_4) [18] is a non-flammable insulating fluid that was introduced commercially in 1979 but only used for small power transformers. On the other hand, the flammability issue became less of a problem when pressure-sensitive current shut-off devices were introduced in capacitors and transformers [1].

2.2 ELECTRICAL CONDUCTION AND MOBILITY IN DIELECTRIC LIQUIDS

An earlier review of electrical conduction and breakdown in liquid dielectrics written by Goodwin and Macfadyen in 1952 [19] states that strong fields produce conduction by field emission from the cathode, together with ionization of the liquid molecules by electron collision. A more comprehensive review was made by Lewis [20] in 1959. The conductivity of pure dielectric liquids has been studied under two main headings. At strengths up to 100 kV/cm (low and intermediate field), a portion of the current in this field strength region is due to the presence of ions produced by dissociation or by impurities. At higher field strengths the current tends to increase rapidly as the breakdown value is approached. In this range, the conditions of the electrodes and the liquid have a marked influence [20]. Sharbaugh and Watson pointed out that at high field strengths the conduction process is known to involve emission of electrons from the cathode by either (1) cold emission, sometimes called field emission, in which electrons tunnel through the surface potential barrier, or (2) field enhanced thermionic emission, usually referred to as Schottky emission. The latter process is a

consequence of the lowering of the work function barrier by the applied field so that appreciable thermionic currents are emitted even at room temperature [21].

Based on the electrolytic dissociation and electrode reactions theory and taking advantage of electrochemical knowledge, Felici gives more detailed work on the conduction in liquid dielectrics in [22]. The conductivity of a liquid dielectric could be divided into three divisions, low-voltage, intermediate voltage and high voltage. The low voltage conductivity of a liquid dielectric is ultimately controlled by its capability of dissolving impurities that are prevalent everywhere and ionizing the electrolyte. This is related to the solvating properties of the liquid. Every sort of physical or chemical bonding is brought about by the interaction of electric charge distributions whose carriers obey the laws of quantum mechanics. In the intermediate voltage regime, the conduction is controlled by the kinetics of ionic dissociation, a state of affairs never encountered in conventional electrolysis. The ions that are moving in any volume element of the liquid are no longer in equilibrium with neighbouring electrolyte molecules, but were created elsewhere at some distance by irreversible dissociation. It could be objected that the kinetics of electrolyte dissolution are also involved, but dissolution and ionization are intimately related.

At the same time, space charges are usually observed in the vicinity of electrodes. These are mostly "heterocharges", i.e., charges having a sign unlike that of the electrode they are adjacent to. High voltage conduction is always attended by space charge

development, but in a very erratic and non-reproducible way. Ionization by electronic collisions does not play any part in this phenomenon, nor does ionization by positive ions. Nevertheless, the appearance of homocharges has been frequently recorded, and this hints at mechanisms that are fundamentally different from these active at low and intermediate voltage, for homocharges cannot arise from ions generated in the bulk of the liquid, but must be created at the electrodes themselves. The residual ions responsible for low-voltage conduction play an essential part in the triggering of interface phenomena. The role of the field is merely to cause ions to gather at the interface and to set up some sort of double layer which strongly affects the barrier. This process is controlled by ion concentration and velocity, and at the same time by kinetics of ion neutralisation. As an obvious consequence, actual carrier injection at interfaces does not depend on field strength alone, but much more on the delicate balance between those competing processes [22].

Gallagher later [23] pointed out that electrode effects dominate the current-controlling process and, in air-saturated liquid, the anode may exercise a much greater control than previously assumed [20,21,24-26]. It became apparent that electrical conduction processes caused by quasifree electrons, and holes, can also play an important role [27]. Following the electrolytic theory, Felici explained another mechanism in the conduction liquid [28] which is described briefly as follows. Electrochemical conduction has two sources: (1) electrolytic dissociation of solutes or (rarely) of the liquid itself, (2) carrier injection at liquid/electrode interfaces. The latter should not be confused with

electron emission. First, positive injection occurs as frequently as negative injection. Secondly, the microscopic mechanisms are vastly different. Recent work done by Tobazeon [29] proved that ionic processes also play a significant role at very high fields which includes: (1) ion injection at the anode or at the cathode; (2) field-enhanced dissociation of tiny amounts of ionizable impurities, or of the liquid itself; (3) increase in the ionic mobility, its possible variation with the field being identical to the electronic mobility increase.

Ion or electron charge carrier mobilities are very important in the theory of conduction. It could help to identify the main charge carriers which are involved in prebreakdown conduction processes. There are two types of ions normally present in a liquid. The first, which is quickly removed from the body of the liquid on application of a field is most likely to arise from dissociated electrolytic impurities, while the second is continuously regenerated and is probably produced by partial dissociation of the dielectric itself. Positive or negative ion mobilities are of a much lower order of magnitude corresponding to the greater mass involved [26]. Measurements of the mobilities of ions in liquid helium indicate that usually the negative carrier is not a free electron, and the evidence suggests that impurities are acting as trapping agents for the electrons [21]. The quasifree electrons were found to have mobilities four to five orders of magnitude greater than those of negative ions [23].

This discovery divided the mobility of charge carriers into "slow" and "fast"

models. For slow charge carriers, the spread in values for negative (μ_-) and positive (μ_+) carrier mobilities may be caused by the method of charge injection. Negative ions in many insulating liquids result from the capture of electrons by impurities. Oxygen appears to be the dominant impurity, but other electron scavengers may also be present. It is most improbable that electron attachment will occur to the molecules of liquids. Fast (quasifree) electrons can exist in liquid argon, krypton, xenon and methane, and fast electrons can also exist in ultra-pure hydrocarbons such as n-hexane and n-pentane. The transport of positive ions has not been examined to any large extent.

Although these liquids exhibit similar chemical and physical properties, the electrons have widely different mobilities in those hydrocarbons which range over three orders of magnitude. Molecular structure appears to influence the mobility of quasifree electrons (μ_e) in two ways. First, μ_e is observed to increase with increasing sphericity of the molecules. Secondly, the electrons seem to lose their energies in the excitation of molecular rotations. μ_e is determined by a series of jumps between short-lived traps, which are created by particular configurations of groups of molecules [23]. According to this model, an injected electron travels some distance d before being trapped. After a time t the electron escapes from the trap and travels another free path before being trapped again, and d is much smaller than the total interelectrode distance. A free electron would be expected to have a much larger mobility than a trapped electron, so that a measurement of the mobility should enable one to identify the charge carrier [21].

2.3 PHENOMENA ASSOCIATED WITH THE PREBREAKDOWN PHASE IN DIELECTRIC LIQUIDS

2.3.1 THE METAL/DIELECTRIC INTERFACE-DOUBLE LAYER PHENOMENON

The double layer is an interface region which arises when an electrode comes into contact with an electrolyte. Since electrodes can be made of a variety of metals, semiconductors, and composite materials, and the electrolytes can occur in different states, a large variety of interfaces can arise across which electrochemical reactions can proceed [30]. In the last decade the importance of the influence of the electrical double layer -the metal/dielectric interface- on the behaviour of insulation involving liquids has been emphasized.

It is well known that a metal has a high concentration of mobile electrons, while a dielectric insulator has nearly none. When these two materials are brought together, the second law of thermodynamics predicts that a transfer of electrons will take place from the metal to the dielectric to relieve the concentration gradient. This transfer is limited because of the build-up of image charges. Nevertheless, some electrons will escape the metal and find their way into the dielectric [1]. From the electrochemical point of view, the schematic structure of the double layer region formed between a metal electrode and an electrolyte solution is shown in Figure 2.1 [31]. The essential modern theory of the double-layer combines an aspect of the "fixed layer" theory of Helmholtz

(also referred to as the compact layer or Helmholtz double-layer) with the idea of a distribution of ions (inherent in the Gouy-Chapman treatment in the diffusion layer)

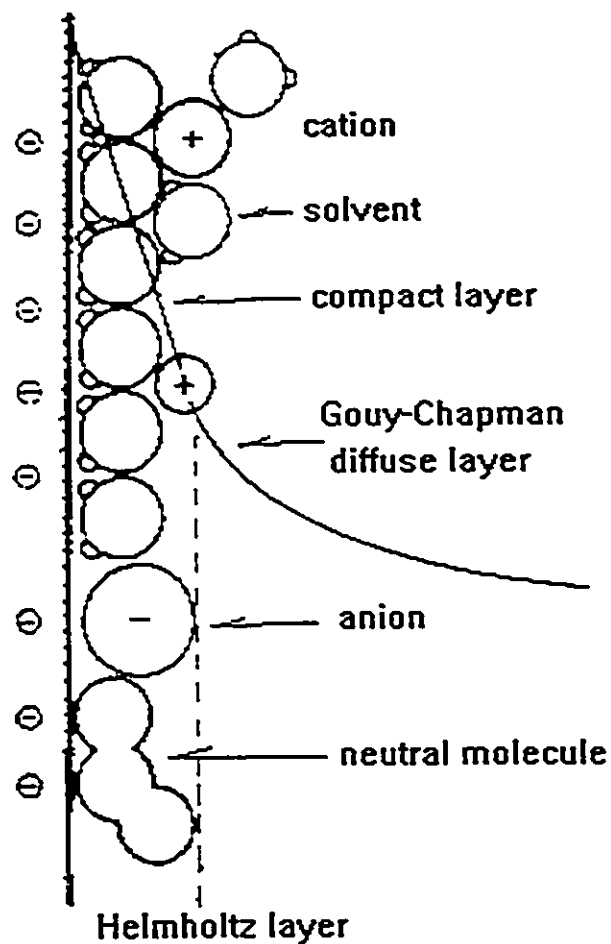


Figure 2.1 Potential profile in the double-layer

determined by the opposing effects of ion interaction and thermal disordering.

The compact layer is defined as being the layer which consists of the closest ions of finite radii to the plane of the metal-liquid interface. The diffuse layer is intermediate to the compact layer and the bulk liquid. This diffuse layer contains, for various reasons, ions that may be chemisorbed at the metal-liquid interface. The latter effect is related to that implicitly involved in Helmholtz's picture of the double-layer (shown in Figure 2.1), though the potential profile very near to the interface can be sufficiently accounted for by the introduction of the recognition that real ions have finite, and not zero, radii. The charge distribution then is cut off at a certain critical average distance from the interface with the result that the potential profile is a discontinuous one as shown in Figure 2.1 [31].

It is noted that the prediction of the sign and the value of the net charge on the solid is rarely possible, but that the charge distribution in that zone of the liquid referred to as the diffuse layer follows the Poisson-Boltzman equation. The diffuse layer is constituted by charges which are only weakly bound to the metal. These charges can therefore be moved by an electric field and affect the electrical behaviour of liquid insulation. As a result, a double layer is an interfacial region between two homogeneous phases. In this region the charged constituents have been separated so that each side of the interface is electrified. The charges on the two sides are equal in magnitude but opposite in sign, thus making the interphase region electrically neutral as a whole. The

distribution of particles in the double layer region could be modelled as a parallel-plate capacitor (or two capacitors in series) [32]. Some of the ionic charges exist in the first layer (Helmholtz layer) in a partly rigid sheet on the solution side, other particles were scattered out into the solution (diffusion layer). The majority of sites on an electrode surface are occupied by water molecules, due to image forces, dispersion forces or chemical (bonding) forces [32]. All this indicates that even an uncharged electrode has an attraction for water molecules, and the forces which bind water molecules into networks in the liquid phase may be overcome in this process.

When an electric field is applied to a liquid, the diffuse layer at each wall is swept away. Their movement contributes to the transient current density, which may explain a transient current, and the compact layer may modify the stationary current density [33]. The potential variation across a double layer, consisting of two regions, a linear region corresponding to the ions stuck on the electrode, and an exponential region corresponding to the ions which are under the combined influence of the ordering electrical and the disordering thermal forces [32]. The value of the total capacitance, which varies with a change in potential, has become dominated by the diffusion layer capacitance. Since this total capacitance is modeled by two capacitors in series, this electrode-liquid interface has a total differential capacitance which is given by the Helmholtz and Gouy diffusion capacitances in series. Meanwhile, the forces of attraction between water molecules and the electrode will still operate, and therefore, there will still be a water layer. In addition, the charge on the metal will stimulate the water molecules to orient

themselves (charge implies field, and dipoles tend to align with fields).

2.3.2 CHARGE INJECTION AND CHARGE CARRIER CREATION

It has been known for a long time that charge carriers may appear either in the bulk of the liquid or at the surface of metallic electrodes. Most often, both mechanisms act at the same time by the strong dependence of the static current on the impurities or the metal of the electrode [34]. The creation of carriers in liquids is a two-step process: the first, ionic dipole-formation, and the second, separation of these charges by the applied field. Injection of charge carriers by a metallic electrode can also be represented similarly by a two-step process, first creation of charge carriers at the metal/liquid interface, and then extraction of ions out of the image-force region. According to the values of the kinetic constants related to both steps, the injection current density increases quickly with the field, or saturates [35].

The experimental studies [35] had shown that the electric field does produce ion injection. It has become evident that there exists only a limited number of such injection sites on the metal surface. This means that only a small fraction of an electrode surface actually participates in the injection process. Moreover, under d.c. excitation the observed current is mainly due to the events taking place in the immediate vicinity of the two electrodes. This current has very little to do with the actual transport of charge across the dielectric liquid. The injected electrons rapidly lose their energy to the

dielectric. These "thermalized" electrons polarize the surrounding molecules and thus form clusters that last for a few pico-seconds [1]. During that time, the electron-cluster will barely move under the influence of the electric field. Alternately these electrons may attach themselves to molecules having significant electron affinities such as O_2 , polar or aromatic molecules, and form stable anions. These anions as well as the clusters will diffuse through the dielectric fluid and eventually arrive at the anode to be discharged there. The rate of transport will depend on the size of these ions or clusters, the local viscosity and the electric field. In the absence of such electronic traps, it is possible to observe the transport of more or less free electrons. The restriction to low electrical fields is required because as the externally applied potential difference increases, the average kinetic energy of the injected electrons increases as well as the electric field in the immediate vicinity of the injecting electrode [1].

Considering the states of injection: there are the transient state and the steady state. In the transient state of injection, information about the sign and the mobility of the injected ions is obtained. With the steady state the only measurable parameter is the injection current density. It appears that in the transient state of injection, the injected ions may be anions of the dissolved electrolyte that are extracted from a charged layer at the electrodes, whereas in the steady state the injected ions are created by electrochemical reactions [34]. The ions are extracted by the field from a reservoir at the double layer, and a Schottky-like description of the effect accounts very well for the current flowing. In any case, the injection of ions as distinct from electrons appears to

be a universal phenomenon [36].

2.3.3 ELECTRODE PROCESSES

Electron transfer from the cathode to the liquid, or from the liquid to the anode, represents an important mechanism for the injection of charge carriers in liquids. The formation of a double layer at the electrodes enhances the electric field strength. It has been natural to invoke electron injection at the cathode as an important factor since high fields will lower the potential barrier to electron transfer across the interface whether it occurs by a thermally activated or tunnelling process. Under zero field conditions, the metal and liquid in contact will attempt to reach an equilibrium by electron exchange (described previously). The energy states involved will be for the metal those both occupied and empty near the Fermi energy E_F , and for the liquid the band of empty electron states with a band edge at V_0 and localized levels E_t below the band of occupied donor states centred on E_d . The contact situation would then be as in Figure 2.2. The equilibrium would require electron transfer from the liquid to the metal [26].

Conditions will change after a potential is applied between the electrodes. At the cathode the additional potential difference across the interface region will encourage a reverse transfer of electrons back into the liquid while at the anode more positive ions will be injected [26]. Carrier injection of this sort will make the liquid more conductive, but it is also possible for an applied potential difference to have the opposite effect. If

residual ions already exist in the liquid as a result of impurity dissociation, then they can be transported to the electrodes and neutralized at electrodes under sufficient applied voltage (over potential) to give $E_+ \leq E_f$ and/or $E_- \geq E_f$ as shown in Figure 2.3.

Efficient electron transfer into the liquid from the cathode will require a high field at that electrode. This can be obtained if any positive ions or holes in E_d states which drift to that electrode are not readily neutralized, and thus build up a positive space charge Helmholtz Layer (compact layer). In practice, most electrodes will be covered with a natural oxide or other semi-insulating layers.

A number of authors have determined the emission characteristics of similarly covered metal electrodes placed in a vacuum rather than a liquid. In particular Watson (1976) [38,47] and later Latham and his co-workers (1982) [37] have provided a so-called diagram model to explain them. The essential ideas are expressed in Figure 2.4. It is suggested that micro regions of the electrode surface of perhaps 10^{-8} m radius contain oxide or other semi-insulating inclusions to a thickness of about 10^{-7} m. The layer is considered to be a wide band gap insulator or semiconductor but with many imperfections which will act as carrier traps as in an amorphous solid. It is important that a relatively narrow (Schottky) barrier can be expected at the metal-insulator interface. When a field is applied, it penetrates the layer and encourages electrons to tunnel from the metal into the conduction band of the insulator-semiconductor interface (Figure 2.4).

When the applied field is sufficiently strong and the traps become filled, free electrons of high energy will be produced. These free electrons are swept to the outer face of the oxide to create a pool of electrons. Some holes may also be produced by collision ionization and these will drift back to the metal face to enhance electron tunnelling. The condition for electron emission into the vacuum would be that the applied field should generate a potential drop to compensate for the Schottky barrier as well as any resistive drop in the layer and the electron affinity at the vacuum interface [37].

This model requires little modification if it is applied to electron emission into a pure hydrocarbon liquid [26]. This is the case as the conduction band states, at an energy V_0 , are close to the vacuum level. Moreover, the electric fields at breakdown in a liquid are generally much greater than those suggested by Latham as necessary for barrier lowering, and the relative permittivities of oxide and liquid will be more favourable than oxide and vacuum. In the liquid case it will also be possible for positive ions or holes from the liquid to be fed back to the oxide surface. Moreover, the energy level E_d of this band of states will be about the same as that of the valence band of the oxide. As a consequence, the hole states could be transferred readily from the liquid through the oxide to the metal interface where they will enhance electron tunnelling.

If insulating layers can occur on a metal cathode, they may be expected also on the anode. However, the energy states are such (Figure 2.5) that electrons of energy V_0

and even anions due to impurity trapping will be more readily neutralized than the corresponding cations at the cathode. With a sufficient influx of electrons and negative ions and a finite rate of neutralization through the anode surface layer it would be possible to build up a dynamic Helmholtz layer. It is possible, under those conditions that even a diffusing space charge layer would raise the energy of electron states in the liquid with respect to the metal Fermi energy E_F . At appropriate sites on the anode, where the double layer could generate a potential drop, electrons would tunnel from donor states to the metal (Figure 2.5). Thus positive hole injection into the liquid would occur and could be as localized as electron injection at the cathode. Its occurrence, however, would depend on a precursor, namely sufficient supply of negative charge from the liquid to establish and maintain the initiating double layer on the anode [39]. Both cathode and anode injection processes can depend in a complex way on the interfacial processes.

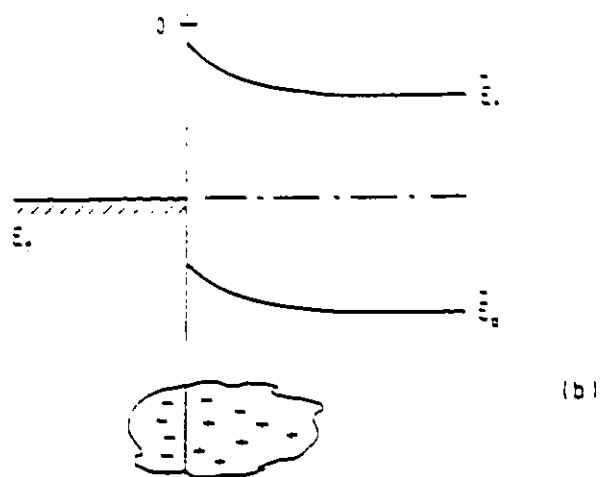


Figure 2.2 Metal electrode and liquid interface after contact equilibrium is reached with positive hole (ion) space charge (Helmholtz and Gouy) layer in liquid'

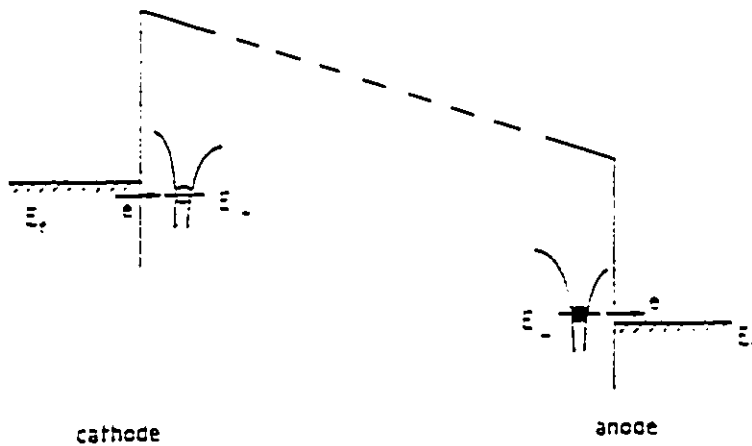


Figure 2.3 Neutralization of ionic impurities (E_+ , E_-) at electrodes under sufficient applied voltage (over-potential to give $E_+ \leq E_r$ or $E_- \geq E_r$)

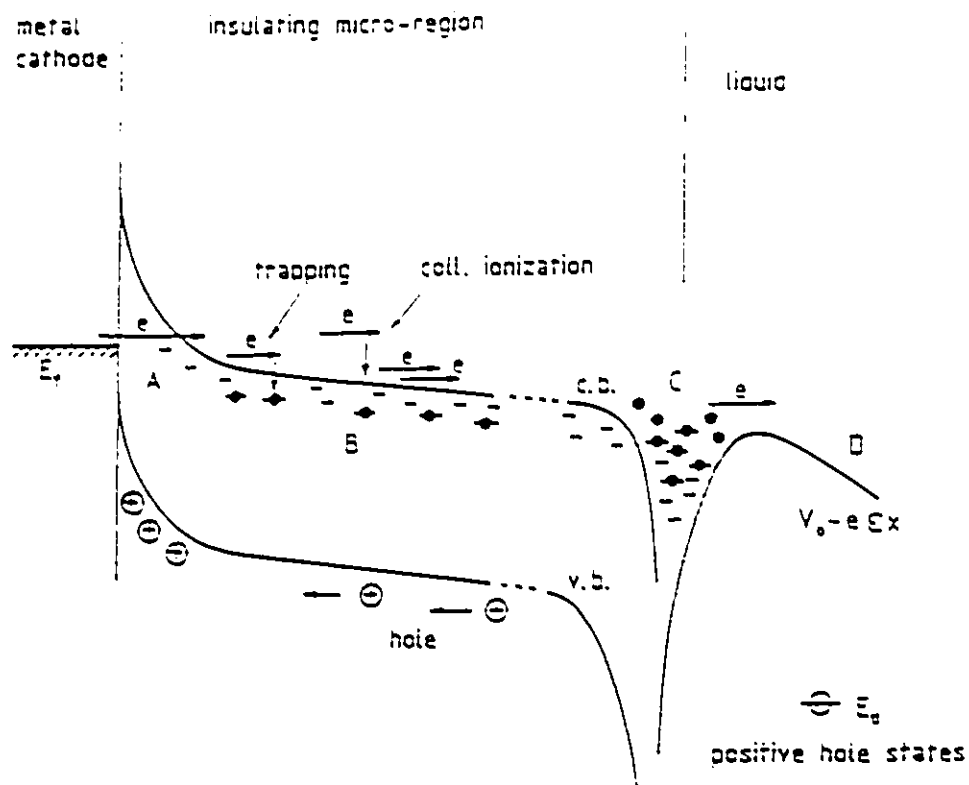


Figure 2.4 Energy states for an insulating micro-region on a metal cathode. Electrons tunnel from cathode to conduction band of insulator through Schottky barrier.

- Electron traps become filled,
- Electrons accumulate at electron-affinity barrier at insulation-vacuum interface,
- Holes produced by collision ionization drift to A and enhance electron tunnelling. Electrons with enhanced kinetic energy emitted over barrier C into liquid conduction band,
- Positive hole states of liquid E_L , drifting to interface, readily transfer holes to insulator valance band and, thence, to barrier A.

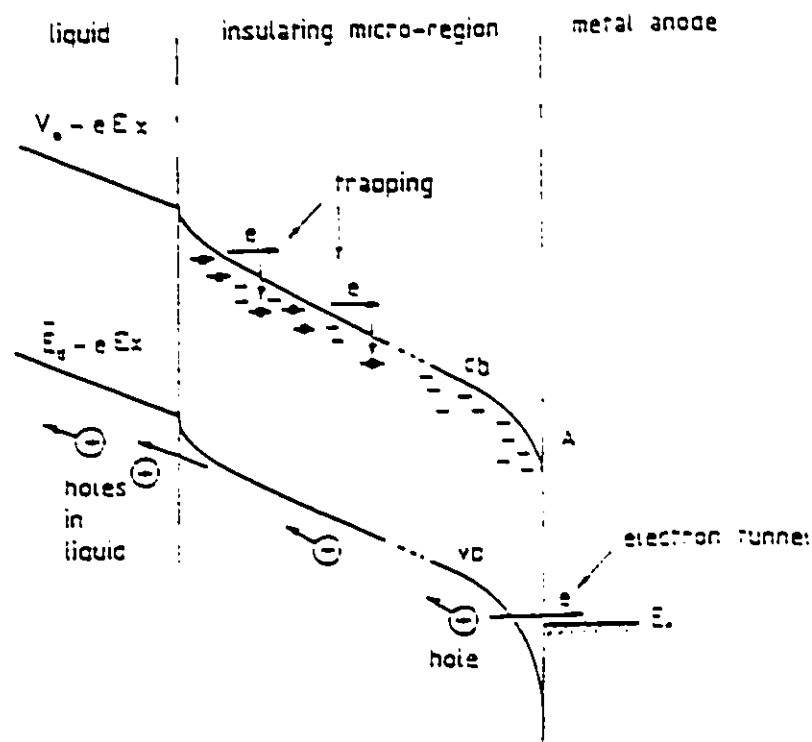


Figure 2.5 Energy states for an insulating micro-region on a metal anode

Situation corresponding to Figure 2.4 but at an anode. Electrons from liquid states V_0 are held in bulk and interface trap states of insulator micro-region, establishing a strong field across region. This field, enhanced by applied field, reduces barrier at insulator metal interface A so that electrons tunnel from valence band of insulator to metal states near E_F . Holes drift to outer liquid-insulator boundary and readily move into liquid as positive hole (ion) states.

2.3.4 SPACE CHARGE EFFECTS

The concept of "space charge" was introduced to distinguish these entities from the surface charges which are the only ones present on perfect dielectrics or on perfect conductors. Electrical charges may exist in a dielectric either before the application of an electric field or in consequence of the application of such a field. Among the causes of the spontaneous formation of space charges here are the following sources: electrolytic dissociation; ionization by radiation; and intrinsic liberation (thermal) or extrinsic liberation (caused by impurities) of electrons or holes [40]. All these mechanisms are characterized by the fact that they give rise to equal numbers of positive and negative charges. It will be assumed generally that before the application of the electric field, their respective densities are equal at all points except possibly in the vicinity of the electrodes. After the application of the electric field the charges may be formed either in the bulk dielectric or near the electrodes.

Considering the type of space charges in insulating liquids, it is possible to divide them into two groups: liquids containing heterocharges and liquids capable of forming homocharges. Heterocharge liquids are those in which the charges formed in the vicinity of each electrode are opposite in sign to the charge of the electrode; the charges appearing in homocharge liquids have the same sign as those of the electrodes (those which are not connected to earth) [41]. Liquids classified as homocharge include highly viscous dried oil, and heterocharge liquids are dry liquids of low viscosity such as

silicone oil. Heterocharge liquids will produce homocharges in the liquid as well as heterocharges when moist. According to Gauss' theorem, homocharges create increasing electric fields as seen by an observer moving away from the electrodes, while heterocharges create a decreasing field for the same observer [42]. As an example [41] Figure 2.6 shows several conventional distributions of space charges and the resulting electric field distortion in a dielectric liquid. The sign of the space charge is that of the variation of the electric field.

Consider the case of planar electrodes, as shown in Figure 2.6, for a voltage V across a gap of magnitude d with an electric field E directed along the x axis. This electric field E is distorted by the net space charge with density $\rho_e(x)$ dependent only on the x coordinate. Gauss' theorem requires that the slope of the electric field distribution be proportional to the local charge density:

$$\nabla \cdot E = \frac{\rho_e}{\epsilon} \text{ ----- } \frac{\partial E}{\partial x} = \frac{\rho_e}{\epsilon} \quad (2.1)$$

For no volume charge shown in Figure 2.6a, the electric field is uniform given by $E_0 = V/d$. The electric field drops at a charge injecting electrode, but its average value E_0 remains constant at V/d . Charge injection thus causes the electric field to increase above the average value at other positions. In Figure 2.6b, unipolar injection has the electric field maximum at the non-charge injecting electrode, thus possibly leading to electrical breakdown at lower voltages. The strongest distortion due to unipolar space charge occurs for space charge-limited injection at one electrode where

the injected charge density is infinite so that the electric field at the injecting electrode is zero. The electric field at the non-injecting electrode is then about 50% higher than the average field value. For bipolar homocharge injection as shown in Figure 2.6c, positive charge is injected at the anode and negative charge is injected at the cathode, so that the electric field is lowered at both electrodes and is largest in the central region. Figure 2.6d shows such a bipolar heterocharge configuration occurs when the dielectric is ionized so that free ions are attracted to their image charges on the electrodes.

The sign and magnitude of the space charge depends strongly on the electrode material and voltage polarity. Although injected space charge can increase the attainable system voltage and therefore the stored energy, the usable energy delivered to a load is less than the space-charge-free capacitive energy storage value of $(1/2)CV^2$ due to energy dissipated as the injected charge migrates to the electrodes, where C is the capacitance. The unipolar charge injection that increases the electric field at the non-charge-injecting electrode leads to early electrical breakdown and bipolar homocharge injection at both electrodes where injected charges shield the electrodes, causing lower electrode fields.

2.3.5 MAGNETIC FIELD EFFECTS

Only a few papers have been published on the possible influence of an applied magnetic field upon the conduction or breakdown process of liquid dielectrics due to the importance of other factors. If breakdown is initiated by collisional ionization processes

involving hot electrons, then it might be expected that a magnetic field would increase the electron collision frequency because of the Lorentz forces and thus raise the electric field strength [43]. Savenu and Mondescu [44] investigated the influence of a magnetic field on the electric conductivity of liquids. They assumed that the magnetic field caused a change in the collision frequency between mobile charges and the liquid molecules, thereby altering the conductivity. A small number of test results of magnetic field perturbation of conduction have been reported for polar liquids, water and ethyl alcohol. As a result, the conductivity remained constant for magnetic flux densities up to 2×10^{-2} Tesla (T), and thereafter, decreased linearly to another constant value up to 3×10^{-2} T, the maximum flux density used. It was also shown that the effect was undetectable for non-polar liquids, benzene and transformer oil, in which the conductivity was independent of magnetic field up to the maximum value [44].

Further work was carried out by Gallagher [45] who reported a 10% positive increase with a 0.6 Tesla magnetic field in the direct breakdown voltage of sphere-sphere and point-sphere copper and aluminum electrode configurations at $100 \mu\text{m}$ gap separation in pure n-hexane. More significant, however, was the observation of almost no influence upon the pre-breakdown current except when the electric stress was initially applied. It suggested that impurity particles which may oscillate between the electrodes, donating and acquiring opposite charges at each electrode, will experience a small Lorentz force acting in the same direction during each traverse of the gap and some particles may be ejected from the active region of the gap after several oscillations. Microscopic

examination of the gap revealed particles between the electrodes, but their motion did not seem to be affected by the presence of a magnetic field and even the rapid application of the field did not deflect any particles which could be seen moving in the liquid [45].

Secker and Hilton [46] have investigated the magnetic influence upon the breakdown voltage of brass spheres in hexane liquid using a ramp voltage generator with a growth rate of 0.625 kV/s. The results indicated that for 100 and 150 μm gap separations the breakdown voltage increased 2 - 4% with magnetic field of 0.02 T but 7% decrease between 0.02 and 0.2 T. There appears to be no simple explanation of the phenomenon observed. Secker assumed that the magnetic field interacts with charge carriers in the interelectrode spacing, therefore, modifying their trajectories so as to perturb the onset of breakdown. For such trajectory modification, he suggested that the majority of the charged particles, present in the inter-electrode space, must be free electrons to explain such effects. The result of that investigation, however, did not positively confirm the existence of a magnetic perturbation of the conduction process itself.

Watson and Girgis [5] proceeded in this investigation and confirmed the existence of such a magnetic field effect in the case of prebreakdown current of copper hemispheres in silicone liquid which, like hexane, is non-polar, but asserts its presence down to magnetic flux densities as low as 3.4×10^{-3} T. It is shown that under the action of a weak magnetic field, for spacings between 0.6 cm and 1.0 cm there is a decrease

in the prebreakdown current but it increases from then up to 1.4 cm. In magnitude and sign the perturbation is strongly dependent upon the gap separation, and the range is much wider than those investigated in hexane.

Magnetic influence upon breakdown has been observed and reported in other situations such as vacuum and a low density gas. For instance a magnetic perturbation in vacuum breakdown was reported by Watson [47] as being a surface phenomenon in the oxide layer present on metallic electrode surfaces, upon exposure of the metal to the atmosphere. It has been suggested that a weak magnetic field acting transverse to the electric field can influence the current emitted by a protrusion through a magneto-transport effect and the resulting current reduction modifies the breakdown voltage. This effect is significantly influenced by the relative magnitude of the surface oxide work function and that of the inner potential barrier at the underlying metallic junction [47]. Moreover, the influence of magnetic fields on dielectric surface breakdown voltage has been investigated under pulsed voltages by Krompholz, et al. [48,49]. Insulation effects dependent on the polarity of the magnetic field begin at flux densities of 0.2 T. Ohki and Saito reported [50] that the shape of the electrode affects impulse flashover voltage along the surface of a solid insulator with a magnetic field. When the high voltage electrode is point shaped, the flashover voltage increases steadily with the increase in magnetic flux density regardless of the polarity of the applied impulse voltages. Lehr et al. [49] pointed out that the correct orientation of a magnetic field can result in substantial increases of the surface flashover voltage, both under vacuum and with a low

density background plasma. The "wrong" orientation, however, can result in a decrease in the flashover voltage.

2.4 ELECTROHYDRODYNAMIC (EHD) PHENOMENA

The electrohydrodynamic (EHD) motion of liquid dielectrics has been studied for various types of configurations. The main research has involved the development of theoretical models for the phenomenon, and two independent sources for the body forces that cause it are identified: polarization forces and forces on charged liquids. An excellent review of the phenomenon of electrohydrodynamic motion was written by Felici and Lacroix of the work by the C.N.R.S group at Grenoble [51,52]. Additionally, Chang and Watson explored this EHD phenomenon. EHD motion occurs when space charge exists in poorly conducting liquids subjected to sufficiently high fields for a voltage-related stability limit to be exceeded. The necessary voltage for the onset of motion ranges from tens of volts to hundreds depending on the physical details of the system [53]. The driving energy comes from the electric field. The motion results from significant variation in space charge density in the inter-electrode space. In insulating liquids there is no significant charge creation or loss within the liquid. Charges are injected or removed at the electrodes. With the onset of electroconvection, charge transport takes place by means of liquid motion. The electrically driven liquid travels much faster than ions can drift through a stationary liquid under the same field. As a result a charge carrier can be regarded as immobile with respect to the surrounding

liquid. The motion is characterized by jets or streams of liquid leaving the injecting electrode and travelling towards the opposite electrode against a counterflow of uncharged liquid [53].

Mathematically speaking, each little volume of fluid in the interelectrode region experiences two forces. Assuming a space charge density ρ_e , the electrostatic force per unit volume will be: $f_e = \rho_e E$, where E is the electric field vector. The fluid will also experience polarization forces. If ρ is the specific mass density and ϵ the dielectric constant of the liquid, the polarization forces per unit volume will be

$$f_p = \frac{E^2}{2} \nabla \epsilon + \nabla \left(\rho \frac{\partial \epsilon}{\partial \rho} \frac{E^2}{2} \right) \quad (2.2)$$

For a homogeneous fluid at constant temperature it holds that $\nabla \epsilon = 0$, so Equation 2.2 becomes:

$$f_p = \nabla \left(\rho \frac{\partial \epsilon}{\partial \rho} \frac{E^2}{2} \right) \quad (2.3)$$

Combining f_e and f_p , the total force f is, therefore, as:

$$f = f_e + f_p = \rho_e E + \nabla \left(\rho \frac{\partial \epsilon}{\partial \rho} \frac{E^2}{2} \right) \quad (2.4)$$

This force also has to be equated to

$$f = \rho \alpha - \eta \nabla^2 u + \nabla p \quad (2.5)$$

according to basic hydrodynamics [51]. Where (α is the acceleration, u the velocity and

η the viscosity), $\rho\alpha$ is the acceleration term, $k\nabla^2 u$ is the friction term and ∇p is a pressure gradient. So, the combination of Equation 2.4 and Equation 2.5 yields:

$$\rho_e E + \nabla(\rho \frac{\partial \epsilon}{\partial \rho} \frac{E^2}{2}) = \rho \alpha - k \nabla^2 u + \nabla p \quad (2.6)$$

It will be assumed now that there is no EHD motion. The liquid being at rest, the acceleration term $\rho\alpha$ and the friction term $k\nabla^2 u$ become zero, so Equation 2.6 becomes:

$$\rho_e E + \nabla(\rho \frac{\partial \epsilon}{\partial \rho} \frac{E^2}{2}) = \nabla p \quad (2.7)$$

Since the right hand side of Equation 2.7 is a gradient of a scalar quantity (p), its curl is equal to zero. The same holds for the second term of the left hand side of Equation 2.7. Thus by taking the curl of both of its sides, Equation 2.7 yields:

$$\nabla \times (\rho_e E) = 0 \quad (2.8)$$

By vector analysis it is true that

$$\nabla \times (\rho_e E) = \rho_e (\nabla \times E) + (\nabla \rho_e) \times E \quad (2.9)$$

But since E is the gradient of the potential, it holds that

$$\nabla \times E = 0 \quad (2.10)$$

so Equation 2.9 becomes:

$$\nabla \times (\rho_e E) = (\nabla \rho_e) \times E \quad (2.11)$$

Finally, combining Equations 2.8 and 2.11 the conclusion is

$$(\nabla \rho_e) \times E = 0 \quad (2.12)$$

as a result of the assumption that the liquid is at rest. However, it is obvious that Equation 2.12 cannot hold everywhere in the interelectrode region. When charge is injected into the liquid by electrodes, as the case is with high voltage experiments, EHD motion prevails throughout the liquid. Cross reported [53] the EHD flow patterns for intermediate and high voltages being as shown in Figure 2.7 for a parallel plane electrode gap with a spacer. The EHD motion affects liquid breakdown by the creation of local pressure drops that facilitate generation of microbubbles, especially on electrode surfaces. Finally, EHD motion rearranges the space charge distribution in the liquid in a way that significantly modifies the electric field.

There will be a considerable error if it is assumed that the electric field in a stressed liquid dielectric under electrohydrodynamic motion is given by Poisson's equation with the assumption of ion drift through a stationary liquid. Additionally, it may be possible that liquid involved in rotational motion in a vortex close to a solid surface generates a local streaming electrification, so that more charge gets into the liquid and influences the prebreakdown and breakdown processes [51]. After several years of research work, Watson recently proposed a new EHD model. It is the first time that both the electrostatic and electrodynamic fields have been combined into the electrical prebreakdown theory. More details will be given in Chapter V.

2.5 GENERAL BACKGROUND OF BREAKDOWN PHENOMENA IN DIELECTRIC LIQUIDS

Generally speaking, at the end of the last decade, there were two main categories on liquid breakdown [24,43,54]: (1) the electronic theory: the breakdown results from electron multiplication, a gaseous phase being possibly generated (as a consequence of ionizing collisions); and (2) the bubble theory: gas bubbles are formed first (several mechanisms are possible), grow, ionize, and lead to breakdown. A new mechanism of electric breakdown in liquid dielectric involving electro-hydrodynamic instabilities has emerged in the past decade due to progress in understanding electronic conduction and the streamer mechanism [27,55,56]. This process is characterized by a streamer which has a fast growth rate and that leads to the eventual development of the overall breakdown channel. It is very important to mention that the formation of low density regions are necessary but not sufficient to cause breakdown. They occur at voltages below the critical breakdown voltage and they occur even in the purest of insulating liquids [25].

Filici [57] examined a free gas bubble in an electrically stressed liquid. The insulating bubbles are stable against any imaginable kind of disturbance and will thus survive. After ignition (partial discharge), strong instability and break-up is the commonest occurrence; tremendous field concentration may occur and trigger intrinsic breakdown of the liquid phase. When the voltage across the bubble parallel to the

applied field is sufficiently large ignition occurs. Bubble ignition is the result of the relationship given by Paschen's law. The preceding treatment only gives necessary conditions for bubble initiated breakdown, and does not predict the actual breakdown strength. Ignition renders the bubble conducting, and then breaks up by sheer instability, causing a tremendous field concentration to appear in the liquid, well beyond its intrinsic strength. Breakdown could then be initiated.

According to Schmidt [54] there are four stages in the development of the breakdown process: (1) electronic stage: Electric charge carrier generation at metal electrodes by field emission or field ionization. Formation of a space charge region. (2) electro-thermal stage: Temperature rise due to frictional motion of charge carriers; formation of low density regions at points of largest energy dissipation; corona light emission; expansion of low density region towards counter electrode; bubble surface instabilities. (3) gas discharge stage: Formation of a gaseous discharge channel from cathode to anode; light emission; high temperatures; rupture of molecular bonds; formation of radicals and ions. (4) physical-chemical stage: Extinguishing of the discharge; temperature decrease; recombination of ions and radicals; formation of molecular products.

Similar to the Schmidt theory, Watson emphasises more the mechanism of liquid breakdown which involves the generation and propagation of vapour channels through the liquid. He introduced a three stage process [58]: (1) the creation of a rapidly

expanding ionized vapour cavity adjacent to the point electrode. (2) the EHD instability of the cavity surface, characterized by the growth of a wave-like disturbance, and (3) the runaway growth of the instability leading to a vapour streamer that bridges the gap and causes the actual breakdown. He assumed that the vapour in the cavity is ionized due to the high field, so that the potential at the bubble surface is close to that of the point electrode. The EHD instability of the cavity surface gives rise to the most characteristic feature of the breakdown process.

Based on the Schmidt theory in the formation of a low density region, Forster and FitzPatrick [59] pointed out that the bond breakage and impact ionization occur within the primary streamer. The resulting expansion of the low density region has been shown to lead to electronic breakdown within this region, further contributing to the degradation process. A primary streamer that does not lead to breakdown will leave behind thermalised electrons and/or ions which are commonly referred to as space charges. These will modify the local field. An electrohydrodynamic instability arises at the leading edge of the primary streamer which gives rise to a serious distortion of the local charge distribution leading to a greatly enhanced local field. Since this process occurs preferentially in the direction of the opposite electrode, the extent of field-induced ionisation increases as the disturbance approaches that electrode which is the secondary streamer. Once the secondary streamer reaches the other electrode, a conductive path is established between the electrodes. Furthermore, current research has shown that prebreakdown streamers in insulating liquids proceed in two distinct ways [56]: a very

slow mode bush-like or mushroom-like in shape, and a comparatively fast one with few filamentary branches. It is shown that the ionized gaseous phase must have a minimum conductivity to allow for the observed propagation. For slow streamers this conductivity level corresponds to a glow or luminescent discharge, while in the fast ones, ionization would reach arcing level.

2.6 THE RAMPED HIGH VOLTAGE TECHNIQUE

Prebreakdown conduction studies in dielectric liquids have been extended through the use of different techniques. An improved test method had been developed in response to the need for closer control in direct-stress electrical breakdown investigations by Brignell in 1963 [2]. In this automatic measurement a high voltage power supply was arranged to give an output voltage which is a slow, linear ramp function of time. The voltage was reset automatically on breakdown, and a recorder and thyatron by-pass circuit completed an automatic system which was capable of making the large number of closely controlled measurements needed for a statistical study. In 1970 Spitzer [60] used this technique successfully for prebreakdown and breakdown measurements on transformer oil. The breakdown measurements were entirely automated following opinions concerning the importance of uniform testing conditions. Voltage application rates were varied and intervals between tests changed over wide ranges without effect. Later Secker and Hilton [61] investigated the breakdown stress in hexane subjected to a transverse magnetic field by using the rising ramp output voltage system basically similar

to the equipment described previously.

Generally speaking, a ramp generator supplies a current which is a linear function of elapsed time and feeds into a high voltage generator thus producing a rising ramp of output voltage. It should be emphasised that all the previous work had been done by increasing the voltage at a linear ramp function of time to a predetermined maximum applied voltage level or up to the breakdown level. A programmable voltage scan generator designed in early 1980 by Rao et al. has been reported [62], and provided the triangle, square, step and ramp voltage waveforms suitable for cyclic voltammetry, polarography, anodic stripping voltammetry and other electrochemical applications with the maximum output amplitude at ± 6 Volt.

In 1976 Watson and Girgis [5] first reported the investigation of the liquid characteristic variation of prebreakdown conduction current with a triangular wave form voltage. In recent years, Watson et al. [6] developed this ramped high voltage test technique with which accurately reproducible current characteristics are obtainable using different viscosities of dimethyl siloxane liquids (silicone oil) as a function of voltage when this is raised and lowered steadily at a uniform ramp rate, the details will be described in Chapter III.

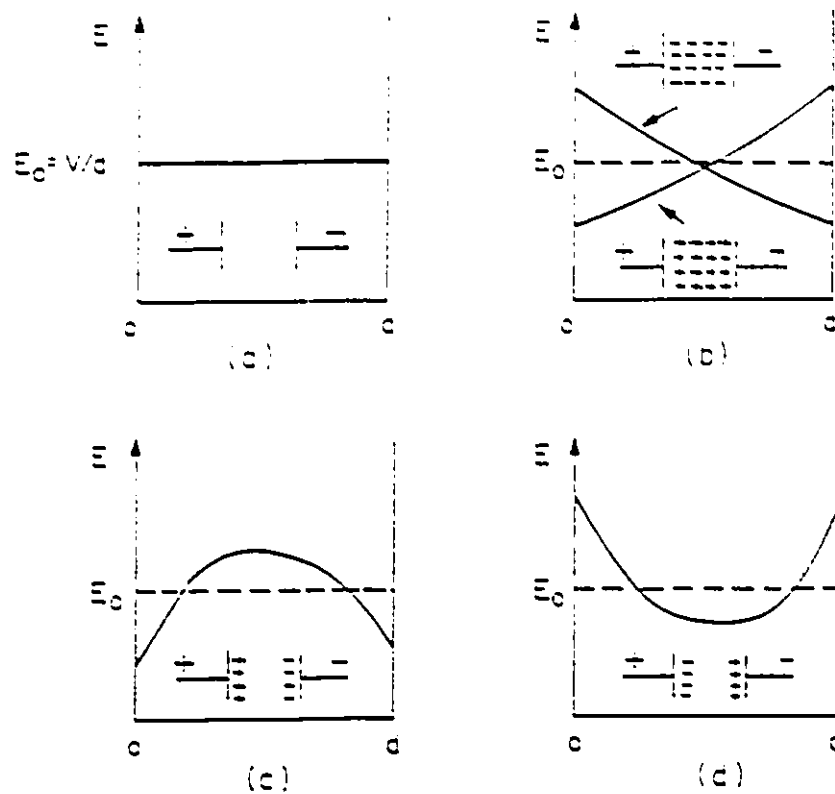


Figure 2.6 Space charge distortion of the electric field distribution between parallel plate electrodes

E_0 is the average electric field.

- (a) No space charge so that the electric field is uniform at E_0 .
- (b) Unipolar positive or negative charge injection so that the electric field is reduced at the charge injecting electrode and enhanced at the non-charge injecting electrode.
- (c) Bipolar homocharge injection so that the electric field is reduced at both electrodes and enhanced in the central region.
- (d) Bipolar heterocharge distribution where electric field is enhanced at both electrodes and depressed in the central region.

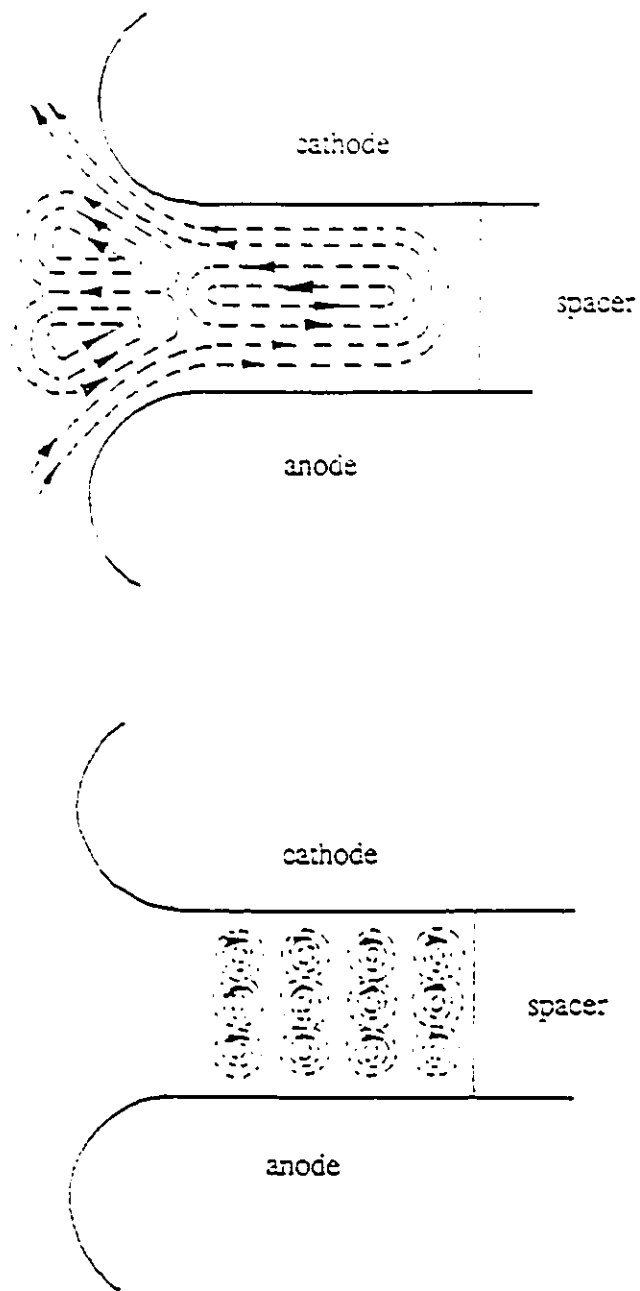


Figure 2.7 Flow pattern for the EHD phenomenon

Chapter III

EXPERIMENTAL TECHNIQUE

The experimental apparatus can be divided into three groups: the high voltage circuit, the test chamber and the devices for measurement and protection. The components of each group are specified below, with special emphasis being placed on those which had to be custom-designed and built, especially components for the measurement and protection devices group. The experimental procedure and the investigation of test conditions will also be included in this chapter.

3.1 THE HIGH VOLTAGE POWER SUPPLY SYSTEM

The high voltage power supply system was made by Del Electronics Corporation and consisted of two separate subassemblies, a high voltage supply tank, model PSO 80-5-9, and a control panel, model RM6-80-5-9. The high voltage power system was capable of delivering up to 80 kV with supplied current from 0 to 5 mA when operated from a 115 V, 60 Hz, single phase source [63]. The high voltage D.C. was generated by connecting the high voltage supply to a motorized variable turns ratio autotransformer (brand name Variac) shown in Figure 3.1. This motorized Variac was used to control the value of the ordinary high voltage supply in order to give a ramping output voltage. The associated control and measurement modules in the set were directly connected to the output terminals of the Variac. The final output ramped triangular voltage waveform

was produced by driving this with an induction stepper motor to create a voltage increasing and decreasing, also shown in Figure 3.1. The high voltage D.C. circuit is shown in Figure 3.2, consisting of a step-up transformer (T) supplying high voltage to the full-wave voltage doubling circuit CR_1 - CR_2 and C_1 - C_2 . Resistor R_1 was the output series limiting resistor. Resistor R_2 provided bleed current for the voltmeter circuit, the over-voltage protection circuitry and the servo regulating circuitry. Resistor R_3 was the high voltage discharge resistor. When the system is turned off, the high voltage discharge solenoid L_1 is de-energized, this discharges the residual high voltage through R_3 . Spark gaps E_1 and E_2 conduct in the event of an open circuit in either the metering or the sensing circuits, to prevent a dangerous voltage build-up at the control panel. Another resistor of $150\text{ M}\Omega$ was used as a high voltage discharge resistor which absorbed the extra energy from the entire high voltage system after the system is switched off. The schematic diagram for the high voltage system is shown in Figure 3.2.

The variation in the voltage due respectively to ripple and regulation was equal to or less than $\pm 0.5\%$ of the high voltage output, and a $\pm 10\%$ line variation for a load variation from no load to full load. The control panel contained electronically controlled voltage and current overload protection. The front panel could be set to trip at from 0-120 % of full rated output voltage and current with front panel trip indication lights. The high voltage output of the unit would automatically de-energize if the output voltage or current should exceed these settings. The servo-motor which drives a variable autotransformer regulator had a zero-start interlock which includes a control panel light

for indicating the zero position and an automatic return to zero upon turn-off. The high voltage was monitored through a resistive voltage divider of $80\text{ M}\Omega$ with a 10 : 3 ratio ($80\text{ M}\Omega : 240\text{ }\Omega$), calibrated by high voltage D.C. voltmeters. The $80\text{ M}\Omega$ resistive divider was measured by means of a Bridge Megger Tester from Thorn EMI Instruments Ltd. The output of the resistive divider was fed to an X-Y recorder. All of the high voltage circuitry, measurement and control devices were grounded. A common grounding point was connected to the laboratory ground provided in the building.

3.2 THE TEST CHAMBER AND THE TEST CELL

A sectional view of the test chamber used in the experimental system is illustrated in Figure 3.3. At the top of Figure 3.3, there is shown a corona-free bushing which was used such that the ramped high D.C. voltage was fed through this into the test chamber and eventually connected to the test cell upper electrode. The middle part of the chamber was a cylindrical plexiglass enclosure in which a window in the front was provided so that the test cell could be moved in and/or out of it for cleaning and preparation purposes. During the test, the window was closed so that the test chamber was relatively isolated from the outside (surrounding area). Below the plexiglass part was the heart of the test chamber within which the test cell was located during the experiments. The test chamber was made of cast steel. This cast steel yoke provided a good magnetic flux path for magnetic field effect testing. A pair of the magnetic

excitation coils and pole pieces which were mounted on each side of the cast steel part will be described later. The bottom part of the test chamber was a plexiglass plate sealed at the cast steel section.

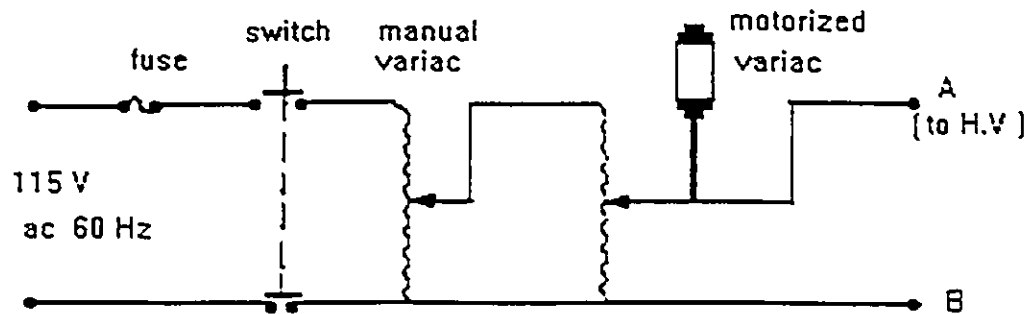


Figure 3.1 Triangular ramp generator circuit

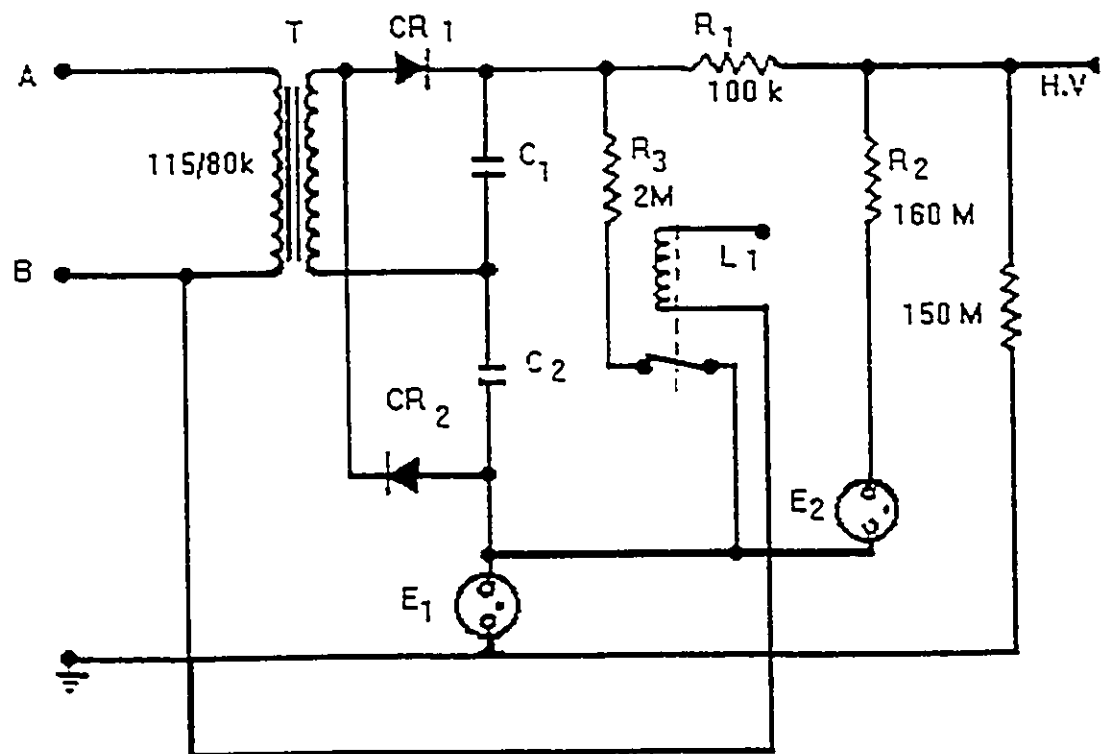


Figure 3.2 High voltage generator circuit

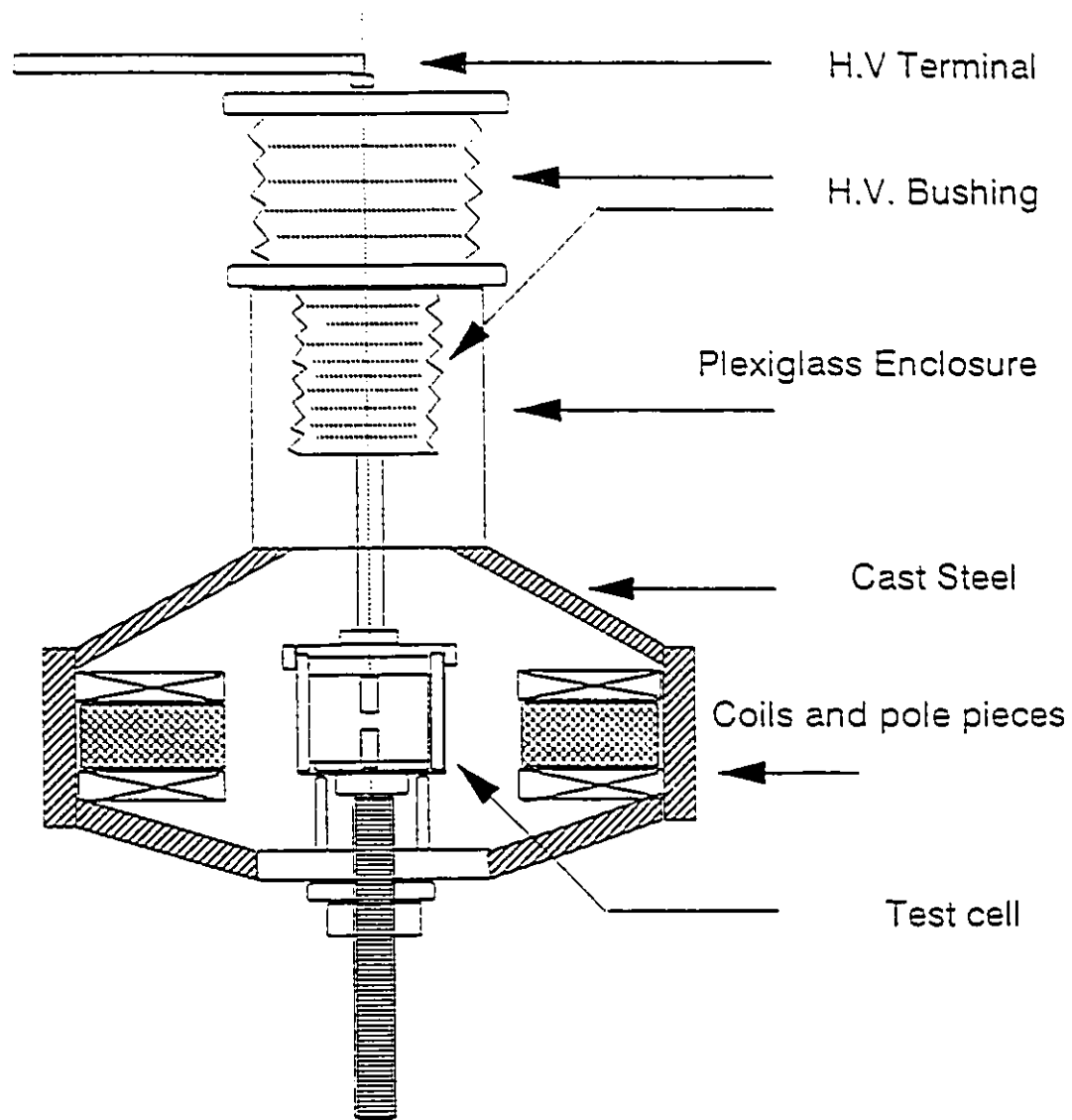


Figure 3.3 Sectional view of the test chamber

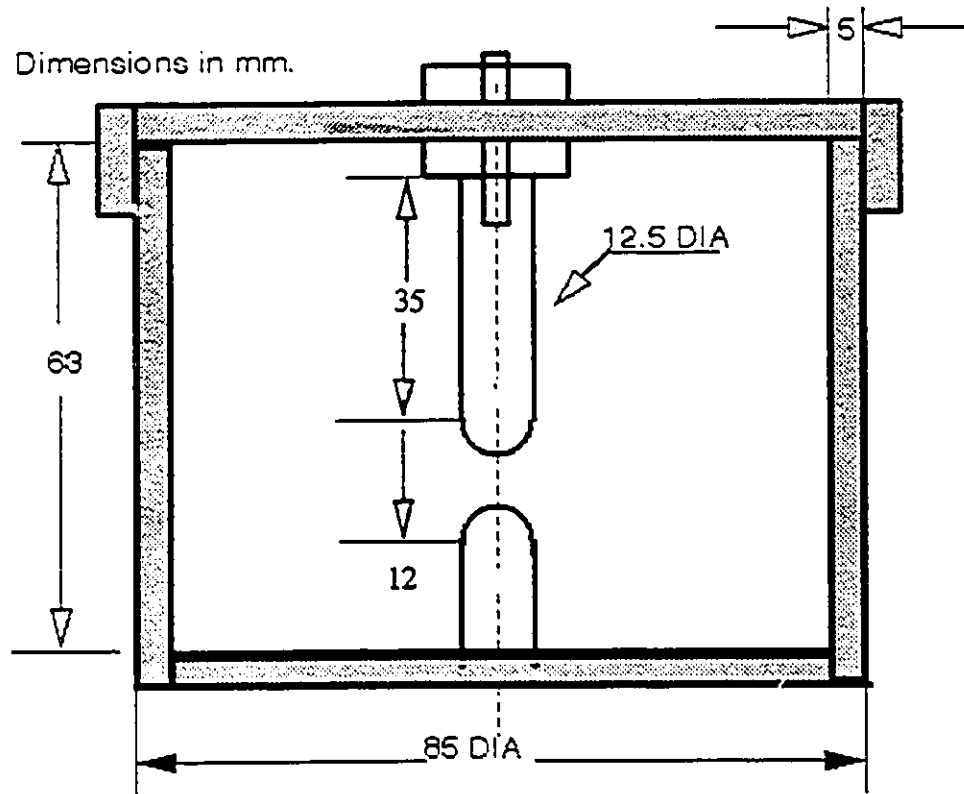


Figure 3.4 Sectional view of the test cell

The test cell for containment of the sample oil and the electrode assembly is shown in Figure 3.4. The test cell was a cylindrical plexiglass container with an internal diameter of 75 mm, a height of 63 mm and a wall thickness of 5 mm respectively. The volume of sample oil for each test was about 200 mL. The cylindrical electrodes, having hemispherically shaped tips, were 12.5 mm in diameter for all the experiments. The electrodes chosen for use in the tests were threaded on to the electrode shafts. The test cell was supported by insulating material which could be fixed to the chamber base during the test. In the test cell, the ground electrode was constructed in such a way that

the electrode gap spacing could be controlled from outside of the test chamber. The ground electrode could be displaced vertically using a threaded arrangement. A micrometer gauge at the bottom, below the chamber base plate, indicated the vertical displacement with a precision of ± 0.01 mm.

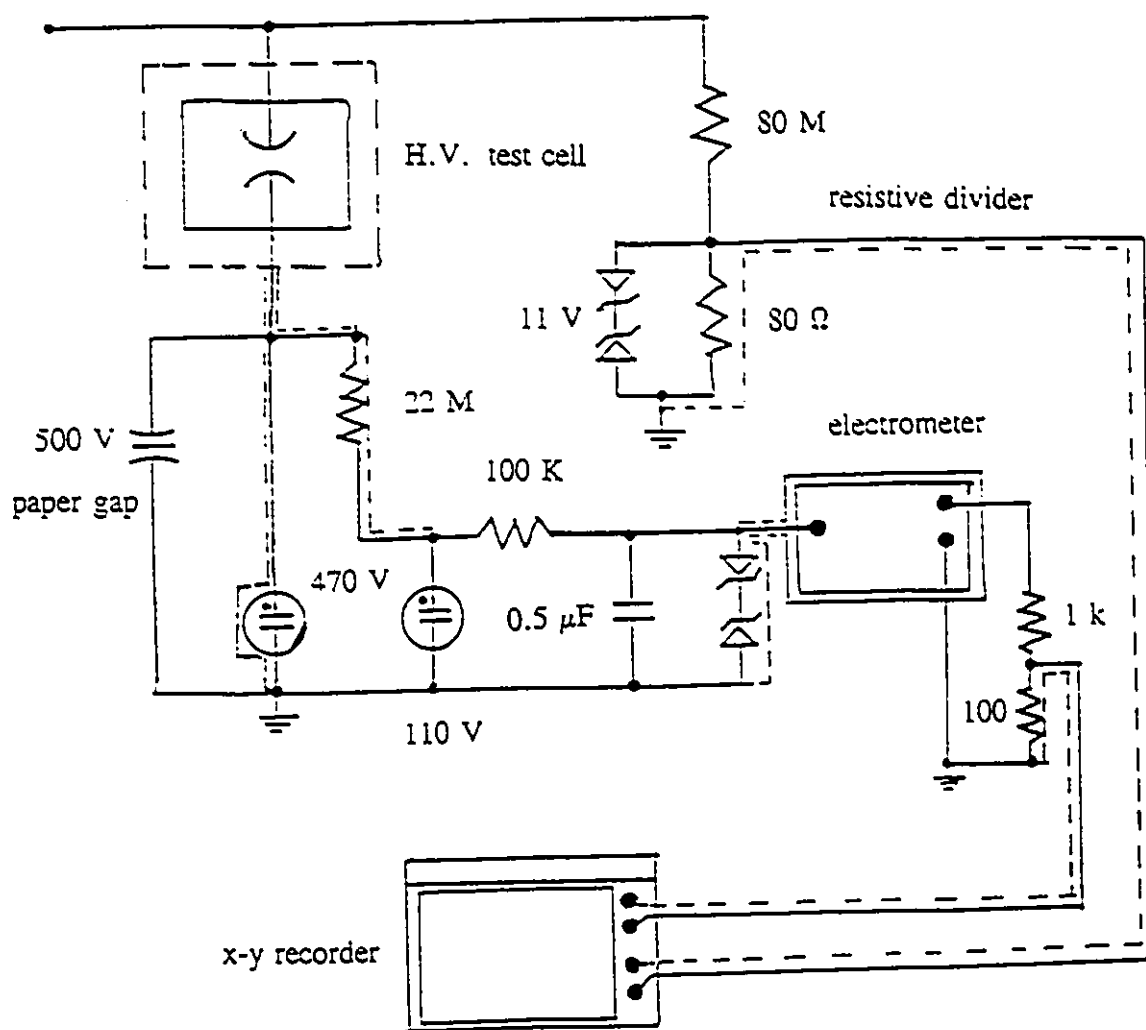
3.3 THE MEASUREMENT AND PROTECTION SYSTEM

The basic instruments of the measurement system were a Keithley Model 616 or Model 617 Electrometer and a Lloyd Model PL3 X-Y Recorder seen in Figure 3.5. The digital electrometer essentially is a digital multimeter, optimized for measurements from a high source impedance, which provided a wide range capability when measuring current, resistance, and charge in addition to voltage. The response current measurements were obtained from the ground electrode of the test cell which was inserted in series with the test gap. When the model 616 was used as an ammeter in the experiments, it was set to the 1×10^{-5} A range by utilising the automatic sensitivity and, with either "Fast" mode of operation for the low current test or "Normal" mode of operation for higher current measurement (rarely used for the present series of experiments). For the model 617 meter, it was set to the 1×10^{-6} A range. The input cable from the ground electrode was used with the model 6101A cable which was a straight through probe and shielded lead equipped with 0.8 m of shielded low noise cable terminated by a Teflon-insulated UHF connector.

The X-Y recorder had two functions, one was a self-balancing potentiometer recorder which plots one variable D.C. voltage as a function of a second variable D.C. voltage. One variable was applied to the arm servomechanism which controls the arm movement along the X-axis; the other variable was applied to the pen servo mechanism which controls the pen movement along the Y-axis. The combination of the two motions generates a plot of X vs. Y. In this case, the X-Y recorder was used as measuring voltage (V) vs. current (I) in the X-Y mode. The voltage value was obtained directly from a resistive voltage divider and, the dielectric prebreakdown current input was from the 1.0 V analog output of the electrometer for model 616 or 2.0 V analog output for model 617. Another function performed by the X-Y recorder was that of plotting V or I vs. time by setting a voltage (or current) timebase so that the X axis can be made to move at a constant speed. The period for one cycle of the test, which was fixed by the motor driven Variac, was 10 seconds. The voltage rise and fall times were each 5 seconds. The record of the applied voltage (V) and typically observed response currents (I) as a function of time for silicone oil are shown in Figure 3.6.

The protection system was designed to protect the measurement system from high voltage and large current hazards if liquid breakdown or flashover across a surface were to occur, and to eliminate the noise and interference from outside. A combination of a paper gap of 0.10 mm which fires at about 500 V, two sets of gas filled surge arrestors

Figure 3.5 Schematic diagram of measurement and protection systems



operating at 470 V and 110 V respectively, and a set of back to back Zener diodes operating at 11 V, were used in this protection circuit shown in Figure 3.5. All protective devices used were previously tested. The current measurements with and without the protection circuitry, under the same conditions, showed no effect on the values obtained for the current response [7].

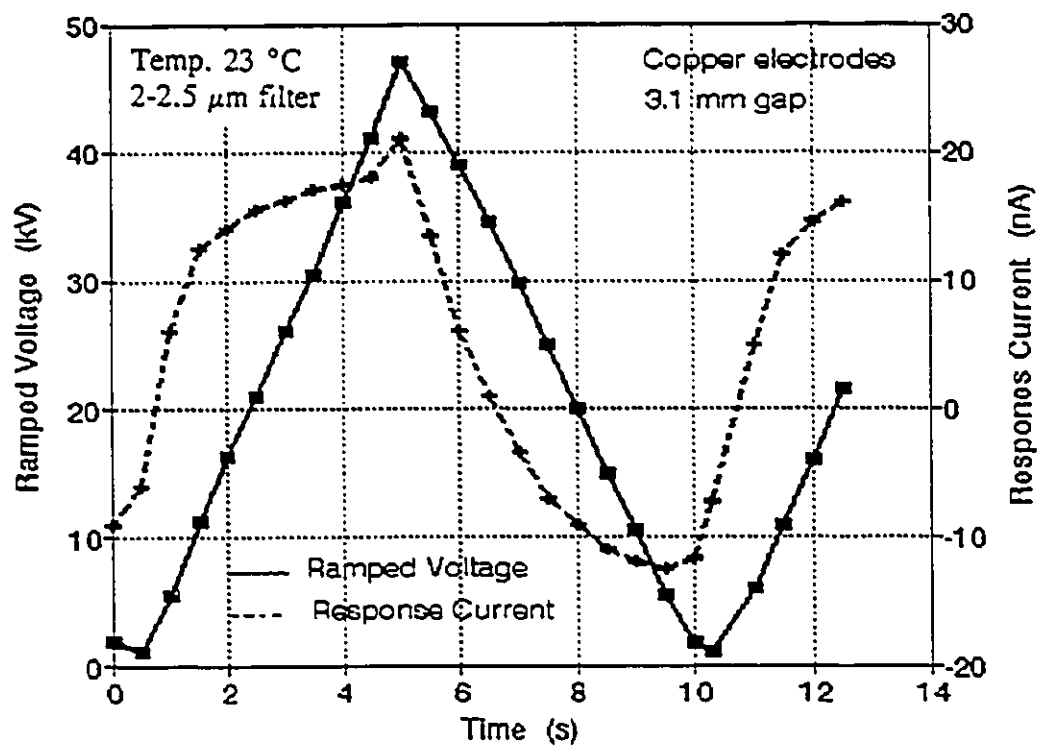


Figure 3.6 Waveform of ramp voltage and the response current as a function of time in silicone oil

3.4 THE PROPERTIES OF LIQUID DIELECTRICS AND THE ELECTRODE MATERIALS

The liquids which were used for the experiments were, (1) dimethyl siloxane (silicone oil) with viscosity of 5×10^{-6} m²/s from Dow Corning Oil Company; (2) transformer oil type Voltesso 35 from Imperial Oil Ltd. ; (3) Di-iso-octyl phthalate liquid (ester oil) from BDH Inc.; (4) castor oil from BDH Inc.; (5) Polybutene H-1900 from Amoco Chemical Company; and (6) Dodecylbenzene from City Chemical Corporation.

The silicone fluids are characterized by good stability below their flash point and a reasonable degree of fire resistance. The electrical properties of silicone oil follow the same pattern as those of chlorinated aromatic hydrocarbons, for which reason these materials are also used in capacitors and equipment operating at high and low temperatures and frequencies. Generally, the electric strength is affected by moisture and solid impurities, but the important feature of the breakdown process is the formation of a bridging deposit, probably of silica, silicon carbide and cross linked polymer, between the electrodes at low current densities.

Transformer oil is made up of low viscosity, petroleum-based oils. They have been used as liquid dielectric since even before 1887 [15]. As the least costly and most efficient insulation for high voltage apparatus, mineral oils are the most important and most commonly used insulating material in the power industry. This will likely remain

the case in the future as well. The properties of a mineral oil are dependent upon its composition. General conclusions can be drawn from a knowledge of the hydrocarbon distribution of the mineral oils [14]. The low viscosity naphthanic petroleum oil is related to a particular family of hydrocarbons which are also known as the cyclo-paraffins. Naphthanic crude oil contains more aromatic compounds which remain fluid at comparatively low temperatures such as - 50 °C [15]. Paraffinic crude oil does not satisfy the above mentioned low temperature requirement. This difference was caused by the dissimilarity of the saturated (paraffinic) hydrocarbons that made up part of the crude oil. One of the concerns with mineral based insulating oil is its flammability or explosive hazards associated with it in particular conditions.

The organic esters are synthetic fluids which are oily liquids and can be made thermally stable and with a low degree of flammability. The relatively recent interest in organic esters for electrical insulation and dielectric application is because the organic esters are made from those materials most easily available and have the best essential properties. Responding to inhibitor treatment, they can be produced as products of excellent stability. The permittivity of esters is higher than that of transformer oil and silicone oils. Unfortunately, in general they have a poor hydrolytic stability [15].

Castor oil has been used successfully in d.c. capacitors from the early days of capacitor manufacture, although its loss characteristics were never low enough for a.c. use. Castor oil's most positive attribute is its ability to withstand d.c. stress in a total

insulation system. This is considered to be due to its good wetting ability and linking of the oil hydroxyl (OH) groups to paper cellulose which produces excellent lateral impulse strength by conduction along the cellulose fibre. Castor oil is unstable and has high losses at elevated temperatures and elevated frequencies of excitation.

Polybutene (or olefin) liquid belongs to the synthetic hydrocarbon group. It is produced by chemical reaction, and the main source of polybutene liquid is from the petroleum and petro chemical industries. They have the advantage of being predominantly mixtures of isomers and homologues of one type of hydrocarbon, therefore they have a simpler chemical composition than petroleum oils. The properties of the polybutenes are in general similar to those of the paraffin hydrocarbons, and their electrical properties can generally be better than those of mineral oil because of their greater purity. The major disadvantages for polybutenes are their oxidation and gassing under disruptive discharge conditions. Polybutenes have been relatively recently introduced into the electrical engineering industry, where their predominant use has been in sealed electrical equipment and systems such as cables and capacitors.

Dodecylbenzene (DDB) liquid belongs to the alkyl-aromatic group of compounds, which is one of the products from the petrochemical industry. They are mostly used for the manufacture of detergents. The properties of the alkyl-aromatic hydrocarbons can be compared to those of the aromatic compounds in mineral oils. These materials are characterised by excellent hydrogen-gas-absorbing characteristics. The thermal properties

of dodecylbenzene are very similar to those of mineral oils. It is unstable under low-oxygen conditions and compares unfavourably with transformer mineral oils, but dodecylbenzene is comparable to high-aromatic and aromatic extract oils.

Table 3.1 gives the summarized typical properties for silicone oil, transformer oil, ester oil, castor oil, polybutene and dodecylbenzene liquid. The silicone oil and transformer oil prepared for the test were vacuum filtered through a 2.0-2.5 micron ceramic filter for degassing and removal of particulate impurities. Unlike transformer and silicone oils, ester oil which has the chemical formula $(C_8H_{17}COO)_2C_6H_4$, and a very high viscosity and water solubility at room temperature, can not be filtered by a 2.0-2.5 micron filter using the existing vacuum system which was used for transformer oil and silicone oil. As the ester oil is more unstable with respect to oxidation and hydrolysis than the transformer and silicone oils in their pure form [15], even after it is filtered, it is difficult to maintain uniform (the same) conditions throughout the experimental period. As a result, the ester oil was tested without filtration at the room temperature of 23 °C, the humidity being below 30%. For the same reason, castor oil, polybutene and dodecylbenzene liquid were also tested without being filtered.

The electrode materials used in the experiment were copper (Cu), aluminum (Al), zinc (Zn), magnesium (Mg) and stainless steel (SS). All the electrode materials were supplied by the Technical Support Centre (Workshop) of the University of Windsor. The copper was an electrolytic tough pitch copper manufactured to ASTM B-133 or B-187

E.T.P. 99.9% Copper. The aluminum used was type 6061, a well proven medium strength structural material and had most of the good qualities of aluminum. Zinc and magnesium were chosen pure materials. The stainless steel used was a type 303MX which is "18-8" free machining chromium-nickel stainless steel modified by the addition of sulphur, as well as phosphorus, to improve machinability and non-seizing properties. This was non-magnetic in the annealed state.

The electrodes were polished mechanically using Nevir-Dull Magic wadding polish. After cleaning with Octane and distilled water, the dried electrode would then be immersed in the dielectric liquid which was the same liquid to be used later in the experiment. Even with the most careful cleaning and preparation for the electrodes before the tests, a semi-insulating oxide film will be formed on their surfaces. With respect to the experimental conditions, it is assumed that the copper, zinc, aluminum and magnesium electrode surfaces have been oxidized upon exposure to the atmosphere. Among these metals, aluminum and magnesium have higher reactivities, and are more rapidly susceptible to oxidation. Both aluminum oxide (Al_2O_3) and magnesium oxide (MgO) are very wide bandgap materials. They are regarded as insulators under high field conditions. However zinc oxide is always defined as a n-type semiconductor. Copper is the least reactive among these four materials. Copper oxides are much more difficult to characterize, sometimes being presented as p-type semiconductors and otherwise as conductors [64].

Table 3.1 The Insulating Fluids Properties

Property	Transformer Oil	Silicone Oil	polybutene	castor oil	Dodecylbenzne	Ester Oil
Flash Point °C	150	300	> 153	285	> 132	200
Gravity gm/cm ³	0.87	0.96	0.9	0.96	0.87	0.98
Viscosity c.s. 0°C	86	15				330
20°C	47	5.5		1020		75
100°C	2.9	2.0	4069		2	4.43
Pour Point °C	- 51	- 55	18	-15	-55	- 30
Water Content mg/kg	< 15	25*				500
Water Solubility	45	200				200 - 600
Breakdown Voltage kV ⁺	> 35	35*	35		60	60*
Power Factor %, 100°C	< 0.5	0.02*	0.3	0.2	0.4	0.1*
Resistivity GΩm 90°C	600- 2000	1000	1-600		1-70	1-1000*
Permittivity 90°C	2.2	2.5	2.1	4.7	2.5	4.3

* Given results dependent on efficient drying and cleaning of the insulating fluids.

+ Measured under IEC ASTM D1816 (2.5 mm gap)

3.5 THE MAGNETIC FIELD SUPPLY

The magnetic field supply shown in Figure 3.7 consisted of an A.C. supply, fed through an isolation transformer (115 V, 500 VA, 60 Hz). A variable autotransformer varying from 0 to 140 V (0-140 V, 4.5 A, 0.63 kVA, 60 Hz) was connected after the input transformer, then a bridge rectifier is used to rectify the A.C. Two parallel coils ($32\ \Omega$, 188 mH) are connected in series with the D.C power supply and an ammeter. The chamber and cores constitute a magnetic circuit. The D.C. current could be produced by varying the supply current from 0 to 4.5 A. The corresponding transverse magnetic field between the pole pieces then was varied through the range of 0 to 0.06 T. The D.C. polarity was preserved so as not to lose magnetic field direction information when tracing and plotting fields.

The magnetic flux density had been measured by the author at various horizontal distances within the effective area between the poles (120 mm spacing), the north pole being the reference shown in Figure 3.8. The centre point of the north poles is shown as the vertical reference. Between the active region of the electrodes an approximately uniform transverse magnetic flux density up to 0.025 T could be maintained and can be measured by a Gaussmeter. As the magnetic flux density increased, the non uniformity of the magnetic field became more obvious as shown in Figure 3.8. When 0.045 T was obtained in the central area for example, a field of more than 0.06 T was obtained at the pole faces. Another problem with high magnetic flux density was

that due to the large D.C current and limited space, the poles can become quite warm during the experiment.

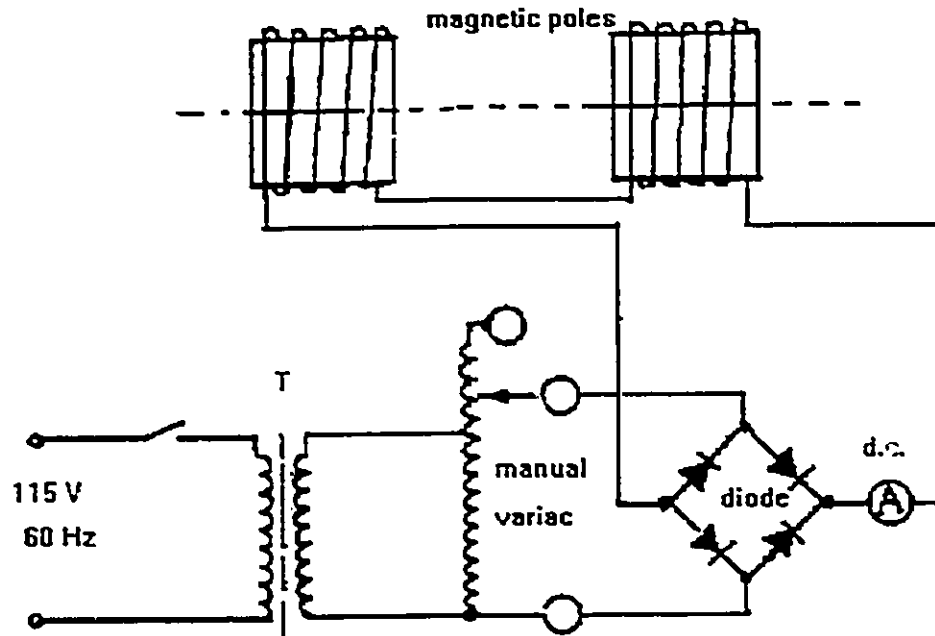


Figure 3.7 Electromagnetic power supply circuit diagram

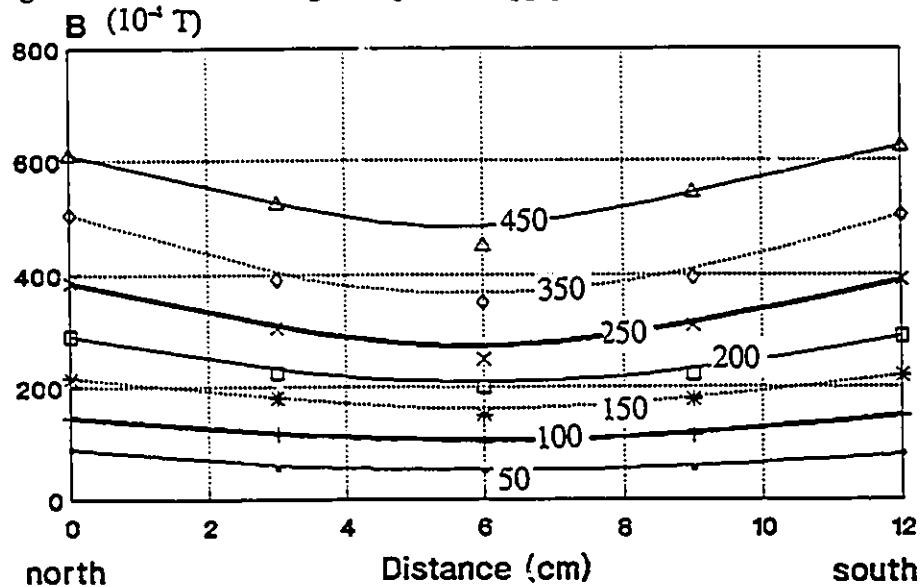


Figure 3.8 Variations in flux density between the magnetic poles

The magnetic flux density was measured by the Gaussmeter Model 912, RFL Industries Inc. This Model 912 Gaussmeter was a compact, portable instrument used to measure magnetic fields. The instrument is capable of measuring D.C., A.C. and Peak magnetic fields from 10^{-6} T to 10 T using Hall-effect probes. Nominal accuracy is within $\pm 0.5\%$. Operating temperatures were from 0 °C to 40 °C and the temperature coefficient was less than 0.05% /°C (instrument only), while that of the Hall-effect probe itself was usually of the order of 0.1×10^{-4} T /°C.

3.6 EXPERIMENTAL PROCESSING PROCEDURE AND DATA-GATHERING

Prior to each group of experiments, the electrodes and the dielectric liquids to be used in the test were prepared following a procedure which is similar to that used originally by previous researchers such as Girgis, Abiri and Esendal [7,8,9] respectively: The electrodes were polished mechanically using Nevir-Dull Magic wadding polish. After cleaning with Octane and distilled water, the dried electrode would then be immersed in the dielectric liquid which was the same liquid to be used later in the experiment. Before pouring the insulating liquid into the test cell, the electrodes were screwed on the top and bottom parts of it. The test cell with the electrodes was rinsed several times with filtered and degassed insulating liquid. Finally the dry and cleaned oil was put into this cleaned test cell carefully. The test cell was then ready to be placed within the test chamber. The electrode gap spacing was initially adjusted by raising the lower electrode until it

was in contact with the upper one as verified with an ohmmeter continuity check. The gap spacing in experiments was set with a micrometer attached to the lower connecting rod. Errors in gap setting introduced by the tolerance limitations of the threaded mechanism were negligible. After the gap space was adjusted, the system was allowed to rest for 15 minutes before starting the test. Gap separations from 0.5 to 8.0 mm were investigated. All the tests were made at room temperature, around 23 °C, and at atmospheric pressure. The liquid in the test cell was replaced with each new set of electrodes or after an occasional breakdown during the experiment.

For each combination of electrodes, spacing and oil type, an initial conditioning procedure was followed by establishing the maximum voltage swing at 20 kV and ramping up and down 50 times (50 cycles). This process was repeated in steps of 5 kV up to a specific test voltage, one hundred further ramping cycles at the same voltage were carried out without recording. Sometimes more cycles were needed for the purposes of response current stability and reproducibility. A further 15-30 consecutive V-I plots were superimposed on the same graph paper from the X-Y recorder in order to assure reproducibility. A copy of the recorded V-I characteristics is presented in Figure 3.9 for an average of 30 successive cycles which indicates the reproducibility to be quite good with a tolerance of $\pm 5\%$. With the triangular waveform voltage, the V-I characteristics appear as a loop after one complete cycle. This occurs because the total current flowing is different when the voltage rises from when it is falling, e.g. when dV/dt is positive as shown in Figure 3.9 as V_{up} , and V_{down} when the voltage ramp was

reversed. It was also noticed from the graph that through all the experimental records, there is a small residual voltage at the bottom coordinate of the loop. The value of the residual voltage is dependent on the maximum applied voltage. As the maximum applied voltage increased, the value of the residual voltage grew larger. This phenomenon will be analyzed in section 3.7.2 and Appendix A. Under very high electrical stress, in some cases the response current may have some variation in the high voltage section of the graph shown in Figure 3.10. All the data analyzed later were the average of those 15-30 loop results with the tolerance of $\pm 7\%$.

Generally speaking, the response current measured from rising and falling ramp function voltage consisted of two components, one of which appeared to be the "displacement" current I_d mainly due to charging and discharging of the capacitance of the insulating liquid, and the other appearing to be the "conduction" current I_c which was passing through the liquid. In order to extract the "conduction" component from the data given in the V-I loop as shown in Figure 3.9, the average values of curve V_{up} and curve V_{down} were taken for any particular applied voltage. The method of calculating the conduction current may be illustrated as follows:

$$I_1 = I_c + I_d \quad (3.1)$$

$$I_2 = I_c - I_d \quad (3.2)$$

Where, I_1 is the total current during the positive dV/dt cycle,

I_2 is the total current during the negative dV/dt cycle,

I_c is the conduction current, and

I_d is the displacement current.

By summing the Equations 3.1 and 3.2, the following relationship was obtained indicating that

$$I_c = \frac{1}{2} (I_1 + I_2) \quad (3.3)$$

At any fixed voltage, the current conducted through the sample liquid was in fact the "mean" value of the curves 1 and 2 of Figure 3.9, and more accurately, was called the "mean" current response. Re-plotting the conductive current versus the applied voltage on a log-log scale, as shown in Figure 3.11, indicated two sharply divided linear regions of different slopes in the high field regime. In the case of a sharp division between the two regions of the high field regime, each originated from a different point that will later be called a "threshold point". The specific threshold coordinates were designated I_{th} and V_{th} for current and voltage respectively.

In the high field region the data displayed a straight line in logarithmic coordinates as shown in Figure 3.11. The conduction current response on a log scale show that $\log I$ varies directly with $\log V$ in Equation 3.4 below, in which s is the slope of the linear region and C_1 is a constant, where the mean current I_c is normally written as I .

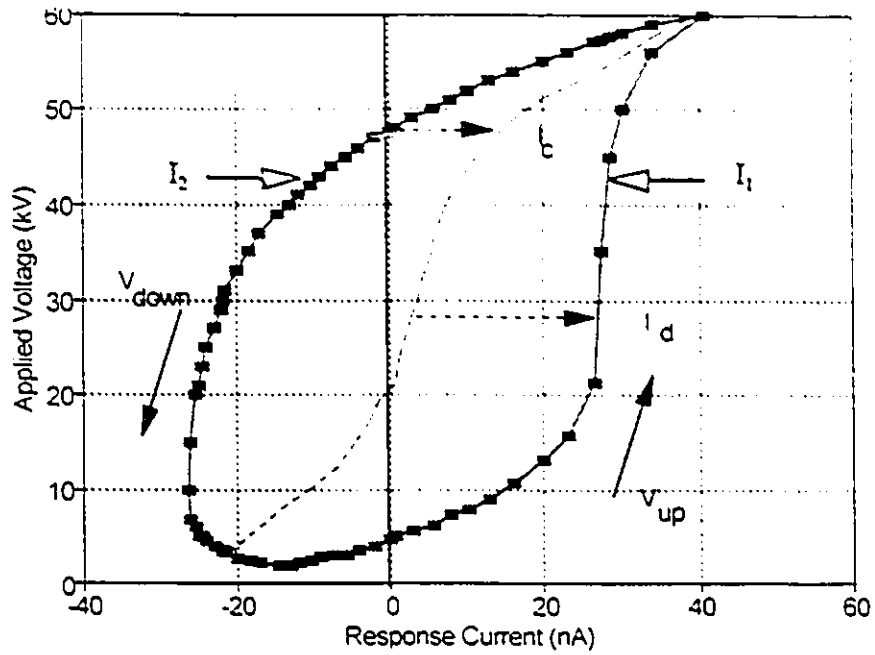


Figure 3.9 A V-I characteristic loop for silicone oil

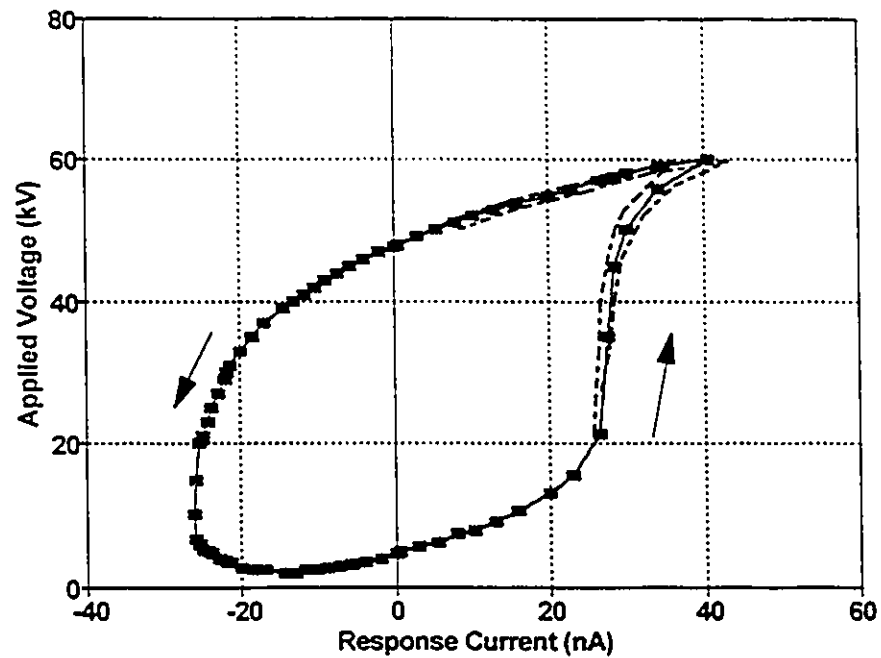


Figure 3.10 A V-I characteristic loop for transformer oil at a relatively high electric field level without current turnover phenomenon

$$\log I = s \log V + C_1 \quad (3.4)$$

This can be expressed as a power law of the form of equation 3.5, indicating that the current response in the prebreakdown region varies as a power of the applied voltage, s being the appropriate exponent.

$$I \propto V^s \quad (3.5)$$

As the conduction current data was obtained from the addition of current responses to positive and negative voltage ramp rates, using the same raw data and the Equations 3.1 and 3.2, the "displacement" current data could be obtained by taking the difference between the current response to rising and falling voltage ramp rate, as seen in Equation 3.6,

$$I_d = \frac{1}{2} (I_1 - I_2) \quad (3.6)$$

The variable I_d was called more accurately, the "differential" current response. All current response analyses here were determined from the averaged values I_1 and I_2 . Replotting the displacement current versus the applied voltage on a log-log scale, as shown in Figure 3.12, indicated two sharply divided linear regions of different slopes in the high field regime. As the measurement begins at the top where the maximum applied voltage is, and towards where the applied voltage decreases, the displacement current,

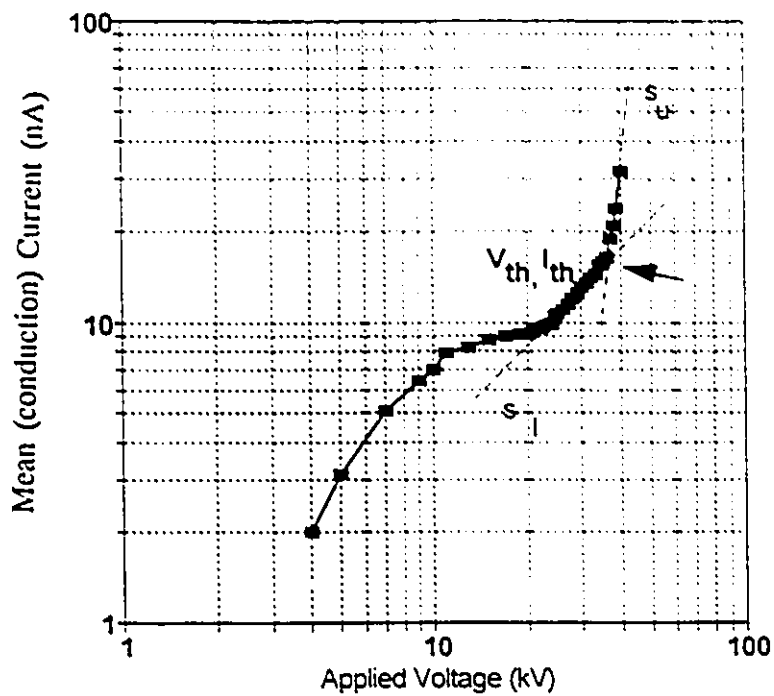


Figure 3.11 Applied voltage versus mean current response

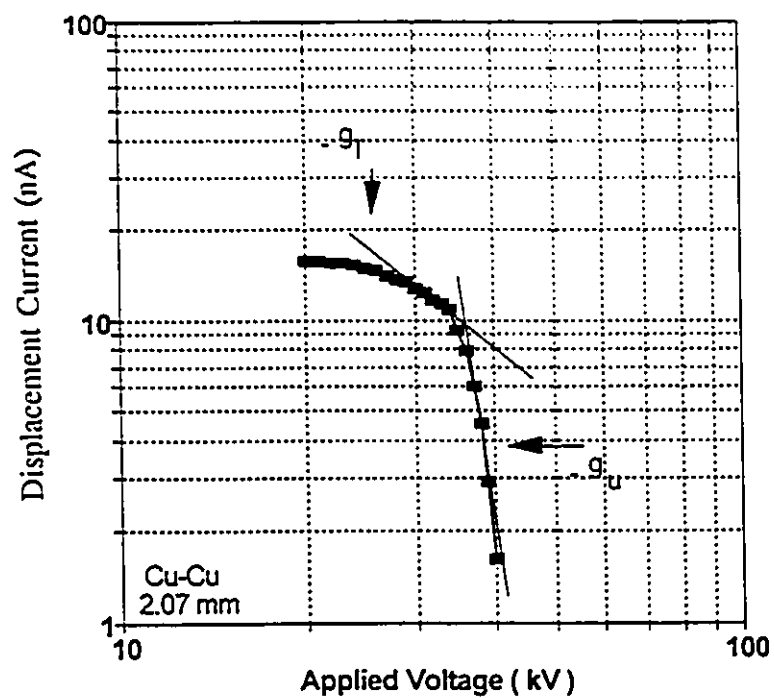


Figure 3.12 Applied voltage versus displacement current response

thus, can also be expressed as a power law of the form of Equation 3.7:

$$\log I_d = g \log V + C_2 \quad (3.7)$$

$$I_d \propto V^g$$

where g is the appropriate exponent for displacement current. Again g_l and g_u are presented for the lower and upper slopes respectively.

3.7 PREBREAKDOWN TEST CONDITIONS

3.7.1 BACKGROUND NOISE EFFECTS ON THE EXPERIMENTAL SYSTEM

The high voltage supply system and the test chamber have been described previously in section 3.1 and 3.2. When examining high voltage test results, it is necessary to estimate the background current effects which come from the high voltage equipment and experimental setup. The effects could possibly come from the surface of the test chamber, due to leakage current passing across its surface to the ground electrode. Another possible cause is an environmental one such as the presence of a high electrostatic field. Figure 3.13 gives the V-I characteristics resulting from the various maximum applied voltages without the test cell being present. When compared to the experimental results with the test cell containing silicone oil, this figure shows the same

characteristic loop but at very much lower current levels of about 10^{-11} A. Thus the current with the applied voltage increasing is larger than the current when the applied voltage is decreasing. Table 3.2 is a record of those residual currents measured for each applied voltage value. As the maximum applied voltage increased, the value of residual current also increased in direct proportion.

The corresponding resistance R given by the ratio of the residual voltage versus the current at the bottom of each loop is given in Figure 3.13. Since the residual voltage is also directly proportional to the maximum voltage, V_m , shown in Table 3.3, then another ratio R^* is obtained. By connecting all the coordinates under each maximum applied voltage level, a straight line is drawn starting from the zero coordinate and hence an ohmic condition is indicated in Figure 3.13. The slope of this straight line is equivalent to the corresponding resistance. The calculation of the corresponding resistance value is shown on Table 3.2, by using Ohm's Law, R is approximately $1.3 \times 10^{13} \Omega$ without the test cell present. Since this value is higher than any resistance of the H.V. power supply, it would appear to be the surface resistance of the test chamber. R^* , the ratio between the maximum applied voltage and its corresponding residual current is also calculated here in the Table 3.2. The R^* value is a constant for each applied voltage approximately $3.0 \times 10^{14} \Omega$. Thus it could be presumed that R and R^* are independent of the applied voltage.

Table 3.2 The Corresponding Resistance R^* under Different Maximum Applied Voltage

Applied Voltage V_m , kV	10	20	30	40	50	60
Residual Voltage V , kV	0.35	0.83	1.3	1.6	2	2.6
Current $I \times 10^{-11}$ A	5.2	9.2	14.2	18.6	24	28.4
$R = V/I \ 10^{14} \ \Omega$	0.12	0.13	0.15	0.13	0.14	0.13
$R^* = V_m/I \ 10^{14} \ \Omega$	1.92	2.1	2.1	2.1	2.1	2.1

Table 3.3 The Residual Voltage Versus the Maximum Applied Voltage

Applied Voltage V_m , kV	10	20	30	40	45	50	55
without test cell, kV	0.35	0.83	1.3	1.6	1.75	2.0	2.2
with test cell, kV	0.1	0.75	1.0	1.375	1.375	2	3.25

For a typical experimental measurement, the current range selected on the electrometer is usually the micro ampere range, a level which is larger by a factor of one thousand times than that of the background level. As a result the background has no significant effect on the experimental results.

3.7.2 RESIDUAL VOLTAGE, CURRENT AND THEIR CORRESPONDING RATIO

Throughout all the experimental records, a small residual voltage and current at the bottom coordinate of the loop has been noticed after each cycle. Although the experiment was run for several hundred cycles, these residual coordinates remain at the

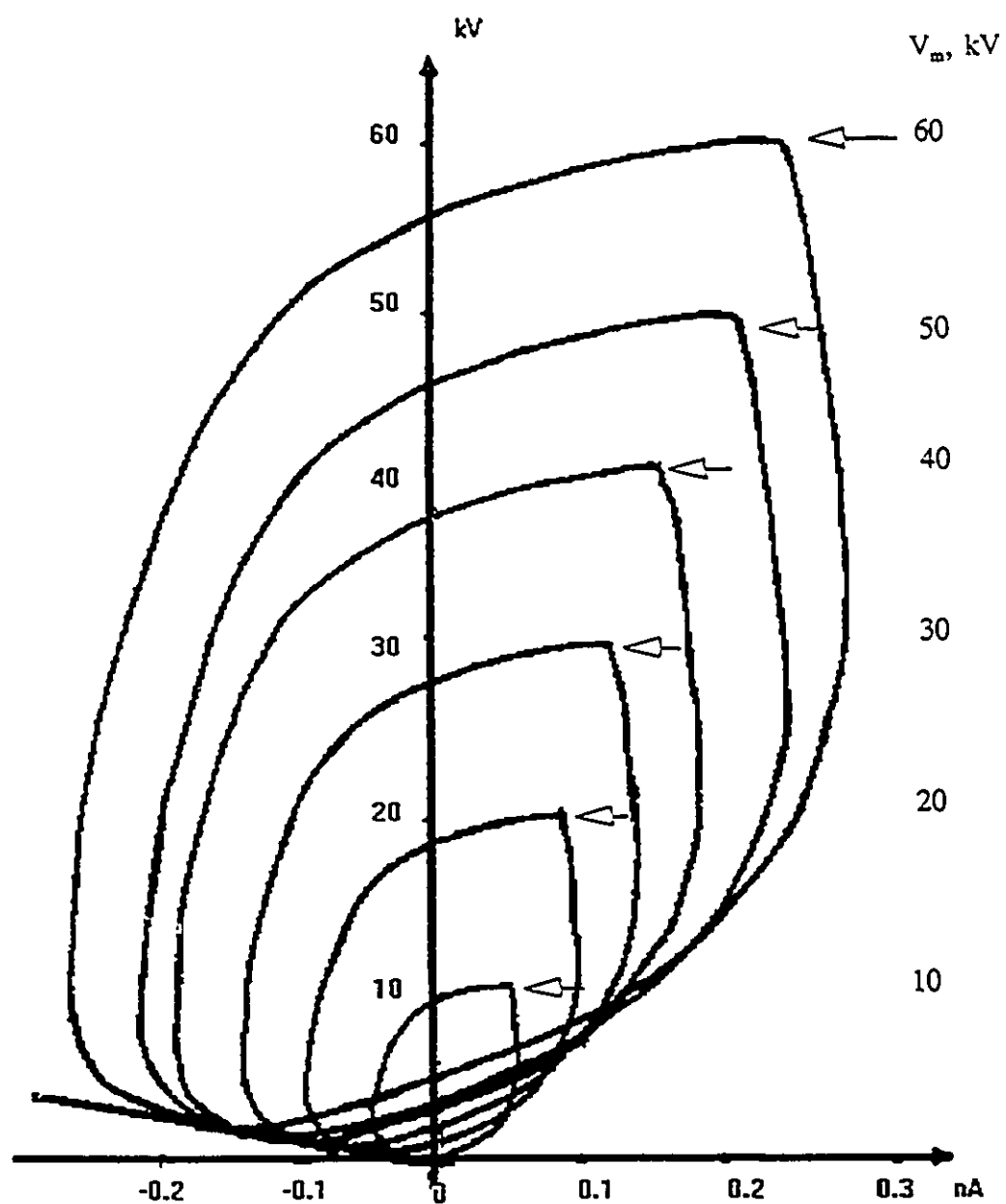


Figure 3.13 The V-I characteristic loops without the test cell present

same value. The voltage value is positive since a positive voltage was applied and the current value is negative. These coordinates on the loop move upward and to the left as the maximum applied voltage is increased which means that both the residual current and voltage values depended on the maximum applied voltage. This phenomenon also appears on the background test shown in Figure 3.13. As was the case with or without the test cell, the corresponding resistances which were measured with the test cell were found to be practically constant when the maximum applied voltage was increasing. Particularly, the residual voltage values both with and without the test cell are very close, as shown in Table 3.3. This means that the residual voltage values are not related to the test sample, electrode material, and the test environment. It depends only on the maximum applied voltage and the equipment setup. Unlike the residual voltage values, the residual current value is about 10^2 times larger during normal experimental conditions for silicone and transformer oils than the value without the test cell present. Moreover the corresponding resistance is lower than that without the test cell. The resistance changes when the gap distance between the electrodes is varied. Table 3.4 contains typical examples of the residual resistance measured from silicone oil with four different electrodes.

Figure 3.14 is the relationship between the corresponding resistance R and the gap distance. Figure 3.14 reveals almost a straight line and R could be described by

$$R = (110 + 18d) \text{ } G\Omega \quad (3.8)$$

where d is the gap distance in mm.

Although the residual voltage value does not change with or without the test cell present, its corresponding current value does. To understand this phenomenon, it is necessary to examine the experimental setup system thoroughly. The high voltage power system could be modelled by a circuit consisting of capacitors and resistors from the viewpoint of the equivalent circuit shown in Figure 3.15. The full analysis has

Table 3.4 The Relationship Between the Corresponding Resistance and Electrode Gap Distance

Gap Distance mm	2.067	3.1	4.12	4.65	6.2	7.75
Zinc Electrode 20 kV	1.33	1.5	1.83	1.67	2.3	2.83
30 kV	1.33	1.83	2.16	2.17	2.17	2.67
40 kV	1.33	1.83	2.16	2.17	2.33	2.67
Average R $1 \times 10^{11} \Omega$	1.33	1.72	2.06	2	2.27	2.72
Al. Electrode 20 kV	1.5	1.17	1.67	2.17	2.17	2.33
30 kV	1.33	1.33	1.5	2	2.5	2.33
40 kV	1.67	2	2	2	2.17	2.67
Average R $1 \times 10^{11} \Omega$	1.5	1.5	1.72	2.06	2.28	2.44
Cu. Electrode 20 kV	1.67	1.83	2	2.16	2.67	2.33
30 kV	1.5	2.33	2.16	2.17	2.5	2.5
40 kV	1.67	1.83	2	2.16	2.16	2.5
Average R $1 \times 10^{11} \Omega$	1.61	2	1.89	2.17	2.44	2.5
Mg. Electrode 20 kV	1.5	1.83	1.5	1.83	2	2.16
30 kV	1.67	1.83	1.5	2.16	1.83	2
40 kV	1.67	1.67	2	2	2.33	2.33
Average R $1 \times 10^{11} \Omega$	1.61	1.78	1.67	2	2.06	2.17

been given in Appendix A. The equivalent circuit could be reduced to a single RC circuit in which the input voltage V_1 represents the power supply triangular voltage waveform and the output voltage V_2 is the voltage across the test cell as shown in Figure 3.16. V_2 is calculated by given Equation 3.9 [Appendix A]:

$$V_2 = V_o \left[\left(\frac{1}{2} - \frac{4b}{\pi^2 (R_1 C)} \right) + \left(\frac{4a}{(\pi R_1 C)^2} - \frac{1}{2} \right) e^{-\frac{t}{R_1 C}} \right] \quad (3.9)$$

where

$$a = \sum \frac{1}{(2n-1)^2} \frac{1}{\left(\frac{1}{R_1 C} \right)^2 + \left[(2n-1) \frac{\pi}{5} \right]^2}$$

$$b = \sum \frac{1}{(2n-1)^2} \frac{\left(\frac{1}{R_1 C} \right) \cos\left[(2n-1)\frac{\pi}{5}t\right] + (2n-1)\frac{\pi}{5} \sin\left[(2n-1)\frac{\pi}{5}t\right]}{\left(\frac{1}{R_1 C} \right)^2 + \left[(2n-1) \frac{\pi}{5} \right]^2}$$

A typical result is shown in Figure 3.17. In this example, the voltage V_2 differs slightly from the voltage V_1 at both the maximum and minimum points. At the bottom of the I-V characteristic loop, the resultant voltage does not go to zero. The difference between the minimum voltage and the zero value is the so called residual voltage, which is very interesting in this case. Figure 3.18 shows the relationship between the maximum applied voltage V_1 and the residual voltages with calculated and measured results

[Appendix A]. The calculated result also shows that the residual voltage is only dependent on the magnitude of the limiting series resistor of the power system and the magnitude of the system equivalent capacitance (Figure 3.16). The test cell has no effect on the applied voltage. Therefore the residual voltage value from the applied voltage remains the same with or without the test cell present. This has been proven by the previous experimental results.

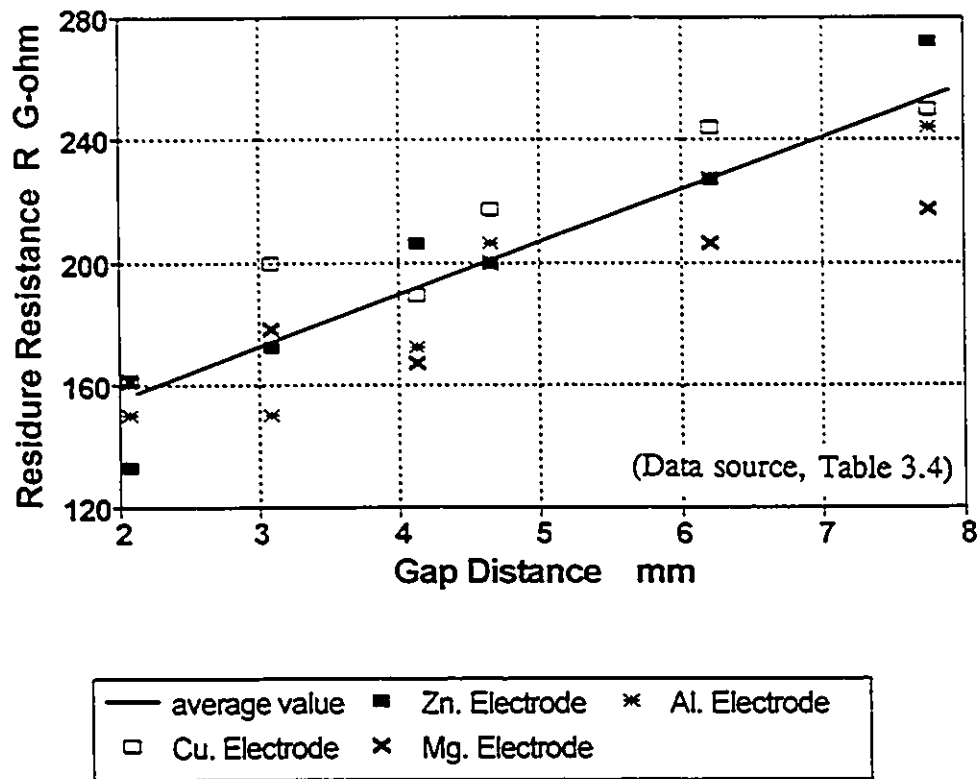


Figure 3.14 The residual resistance as a function of gap distance

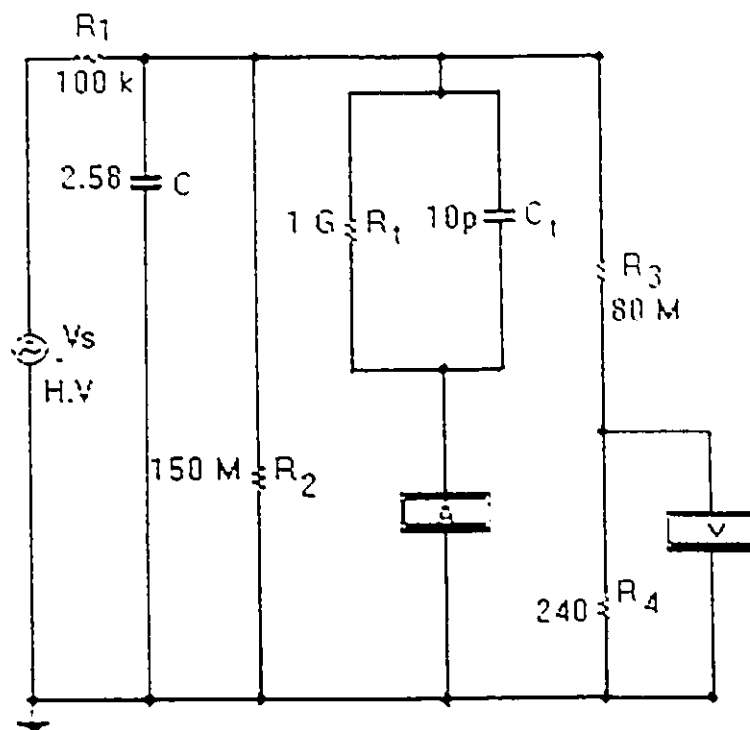


Figure 3.15 The high voltage power supply equivalent circuit

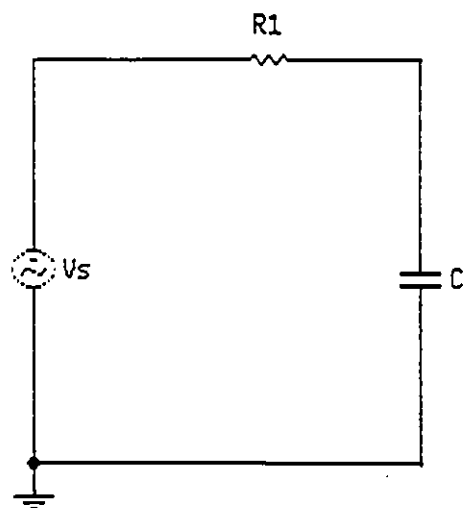


Figure 3.16 The simplified RC circuit from Figure 3.15

The response current is the current which is flowing through the test cell, which depends on the combined parameters of the test cell, oil samples and the supplied voltage. Thus the previous circuit model is not suitable for the current calculation. Figure 3.15 is used in this case. From results of the analysis in Appendix A, the current is calculated by following equation:

$$I_t = I_{C_t} + I_{R_t} = C_t \frac{\partial V_2}{\partial t} + \frac{V_2}{R_t} \quad (3.10)$$

a small amount of negative current is found corresponding to the residual voltage. This also matches the experimental results. The measured current from the test cell contains two distinct components, one from a resistor R_t is directly proportional with the output triangular voltage waveform and its polarity while the other comes from its capacitor C_t and is directly proportional to the output voltage ramp rate and its polarity. At the second half of each cycle, the ramp rate switches from positive to negative, thus there is a negative current through the test cell [Appendix A].

Since this current dominates the total current in the low and medium field regions, the total current appears negative. When the ramp rate switches to positive again, there is a negative current indicated at that time and then it quickly changes to positive as shown in Figure 3.6 and Figure 3.19 as experimental results and calculated results [Appendix A] respectively. This current is dependent on the power supply system as well as the test cell (oil sample).

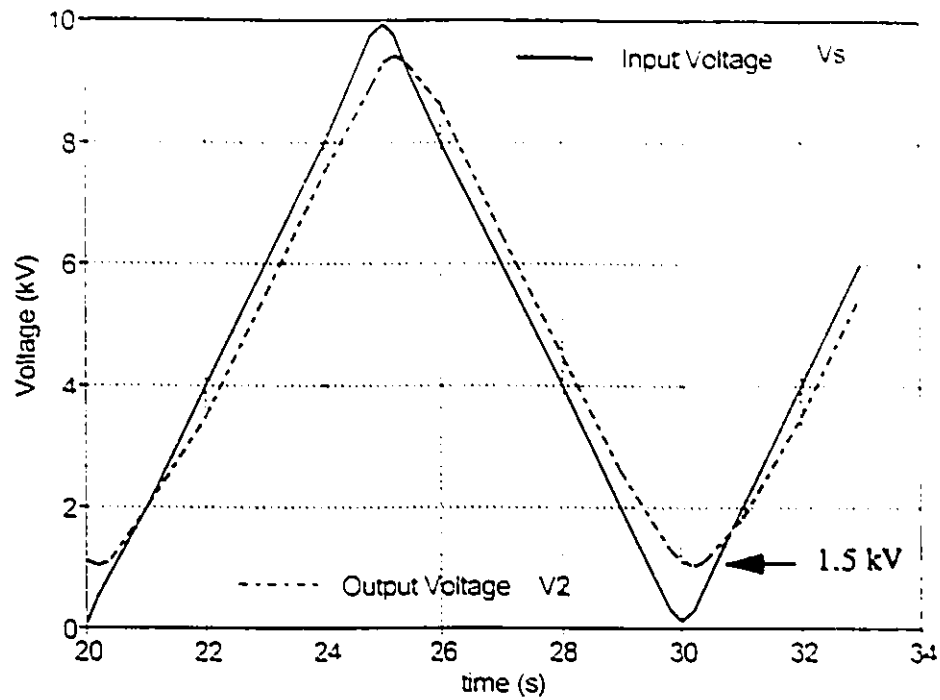


Figure 3.17 The modelling of high voltage power input and output voltage waveforms

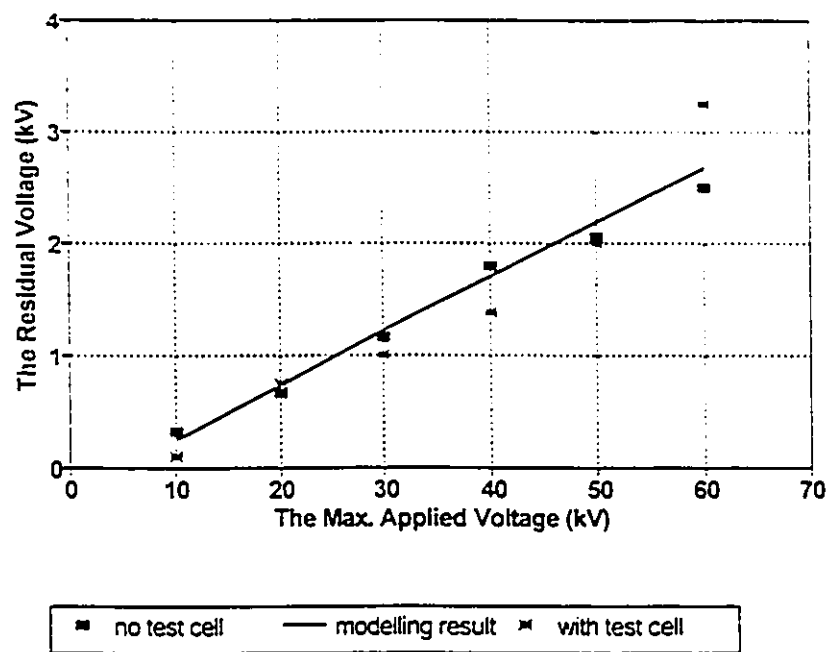


Figure 3.18 The maximum applied voltage versus the residual voltage for the high voltage power supply

3.7.3 CHARGE AND DISCHARGE TIME EFFECTS OF THE TEST CELL

The theory of the residual voltage and its response current has been studied in section 3.7.2 , and the detailed analysis has been carried out in Appendix A. It is clear that the voltage applied to the test cell V_2 is not affected by the presence of the test cell. Furthermore the calculated result of the relationship between the applied voltage and its response current is presented in Table 3.5 using Equations 3.9 and 3.10. It indicates that waveforms of the voltage applied to the test cell V_2 and corresponding response current I_t delay about 200 ms with respect to V_1 , the applied voltage triangular waveform. Since V_2 is not affected by the test cell, it is presumed that the time delay is also independent of the test cell. In other words, there is no significant effect on the time delay with the test cell present.

TABLE 3.5 The Calculated Results of the Supplied Voltage and Corresponding Response Current in the Test Sample

T (second)	V_1 (kV)	V_2 (kV)	I_t (nA)
20.0	0.178	2.366	-388.2
20.05	0.36	2.016	-285.4
20.10	0.76	1.782	-174.8
20.15	1.16	1.683	-87.54
20.20	1.56	1.595	-2.118
20.25	1.96	1.689	51.75

The purpose of this test was to expand the evaluation of the charging and discharging time delay of the test cell by using a high voltage D.C. waveform. The test equipment used for this was: a Brandenburg Regulated High voltage D.C. Power Supply (No. 2707) ; a high voltage resistive divider with a ratio of $10^6:3$ V; a chart Recorder (Model 8376-20). The test was performed at a temperature of 23 °C and relative humidity of 45%. The applied voltage ranged from 3 kV to 8 kV. For a better comparison, the test was first carried out without the test cell connected. The results show that the high voltage D.C. power supply does have a time delay as the power is switched on or off. This type of delay is called the charging or discharging time for the power supply. Figure 3.20 shows the relationship between the applied voltage to the charging and discharging time under different applied voltages. With the high voltage supply output at 3 kV, the values of charging and discharging times are close to 1.9 and 2.9 seconds respectively. As the supply output voltage is increased, there are no significant changes to either the charging or the discharging time. The average charging and/or discharging time is approximately 3 seconds with the voltage ranging from 3 kV to 8 kV. After connecting the test cell to the high voltage power supply, the test is repeated under the same conditions. When compared with the previous test, both charging and discharging times are very close to the data obtained without the test cell. As the voltage increases, the results again show a similar relationship between the charge, discharge time and the applied voltages to the previous one. As a result, regardless of the experimental and measurement errors, the charging and discharging times are very nearly the same value with and without the test cell present. Moreover

they do not change as the applied voltage varies. From this technical perspective, the effect of the charging or discharging time delay of the test cell on the system also appears to be negligible.

Figure 3.21 shows the applied voltage read from the high voltage power supply console vs. the measured voltage from the chart recorder. At the same output level, the measured voltage without connecting the test cell is slightly higher than that of the record which was measured with the test cell connected. Since there is a very simple circuit connection for the experiment, the test cell could be modeled by a parallel capacitor and resistor pair across the power supply output terminals. The inverter frequency of the high voltage D.C. power supply is 33 kHz [65]. It is then suspected that under such high frequency excitation, the capacitance of the test cell effects the total system output impedance (capacitive reactance). Thus, it may cause the high voltage D.C. level and output voltage ripple value to be changed slightly. As a result this may change the output supply voltage or the voltage ratio across the voltage divider to the chart recorder.

3.7.4 THE STABILITY AND REPRODUCIBILITY OF THE EXPERIMENTAL RESULTS

Controlling the stability and reproducibility of the test results has been mentioned briefly in section 3.6. The stability of the response current is demonstrated by checking the V-I loop's location for each cycle. If the loops were retraced through approximately

the same coordinates and continued in the same condition for more than fifty cycles, they were defined as stable. The x-y recorder recorded those fifty cycles with the voltage value on the vertical axis and current value on the horizontal axis. The final data is calculated from the average of those fifty V-I loops. The deviation of the average data is maintained at less than $\pm 7\%$ of the experimental result. It is noticed that the deviation of experimental results is larger at relatively high field than that for at lower fields. If the test results had been difficult to reproduce for each cycle, it could not be considered as being stable. This instability required that the test fluid be replaced when the deviation exceeded the above mentioned value.

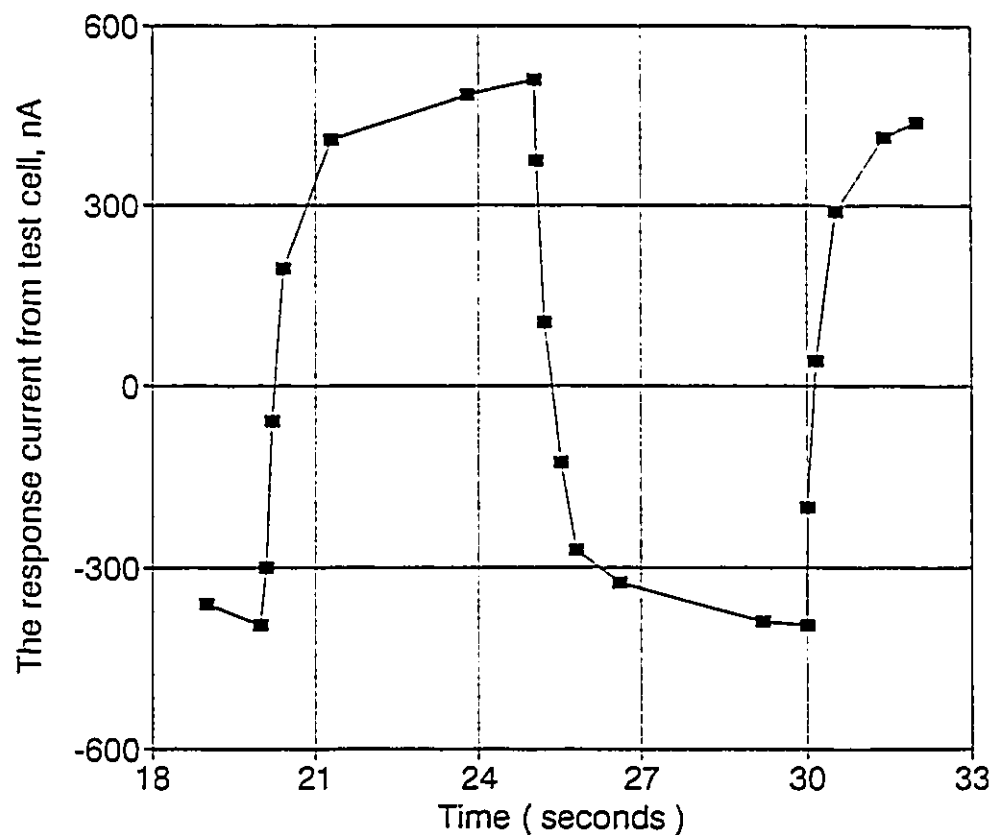


Figure 3.19 The calculated result of the response current

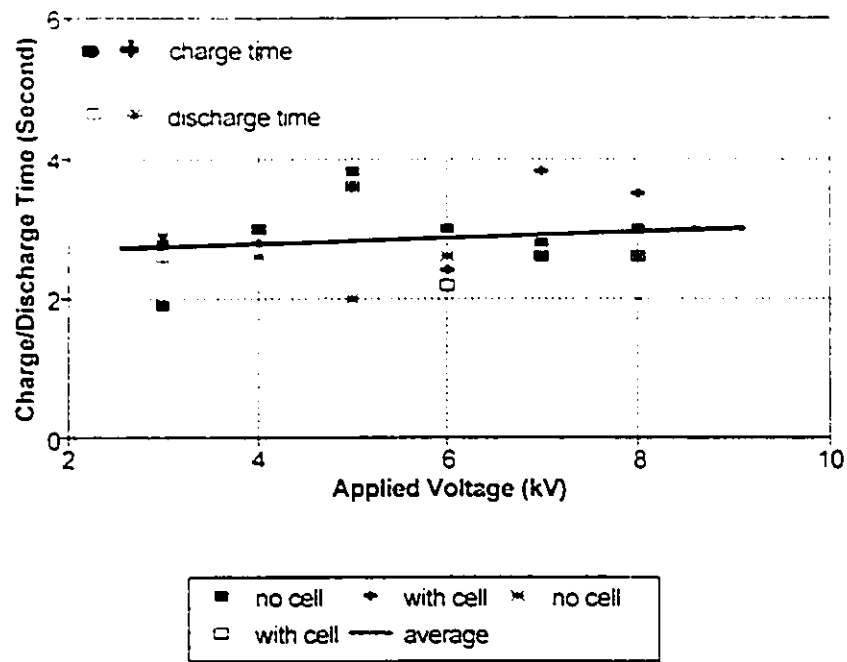


Figure 3.20 Charge/discharge time as a function of applied D.C. voltage

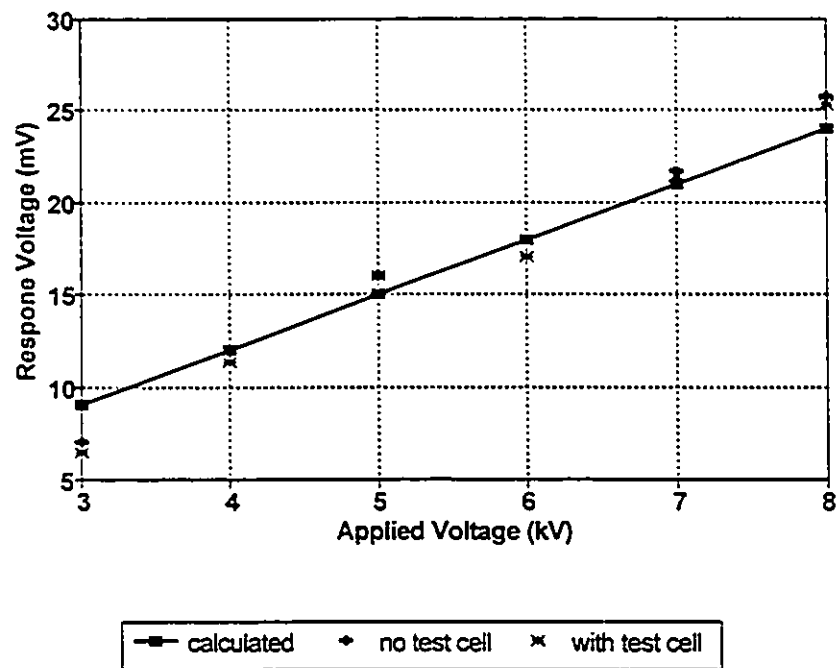


Figure 3.21 The applied voltage versus the recorded response voltage

In the investigation of the liquid prebreakdown and breakdown phenomenon, the non uniform field of a hemispherically capped rod-rod electrode geometry has been used [66,67]. Figure 3.4 shows the geometry of the test chamber which the electrodes are inserted, a test cell made of solid plexiglas ($\epsilon_r = 3.12$), with a dielectric liquid used as the test sample ($\epsilon_r = 2.2$), and air (gas) above the liquid. Thus, the effect of the space between the test cell and the electrodes has been studied thoroughly in Appendix B. During the experiments a meniscus is observed adjacent to the upper electrode and it rises in synchronism with the ramped high voltage [67]. This effect is very noticeable when the peak voltage is greater than approximately 30 kV. A detailed field plotting investigation of the phenomenon was made to gain an accurate knowledge of the field distribution in the interelectrode region and near the gas/liquid interface with and without the meniscus effect at different boundary conditions. The results of the investigation were obtained using the Charge Simulation Based Computer-Aided Design (CSMAD) package for high voltage system modelling [68]. The details of the charge simulation method for the electric field distribution of the test cell is described in Appendix B. This model represents the liquid insulating system used in the laboratory experiments in a way that would be adequately reproduced by the computer simulation. The field distribution near a gas/liquid surface, and the electro-capillarity meniscus phenomenon on the free surface are also taken into account [66]. From the viewpoint of modelling, an improvement in the use of developed charge simulation methods for high voltage systems

achieved in this work [67].

From the charge simulation results, the calculations have been carried out for a variety of boundary conditions. In the basic boundary arrangements for simple electrodes with and without the test cell, the results show that the dimensions of the test cell are large enough compared to the electrode spacing used, to have no significant effect. The edge effect from the test cell slightly changed the field distribution along the dielectric interface but had practically no effect on the values of potential there. It was not expected therefore that the test cell would have any extraneous effect on the prebreakdown processes between the electrodes. The meniscus phenomenon does not affect the field values or the field distribution in the liquid except near the meniscus itself, because of the variation of the dielectric constant and geometry in that region while the voltage is increasing and decreasing.

CHAPTER IV

EXPERIMENTAL INVESTIGATION

4.1 DIMETHYL SILOXANE LIQUID (SILICONE OIL)

4.1.1 INTRODUCTION

Pre-breakdown current flowing in response to a triangular ramped high voltage applied to dimethyl siloxane (silicone oil) has been studied previously by Watson et al. [5,6]. Experimental results with different viscosities of silicone oil from 5 to 1000 (10^{-6} m²/s) have been described in previous work [5,6,10]. The typical experimental results for silicone oil are presented in Figure 3.6 of Chapter III. The figure shows the waveform of ramping voltage and its response current as a function of time. The influence of electrode separation, and geometry upon current conduction in silicone oil led to the following conclusions. Two sharply divided portions of the high field conduction regime displayed a linear relationship between the logarithm of the current and of the voltage as shown in Figure 3.11 of Chapter III as well. The power law could hence be written in the following form,

$$I \propto V^s \quad (4.1)$$

in both portions for a fixed gap separation, the symbol s is observed to be a constant value, either s_u for the upper portion above the threshold point or s_l for the lower one.

At different ramp rates, the threshold current, I_{th} , and threshold voltage, V_{th} at the threshold point, varied linearly with dV/dt [11]. Previous work has also shown that both I_{th} and V_{th} vary linearly with the ramp rate for all gap separations in dimethyl siloxane [6]. The location of the threshold coordinate (V_{th} , I_{th}) and the value of the slope s is moreover influenced by a weak ambient magnetic field [5]. In the previous studies of silicone oil, a weak magnetic field from 34 up to 200×10^{-4} T was applied transverse to the rotational symmetry of the electrode system. As a result the linear relationship between the slope $d(\ln V)/d(\ln \dot{I})$ and gap separation disappeared, giving way to a set of curves which were always concave to the abscissa. The value of the prebreakdown current is to be either increased slightly or reduced according to the electrode spacings.

The resulting current from the rising and falling ramp functions applied to the liquid under test, consists of two components. One of which appears to be the "conduction" current which is passing through the volume of fluid. From the Chapter III analysis, at any fixed voltage the current conducted through the sample fluid volume is in fact the average value of the total current when the voltage was either increasing or decreasing. The "conduction" current data was previously obtained from the addition of current responses to positive and negative voltage ramp rates.

Another current component appears to be the "displacement" current due to charging and discharging of the test equipment capacitance. The "displacement" current data was obtained from the previous experiments that were conducted under the same

conditions as the "conduction" current analysis. All voltage and current values are also plotted on logarithmic scales. Two linear regions are distinctly divided from each other in the high field regime. The typical Log V versus Log I characteristics for displacement current are displayed in Figure 3.12. Each linear region displayed in the high field regime can also be expressed by means of a power law of the form: (refer to section 3.6)

$$\log I \propto g \log V \quad (4.2)$$

$$I \propto V^g$$

where g is the slope of the linear region. g can also be specified as g_u and g_l , the upper slope and lower slope respectively as shown in Figure 3.12. The lower slope g_l represents the current characteristic in the intermediate region, in which the polarity of ramp rate dV/dt is constant through this region. The charge and discharge association process during this portion of the experiment tends towards a saturation level. Thus the value of g_l is small since the slope in this area is rather flat. The upper slope represents the higher field region, in which the ramp rate changes its polarity from positive to negative at the peak voltage value. Thus a large discharge transient current is involved in the process during the ramp rate changes (from a charging to a discharging condition as shown in Figure 3.19). The value of g_u is expected to be larger than that of g_l since g_u has a steeper slope value as shown in Figure 3.12. This can be explained by using the fact that $g - s = (U^2 - 1)^{1/2} > 0$ [90], therefore g must be always larger than s . Moreover, s_u is larger in value than s_l from experimental results, thus g_u is larger than g_l as well.

In the previous work, the V-I characteristics were measured for a fixed maximum voltage excursion of the ramp at each gap separation. Those test methods do not however give any information on the effects upon the values of slopes (s_u , s_l) and (g_u , g_l) of varying this maximum voltage swing. Hereafter throughout this chapter, (s_u , s_l) and (g_u , g_l) will be considered separately with different maximum voltages. The average current characteristic relationship with the electrode gap distance at different maximum voltages will be described later in Chapter V.

4.1.2 THE AVERAGE CURRENT VARIATION WITH MAXIMUM APPLIED VOLTAGE

A typical example of the variation of the slopes with maximum applied voltage in silicone oil is shown in Figure 4.1 for the upper slope, s_u , and those for the lower slope, s_l , is shown in Figure 4.2. The electrodes for both slopes were chosen from five different pairs of materials, Cu, Al, Mg, Zn and Stainless Steel (SS). The gap distance was fixed at 3.1 mm. As the maximum applied voltage was increased, the upper slope s_u decreased slightly and the lower slope s_l tended to increase. Both the upper and lower slope values do not change appreciably regardless of the electrode material used for the tests. Both the upper and lower slope values for the SS electrodes are relatively lower than the others. For Cu and Mg electrodes the upper slope value for the 20 kV maximum applied voltage case is absent from the V-I characteristics graph analysis. This omission is due to the fact that there was no clearly defined upper slope section to the

aforementioned V-I plot. It is understood that the upper slope is primarily dependent on the electrical field strength. Thus it was difficult to measure the V-I characteristic slope if the electrical field stress was not sufficiently high. This phenomenon had been observed from time to time throughout all experiments conducted when the maximum applied voltage was very low.

4.1.3 THE DISPLACEMENT CURRENT VARIATION WITH MAXIMUM APPLIED VOLTAGE

The "displacement" current data are deduced from the difference between the current response to rising and falling voltage ramp rates. The difference between the displacement current and the average (conduction) current is that the displacement current has a direct relationship with the value of ramp rate, dV/dt , and its polarity. When the maximum applied voltage is increased, the ramp rate also increases and as a result, the displacement current is increased as well. It is shown in Figure 3.12 that the upper slope (the slope in the higher field region) changes dramatically when the polarity of the ramp rate reversed at the maximum applied voltage. The lower slopes in the intermediate region vary much less than the upper ones when V_m is varying.

The measured results of the slope from the displacement current data are shown in Figure 4.3 for the lower slope g_l and Figure 4.4 for the upper slope g_u with the maximum applied voltages respectively. Figure 4.3 shows the performance of five pairs

of different electrodes with varying maximum applied voltage at a gap distance of 3.1 mm. The slope value for each electrode material showed a noticeable increase with an increase in the maximum applied voltage. However, as the maximum applied voltage increased, the slope values for each material became closer. Figure 4.4 shows the upper slope values of the displacement current from the same materials described in Figure 4.3. The effect of the magnitude of the maximum applied voltage on the upper slope value is not as clear as for those values of the lower slope. While the upper slope value for the Cu and Al pairs of electrodes are slightly increasing with the maximum applied voltage, others decrease first as the voltage increases and then slightly increase when the voltage increase further. Furthermore, the values of the upper slope are much larger, from 5 to 10 times larger than the corresponding lower slopes of the plot of displacement current versus voltage.

Comparing the slope values from the mean current results in section 4.1.2, the values of upper and lower slopes of displacement current for the five pairs of different electrodes are close in magnitude to each other, especially when the applied voltage is high. Thus the electrode material effect is unclear for the displacement current analysis at this point. In other words, there is no apparent direct relationship between the displacement current and the electrode materials. A further study will be continued in the following section.

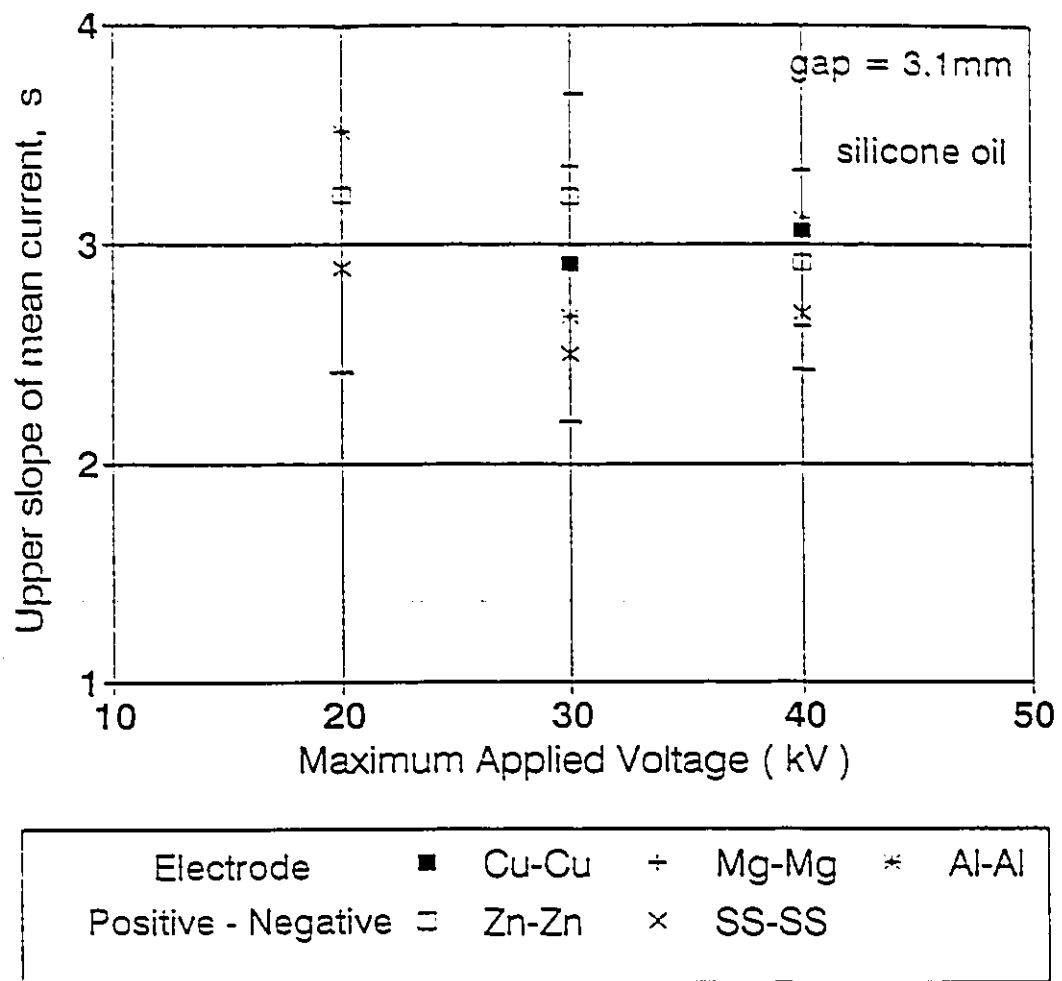


Figure 4.1 The upper slope value of mean current as a function of maximum applied voltage in silicone oil

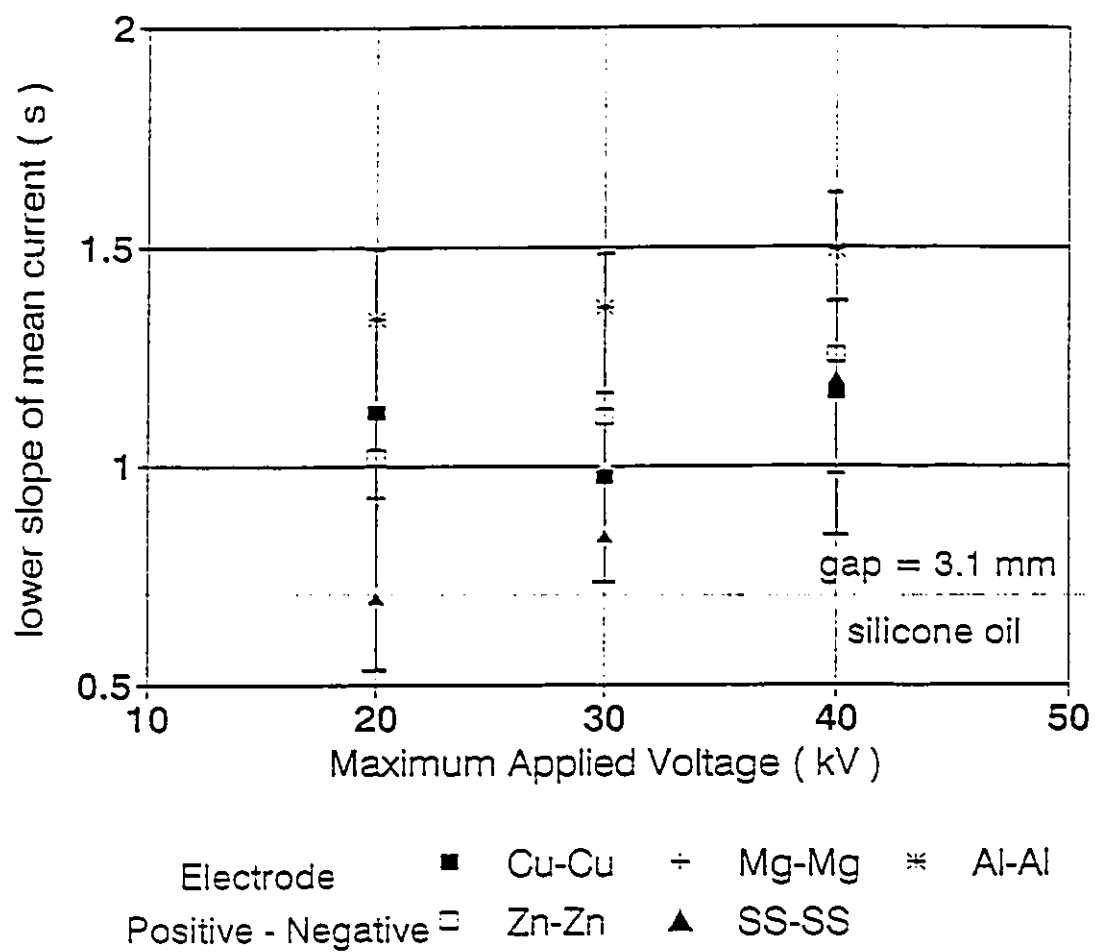


Figure 4.2 The lower slope value of mean current as a function of maximum applied voltage in silicone oil

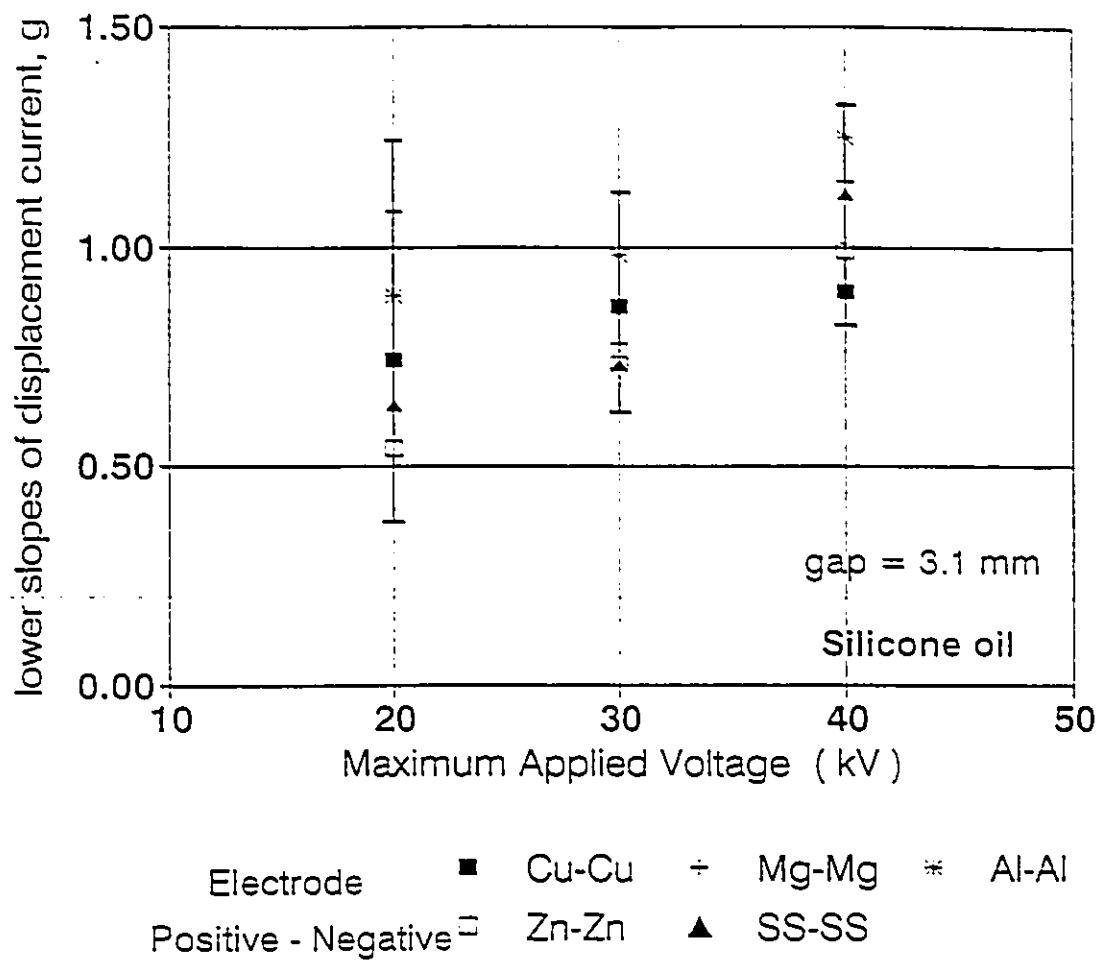


Figure 4.3 The lower slope value of displacement current as a function of maximum applied voltage in silicone oil

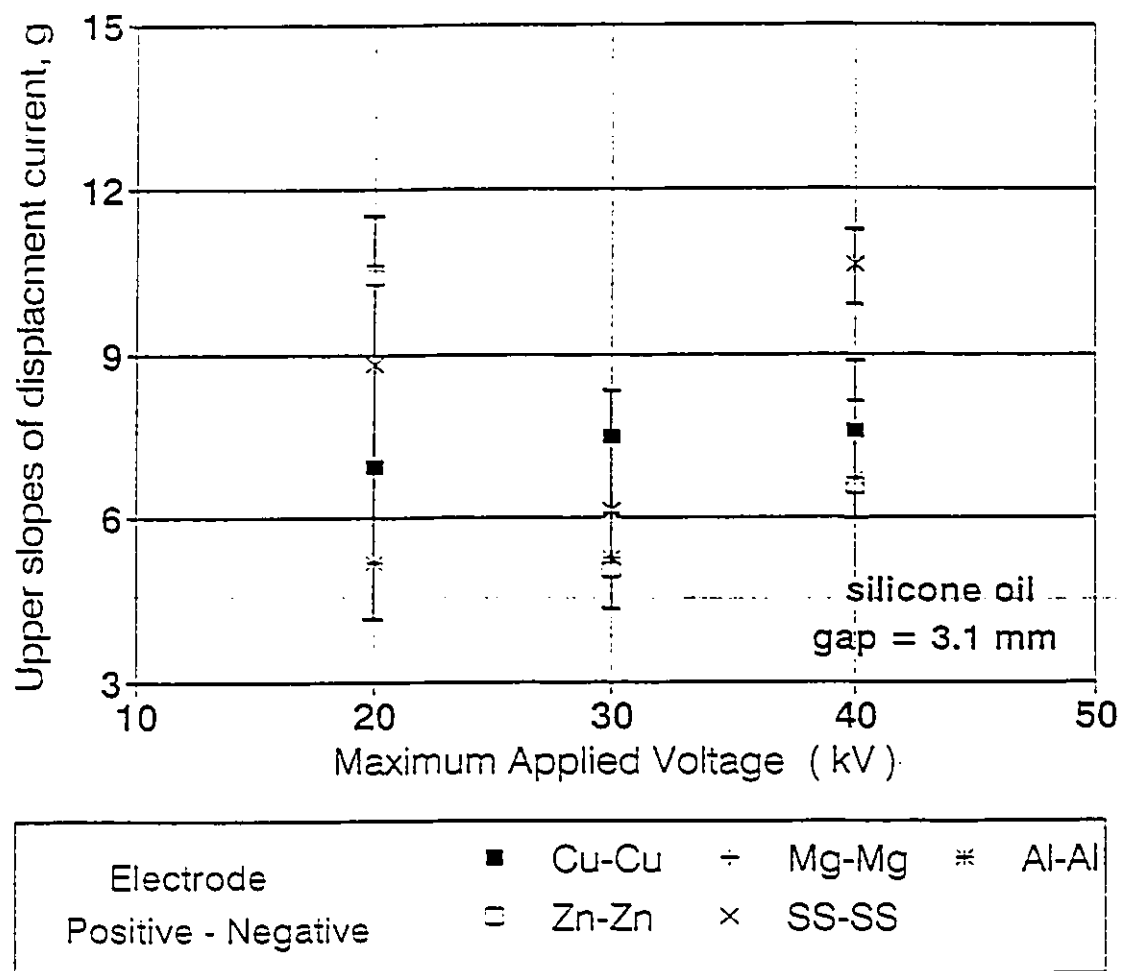


Figure 4.4 The upper slope value of displacement current as a function of maximum applied voltage in silicone oil

4.1.4 THE DISPLACEMENT CURRENT VARIATION WITH GAP DISTANCE

The analysis of the lower slope value for the displacement current will be studied first in this section. In accordance with the methods developed to relate s with electrode gap distance [5], the following analysis will also be used to develop the inverse slope values, $1/g$, in this section. The measurement has been made over a range of gap separations from 2.07 to 7.75 mm. The lower slope values of the displacement current for the maximum applied voltage ranging from 20, 30 and 40 kV respectively are shown in Figures 4.5-4.7. These figures give the relationship between the inverse value of lower slope g_l and the gap separation in four different pairs of identical electrode materials. Figure 4.5 shows that in the 20 kV range, some displacement current slope values g_l for the four electrode materials do not have a strong relationship with the gap distance. The slope values from the Mg and Zn pairs of electrodes seem to increase slightly with an increase in the gap distances. The other electrode materials appear not to fit this same pattern in which the slope values are almost constant. The average slope value of the $1/g_l$ from these four sets of data points is approximately 1.5 appears as almost a straight line. As the maximum applied voltage increased to 30 kV, shown in Figure 4.6, most slope values from these four pairs of electrodes become very close to each other at small gap separations. The average line looks similar to that of the one for the case 20 kV and its absolute value is reduced to a level close to 1.5. Again, there is no significant slope value difference between these four electrode materials, where the $1/g_l$ increases more sharply. It can be seen in Figure 4.7 that in the 40 kV range these

four pairs of electrodes have even closer slope values. The curves of g_l^{-1} vs. gap distance have the general form of a straight line. The slope of the curve increases with the gap distance but does not change significantly. The average value of the slopes is close to unity in the 40 kV range.

The results of the slope values of displacement current, shown in Figures 4.5-4.7 for the 20, 30 and 40 kV ranges, are plotted by using the same graph scales. This gives a better comparison of the results with different voltage levels. The slope values for the four different electrode materials begin to converge to one value as the maximum applied voltage increases. The maximum applied voltage of 40 kV gives better experimental results that are less scattered than others. From this point onward, all the experimental results will be analyzed in the 40 kV range unless otherwise specified.

It is not quite clear so far, what is the main charge source that contributes to the displacement current. It is therefore suspected that dielectric materials or electrode materials would play an important role. Thus, all four of the different electrodes are tested alternately mixed as well as matched. Figure 4.8 gives an example of the inverse lower slope values of displacement current and its relationship to the electrode gap distance. In this figure a Cu electrode is used as the cathode and four other different materials are used as the anode. The slope values are increased with the gap distance for the Al materials as the anode. The data shown in Figure 4.9 was obtained under the same conditions as those in Figure 4.8, but at this time the Cu electrode acted as the

anode with four different materials acting as the cathode. The results from the Mg and the Zn electrodes acting as the anode are close to each other. For Cu and Al electrodes the results are similar, the slope values slightly vary with gap distances. The individual data shown in Figures 4.8 and 4.9 are not identical to each other. The average slope lines, however, are almost identical to each other with either the Cu electrode as the cathode, in Figure 4.8 or as the anode, shown in Figure 4.9. The average slope value from both figures is approximately unity which is the same value as the one obtained from the previous results shown in Figure 4.7. It should be noted that the results have been magnified by reducing the scale of the ordinate axis. Thus, this ordinate scale reduction will provide for a better comparison of the lines.

Other electrode materials such as Al, Mg and Zn are also analyzed by using the same method. The results are shown in Figure 4.10 to Figure 4.15 respectively. Figure 4.10 and Figure 4.11 show the lower slope values for the Al electrode either as the cathode or as the anode with the other four electrode materials acting as the opposite terminal. Figure 4.12 and Figure 4.13 give the results for the Mg electrode. Figure 4.14 and Figure 4.15 show the results when the Zn electrode is used as the cathode as well as the anode. From all these measurements, the average lines from each figure have shown themselves to be very similar to each other. The slope values all increase as the gap separation increases. It is clear that when using currently available measurement technology, the effect of the electrode material on the lower slope of the displacement current line is very small.

The upper slope values of displacement current from the experimental results are analyzed using the same procedure as for that of the lower slopes. Figures 4.16-4.18 represent the inverse upper slopes of the displacement current as a function of the gap separation. Four different pairs of identical electrode materials are used here. The maximum applied voltage also ranged from 20 kV to 40 kV respectively. With the maximum applied voltage at 20 kV, the Al electrode basically has the highest upper slope value (lowest in g_u) among them all, shown in Figure 4.16. The Mg electrode has the lowest value in most cases. The upper slope values from other electrode materials are in between those previously described. Their slope values are shown to be almost a constant value regardless of the gap separation. The average values of these four sets of data are also shown in Figure 4.16 and varied about the value 0.2. The results of increasing the maximum applied voltage to 30 kV can be seen in Figure 4.17. Using the same scale for the ordinate axis as in the 20 kV range (Figure 4.16), all four pairs of slope values are closer to each other. Moreover the slope values from those four pairs of electrodes are not clearly different from one another. However the average value still remains about the same as in the 20 kV case. The upper slope values look very different when the maximum applied voltage was increased to 40 kV as shown in Figure 4.18. All four sets of data are very close to each other. The slope values are almost the same, and the average value is very nearly to a constant, independent of the gap separation.

In accord with the methods developed to relate s_u (upper slope value of the mean current) with the electrode gap separation [5], g_u can also be written in a certain

relationship with the gap distance from the average value curve shown in Figure 4.18. Thus Equation 4.3 is given as:

$$g_u^{-1} = A_g + B_g d \quad (4.3)$$

where d is the gap distance in mm, $A_g = 0.143$ and $B_g = -0.001$. The Equation 4.3 shows that g_u is close to a constant, at approximately 0.14 in the 40 kV range, smaller than those in the 20 kV and 30 kV ranges. Again, these three figures do not give a clear picture of the effect of the electrode materials on the slope values under different electric field strengths. More tests have therefore been carried out by alternately mixing these four different electrodes. The analysis is made in such way that one kind of electrode material is chosen as either the cathode or the anode. Moreover, for a better comparison, a reduced scale of ordinate axis is used in the Figures 4.19 - 4.26.

Figures 4.19 and 4.20 show the inverse slope values for the Cu electrode as the cathode and as the anode at the 40 kV range. With the Cu electrode acting as the cathode, four different anode electrodes give two different results. The upper slope values for the Mg and Cu electrodes as the anode vary little with the gap separation, shown in Figure 4.19. The Zn electrode shares the same pattern as those of Mg and Cu but with smaller upper slope values. When the Al electrode acts as the anode, the upper slope value varies randomly as the gap distance increases. This is the same case as when the Cu electrode is used as the anode with the Zn and Cu electrodes as the cathode i.e. Cu(+)-Zn(-) and Cu(+)-Cu(-) cases. Those results are shown in Figure 4.20. The Mg

electrode presents the same curve pattern as the Al electrode with smaller values. Comparing Figures 4.19 and 4.20, the result is different for a Cu-Mg, and Al-Cu electrodes pairs when Cu acts either as anode or cathode. For the Cu(+)-Mg(-) pair, the slope value increases steadily as the gap distance increases. As in the Cu(-)-Mg(+) case, the slope value is different. Even though the individual data sets from these two figures are very different, the average value for the Cu electrode as the anode and as the cathode are still very close.

Figure 4.21 gives the results of the Mg electrode as the cathode. When the Cu and Al electrodes act as the anode, the upper slope values show the exhibit pattern when compared to each other. The upper slope values increase with an increase in the gap distance. In Figure 4.22, with the Mg electrode acting as the anode, all others electrodes are used as the cathode. This arrangement gives similar results when compared to Figure 4.21. Moreover, the average values from those two figures are very close to one another. Figures 4.23 and 4.24 show the results for the Al electrode. Both figures show that all the materials more or less follow the same pattern, the slope values slightly vary with gap distances. Again, it is apparent that the difference between each slope value is very small. Figures 4.25 and 4.26 show the results for the Zn electrode acting as the cathode as well as the anode. When the Zn electrode is used as the cathode, all four different sets of electrodes materials give almost the same pattern as seen in Figure 4.25. With the Zn electrode switched to the role of the anode, shown in Figure 4.26, all cases but the Cu electrodes as anodes yield similar results to those shown in Figure 4.25.

It is very interesting that the average curves for the upper slope values from all Figure 4.19 to Figure 4.26 are very close to each other. They increase slightly as the gap separation increases.

4.1.5 V-I THRESHOLD POINT

It has been mentioned before that either the conduction current or displacement current will clearly yield two distinct regions originating from a threshold point shown in Figure 3.11 and Figure 3.12. The V-I threshold point for silicone oil has been studied extensively by previous researchers [6,9]. It was shown that the corresponding voltage and current values of each threshold point were directly proportional to the applied voltage ramp rate. The electrode gap distance influenced only the ordinate intercepts of the curves. If that is really true, then the threshold voltage should be proportional to its threshold current. Previous researchers had only derived it theoretically by assuming the existing voltage and current proportionality in their work [9]. Thus, the threshold voltage as a function of threshold current is plotted here in Figure 4.27 based on the most recent experiments. This series of experiments was performed to verify experimentally the V-I proportionality. The results show that V_{th} is directly proportional to I_{th} which proves that the original assumption is correct. The straight line shown in Figure 4.27 represents a plot of the average values of V_{th} vs I_{th} . The gap separation was 3.1 mm. For the straight line plotted in Figure 4.27, the average V_{th} value could be written as

$$V_{th} = V_{tho} + R_{tho} I_{th} \quad (4.4)$$

where V_{th} is in kV and I_{th} is in nA, V_{tho} and R_{tho} are constant values. At a 3.1 mm gap distance, $V_{tho} = (1.0 \pm 6\%)$ kV and $R_{tho} = (1.75 \pm 5\%) 10^{12} \Omega$. The experimental determination of equation 4.4 verifies the existence of the V_{th} , I_{th} proportionality for silicone oil. The ratio of V_{th} and I_{th} is at $10^{12} \Omega$.

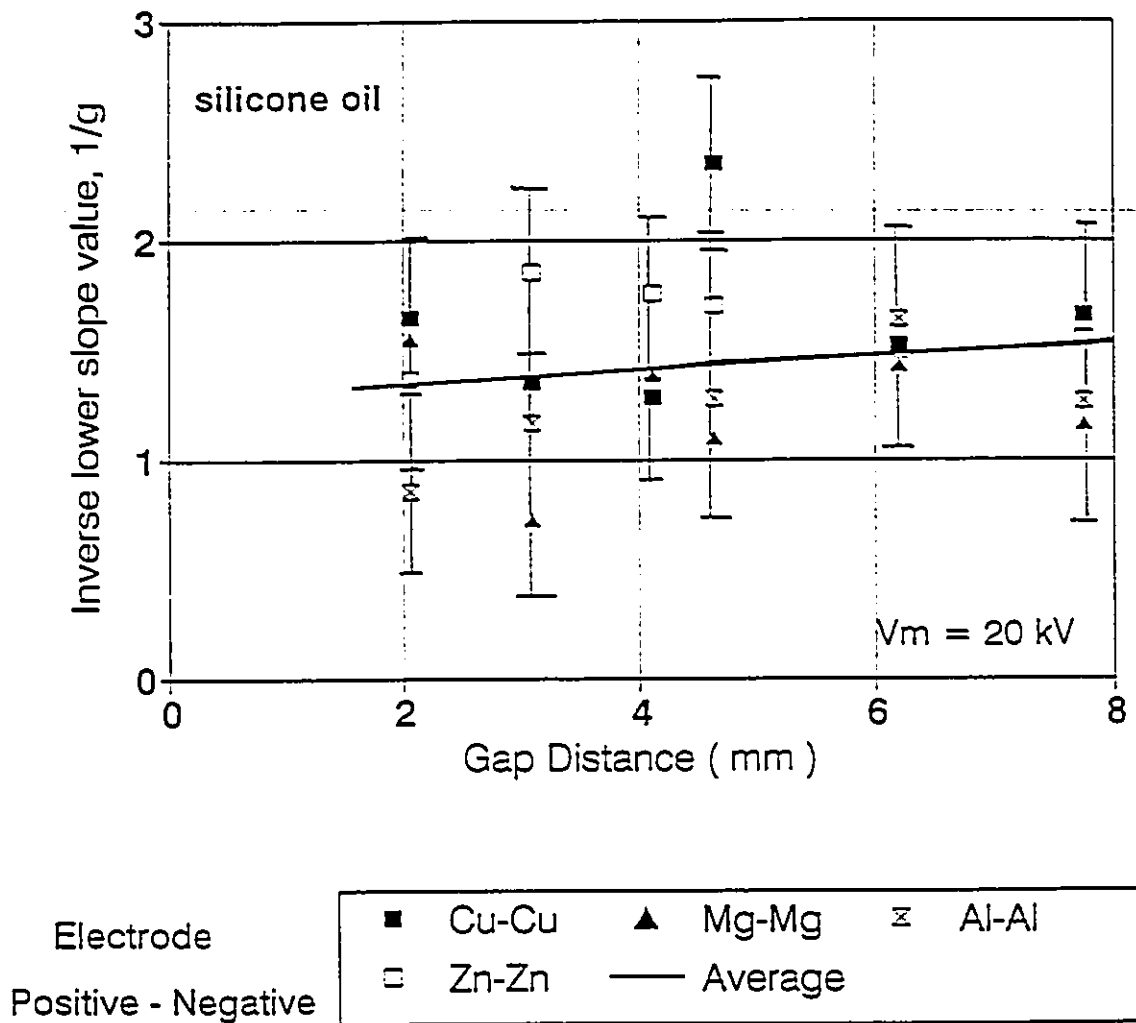


Figure 4.5 Inverse lower slope value of displacement current as a function of gap distance in silicone oil at 20 kV

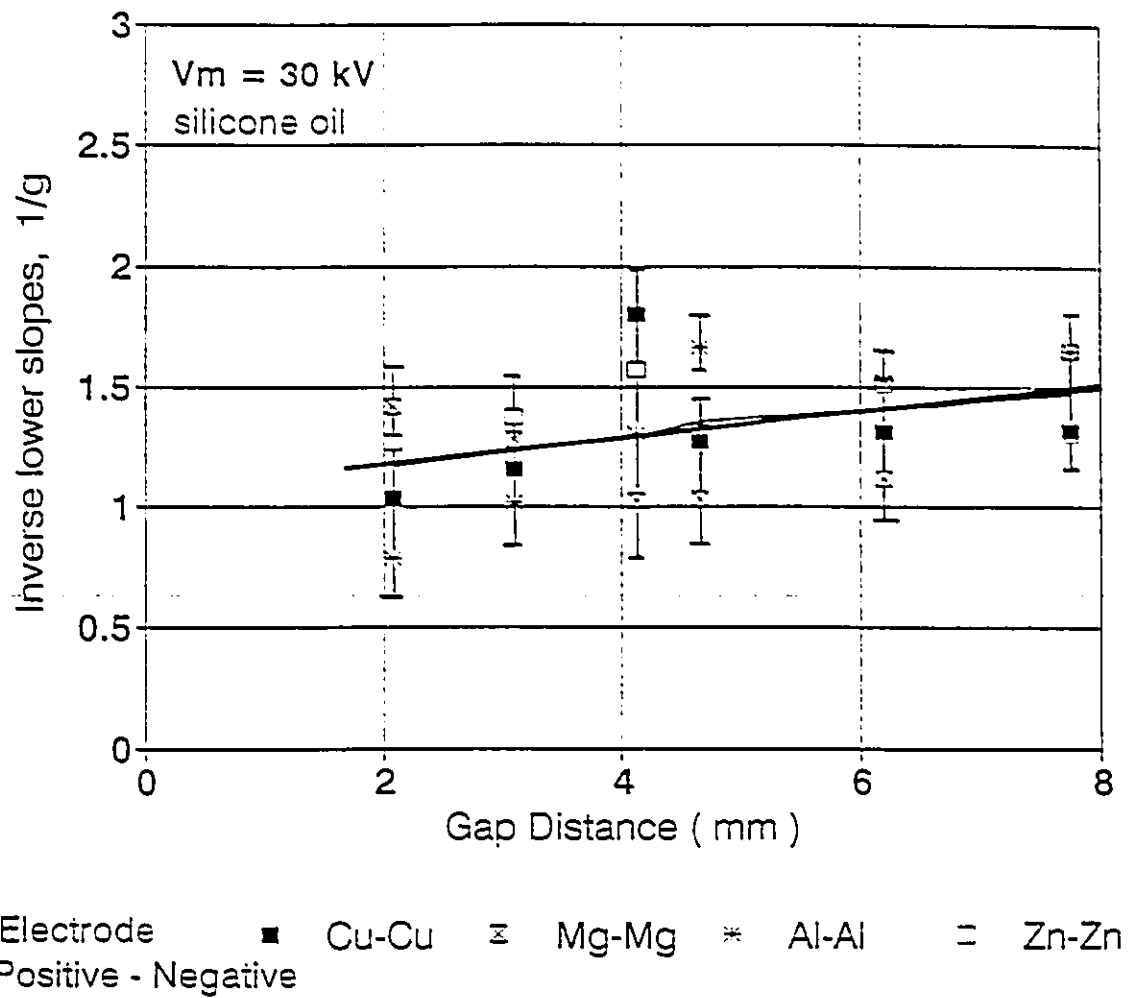


Figure 4.6 Inverse lower slope value of displacement current
 as a function of gap distance in silicone oil at 30 kV

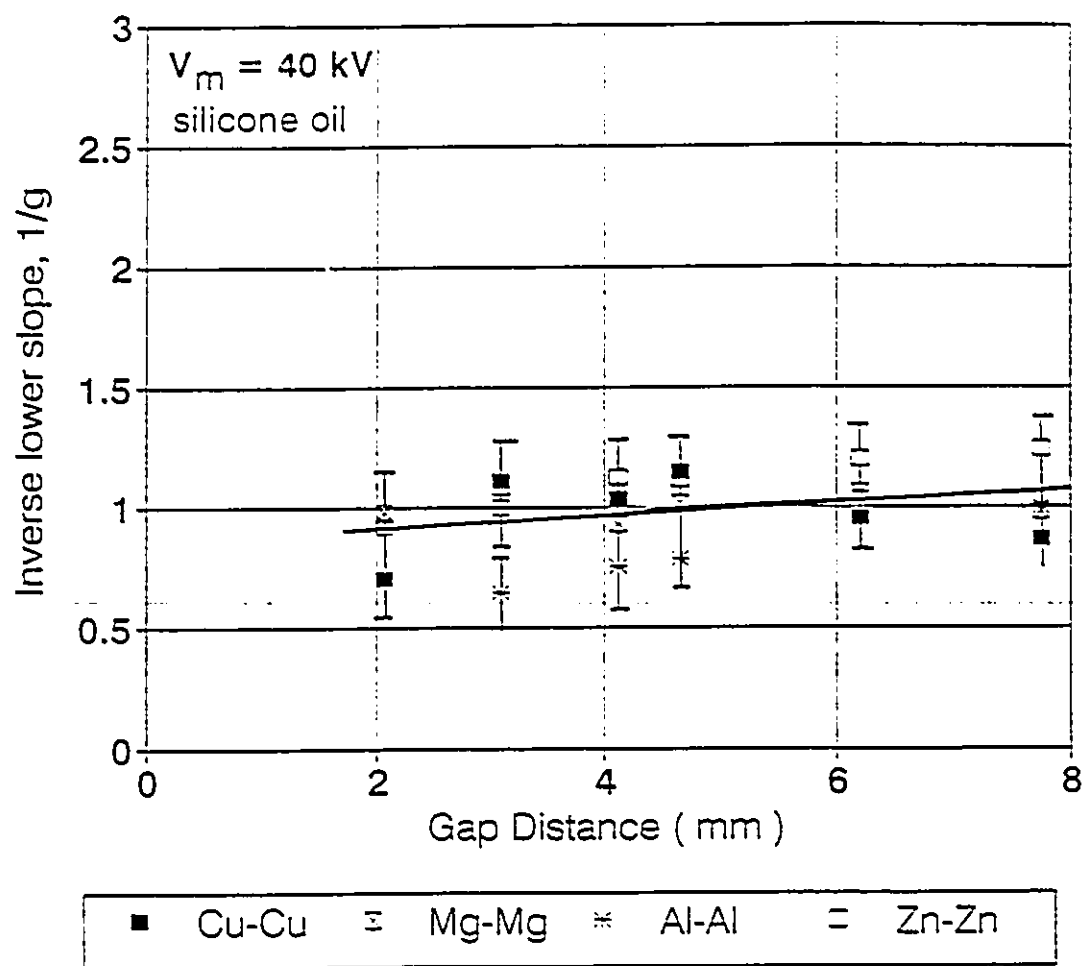


Figure 4.7 Inverse lower slope value of displacement current
 as a function of gap distance in silicone oil at 40 kV

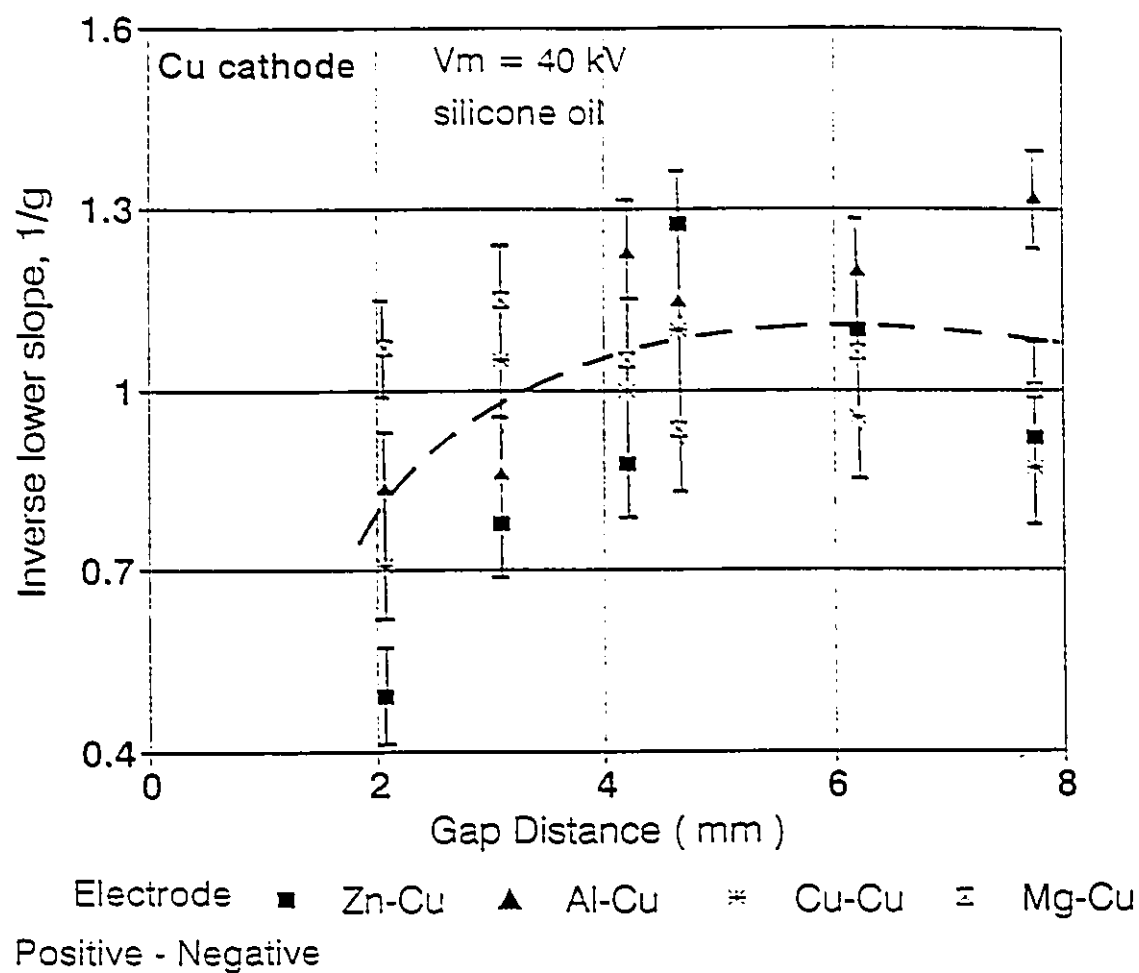


Figure 4.8 Inverse lower slope value of displacement current as a function of gap distance with Cu cathode at 40 kV

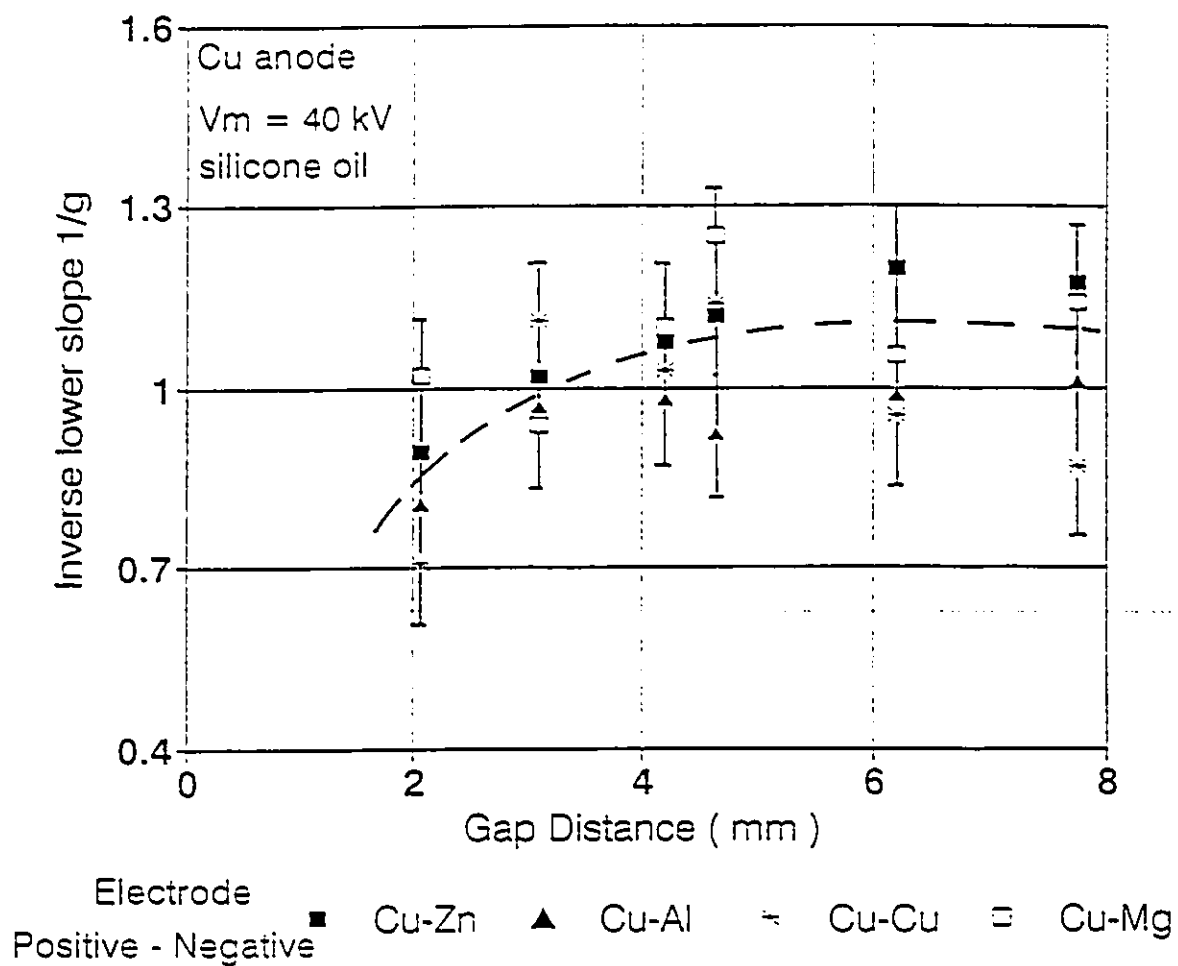


Figure 4.9 Inverse lower slope value of displacement current
 as a function of gap distance with Cu anode at 40 kV

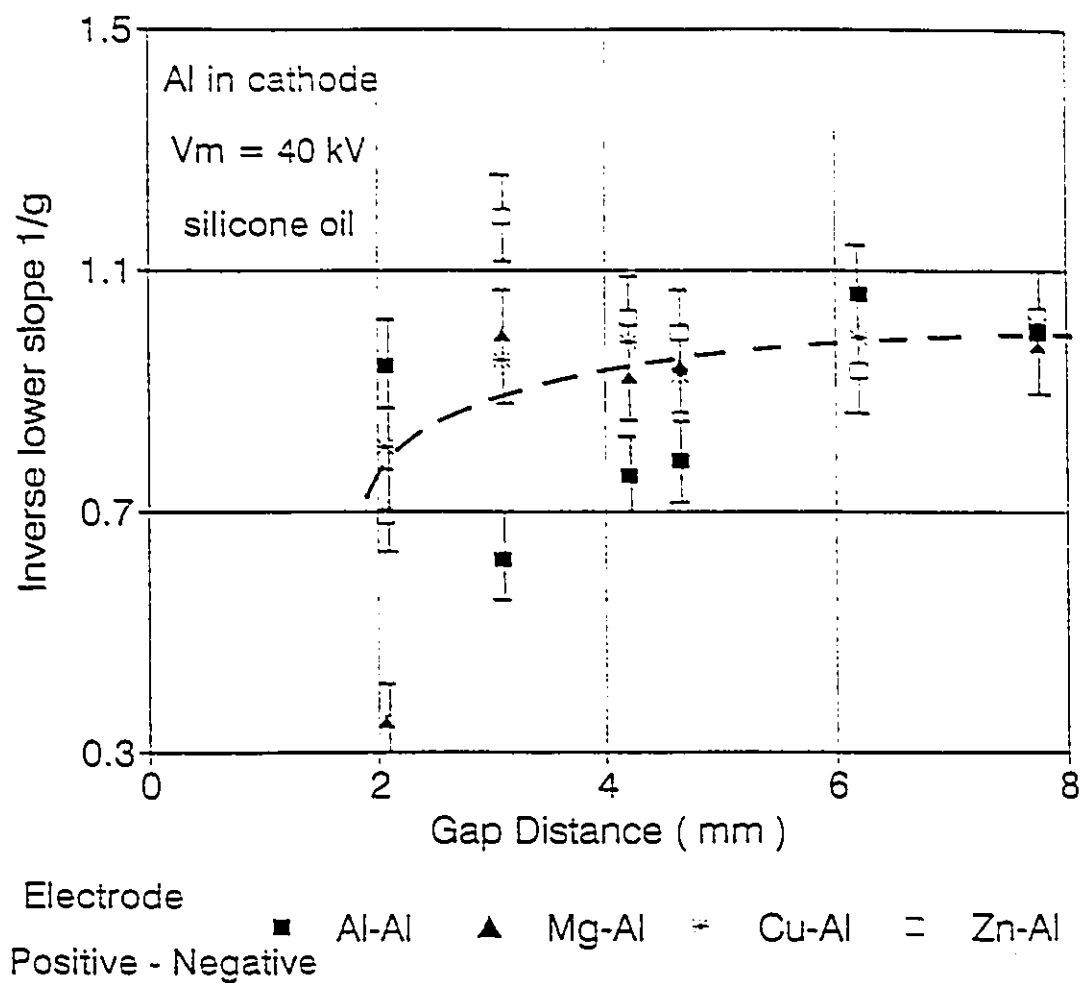


Figure 4.10 Inverse lower slope value of displacement current as a function of gap distance with Al cathode at 40

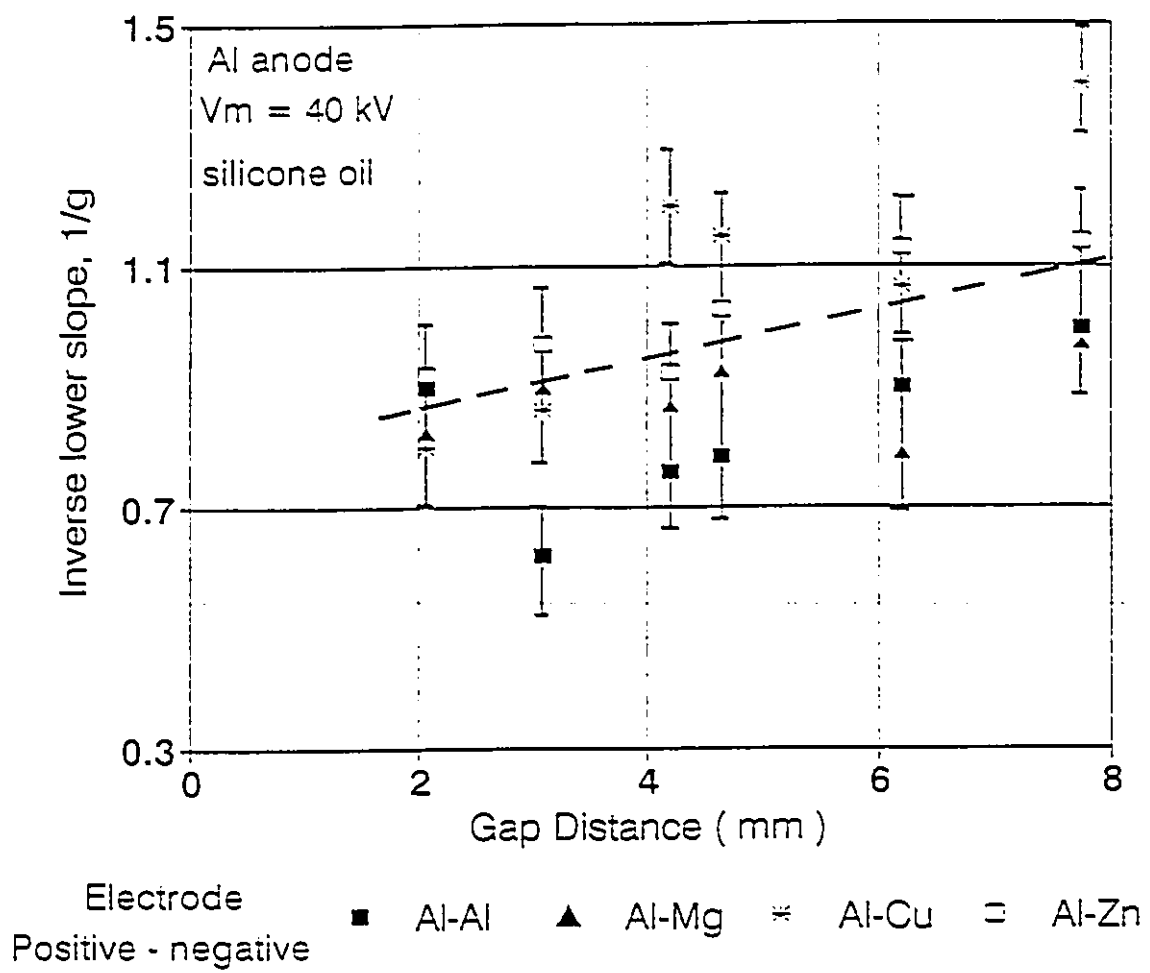


Figure 4.11 Inverse lower slope value of displacement current as a function of gap distance with Al anode at 40 kV

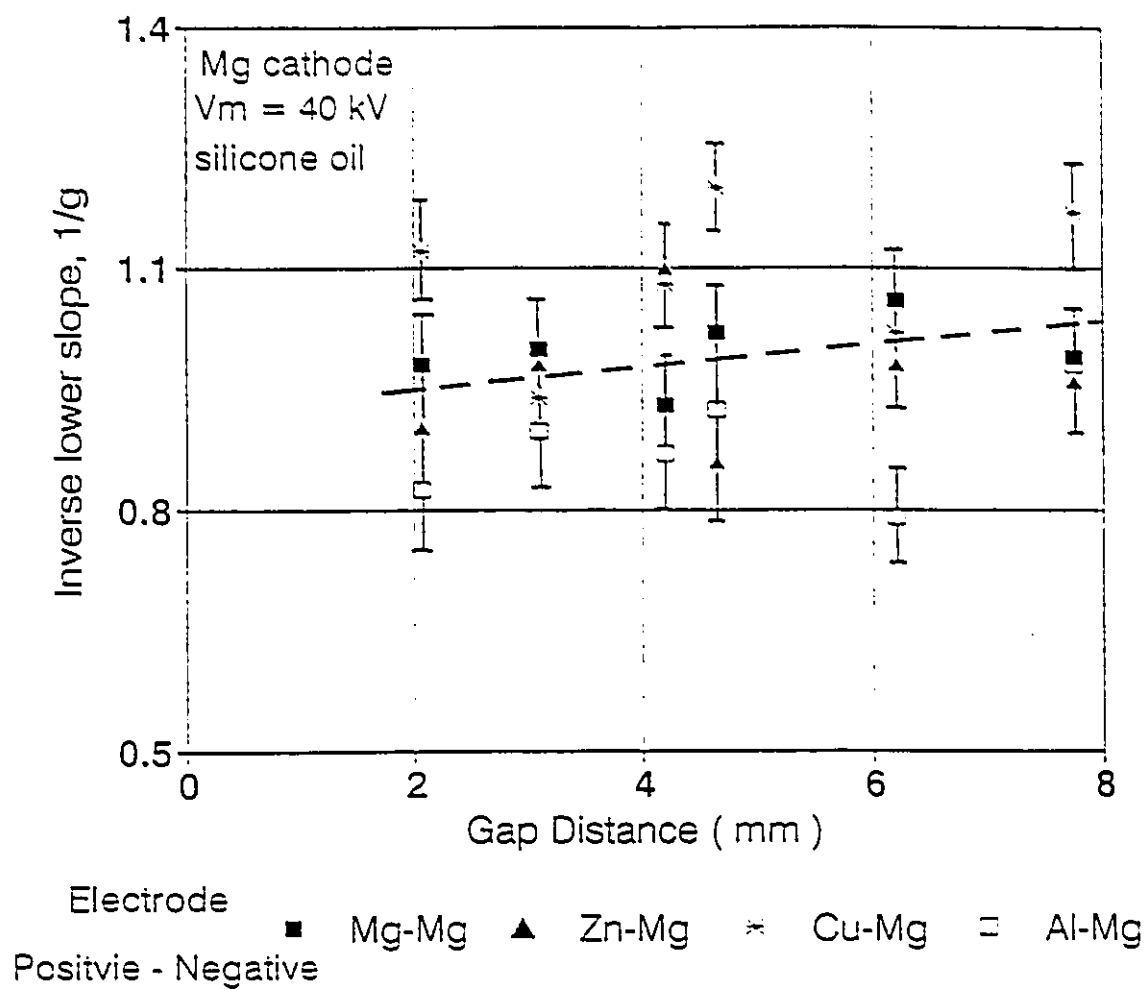


Figure 4.12 Inverse lower slope value of displacement current as a function of gap distance with Mg cathode at 40 kV

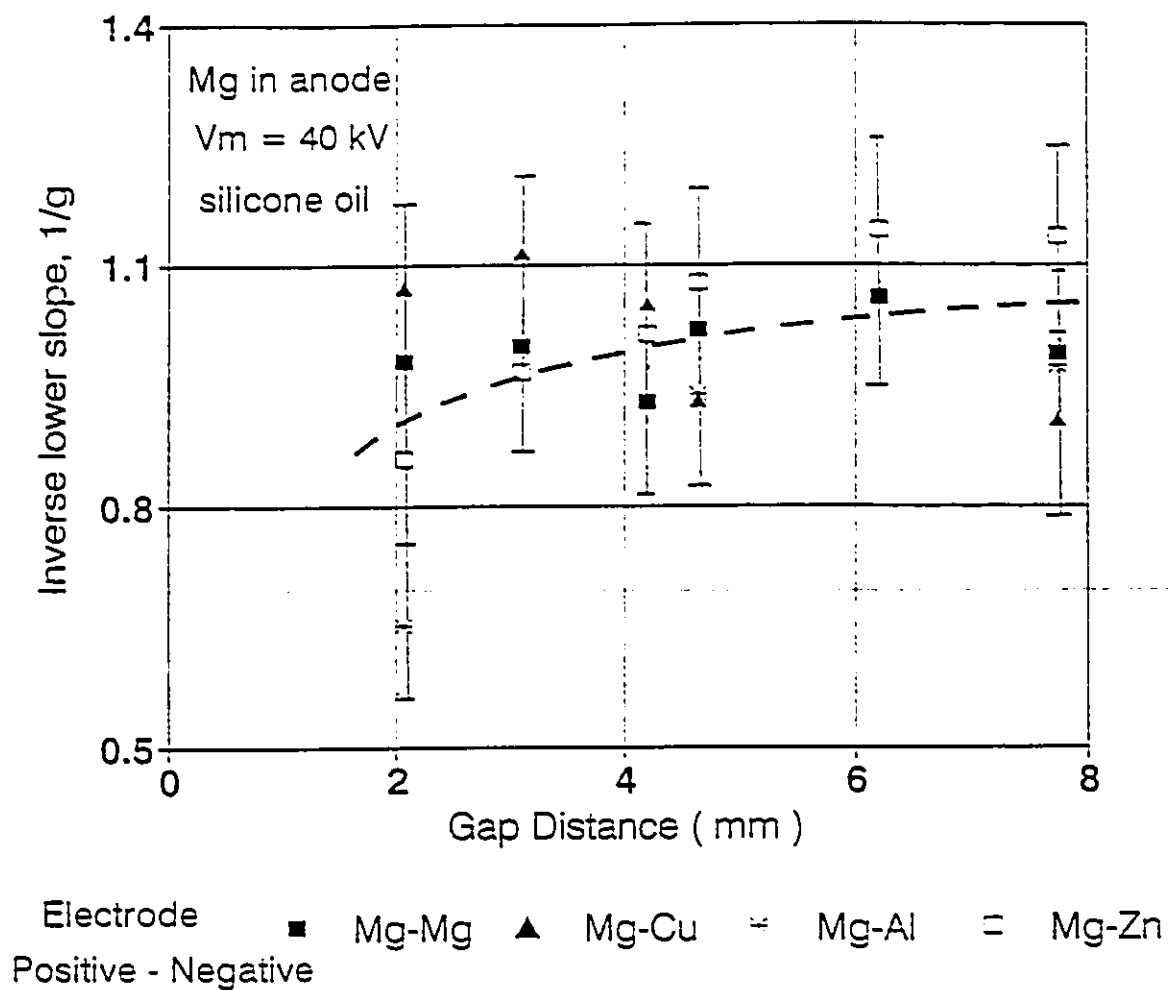


Figure 4.13 Inverse lower slope value of displacement current as a function of gap distance with Mg anode at 40 kV

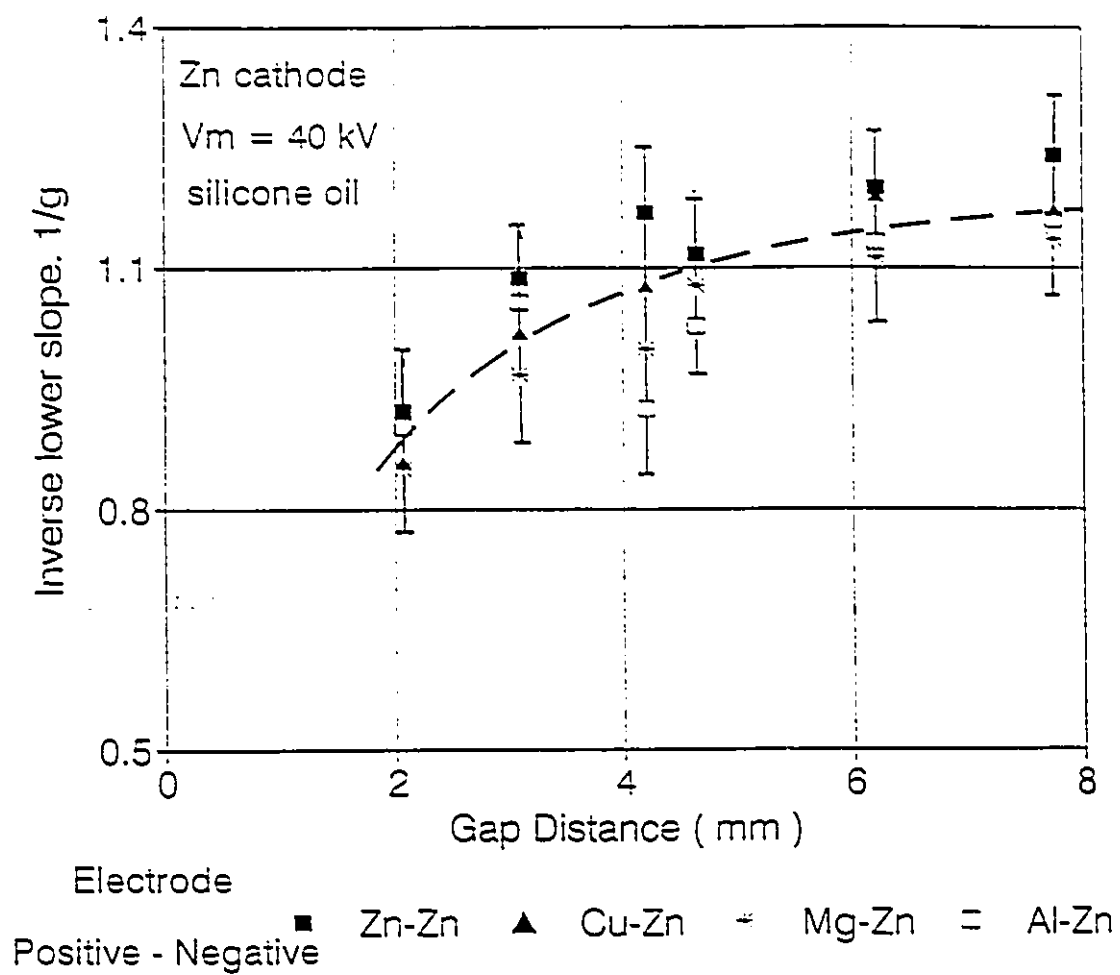


Figure 4.14 Inverse lower slope value of displacement current as a function of gap distance with Zn cathode at 40 kV

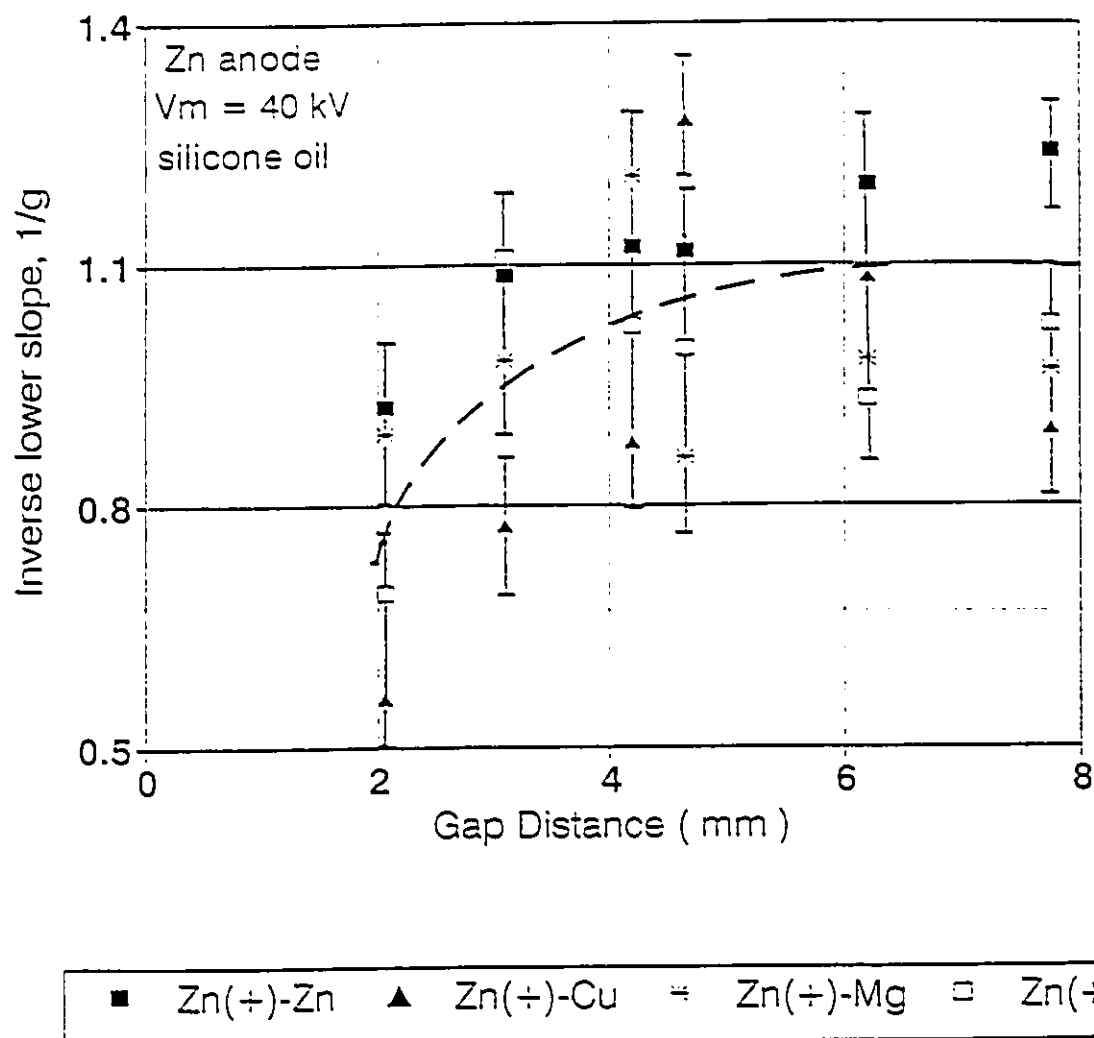


Figure 4.15 Inverse lower slope value of displacement current
 as a function of gap distance with Zn anode at 40 kV

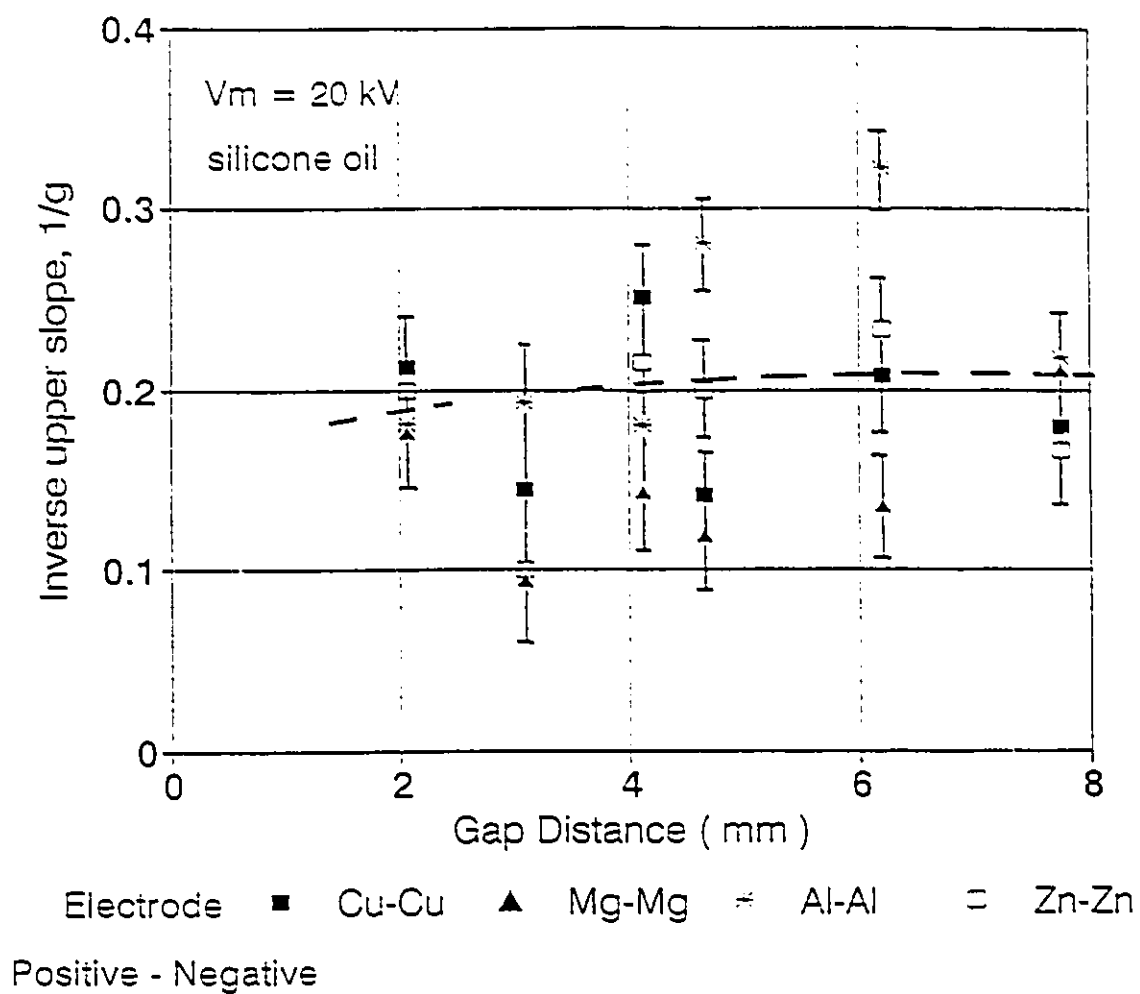


Figure 4.16 Inverse upper slope value of displacement current
 as a function of gap distance in silicone oil at 20 kV

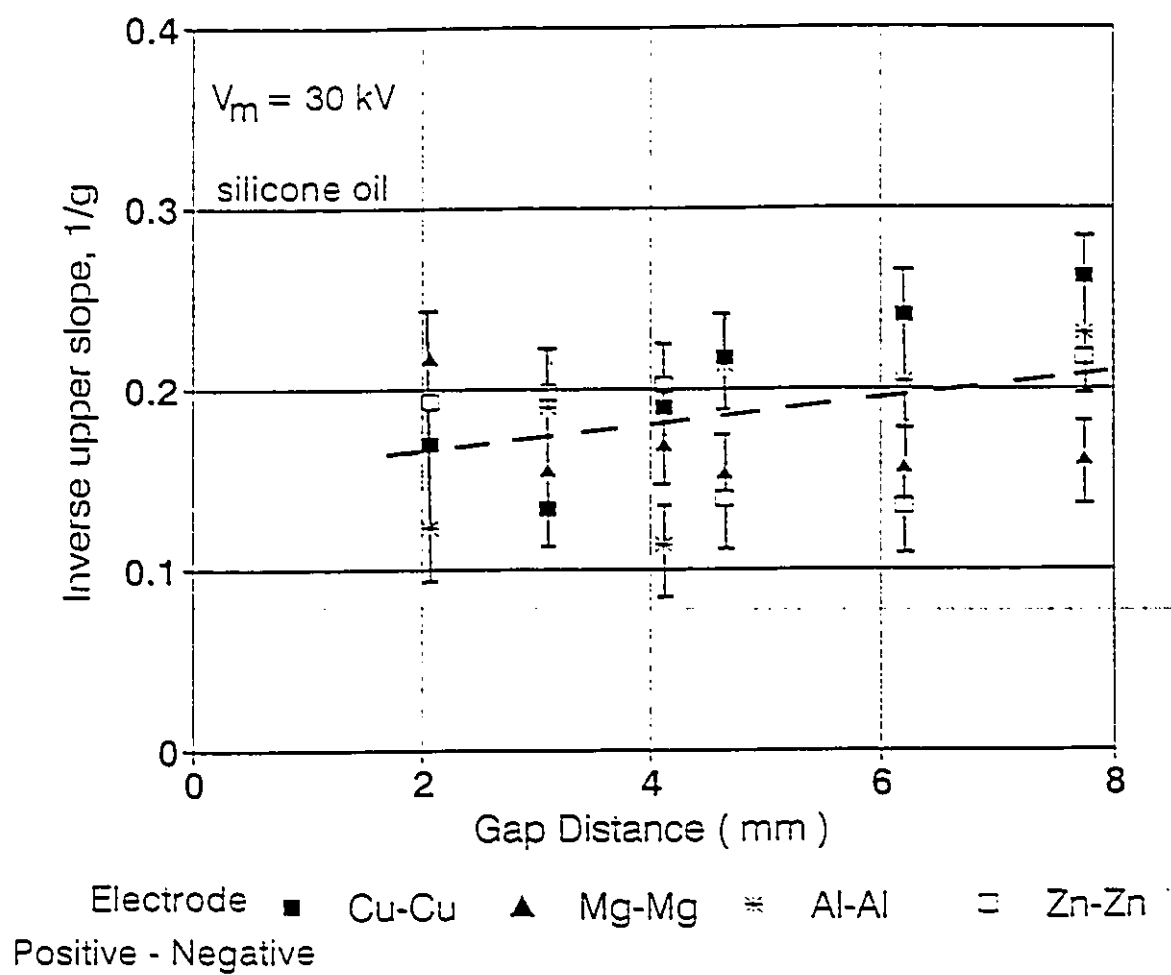


Figure 4.17 Inverse upper slope value of displacement current
 as a function of gap distance in silicone oil at 30 kV

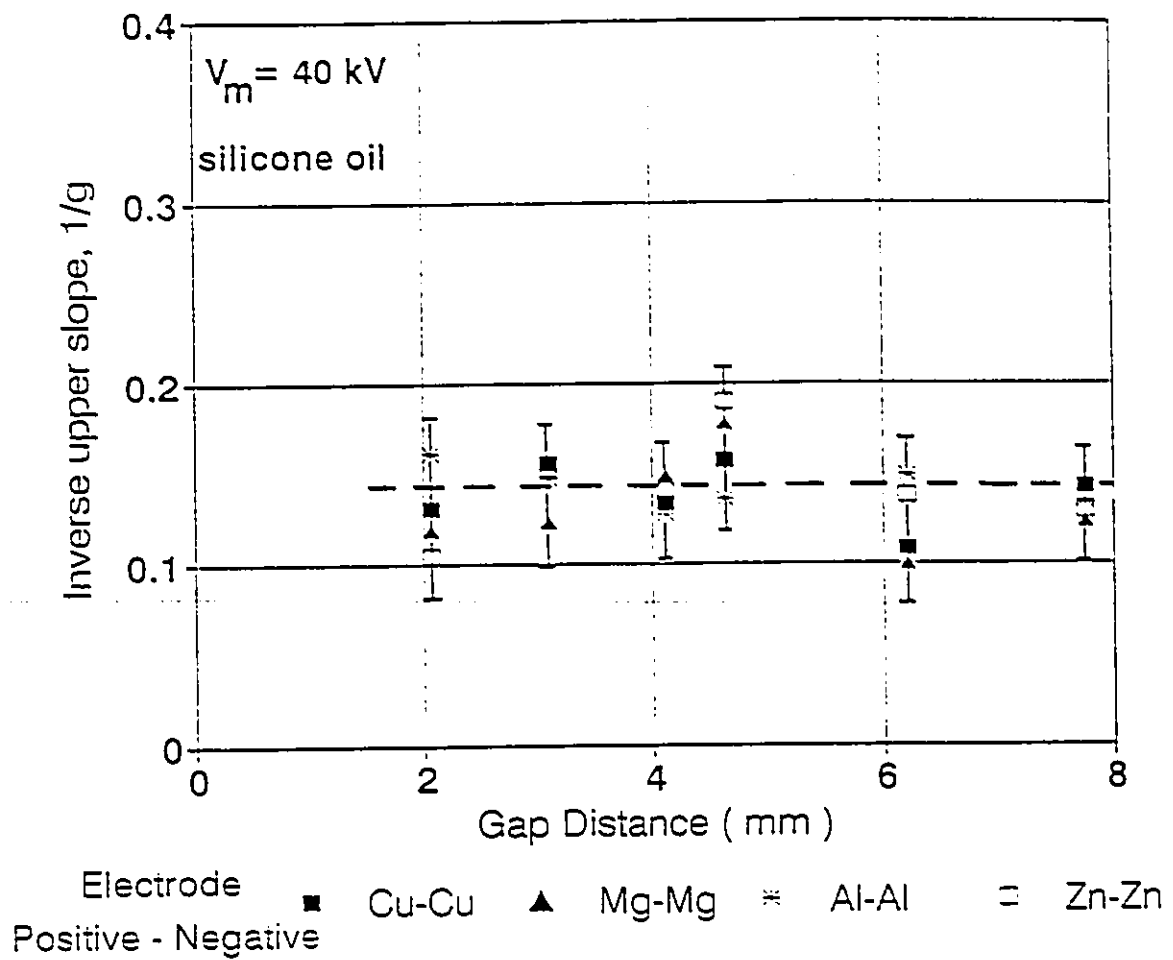


Figure 4.18 Inverse upper slope value of displacement current
 as a function of gap distance in silicone oil at 40 kV

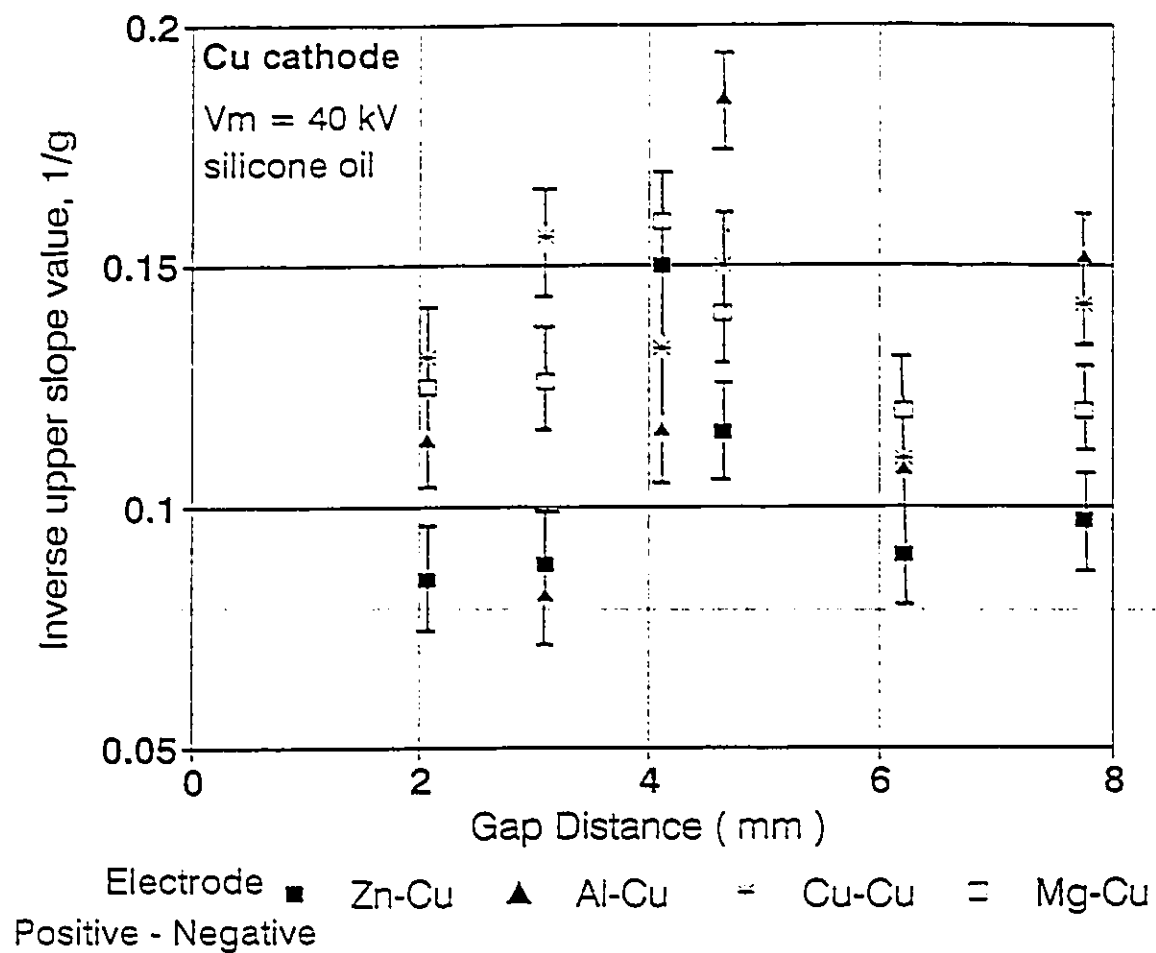


Figure 4.19 Inverse upper slope value of displacement current as a function of gap distance with Cu cathode at 40 kV

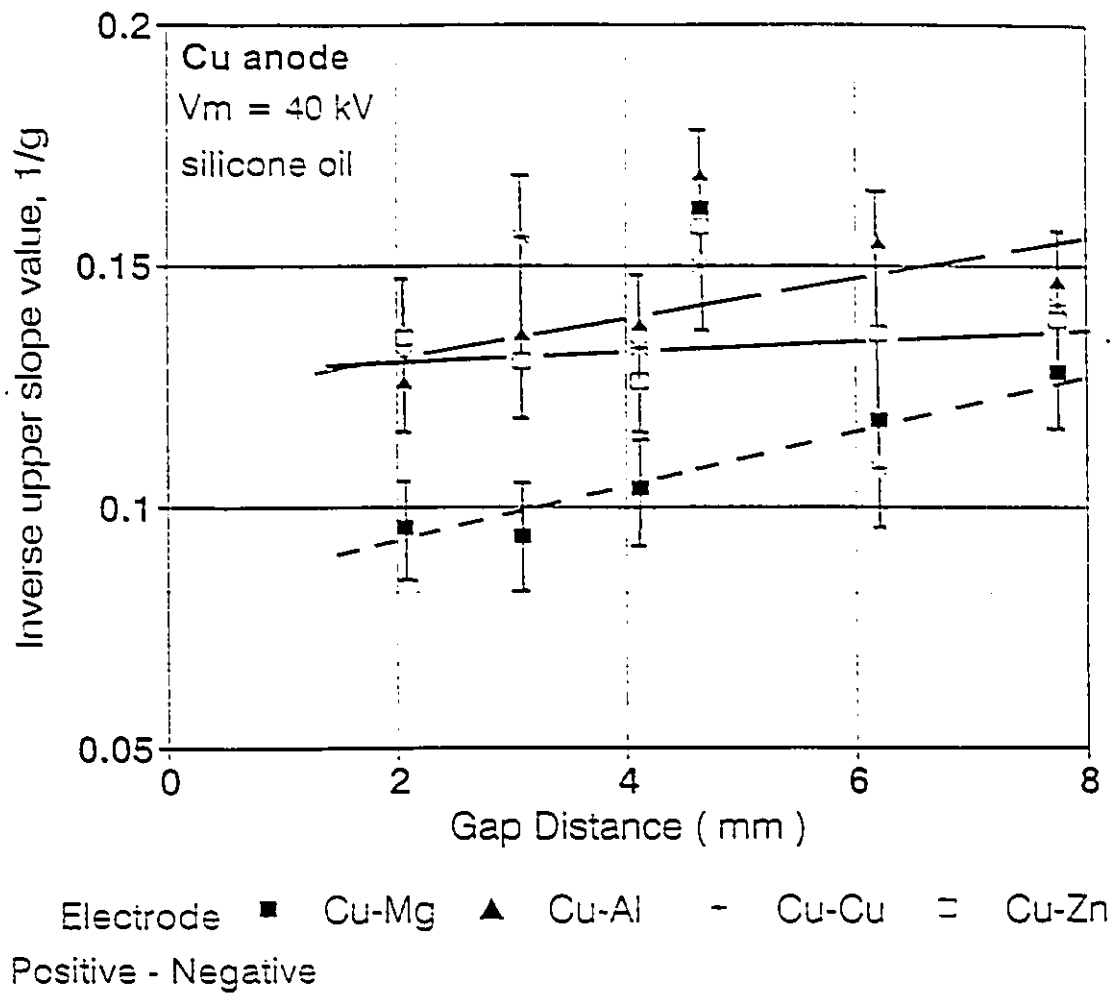


Figure 4.20 Inverse upper slope value of displacement current as a function of gap distance with Cu anode at 40 kV

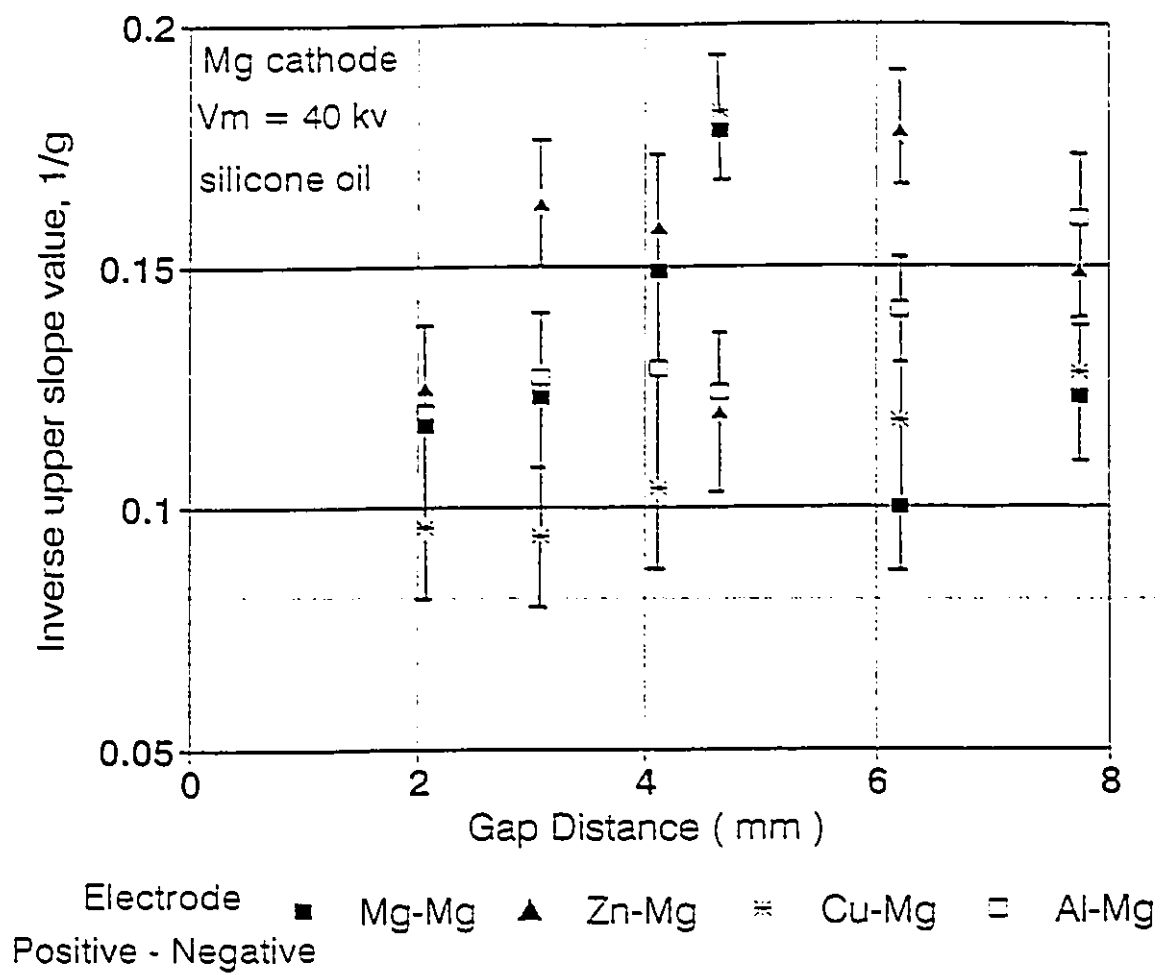


Figure 4.21 Inverse upper slope value of displacement current
 as a function of gap distance with Mg cathode at 40 kV

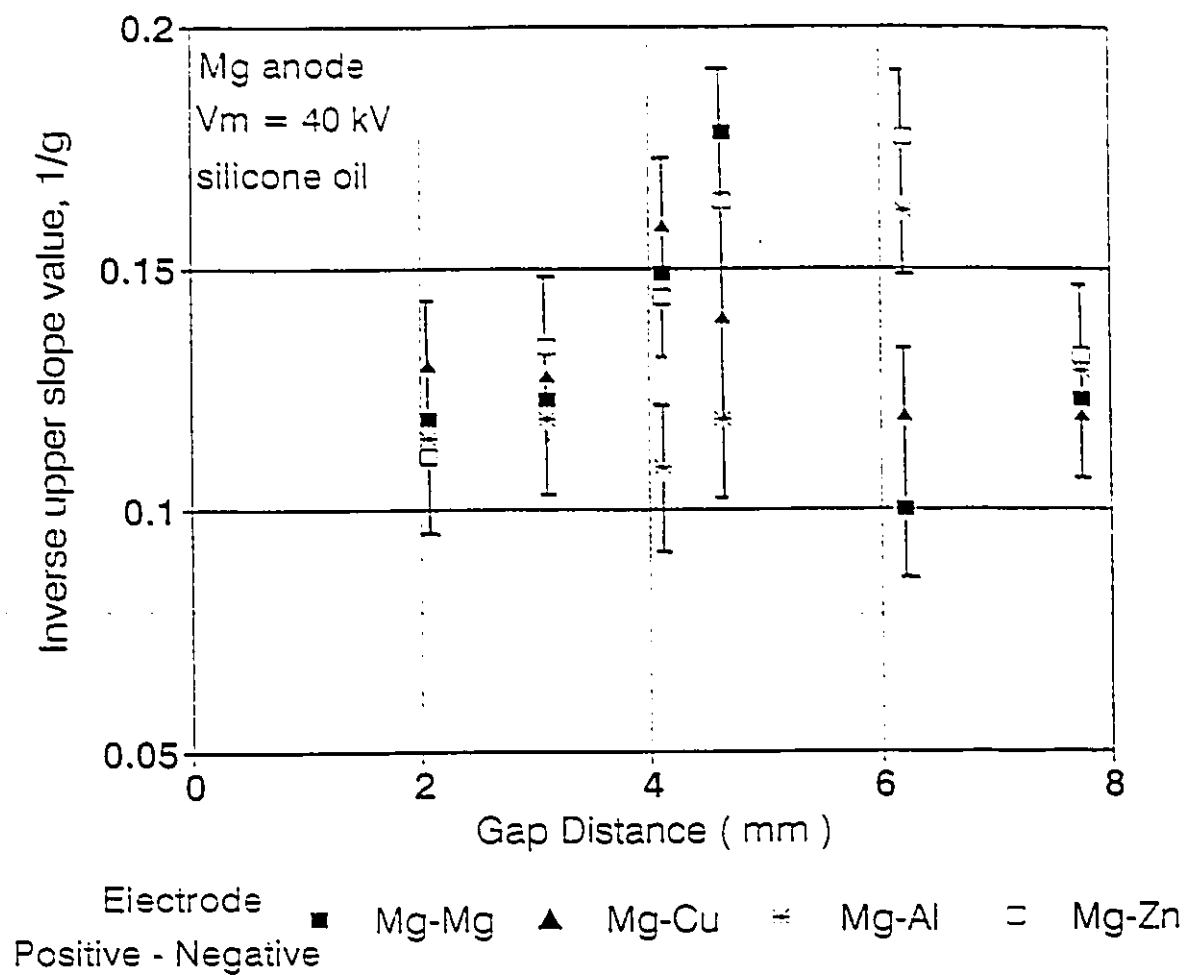


Figure 4.22 Inverse upper slope value of displacement current as a function of gap distance with Mg anode at 40 kV

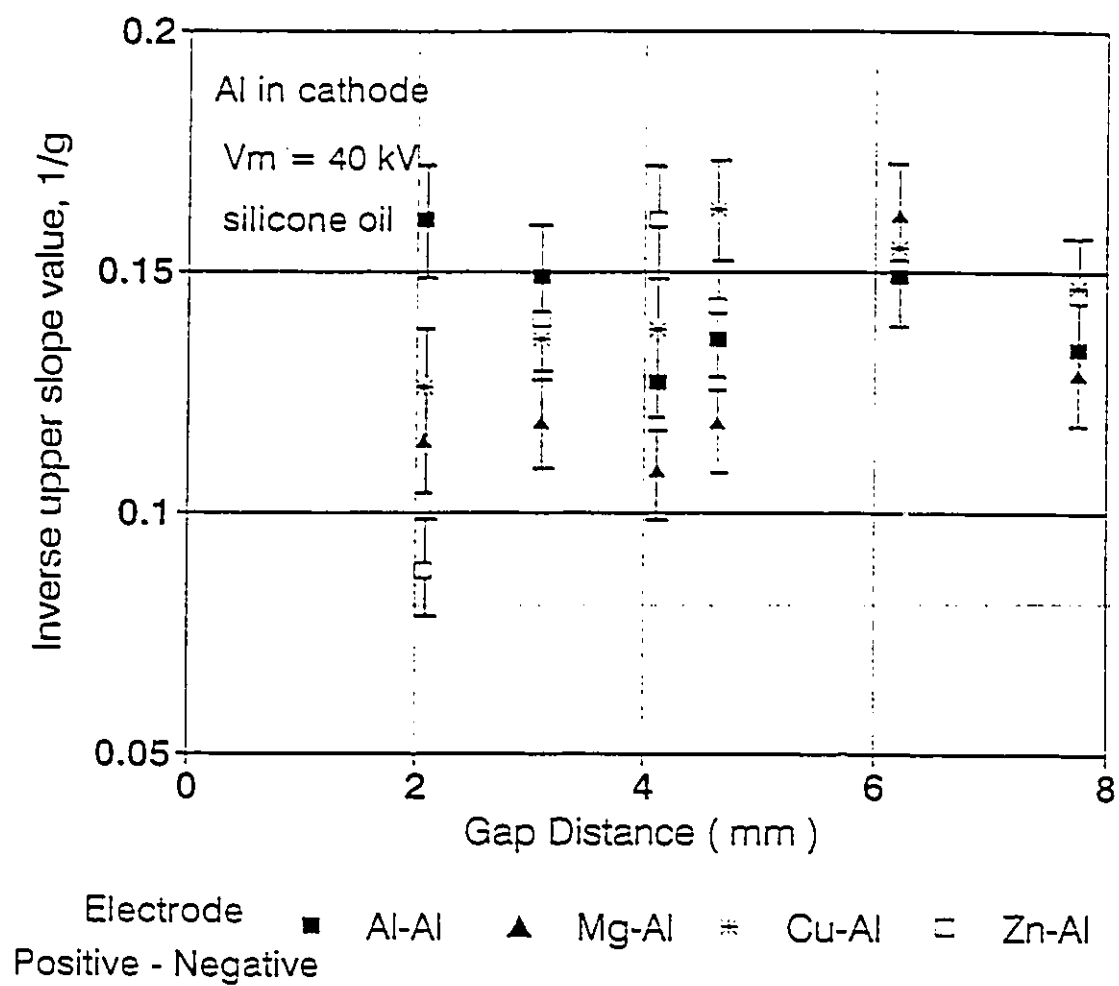


Figure 4.23 Inverse upper slope value of displacement current as a function of gap distance with Al cathode at 40 kV

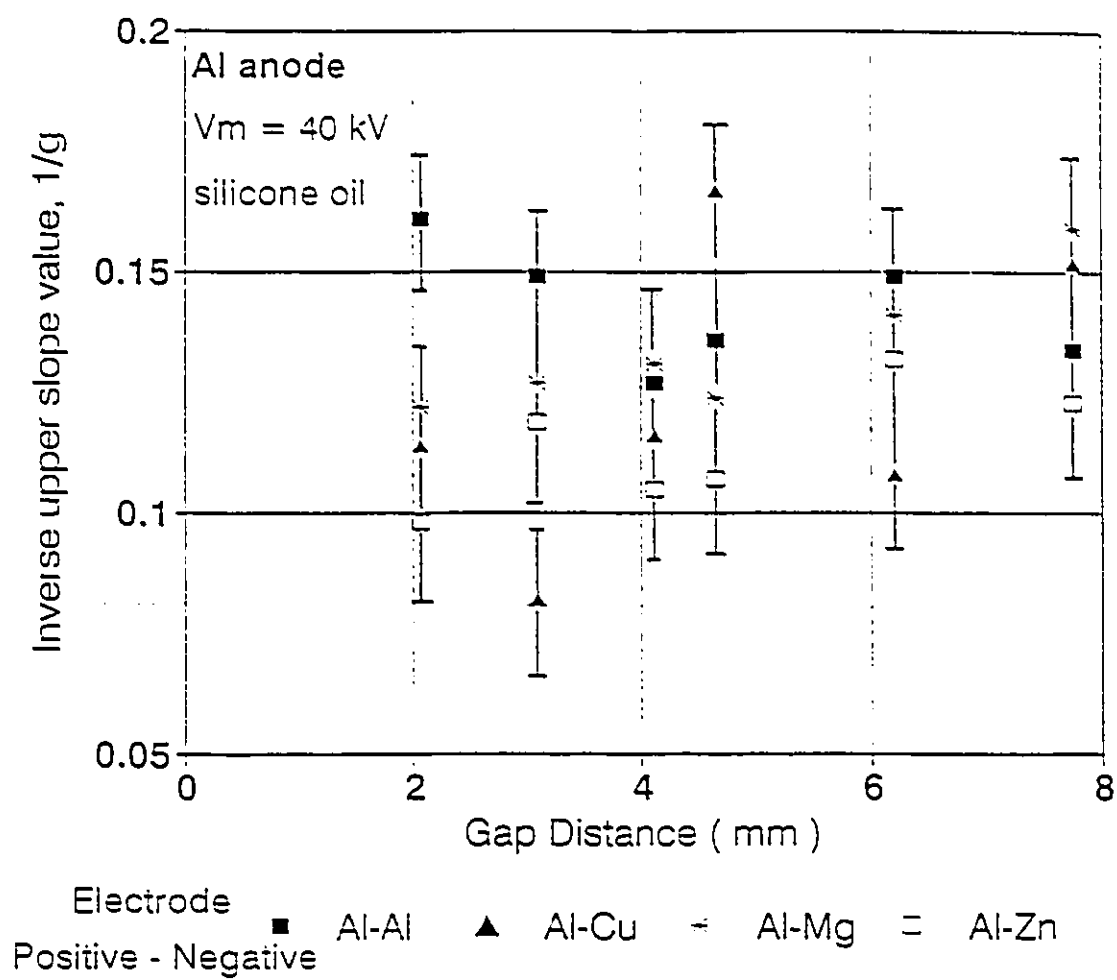


Figure 4.24 Inverse upper slope value of displacement current as a function of gap distance with Al anode at 40 kV

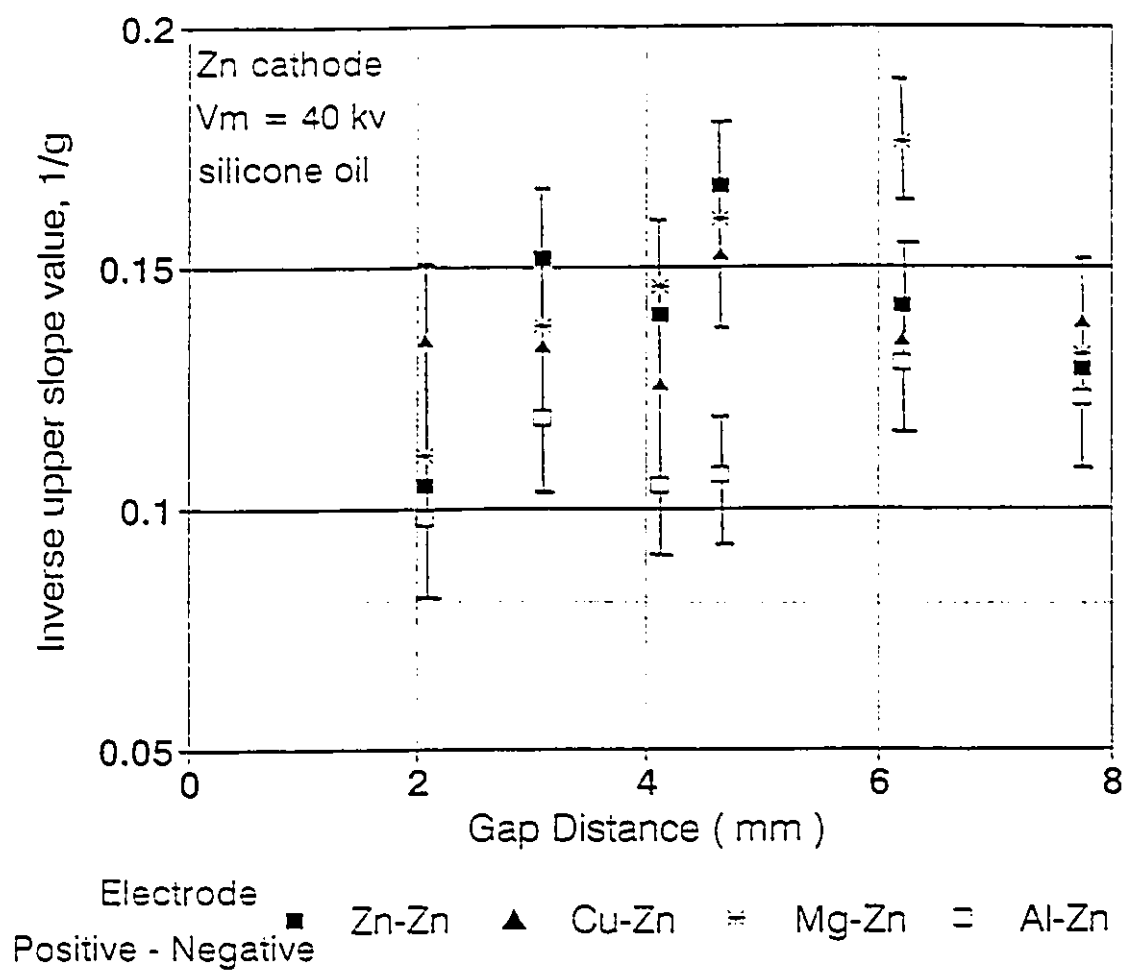


Figure 4.25 Inverse upper slope value of displacement current
 as a function of gap distance with Zn cathode at 40 kV

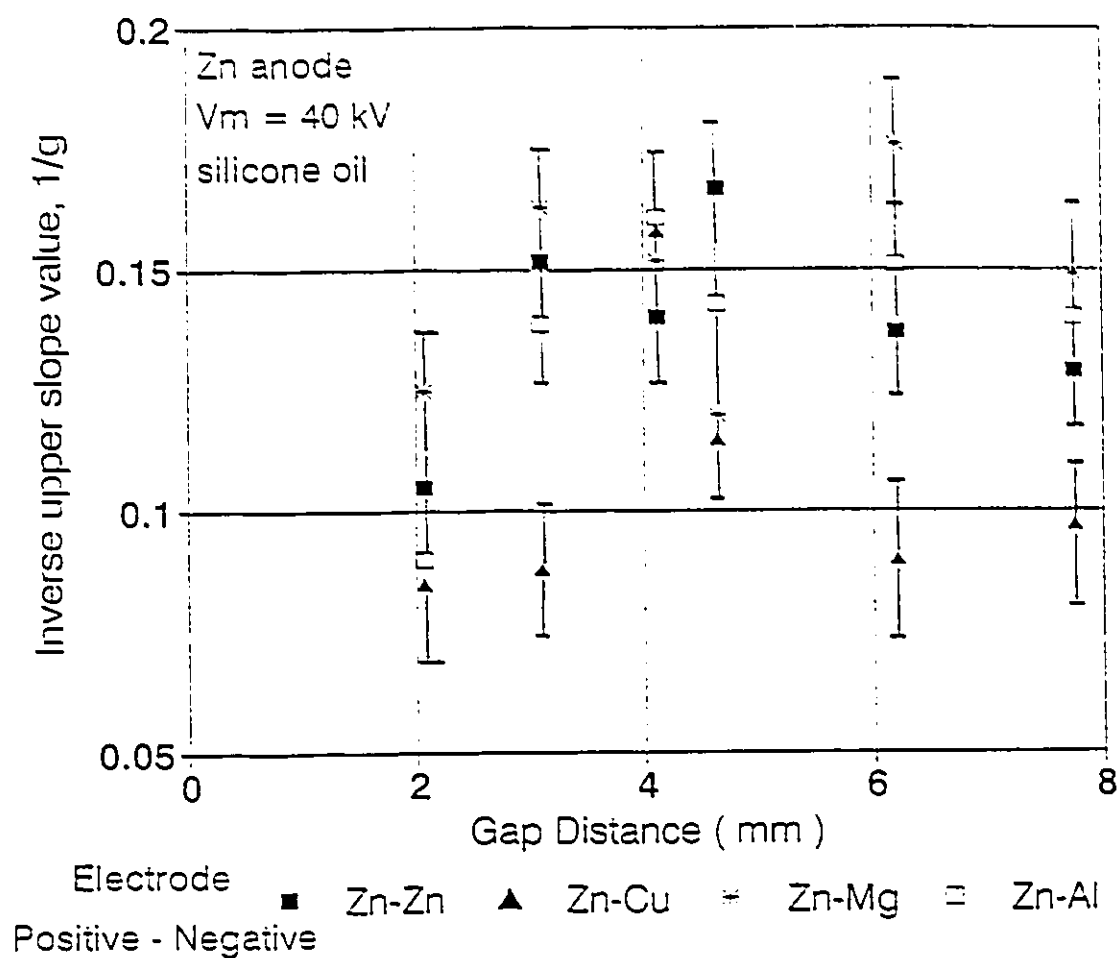


Figure 4.26 Inverse upper slope value of displacement current as a function of gap distance with Zn anode at 40 kV

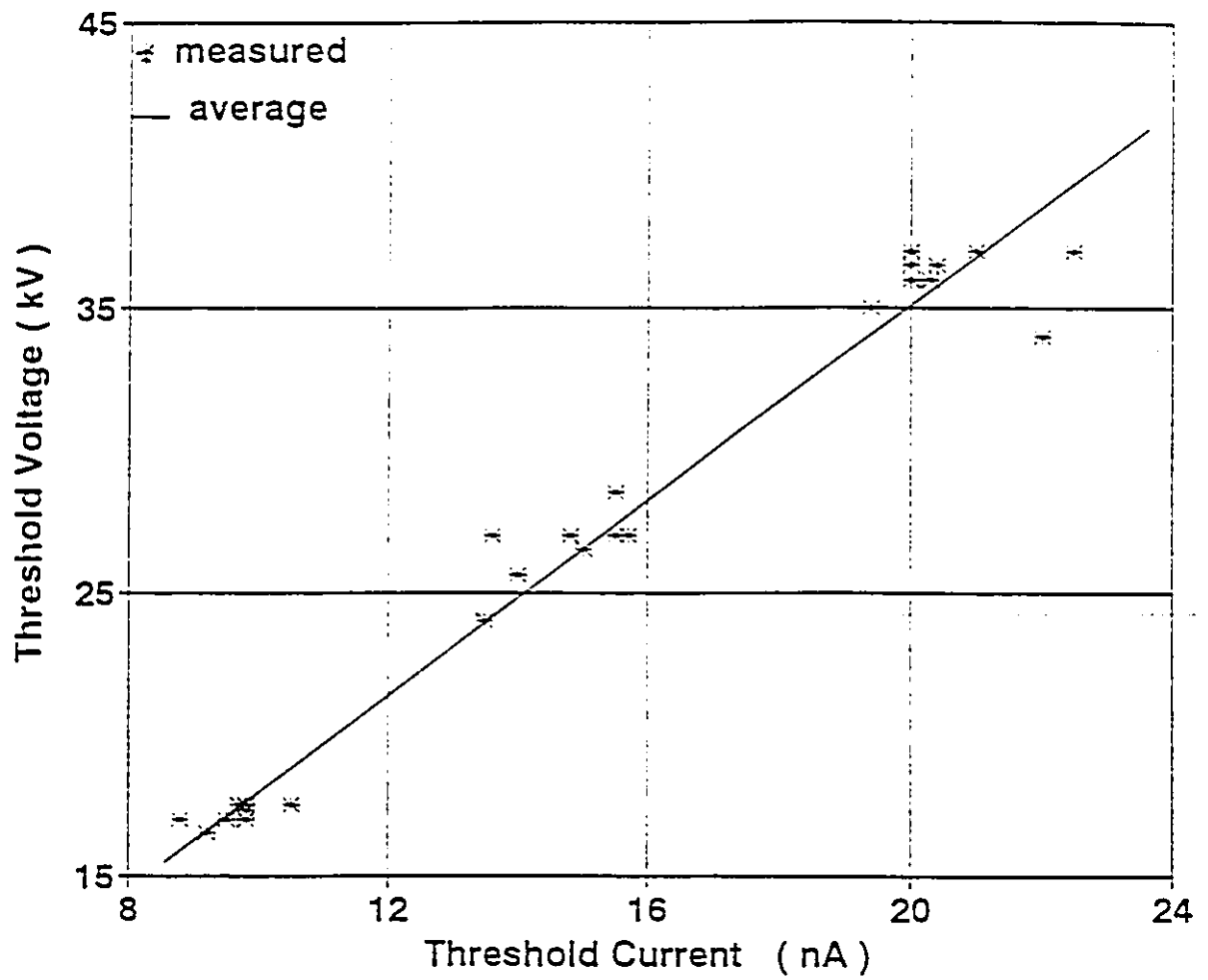


Figure 4.27 The threshold voltage as a function of the threshold current in silicone oil

4.2 VOLTESSO 35 LIQUID (TRANSFORMER OIL)

4.2.1 V-I CHARACTERISTICS WITH MAXIMUM APPLIED VOLTAGE

Voltesso 35 electrical insulating oil (transformer oil) is a mineral-oil type which is manufactured from a quality petroleum base stock blended with an approved oxidation inhibitor. The properties of the transformer oil have been described previously in Chapter III. Typical experimental results for transformer oil are given in Figure 4.28, showing the current response loops as a function of the maximum applied voltage [66]. The figure shows the difference between the response current with voltage increasing and decreasing. It also gives a clear picture of the response current behaviour when varying the maximum applied voltage value (which automatically involved a change in the ramp rate). Figures 4.29 and 4.30 show the applied voltage waveform and its response current as a function of time with different maximum applied voltage values.

For transformer oil, the current responses displayed similar characteristics to those for silicone oil at relatively low applied voltages. An example of this similarity is seen in Figure 4.31. The test results are of the mean current for silicone oil and transformer oil on a log-log scale for a maximum applied voltage of 44 kV. For silicone oil, 44 kV was just below its breakdown voltage value at about 49 kV, but for Voltesso 35 transformer oil, the breakdown voltage was over 65 kV. Thus for better comparison of the properties of these two oils, a common maximum applied voltage was chosen

which was determined by the liquid with the lower breakdown voltage. The transformer oil tested has almost the same current variation with applied voltage as silicone oil.

Moreover these current versus voltage characteristics of the transformer oil also obey the power law $I \propto V^s$ above a specific threshold coordinate. The two linear portions are sharply divided at higher electric fields as shown in Figure 4.31. Figures 4.32 and 4.33 show the log-log mean current characteristics with different maximum applied voltage with Cu electrodes and Al electrodes respectively. This figure illustrates that as the maximum applied voltage increases, both the upper and the lower slope values change as well. The upper slope is observed to vary more obviously with the maximum applied voltage than the lower slope does. At a 3.1 mm gap spacing, when the maximum voltage is increased up to 40 kV, s_u tends to saturate and stays almost constant as the voltage increases. The lower portions of the slopes (lower slope value), s_l change only slightly with an increase in applied voltage, especially in the highest voltage region. Moreover, the Cu and Al electrodes give very similar behaviour, but with aluminum electrodes the values of both portions are somewhat higher as seen in Figures 4.32 and 4.33. It was further found that with increasing maximum applied voltages, the lower slope value increased while that of the upper one decreased. A distinct and quite sharply defined division between these two lines (the threshold point) thus became less easily observed, shown in Figures 4.32 and 4.33. In other words, the exponents in the two power laws, $I \propto V^s$, are thus functions of the maximum voltage excursion. Ultimately, they exhibit a single power law when the maximum applied voltage is extremely high.

Figure 4.34 shows the upper slope and lower slope of the mean current as a function of maximum applied voltage. It shows that both slope values tend to approach the value $3/2$ as the maximum applied voltage value increases. A slope value of $3/2$ has never been measured to date. This is the result of the fact that electrical breakdown of the insulating material occurred before the maximum applied voltage was able to reach the value of voltage giving the $3/2$ slope value.

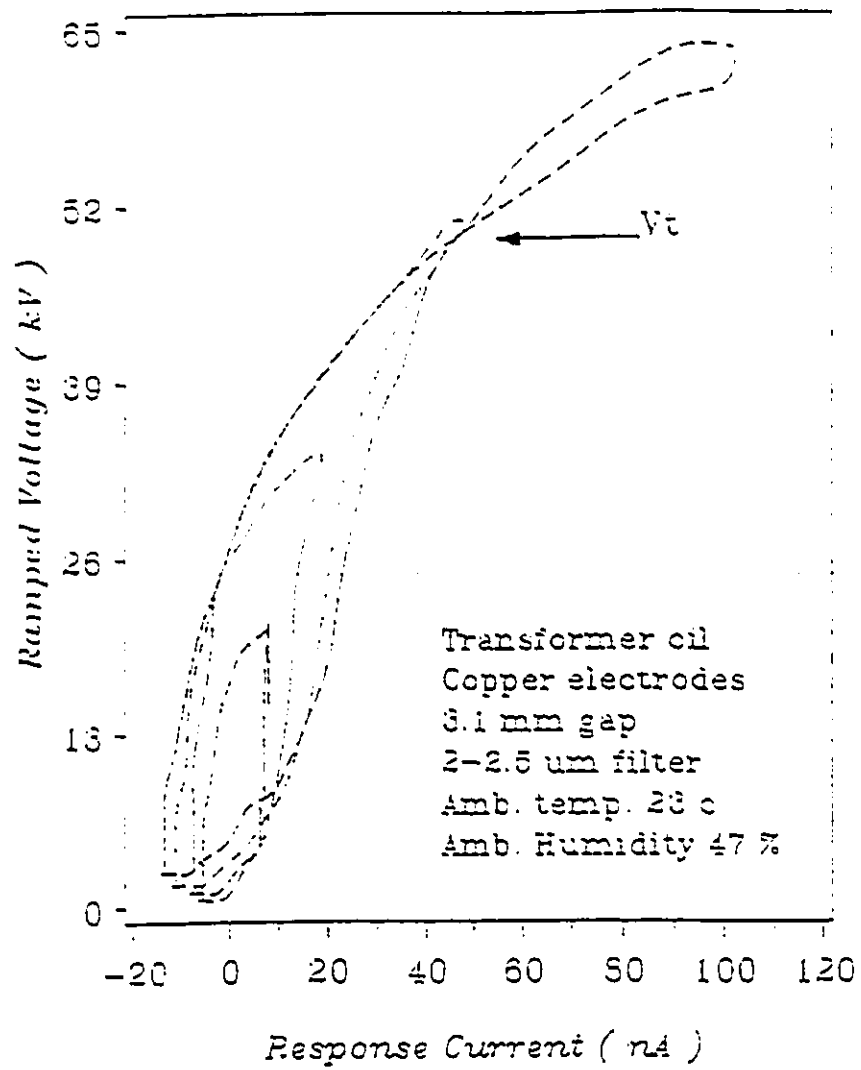


Figure 4.28 Current response loops with different maximum applied ramped voltage in insulating oil

(V_t the current turnover point, above this point in a fixed voltage value, the current with voltage wave increasing is smaller than that of the voltage decrease)

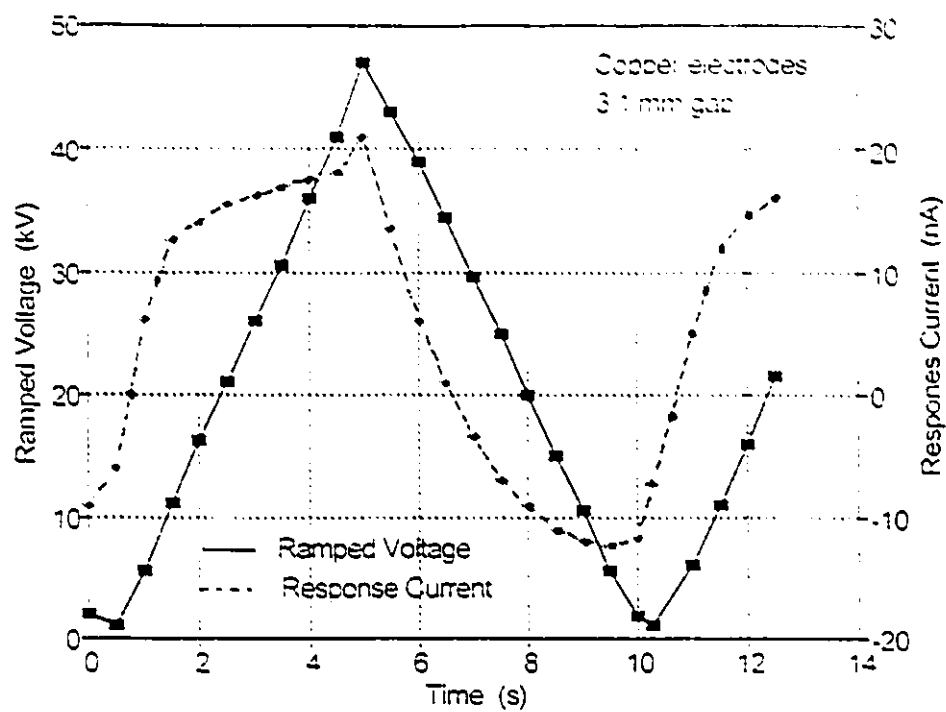


Figure 4.29 The ramp voltage waveform and current response in transformer oil with a relatively low applied voltage

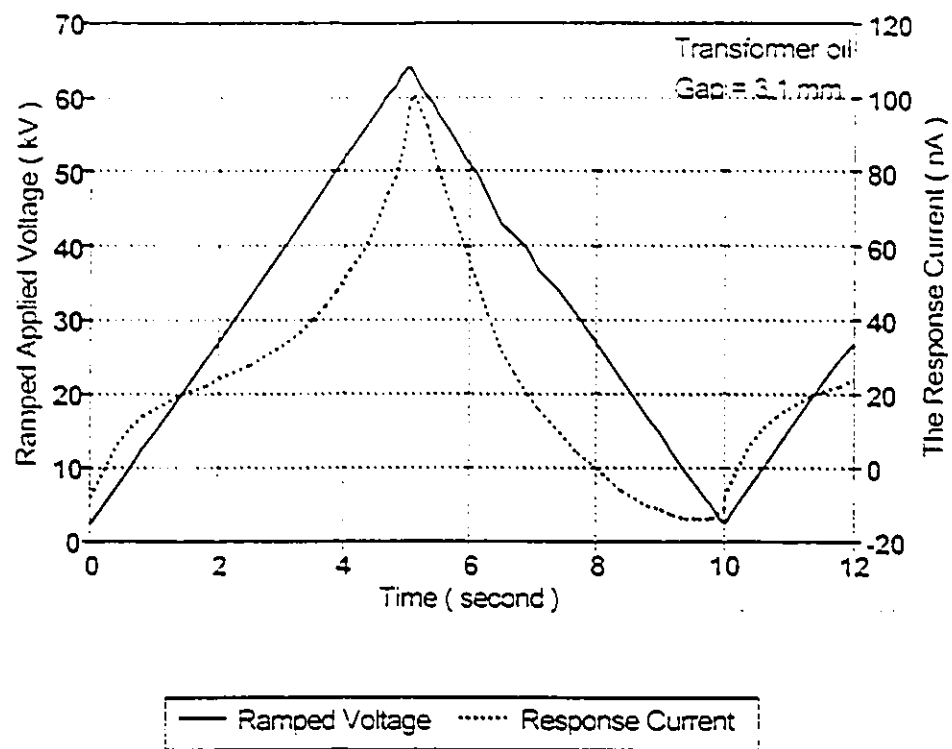


Figure 4.30 The ramp voltage waveform and current response in transformer oil with a relatively high applied voltage

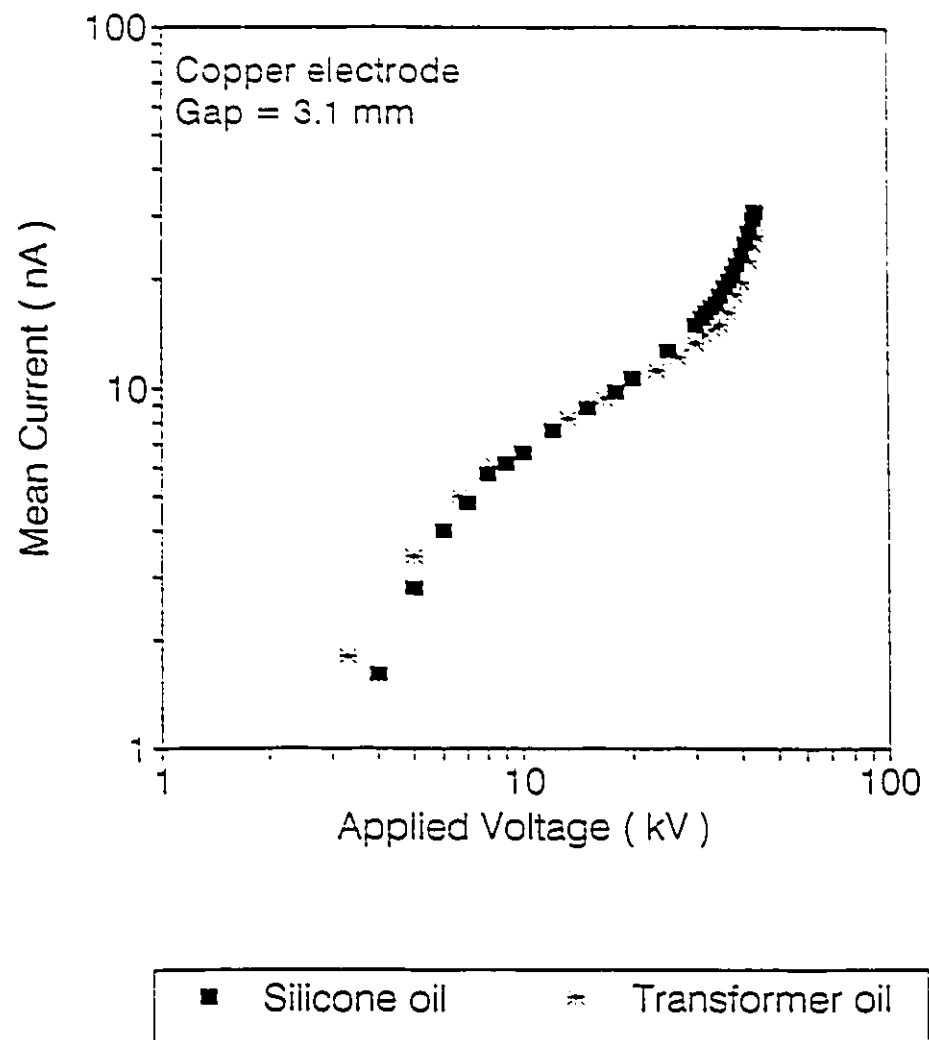


Figure 4.31 Log V-log I of mean current with applied voltage in transformer oil and silicone oils

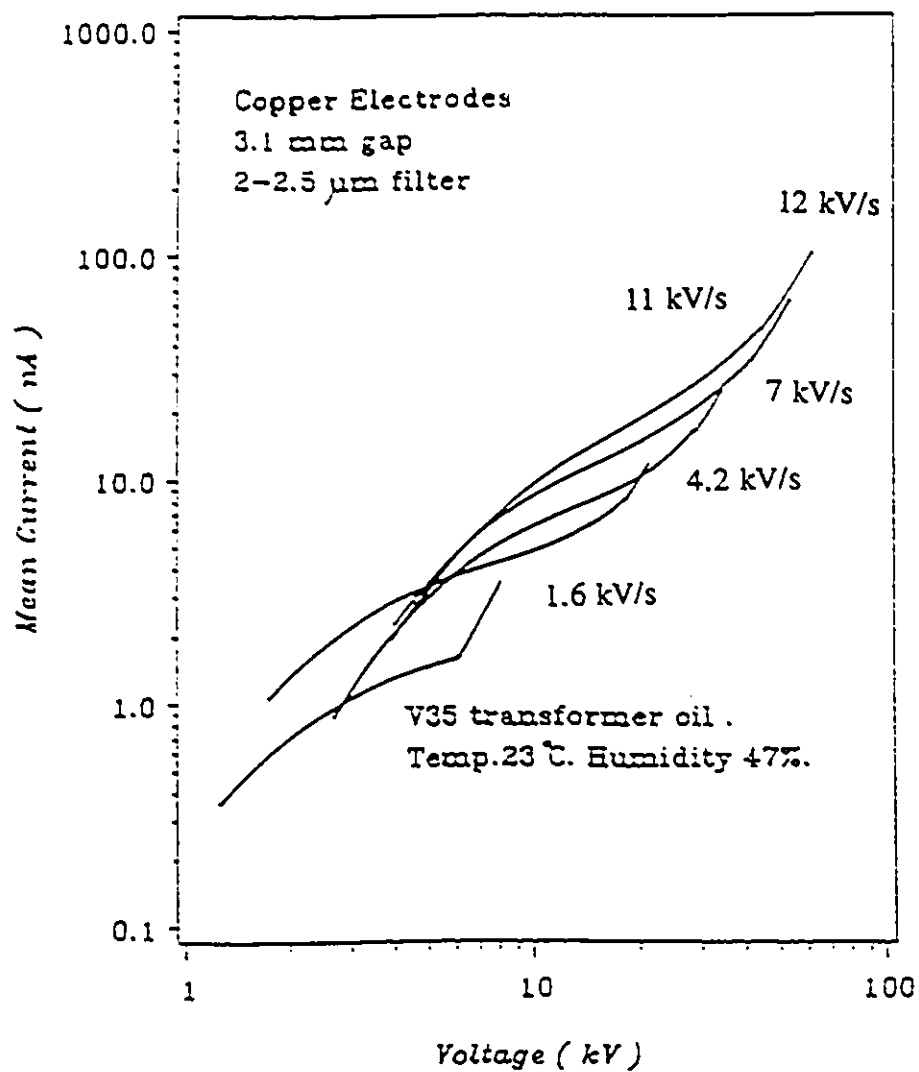


Figure 4.32 Log V-log I of mean current response with different voltage ramped rate with Cu electrodes

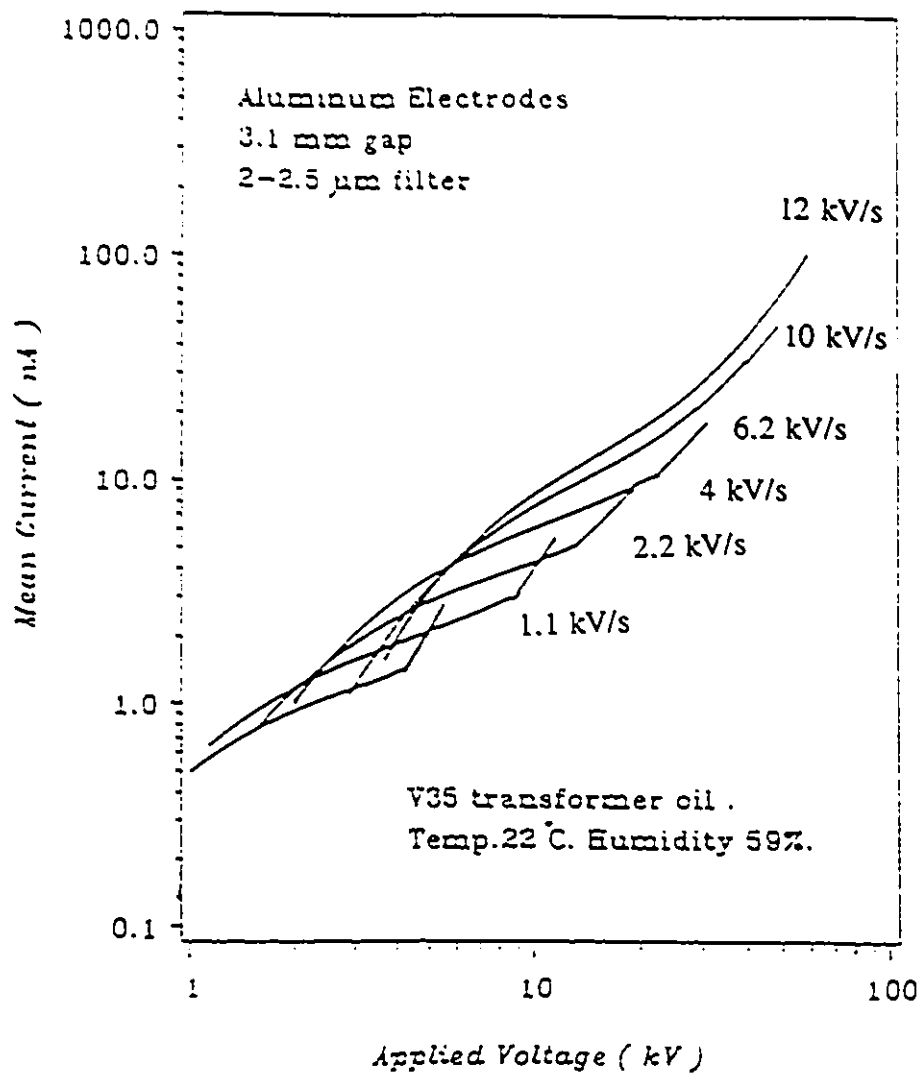


Figure 4.33 Log V-log I of mean current response with different voltage ramped rate with Al electrodes

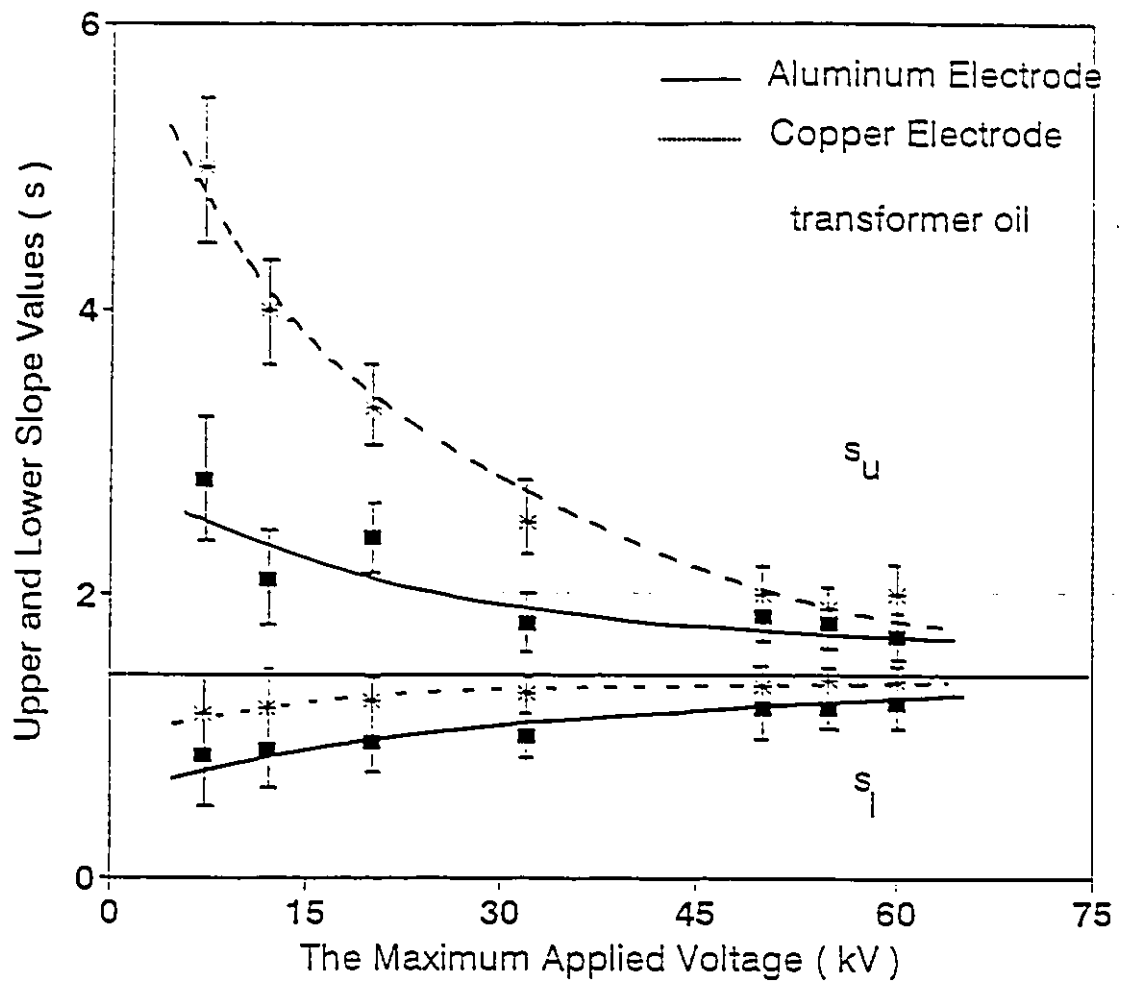


Figure 4.34 Upper and lower slope value as a function of maximum applied voltage in transformer oil

4.2.2 CURRENT TURNOVER PHENOMENON

At a sufficiently high voltage, above the same reproducible level, the so called turnover potential, V_t in Figure 4.28, the current with an increasing voltage applied is smaller than that with a decreasing applied voltage. This behaviour is exactly the reverse of that which occurs below the above mentioned turnover coordinate voltage V_t shown in Figure 4.28. The characteristic shows a current double loop instead of the single one which is usually observed in silicone oil. This is also the case with transformer oil under a relatively low maximum applied voltage. It paradoxically appears to indicate that the displacement current has reversed. Beyond the current turnover, the same power law is still satisfied, beginning from the same distinct threshold coordinate. Usually after the current turnover occurs, the response current will increase faster with increasing applied voltage than before. This is shown in Figure 4.32 where copper electrodes were used. The mean current characteristic with ramped applied voltage was taken from Figure 4.28, the maximum applied voltage having been increased from approximately 6 kV (bottom line) to 65 kV (top line) respectively.

It must be emphasized that the current turnover phenomenon is very sensitive to conditioning, it does not appear every time in the experimental tests in transformer oil. It is clear that this phenomenon is dependent upon the oil sample condition, the maximum electrical field, ramp rate, electrode surface condition and other experimental conditions, etc. Moreover, when turnover of the current response takes place and the log V-log I

characteristic is plotted, its upper linear portion is undisturbed. Actually, the current turnover event does not affect the two linear slopes. It is clear however that in most cases when current turnover occurs, the voltage is close to the breakdown value. Further tests were made with aluminum as well as copper electrodes, shown in Figure 4.33. The threshold point characteristics were similar. Thus the relationship between V_{th} and I_{th} with different applied voltages was not affected by the electrode material.

4.2.3 V-I THRESHOLD POINT

Both Figures 4.32 and 4.33 show that with different maximum applied voltages, the values of threshold voltage and current were slightly changed by using copper and aluminum electrodes respectively. Figure 4.35 is a plot of the voltage threshold point V_{th} as a function of the current threshold point I_{th} for different applied maximum voltages with aluminum and copper electrodes in transformer oil. The voltage and current at the threshold point were increased by raising the maximum applied voltage. The relationship between I_{th} and V_{th} in log-log scale is a straight line up to very high stress levels before current turnover occurs. The relationships between V_{th} and I_{th} for different maximum applied voltages V_m in the absence of the current turnover phenomenon can be written as:

$$V_{th} = k_{th} I_{th}^c \quad (4.5)$$

where $k_{th} = 3.3$ if V_{th} and I_{th} are measured in kV and nA respectively, and $c =$

0.86±0.02.

Figure 4.36 shows the voltage at the threshold point V_{th} as a function of maximum applied voltage V_m . The voltage V_{th} is linear with respect to V_m until the current turnover. Moreover, this could be written as,

$$V_{th} = k_m V_m \quad (4.6)$$

where $k_m = 0.7$ in this case. The threshold voltage is again 70 percent of the maximum applied voltage in this case. From Equations 4.5 and 4.6, the current value at the threshold point as a function of the maximum applied voltage can be expressed by the following equation:

$$V_m = k_{mt} I_{th}^c \quad (4.7)$$

where $k_{mt} = k_m/k_{th} = 4.7$, if V_m and I_{th} are measured in kV and nA respectively, and $c = 0.86 \pm 0.02$. All of these equations are satisfied for both the aluminum and copper electrodes test cases. Evidently, the type of electrode material does not affect the relationship between V_{th} , I_{th} , and V_m when there is no current turnover.

Experiments to determine the influence of gap distance upon the conduction current and its threshold coordinate in dielectric liquids were also carried out with different maximum applied voltages. Figures 4.37 and 4.38 show the threshold current

and voltage as functions of ramp rate in transformer oil with various gap distances using copper electrodes. The characteristics of I_{th} and V_{th} are slightly different from those observed for silicone oil. As with the case of silicone oil, I_{th} is seen to decrease and V_{th} to increase a little with the gap distance at any constant ramp rate. Both I_{th} and V_{th} are fully dependent upon the ramp rate, and they increase with dV/dt . I_{th} and V_{th} vary approximately linearly with the ramp rate. Similar experimental results are also found by using aluminum electrodes [69].

Moreover, the above mentioned characteristics of the threshold coordinates are also changed after the current turnover occurs. After current turnover occurs V_{th} will become less dependent upon the applied voltage. Figure 4.36 shows that the slope value changes before and after the turnover occurs for both Al and Cu pairs electrodes. It is also observed from Figure 4.39 that after the current (loop) turns over, V_{th} value is much smaller compared to the previous one without turnover phenomenon at the same ramp rate, shown in Figure 4.38. As ramped rate at 9 kV/s, gap space at 3.1 mm for example, the values of V_{th} are 38 kV and 20 kV with and without current turnover respectively. Moreover the curves of V_{th} versus dV/dt at different gap spacings are not even closely parallel as they are before current turnover occurs. The location of the turnover coordinate and the slope of V_{th} vs. dV/dt above are, in fact, randomly variable as seen in Figure 4.39. This phenomenon is also found for aluminum electrodes shown in Figure 4.40.

For any specific value of ramp rate the value of I_{th} was found to increase with decreasing gap spacing. For the purpose of estimating the dielectric liquid resistance, the electric field is considered uniform. By contrast V_{th} was observed for any fixed dV/dt value to increase with increasing electrodes gap, d . This could be interpreted to signify on the one hand that an invariant value of threshold electric field strength, $E_{th} \propto V_{th}/d$ exists. The corresponding result for I_{th} on the other hand can be understood in terms of the fluid possessing an electrical resistance $R = d/(\sigma.A)$ where σ = conductivity and A = cross section area.

Each ratio of V_{th}/I_{th} named as R_{th} is computed and a maximum applied electrical field at the electrode tip is also defined as E . Thus replots of R_{th} as a function of E are shown in Figure 4.41. The electrical resistance defined by this ratio is seen to decrease with an increasing electric field. The decreasing rate for this resistance at the threshold point (V_{th}) is written as follows:

$$R_{th} = R_o - kE \quad (4.8)$$

where E is in MV/m, R_o is $340 \pm 20 \text{ G}\Omega$, R_{th} is in $\text{G}\Omega$ and k is a constant value of $12.0 \pm 2.0 \text{ G}\Omega.\text{m}/\text{MV}$. According to Equation 4.8, the breakdown can be defined by the condition that the resistance R_{th} decreased to zero. Hence from Equation 4.8, the breakdown electrical field would be approximately 28 MV/m. By using the standard equation for the electrode geometry used, the relationship between the applied voltage and its maximum applied field is written in Equation 4.9 [70].

$$V = \frac{\sin \theta_1 \ln \left[\tan \frac{\theta_2}{2} / \tan \frac{\theta_1}{2} \right]}{\cos \theta_1 - |\cos \theta_2|} d E_{\max} \quad (4.9)$$

$$\theta_1 = \tan^{-1} \sqrt{\frac{2r}{d}}, \quad \theta_2 = \pi - \theta_1$$

where r is the radius for curvature of the electrode hemisphere, d is a electrode gap spacing. For a $r = 6.25$ mm , $d = 3.1$ mm and $E_{\max} = 28$ MV/m, the corresponding breakdown voltage has been computed to provide a value of $80 \text{ kV} \pm 5 \text{ kV}$. As a result, it appears therefore that at the breakdown condition the value of R_b in Equation 4.9 approaches zero. From direct experimental measurement, the average breakdown voltage of the transformer oil in the same condition usually occurs at approximately 70 kV. Thus it is slightly lower than the calculated result using Equations 4.8 and 4.9. The difference could be due to the nonlinear geometry and the voltage will breakdown before R_b in Equation 4.9 approaches zero.

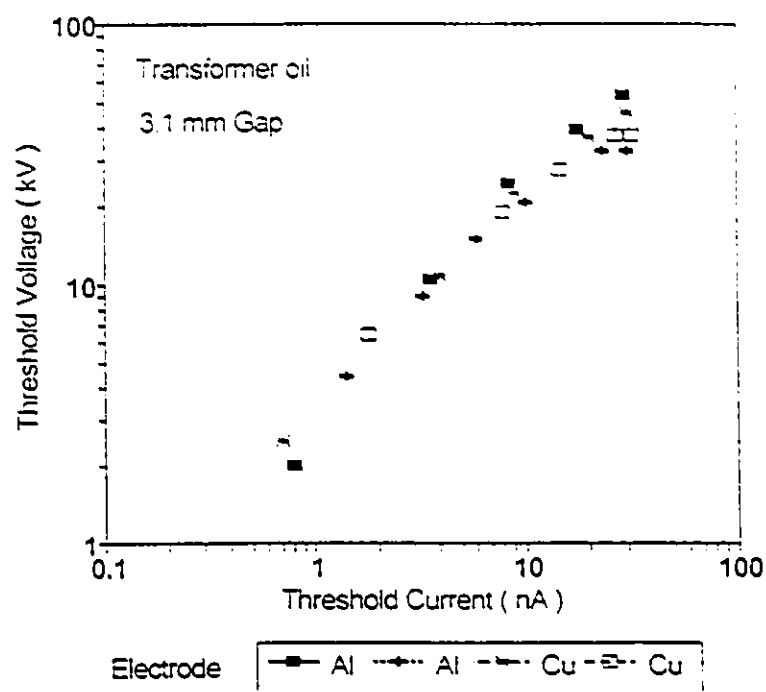


Figure 4.35 The threshold voltage as a function of threshold current in transformer oil

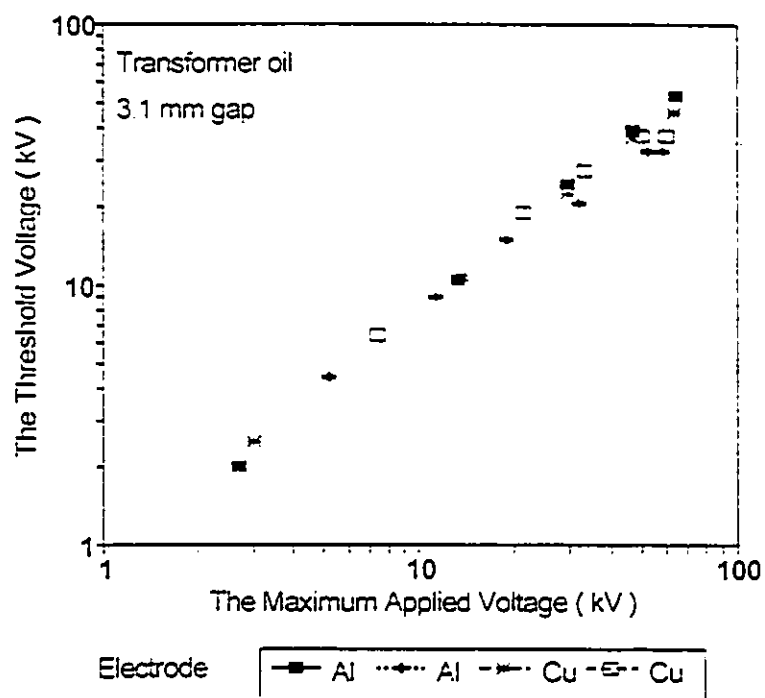


Figure 4.36 The threshold voltage as a function of maximum applied voltage in transformer oil

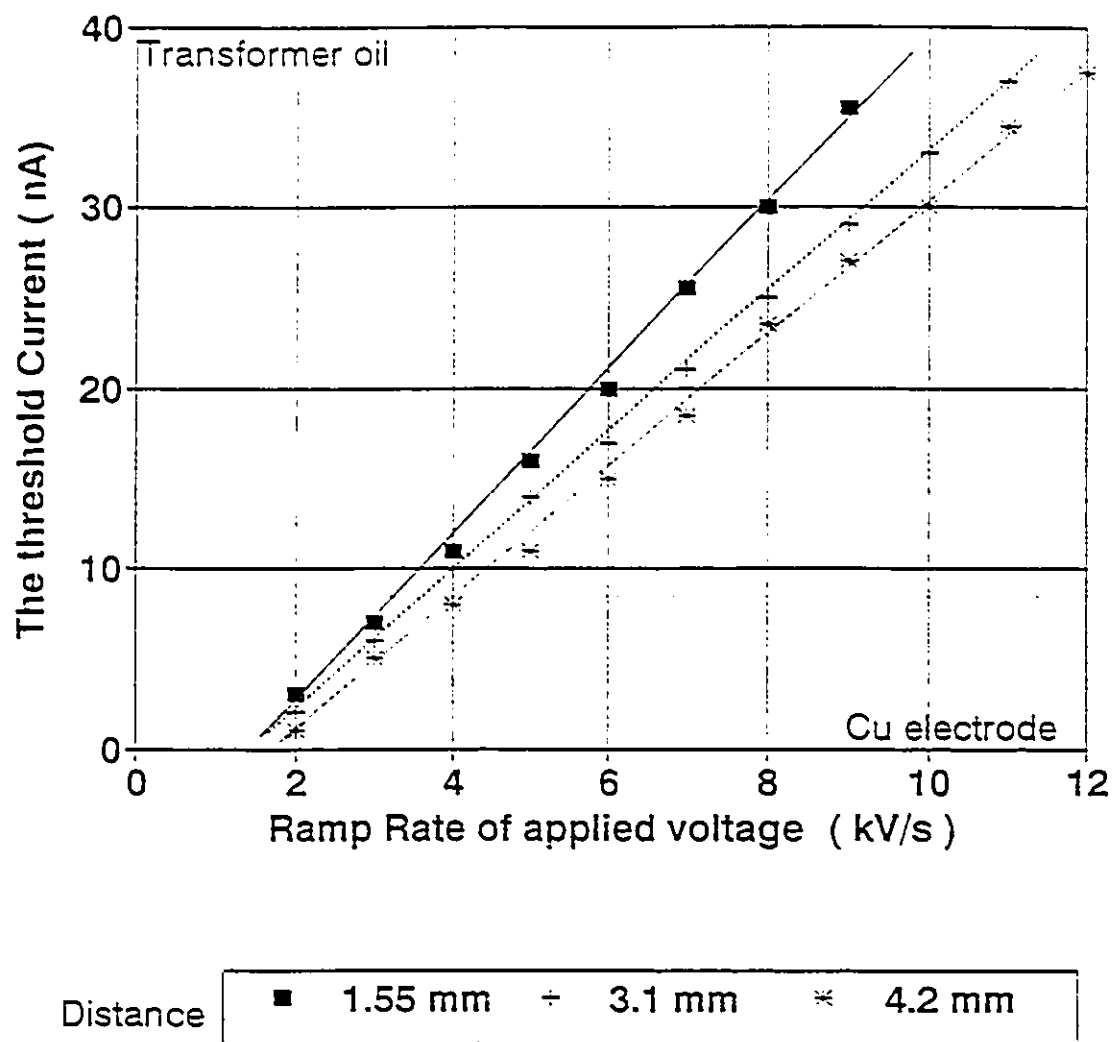


Figure 4.37 The threshold current as a function of ramp rate in transformer oil

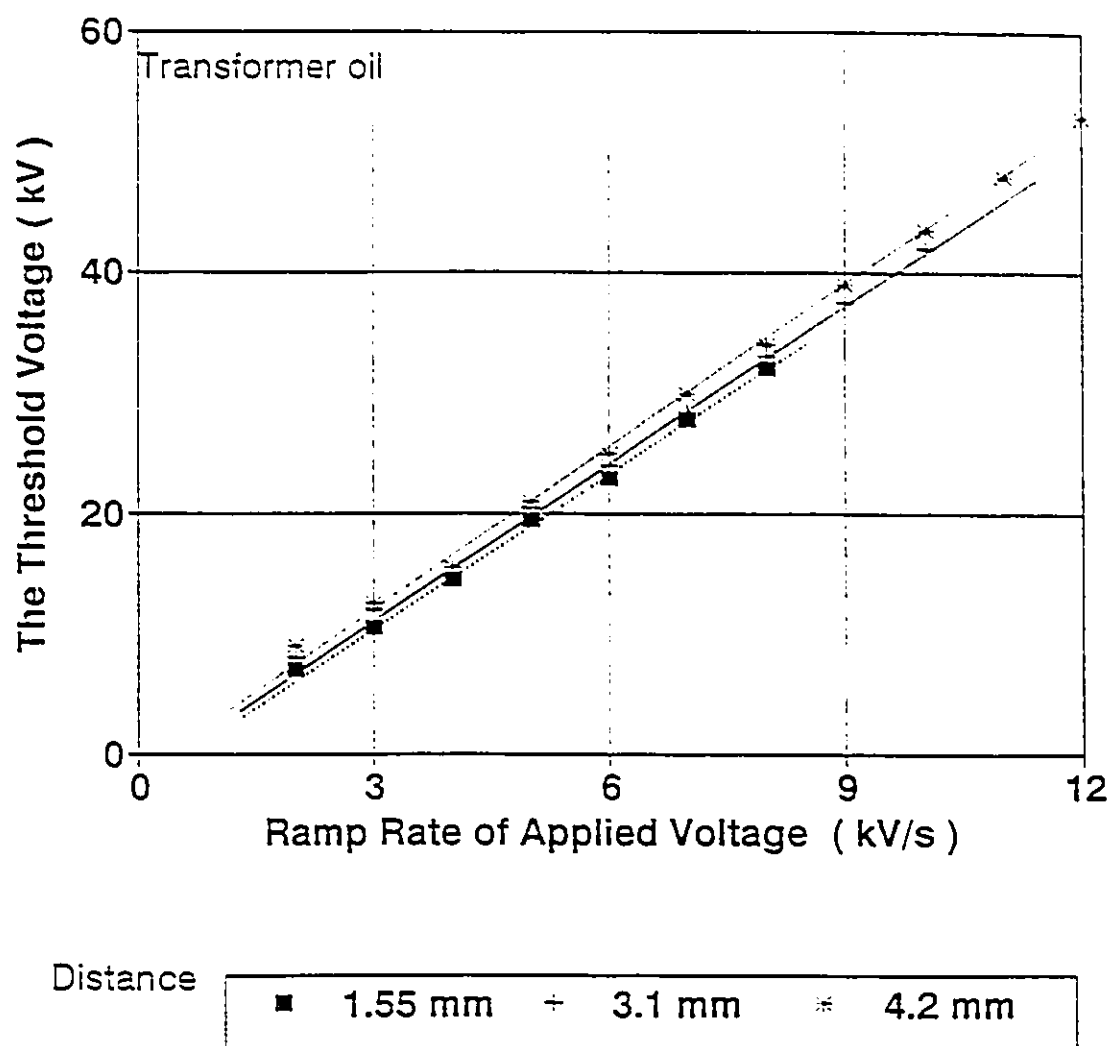


Figure 4.38 The threshold voltage as a function of ramp rate in transformer oil

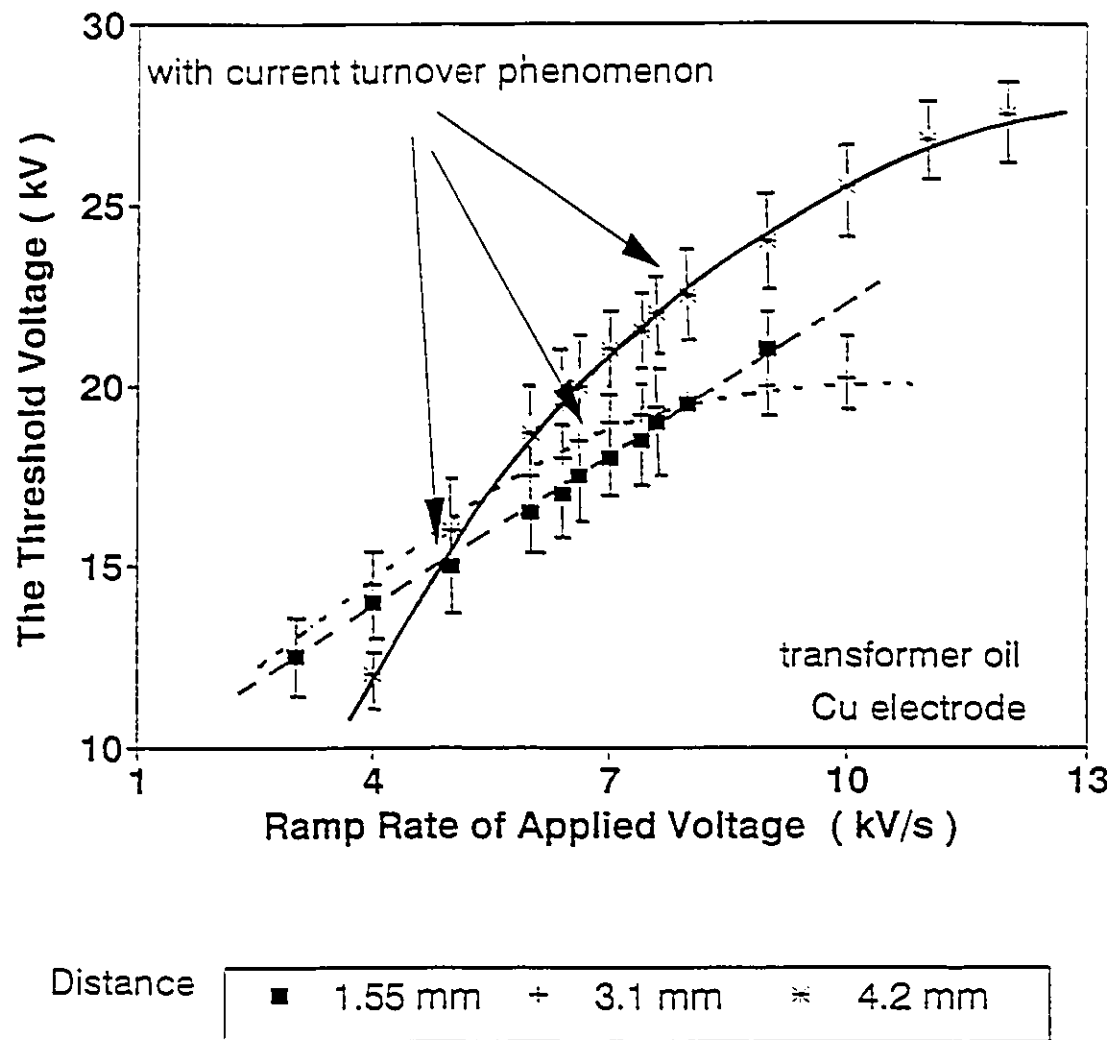


Figure 4.39 The threshold voltage as a function of ramp rate in transformer oil with current turnover phenomenon

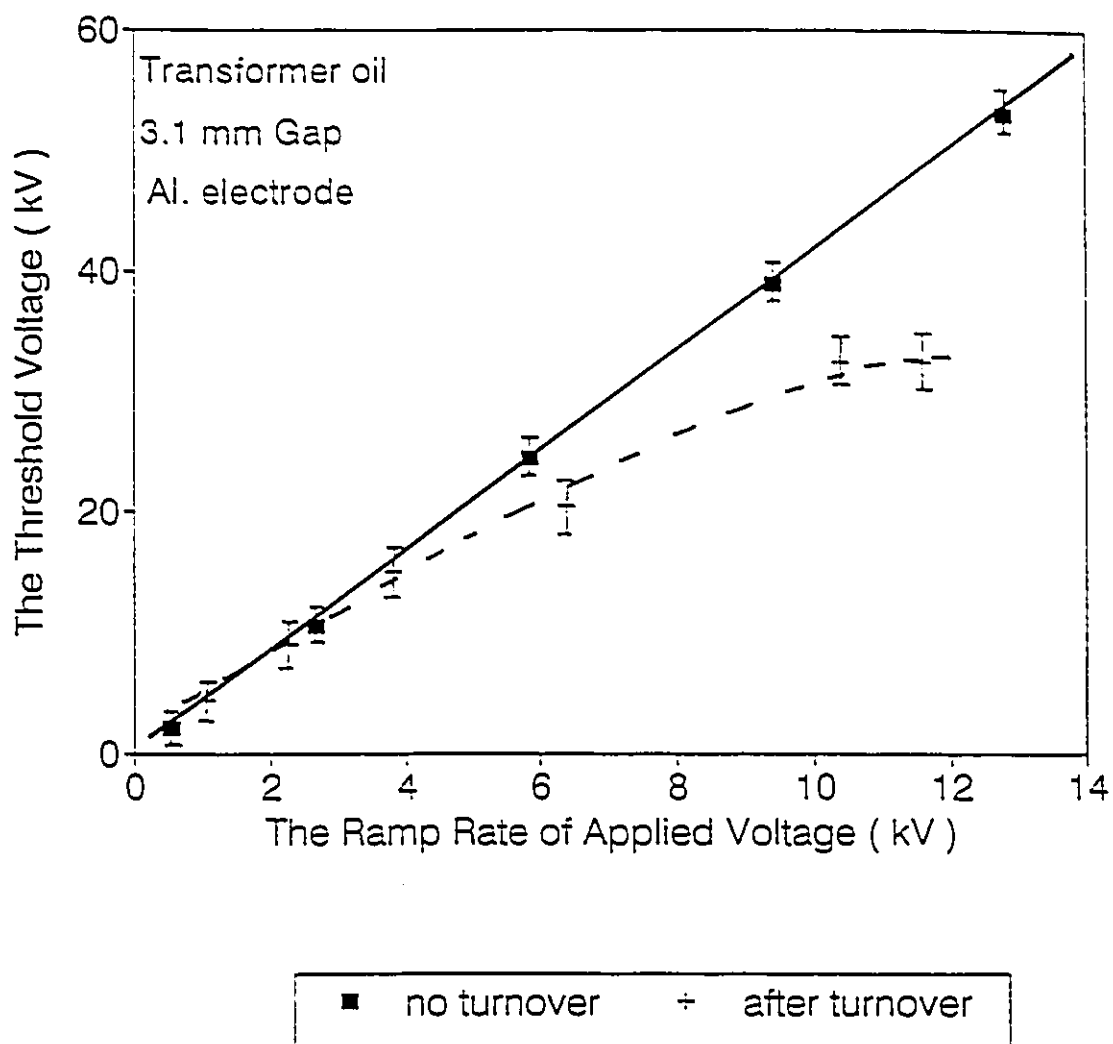


Figure 4.40 The threshold voltage as a function of ramp rate in transformer oil with/without current turnover phenomenon with Al electrode

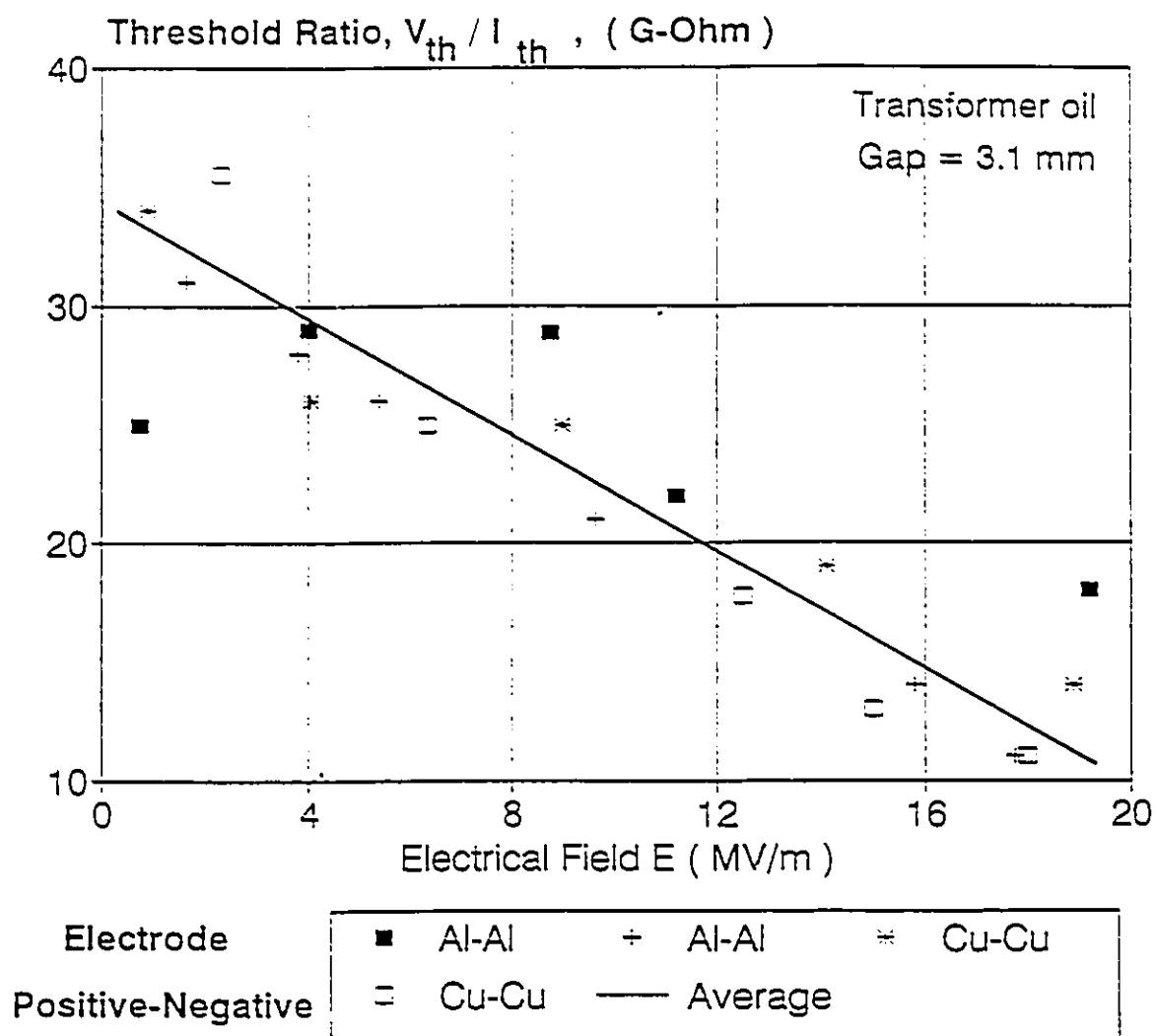


Figure 4.41 The threshold ratio (V_{th}/I_{th}) as a function of electrical field

4.2.4 V-I CHARACTERISTICS AS A FUNCTION OF GAP SEPARATION

The analysis of the upper and lower slope values for the mean current will be studied first in this section. The measurement has been made over a range of gap separations from 1.55 to 6.05 mm. The effect of the electrode materials on the transformer oil as tested was found to be negligible from the previous experiments. The test made here uses copper electrodes. The upper slope values of the mean current for maximum applied voltages of 20, 30, 40 and 50 kV respectively are shown in Figure 4.42. As the gap separation increases, the values of s_u for all of the voltage ranges except 50 kV vary very little and increase slightly. The slope value of the maximum applied voltage at 50 kV yields a different pattern from the others. The slope value increased sharply with the increasing gap separation. As the maximum applied voltage varies, no significant changes in the slope value have been found for all but the 50 kV range. The slope value at 30 kV is greater than that for the 20 kV test. Moreover, the slope value at 40 kV is even greater still than that for the 30 kV test for the entire gap distance range. For the maximum applied voltage of 50 kV, the slope value is the smallest for the smallest electrode gap separation, and becomes the greatest for the largest electrode gap separation, reversing the trend for lower maximum applied voltage.

Figure 4.43 gives an example of the lower slope value of the mean current as a function of the gap distance for different maximum applied voltages. Again, when the gap separation increases, generally, the lower slope value decreases only a small amount.

The lower slope values from all of the tests are very close to 1.5. Unlike the upper slope value shown in Figure 4.42, there is no significant difference between these slope values for the 20, 30, 40 and 50 kV tests. The slope values for these four voltage ranges vary between 1 and 1.5. Both Figures 4.42 and 4.43 show that the upper and lower slope values of the mean current in transformer oil are very similar for the maximum applied voltages of 20, 30 and 40 kV. The upper slope value however is very different for a maximum applied voltage of 50 kV. The slope values change significantly when the electrode gap separation is increased. For transformer oil, the slope value from the $\log V - \log I$ graph shows a dependence on electrode gap spacing that is more pronounced at higher maximum applied voltage levels.

Figures 4.44 and 4.45 show the upper and lower slope values of the mean current at maximum applied voltages of 20 kV and 50 kV respectively. The results of these two extreme cases are plotted together on the same graph in order to further reinforce the different slope behaviours. It is clear that at relatively low applied voltage levels, both the upper and the lower slope values are almost steady and do not change significantly when the electrode gap separation is varied.

The analysis of displacement current for transformer oil is different from that of silicone oil. After the current turnover phenomenon occurred, the sign of the displacement current is reversed as seen in Figure 4.28. At the turnover point, obviously, the displacement current is zero. This means that at this potential the

magnitude of the displacement current with the voltage increasing is equal to that of the displacement current with the voltage decreasing. As a result, the displacement current is changing from a positive value to zero, and eventually to a negative value. Thus, this whole process can not be plotted using a log-log scale.

The $\log V - \log I$ characteristic, however, could be divided into two parts. Below the turnover point, the applied voltage versus the displacement current in the higher field region can be plotted using a log-log scale. This is shown in Figure 3.12 using the test result for silicone oil. Above the turnover point, the $\log V - \log I$ plot is shown in Figure 4.46. It is noted that under these conditions the displacement current has a negative value. Besides the revised sign for displacement current, these two figures appear to be very different. Figure 4.46 shows a curve instead of straight line segments as the relationship between the applied voltage and the displacement current. The displacement current first increases with the applied voltage up to a certain point, then decreases as the applied voltage increases further. The peak current value coordinate varied with the maximum applied voltage shown in Figure 4.46 for 50 kV and 55 kV respectively. Even though the total displacement current changes as the maximum applied voltage varies, the curve of the displacement current versus the applied voltage remains the same shape. Further discussion of this will be addressed in section 5.

For a better comparison with previous analytical work, a series of measurements of the slope value for the displacement current has been made before the turnover point.

Since the turnover phenomenon happened only a few times when the electric field was extremely high, the analytical data for those figures are absent. Figures 4.47 and 4.48 are the slope values of the displacement current as a function of maximum applied voltages at 3.1 mm and 6.2 mm gap separations respectively. There are no significant differences between these two graphs. The relationship between the slope value and maximum applied voltage is basically unchanged for gap distances of either 3.1 mm or 6.2 mm.

Figure 4.49 shows the lower slope value of the displacement current as a function of gap separation for five different maximum applied voltages. When the maximum applied voltage is relatively low, for example 20 kV, the slope values only vary slightly when the gap distance increases and remain the lowest value among these five voltage ranges. When the maximum applied voltage is higher, for example at 50 kV and 60 kV, the slope values decrease steadily when there is an increase in the electrode gap separation, and remain the highest value. With maximum applied voltages of 30 kV and 40 kV, the slope values vary with changes in the electrode separation and the value is ranged between 50, 60 kV and 20 kV. With a large electrode gap distance, the slope values for the five different maximum applied voltages are very close to each other. As the electrode gap distance was decreased, the slope values show greater differences for the different maximum applied voltages. Figure 4.50 shows the lower slope value as a function of maximum applied voltages. When the maximum applied voltage increases, the slope values for all six gap separations increase on average from approximately

1 to 4.

Figure 4.51 shows the upper slope value of displacement current as a function of gap distance. The slope values for maximum applied voltages of 20 kV, 40 kV and 60 kV vary slightly with the gap separation. However, the slope value for maximum applied voltage of 30 kV and 50 kV decrease significantly with an increase in electrode gap separation. Similar to the lower slope values, the upper slope values, for all five maximum applied voltages, are closer at large electrode gap separations. Figure 4.52 shows the relationship between the upper slope value and the maximum applied voltage with different electrode gap spaces. Again, as the maximum applied voltage increases, the slope values generally increase for all the electrode gap separation ranges. Only with 2.1 mm and 4.65 mm electrode gap distances, do the slopes have much higher value.

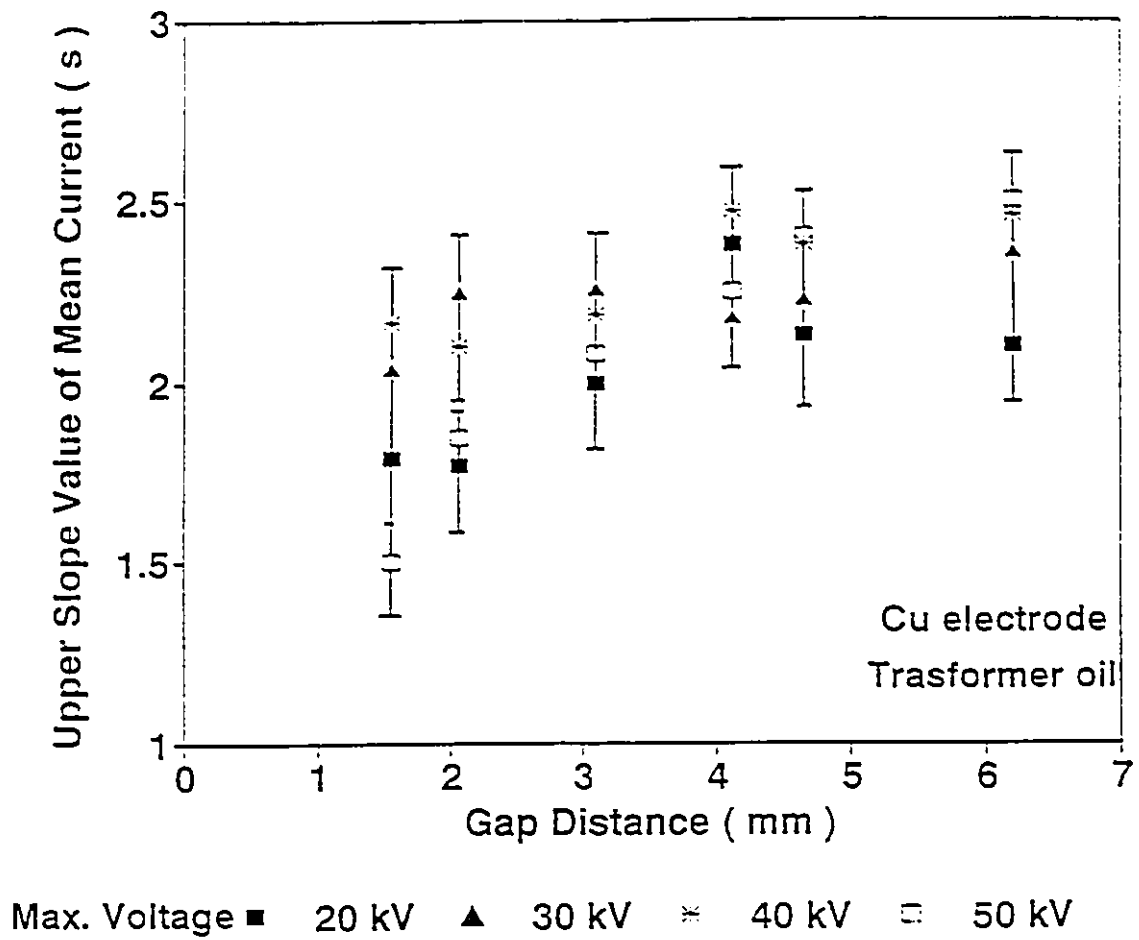


Figure 4.42 The upper slope of mean current with different gap spacings in transformer oil

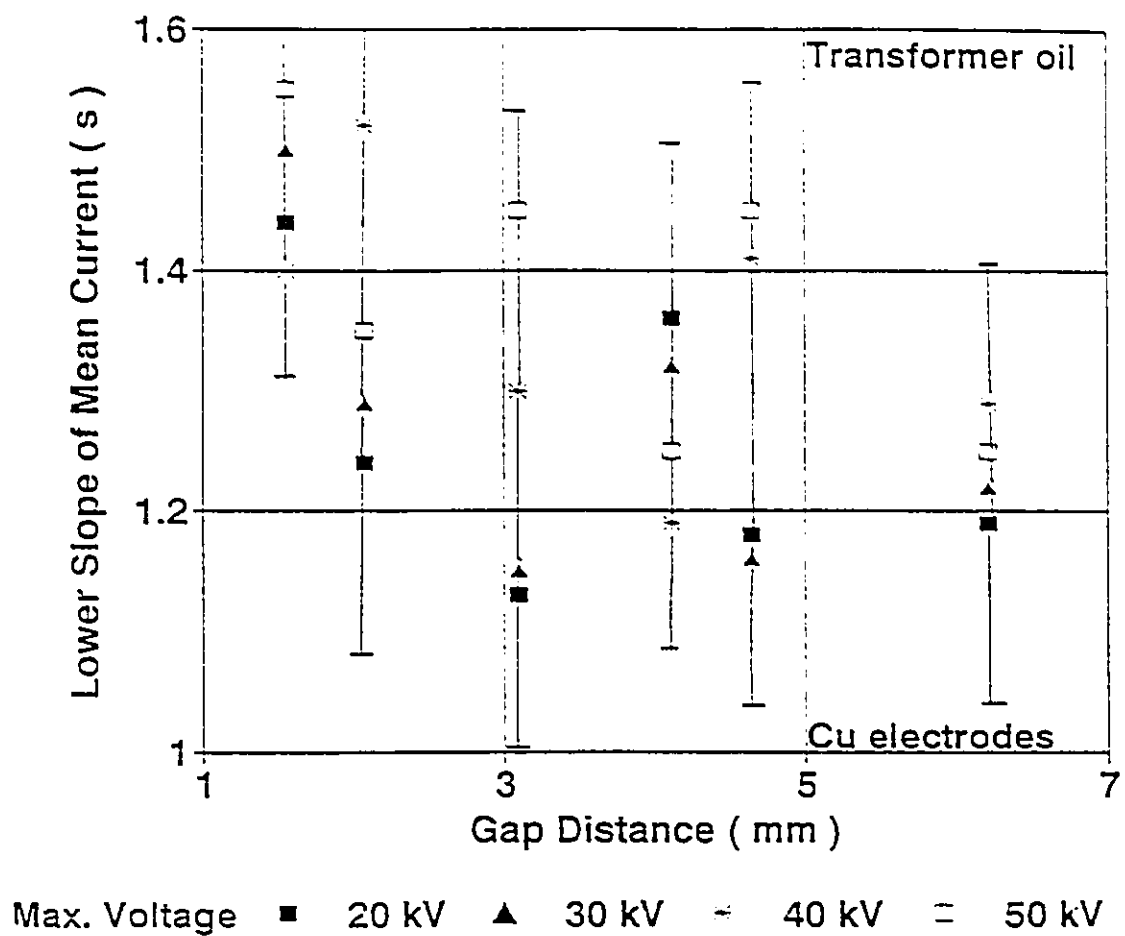


Figure 4.43 The lower slope of mean current with different gap spacings in transformer oil

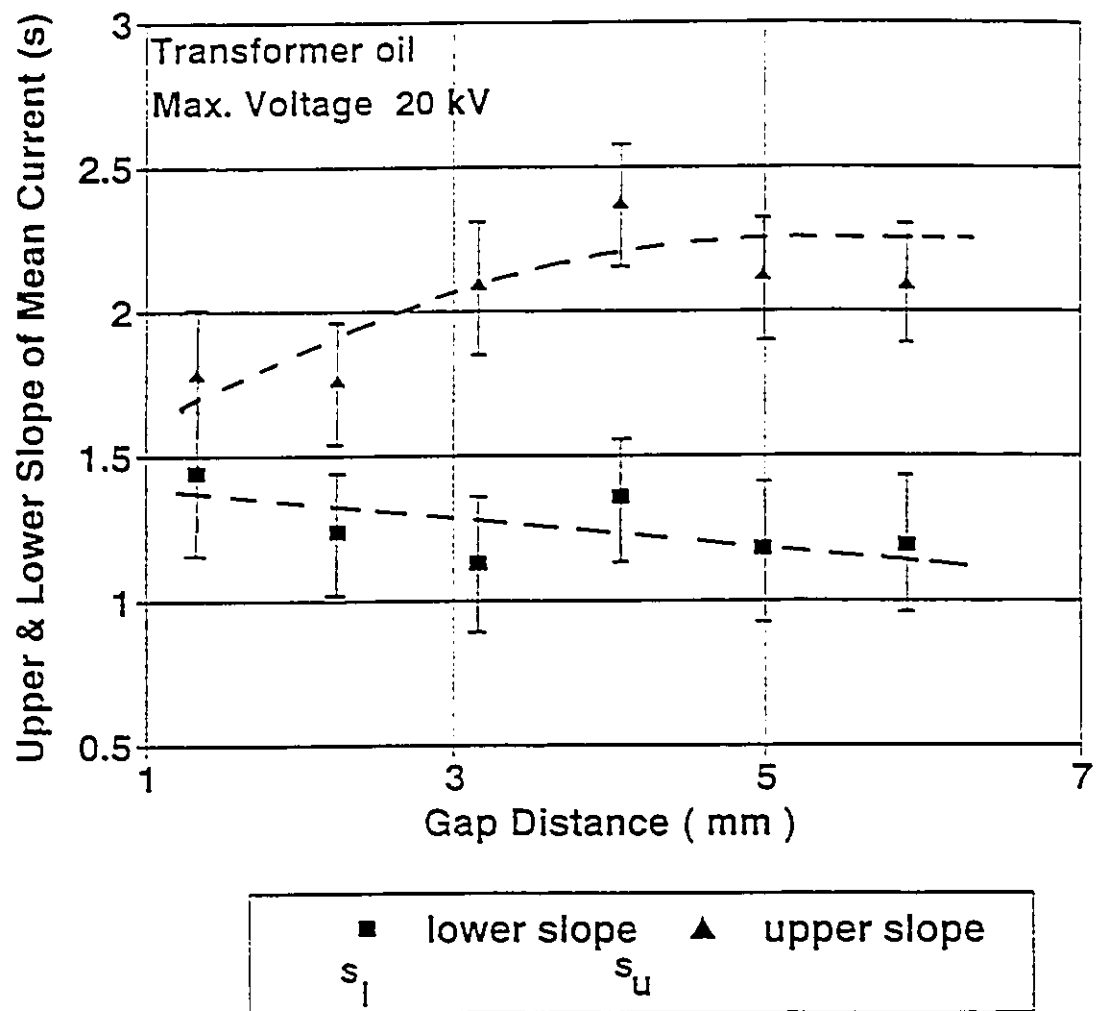


Figure 4.44 The upper slope and lower slope values of mean current with different gap spacings in transformer oil at 20 kV

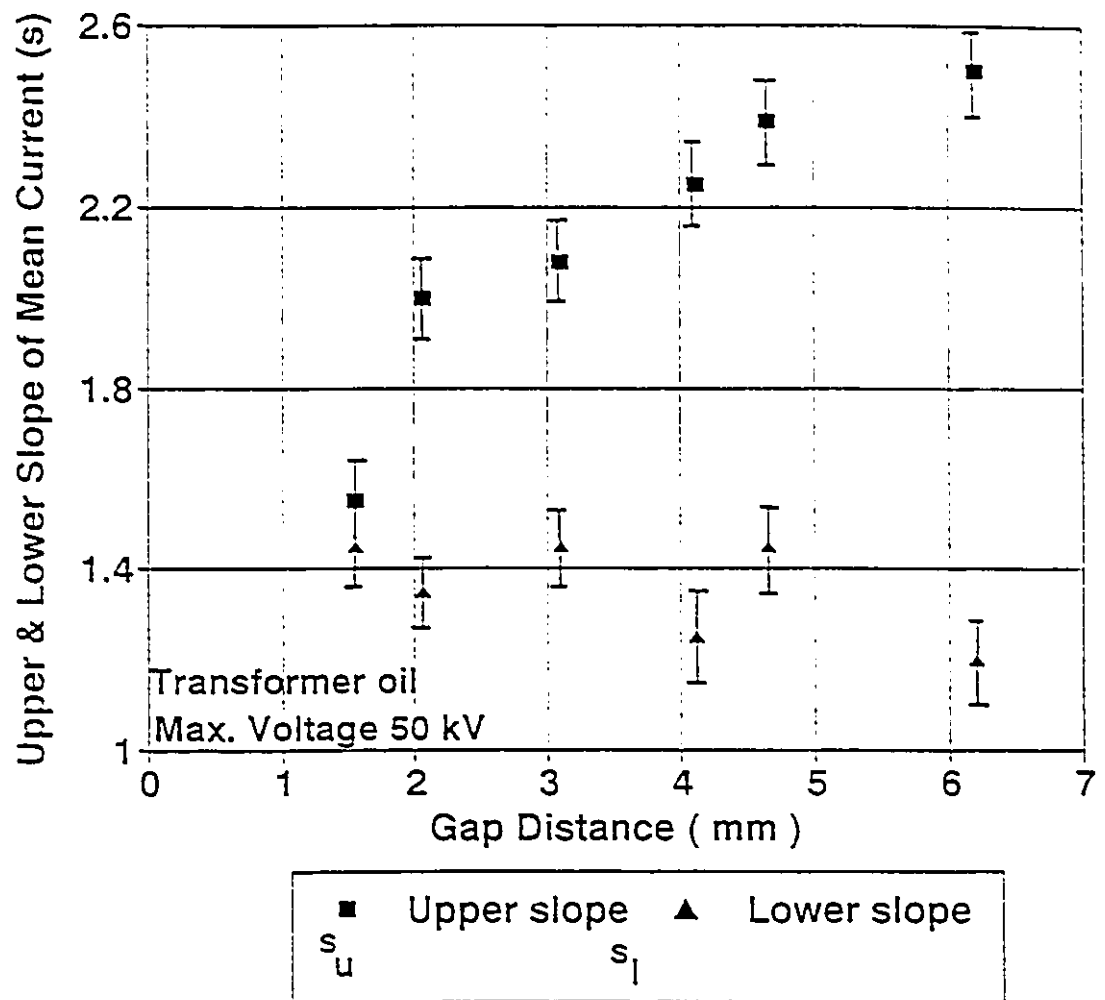


Figure 4.45 The upper and lower slope values of mean current with different gap spacings in transformer oil at 50 kV

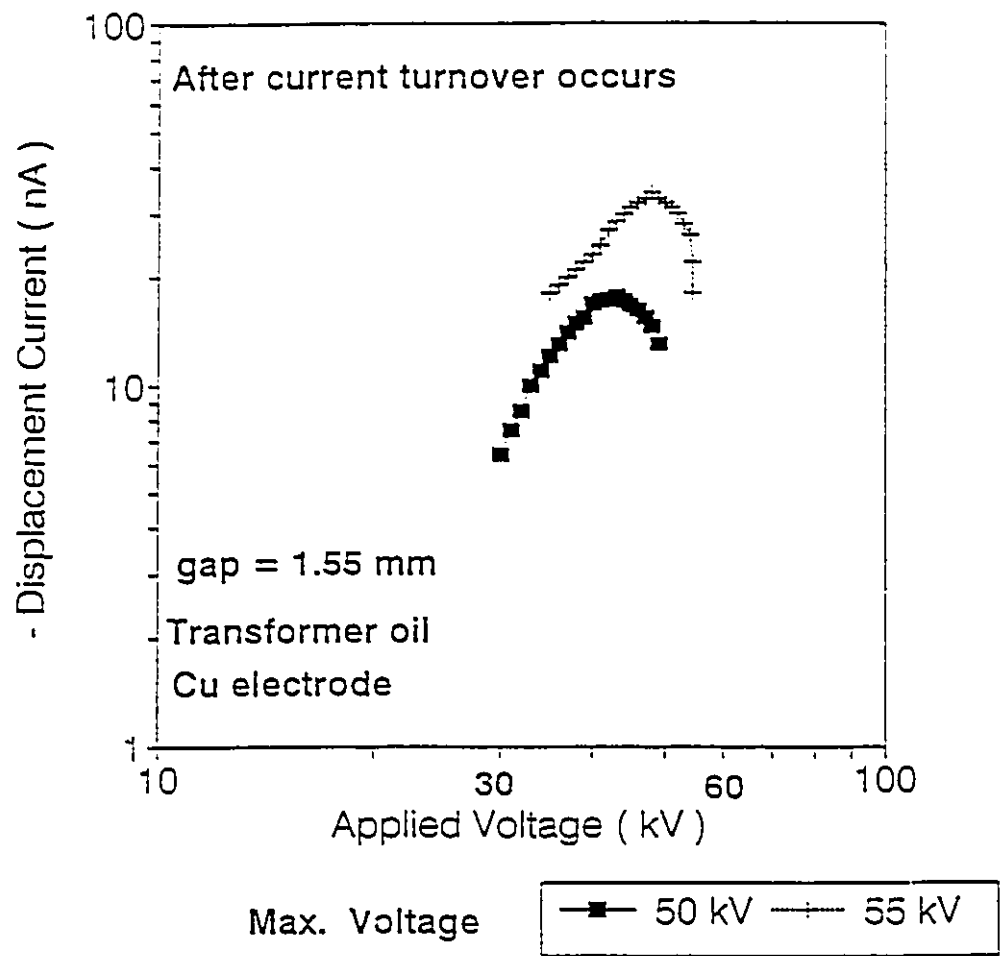


Figure 4.46 Log V-log I of displacement current after current turnover point at 1.5 mm gap space

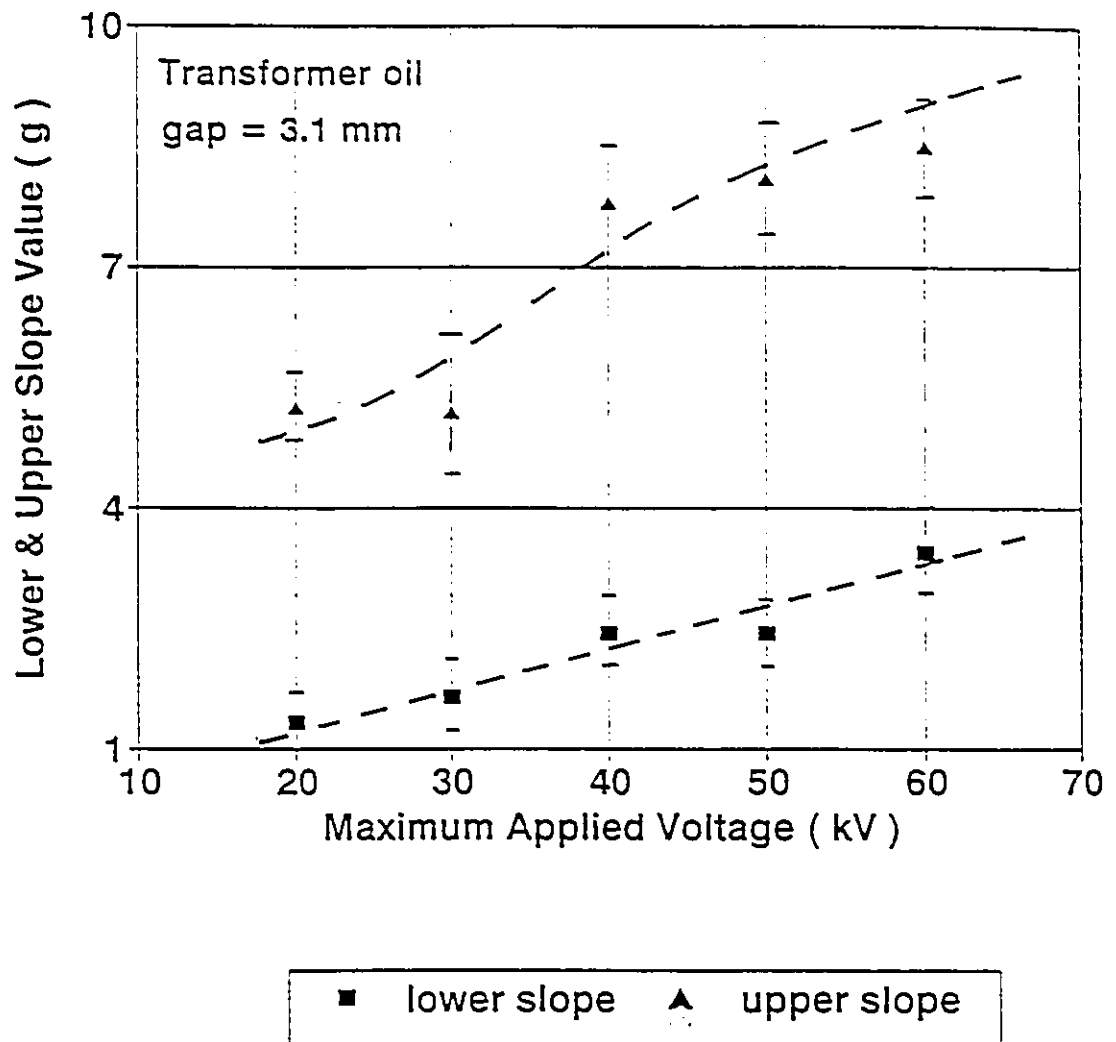


Figure 4.47 The upper and lower values of displacement current at 3.1 mm gap space in transformer oil

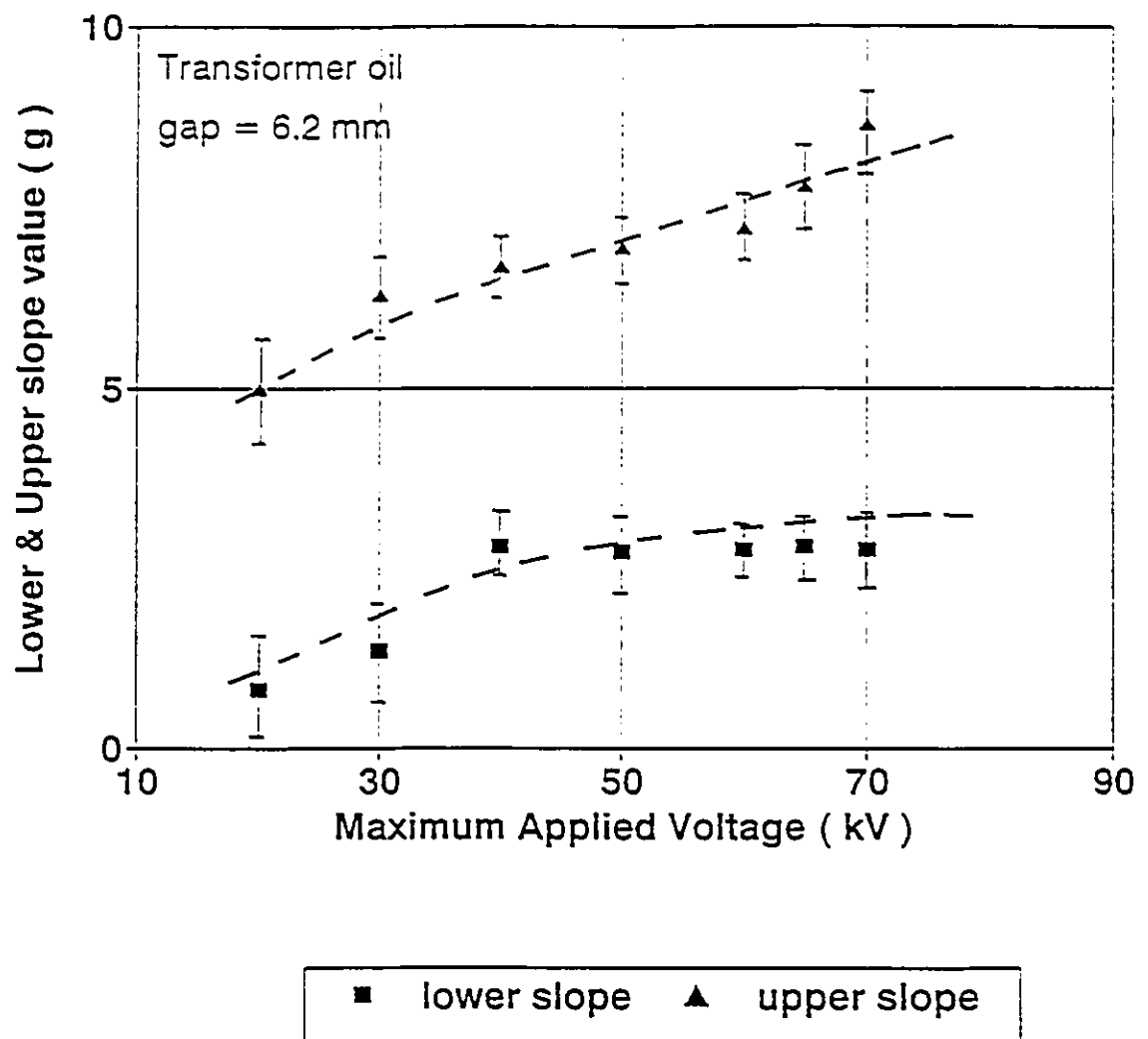


Figure 4.48 The upper and lower slope values of displacement current at 6.2 mm gap space in transformer oil

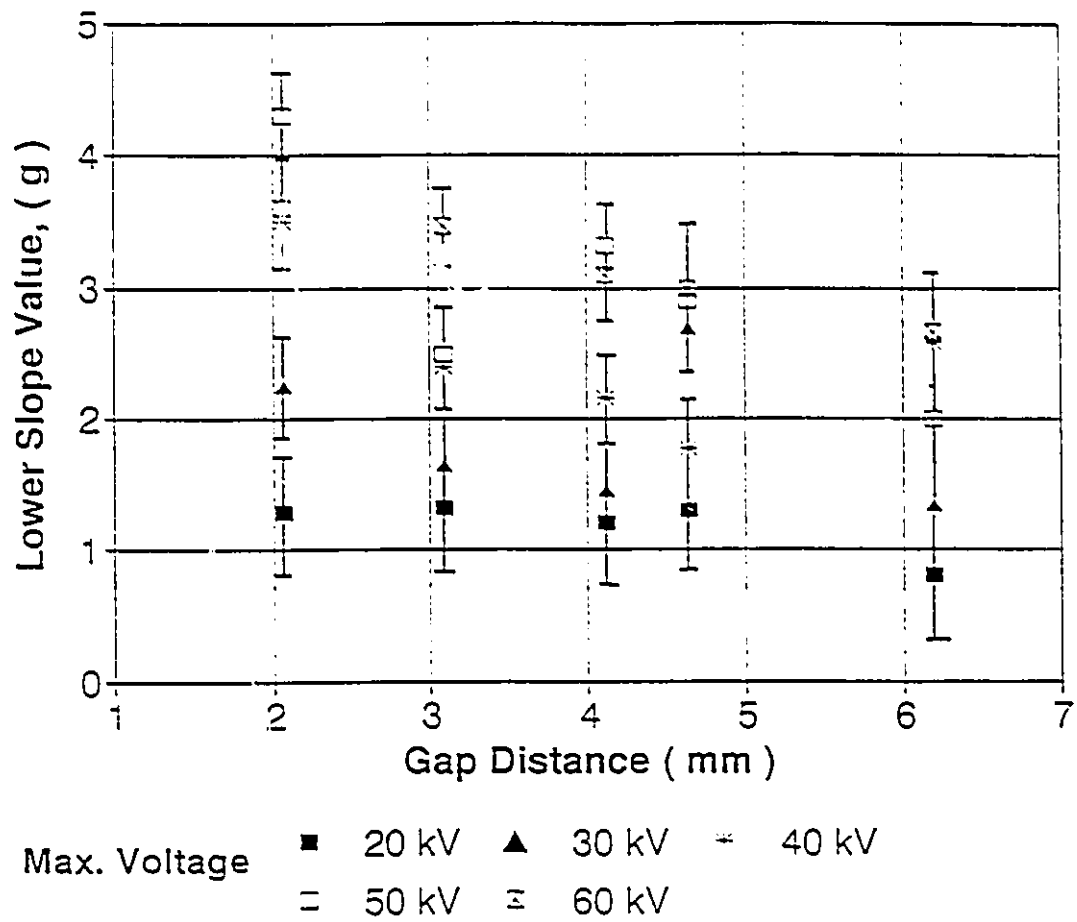


Figure 4.49 The lower slope value of displacement current as a function of gap separation with different maximum applied voltages

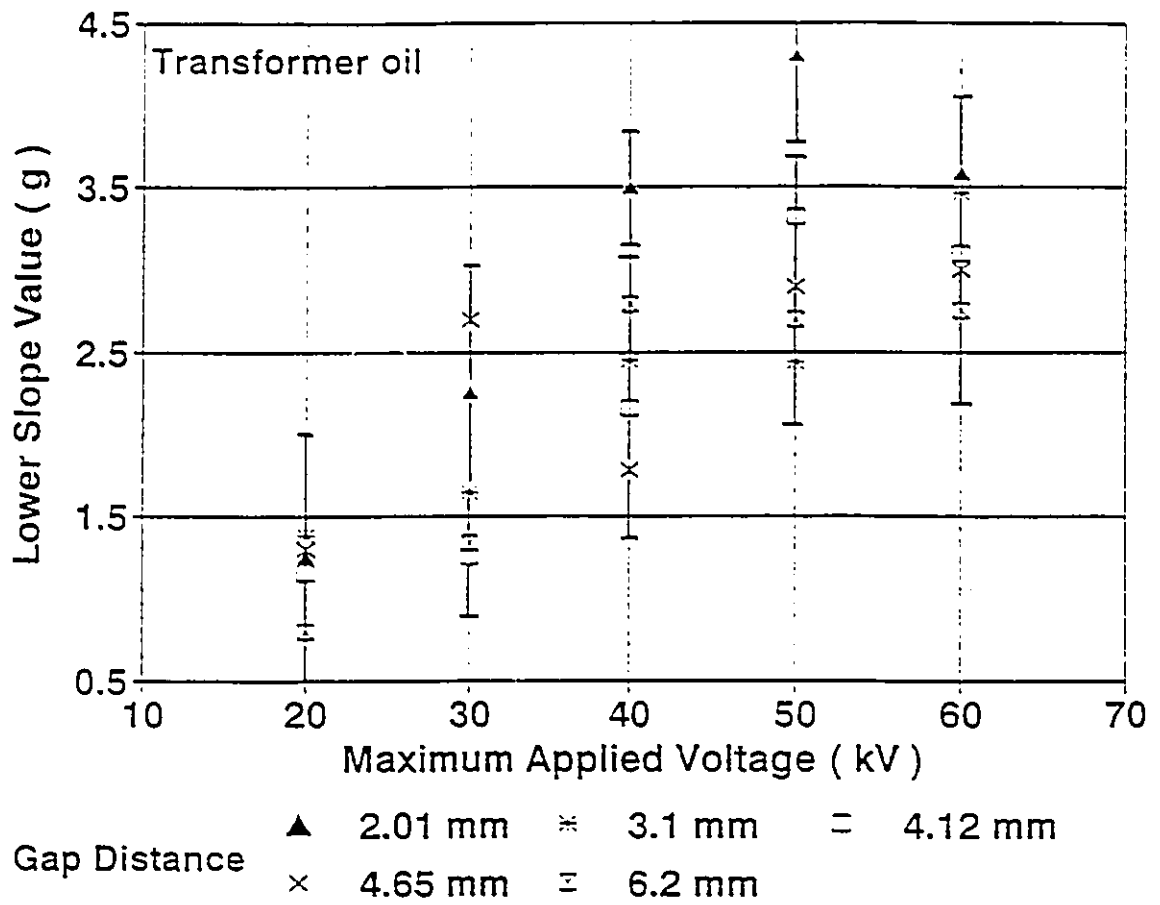


Figure 4.50 The lower slope value of displacement current as a function of maximum applied voltage with different gap separations

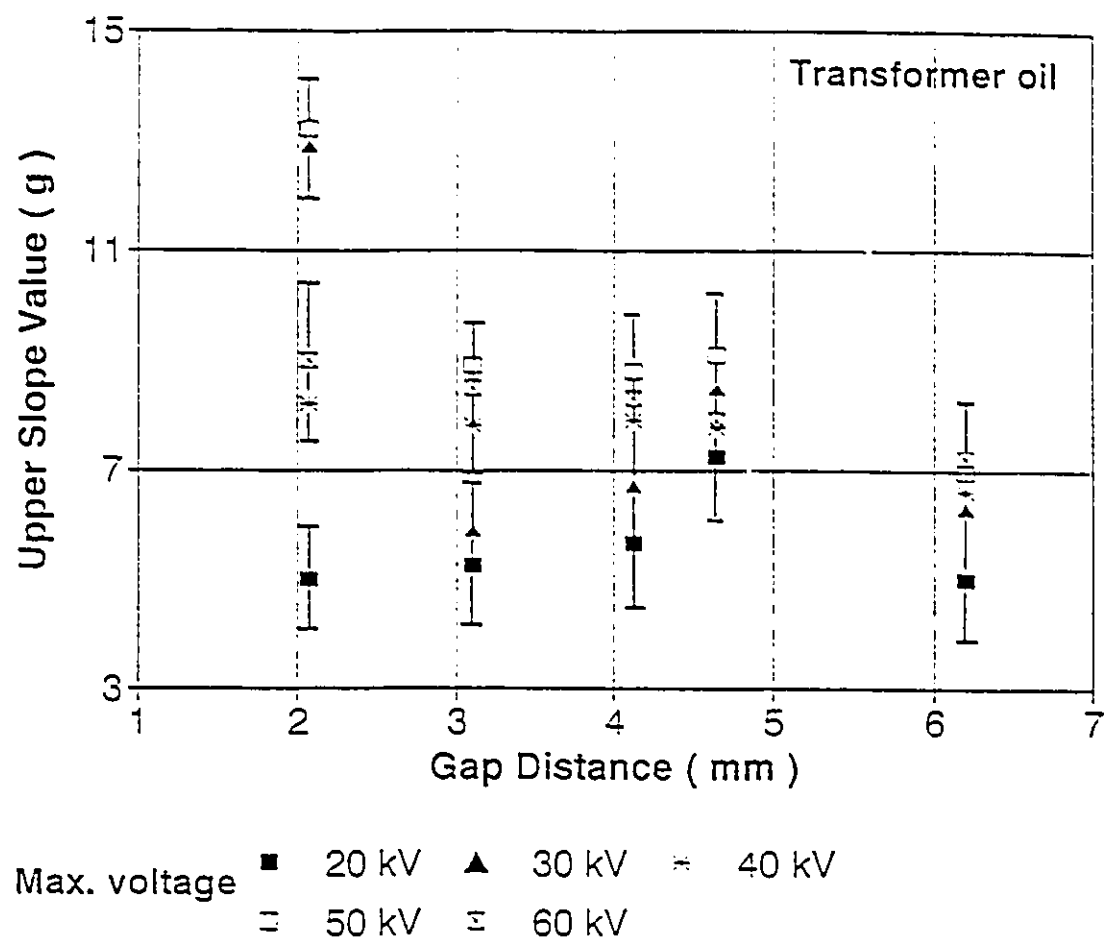


Figure 4.51 The upper slope value of displacement current as a function of gap separation with different maximum applied voltages

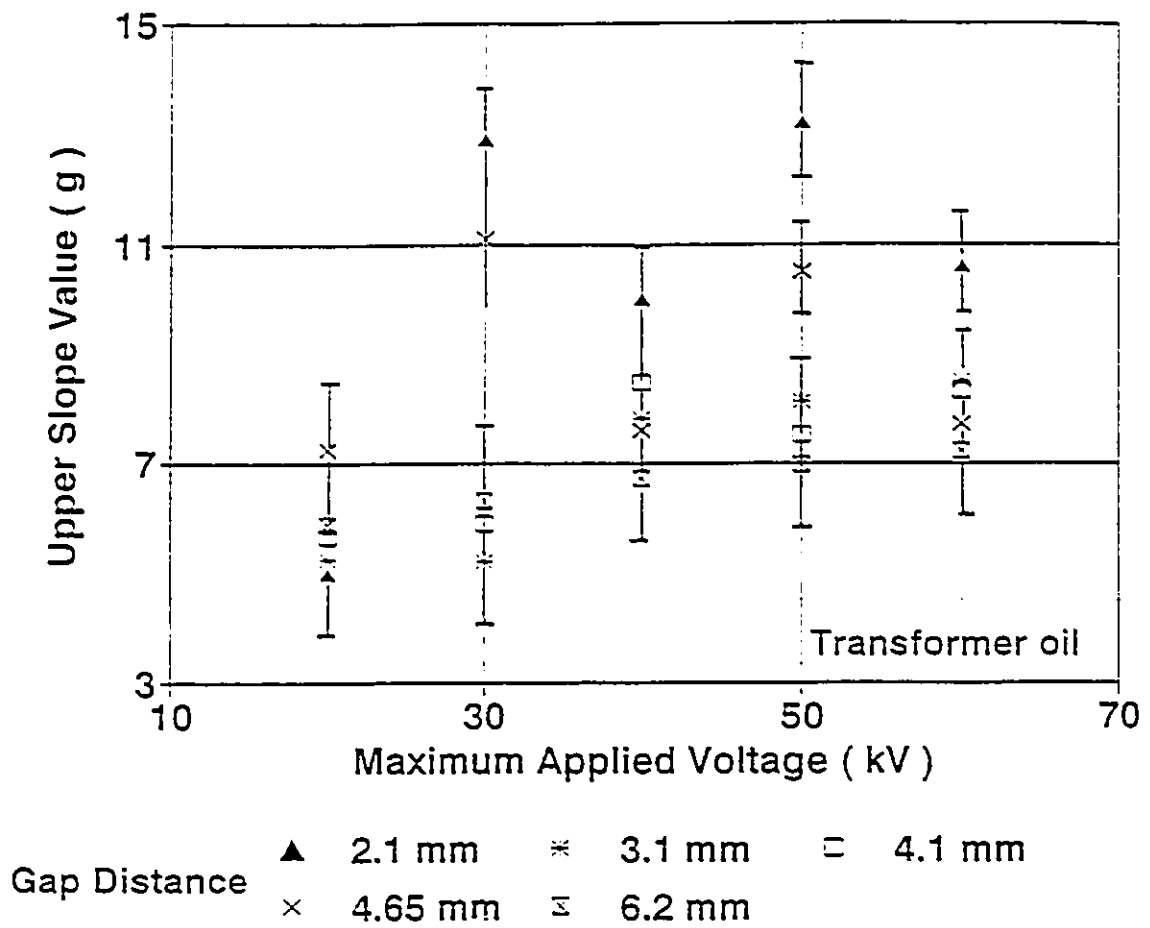


Figure 4.52 The upper slope value of displacement current as a function of maximum applied voltage with different gap separations

4.2.5 MAGNETIC FIELD EFFECT

A review of the existing literature indicates that a magnetic field effect is found to be undetectable for non-polar liquids, such as benzene and transformer oil. The conductivities for these liquids were independent of the magnetic flux density from 10^{-4} T up to 3.4×10^{-2} T [44]. Further work was performed by Watson and Girgis [5] using the high voltage ramp technique. The investigation showed that a magnetic field effect existed in silicone liquid with magnetic flux densities as low as 3.4×10^{-3} T. Thus it is necessary to examine the magnetic field effect for transformer oil under lower magnetic flux densities. The following experiments were carried out using magnetic flux densities from 2×10^{-3} T (20 Gauss) to 2.5×10^{-2} T (250 Gauss). The experimental conditions were the same as previous tests.

There is a significant difference in the V-I characteristic loops for the test cases with and without a magnetic field present. Figure 4.53 shows the upper slope value of the mean current as a function of the magnetic flux density. The gap separation is set at 3.1 mm with five maximum applied voltages ranging from 20 kV to 50 kV respectively. As the magnetic field increases, the upper slope value for all five voltage ranges, except 20 kV, increases at first up to 200×10^{-4} T then decreases as the magnetic flux density increases further shown as a "∩" shape (bell curve). The technique used here, however, is sensitive enough to detect significant trends in the variation of s with magnetic flux density. The larger the maximum applied voltage is, the flatter the "∩"

shape will be. When the maximum applied voltage steeply changes from 20 kV to 50 kV, the slope values are different from one another. Figure 4.53 also shows that slope values for the 20 kV case is plotted randomly. The slope value of the curve for a maximum applied voltage of 50 kV is the highest. From an experimental point of view, Figure 4.53 provides clear evidence that there is an impact of the magnetic field on the upper slope value of the mean current in transformer oil. Figure 4.54 shows the relationship between the upper slope value of mean current and the electrode gap separation. The magnetic field density was 100×10^{-4} T. The result shows that for all but the 20 kV case, the slope values are increased slightly as the gap distance is increased. The slope value result for the 20 kV case increases first as the gap distance is increased then begins to decrease when the electrode gap distance exceeds 4.5 mm. Again, Figure 4.54 presents a similar result to that which was recorded without the applied magnetic field as shown in Figure 4.42.

Figure 4.55 shows the lower slope value as a function of the magnetic flux density. The magnetic flux density was varied from zero to 250×10^{-4} T. The plotted data was obtained from the same experimental results as in Figure 4.53 except that it is for the lower slope value. As the magnetic field density increases, the lower slope value again does show that there is a definite functional dependence throughout although it is small. Like the upper slope value shown in Figure 4.54, the lower slope value also exhibits the "∩" or a bell curve shape as a function of the magnetic field density. Clearly, the lower slope value is changed with a change in the maximum applied voltage.

With a 50 kV maximum applied voltage level the magnitude of the lower slope values were greater than those of the 20 kV and 30 kV maximum applied voltage cases. Figure 4.56 shows the lower slope value as a function of electrode gap distance with a magnetic field density of 100×10^{-4} T. When these results are compared to the results without a magnetic field, shown in Figure 4.43, it is clear that these two graphs are very similar to each other. Furthermore, the slope value is slightly increased with an increase in the maximum applied voltage with the same electrode gap distance.

Figures 4.57 shows the slope value as a function of electrode gap separation with and without a magnetic field present with a maximum applied voltage of 20 kV. This figure shows that the slope value plots are very close to each other. Figure 4.58 represents the lower slope values under the same conditions as those in Figure 4.57. Moreover, Figure 4.58 shows that there is a clear difference for lower slopes, with and without a magnetic field present. The slope values are higher compared to those without a magnetic field present. Considering the various tolerances associated with the experiments (refer to Chapter III), the magnitude of the differences are clearly significant.

Figures 4.59 and 60 show the upper and lower slope values as a function of gap distance with and without a magnetic field supply at 50 kV. Both the upper slope values are increasing and lower slope values are decreasing with an increase in electrode gap distance regardless of whether or not there is a magnetic field presents. When compared

to the results without a magnetic field present, the slope value with a magnetic flux density of 100×10^{-4} T present is smaller for the upper slope and larger for the lower slope.

Figures 4.61 and 4.62 show the upper and lower slope values of displacement current, g , as a function of magnetic flux density. As the magnetic flux density increases, both slope values first decrease sharply with an increase in the magnetic flux density up to 150×10^{-4} T, then begin to increase with the magnetic field density to 250×10^{-4} T which produces the so called the "U" shape. At the 250×10^{-4} T level, the upper slope value will return to the same level as with no magnetic field present. For the lower slope value, the magnitude of the change is not as large as the upper slope value but the trend is identical to that of the upper slope with a clear "U" shape to the plotted results. Figure 4.63 shows the upper and lower slope values of displacement current as a function of maximum applied voltage. Both slope values increase slightly as the voltage increases. When compared with the results when there was no magnetic field present, both slope values are smaller.

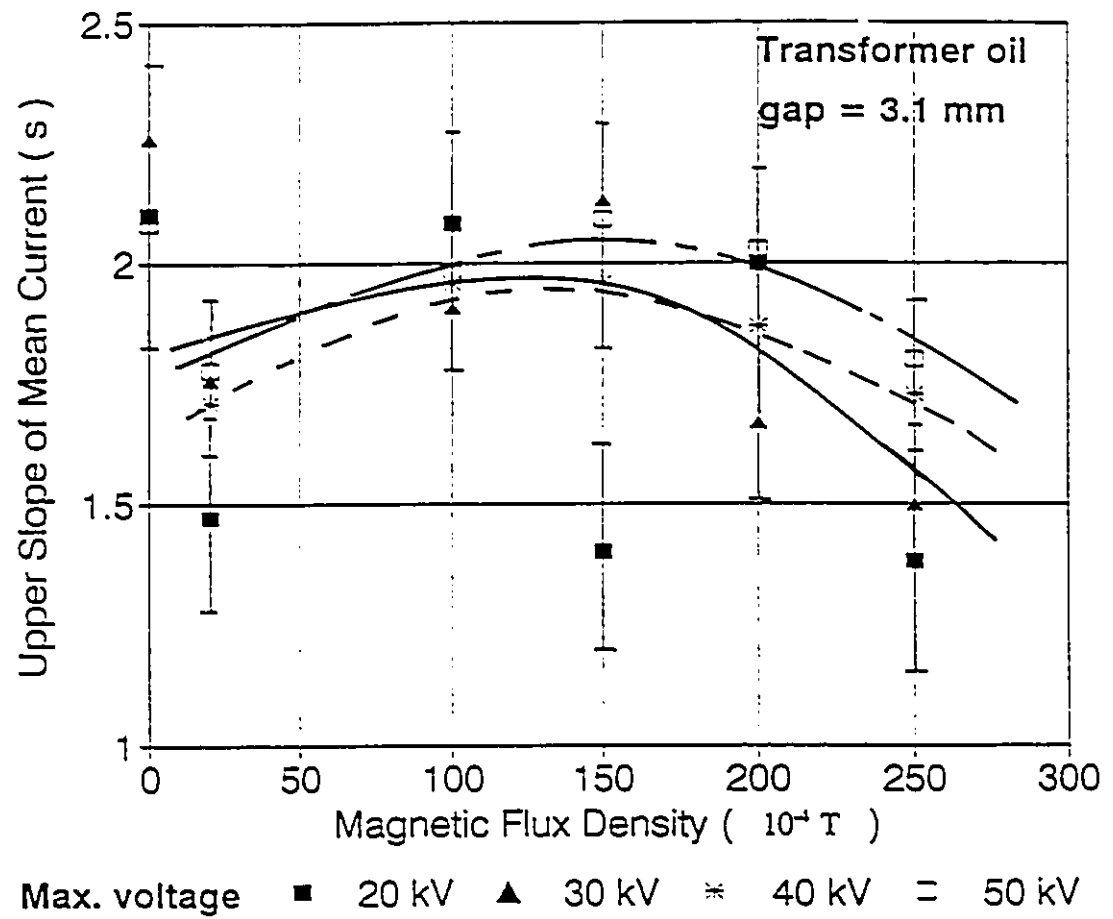


Figure 4.53 The upper slope of mean current as a function magnetic flux density with differing maximum applied voltages in transformer oil

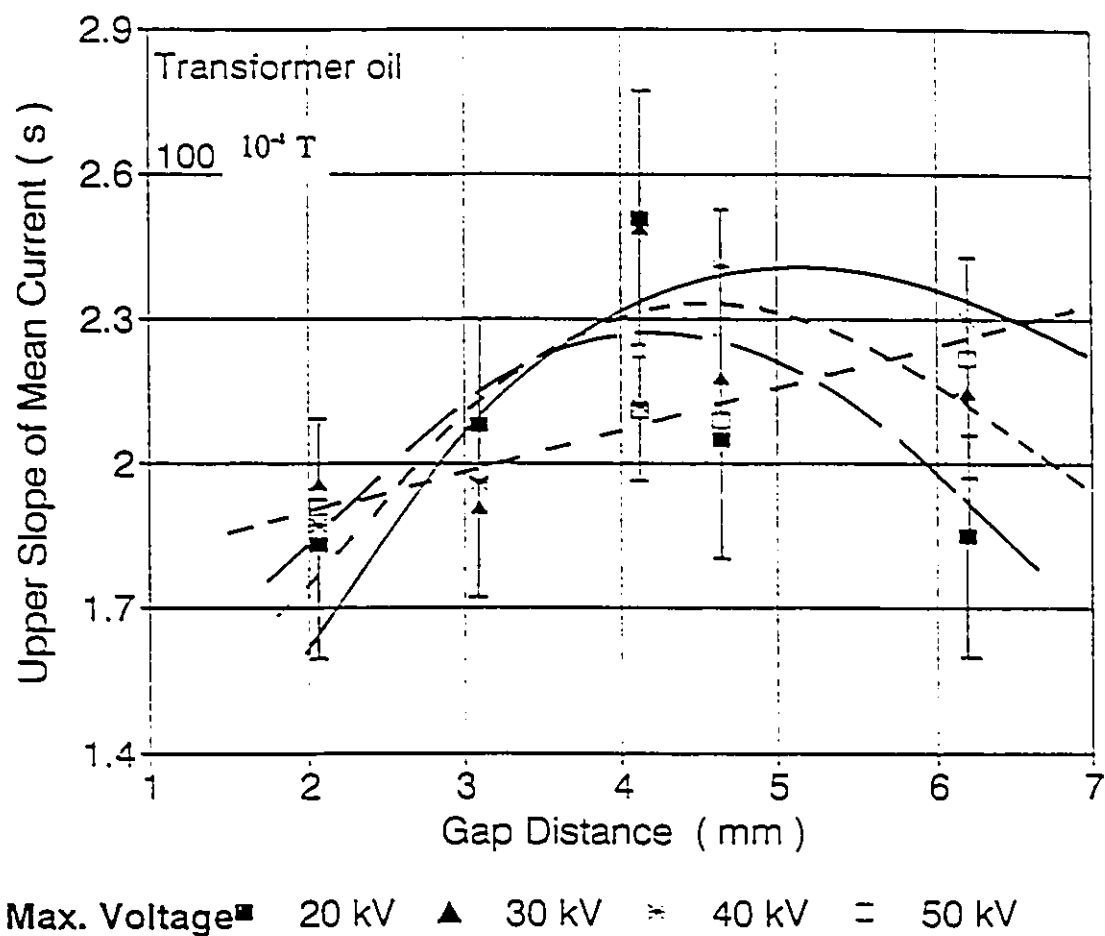


Figure 4.54 The upper slope of mean current as a function of gap spacings at 100 Gauss with differing maximum applied voltages in transformer oil

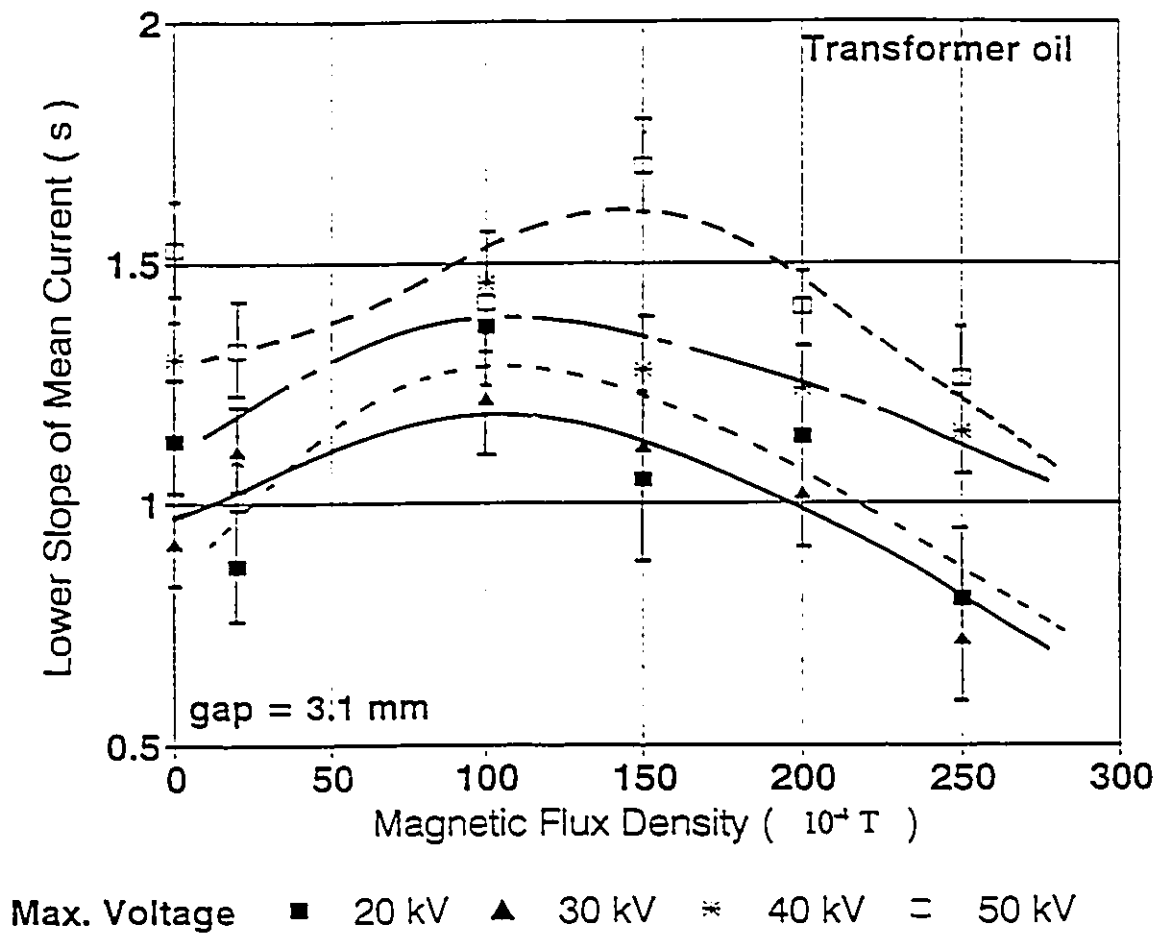


Figure 4.55 The lower slope of mean current with different magnetic flux density with differing maximum applied voltages in transformer oil

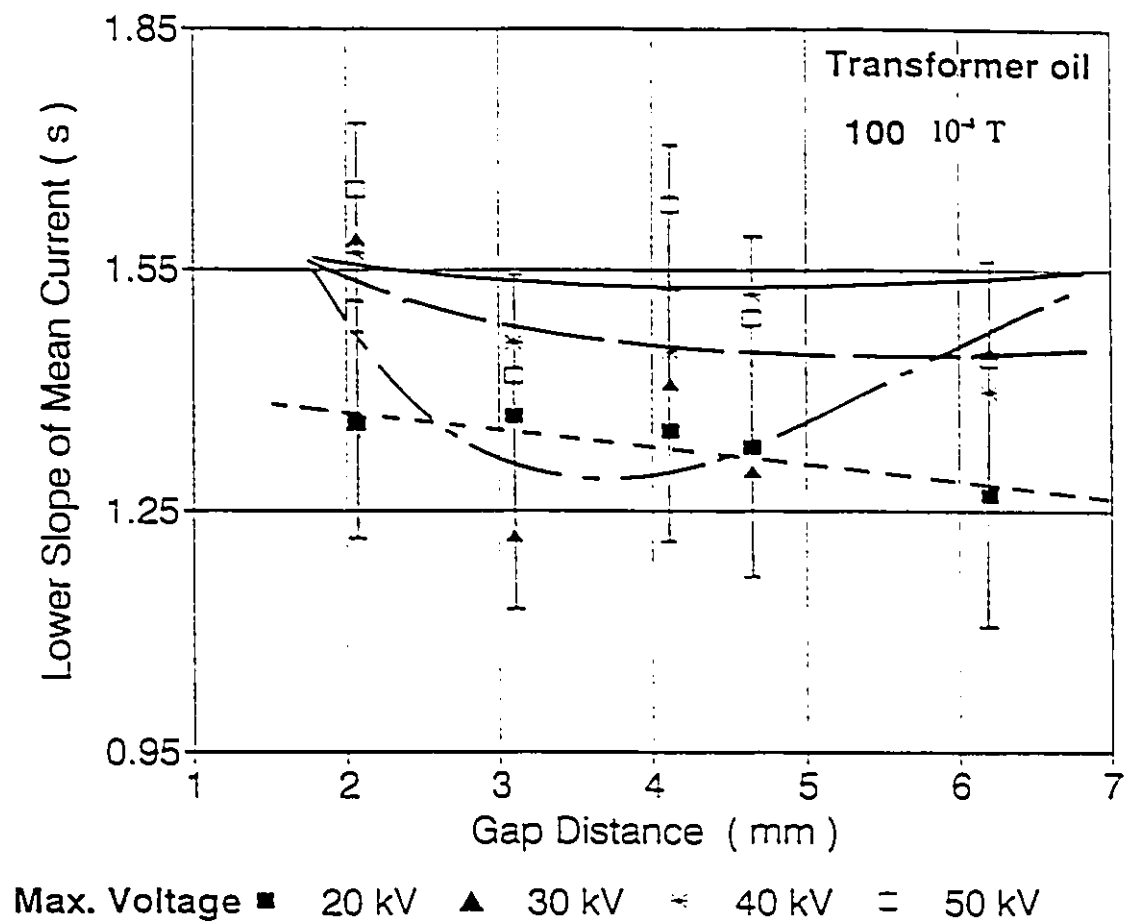


Figure 4.56 The lower slope of mean current as a function gap spacings at 100 Gauss with differing maximum applied voltages in transformer oil

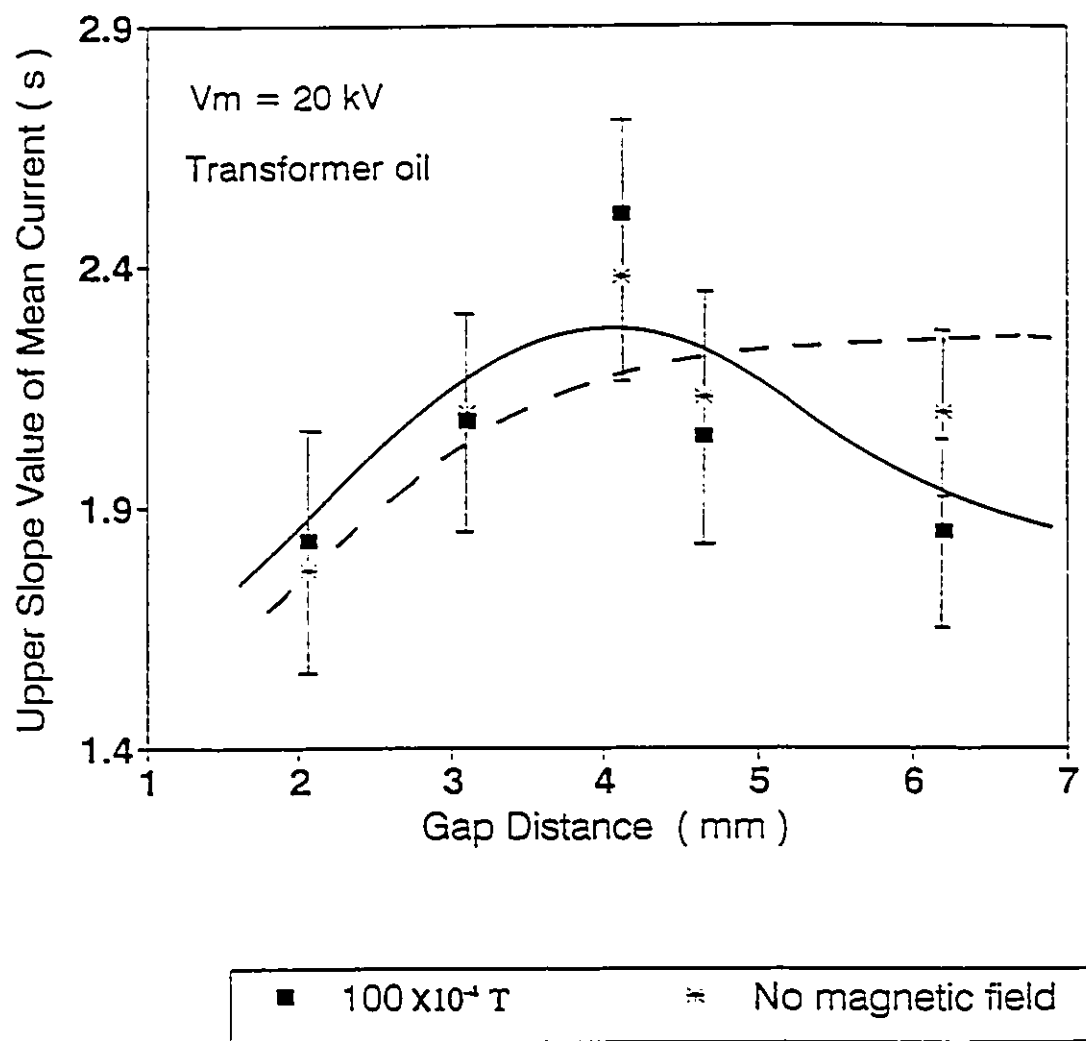


Figure 4.57 The upper slope value of mean current with/without magnetic field in transformer oil at 20 kV

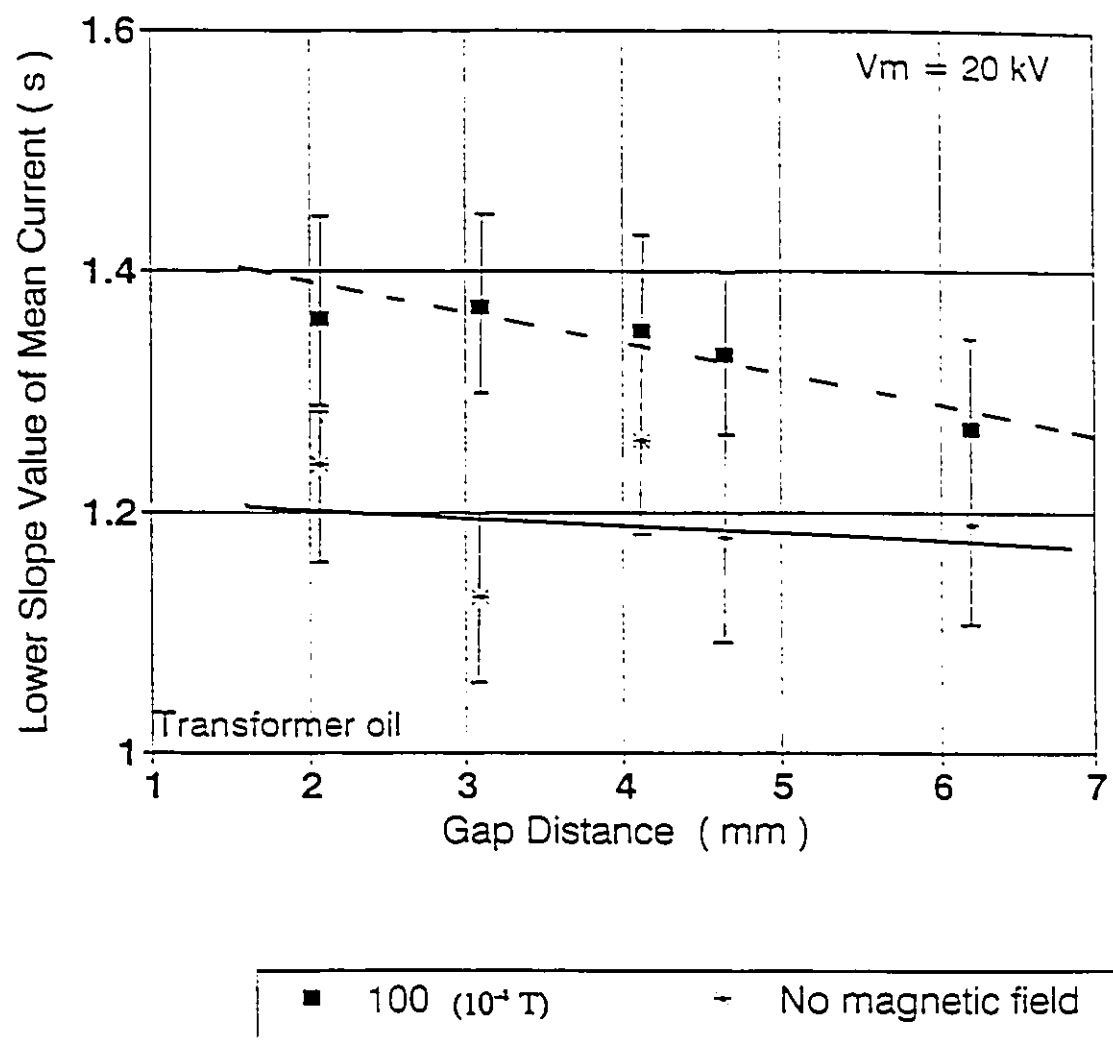


Figure 4.58 The lower slope value of mean current with/without magnetic field in transformer oil at 20 kV

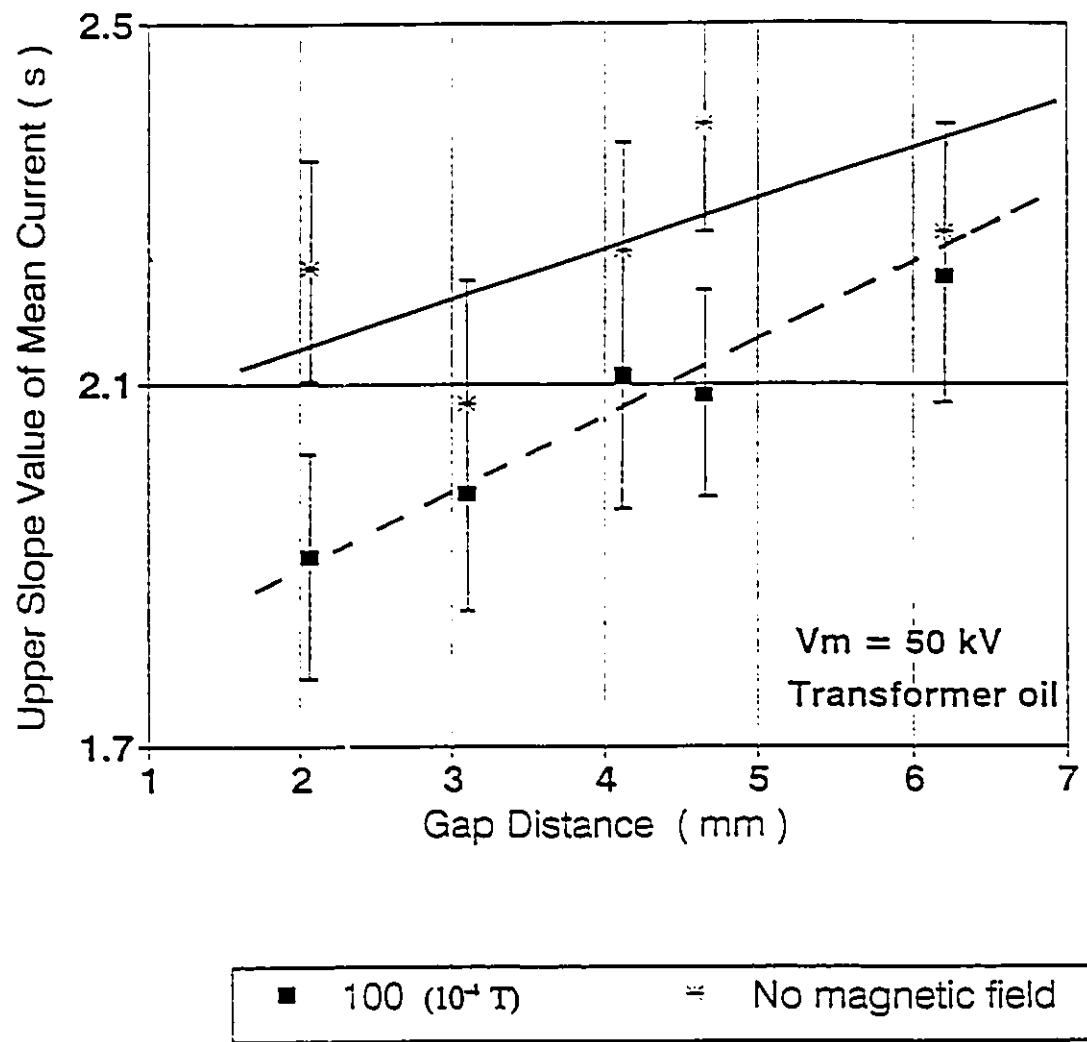


Figure 4.59 The upper slope value of mean current with/without magnetic field in transformer oil at 50 kV

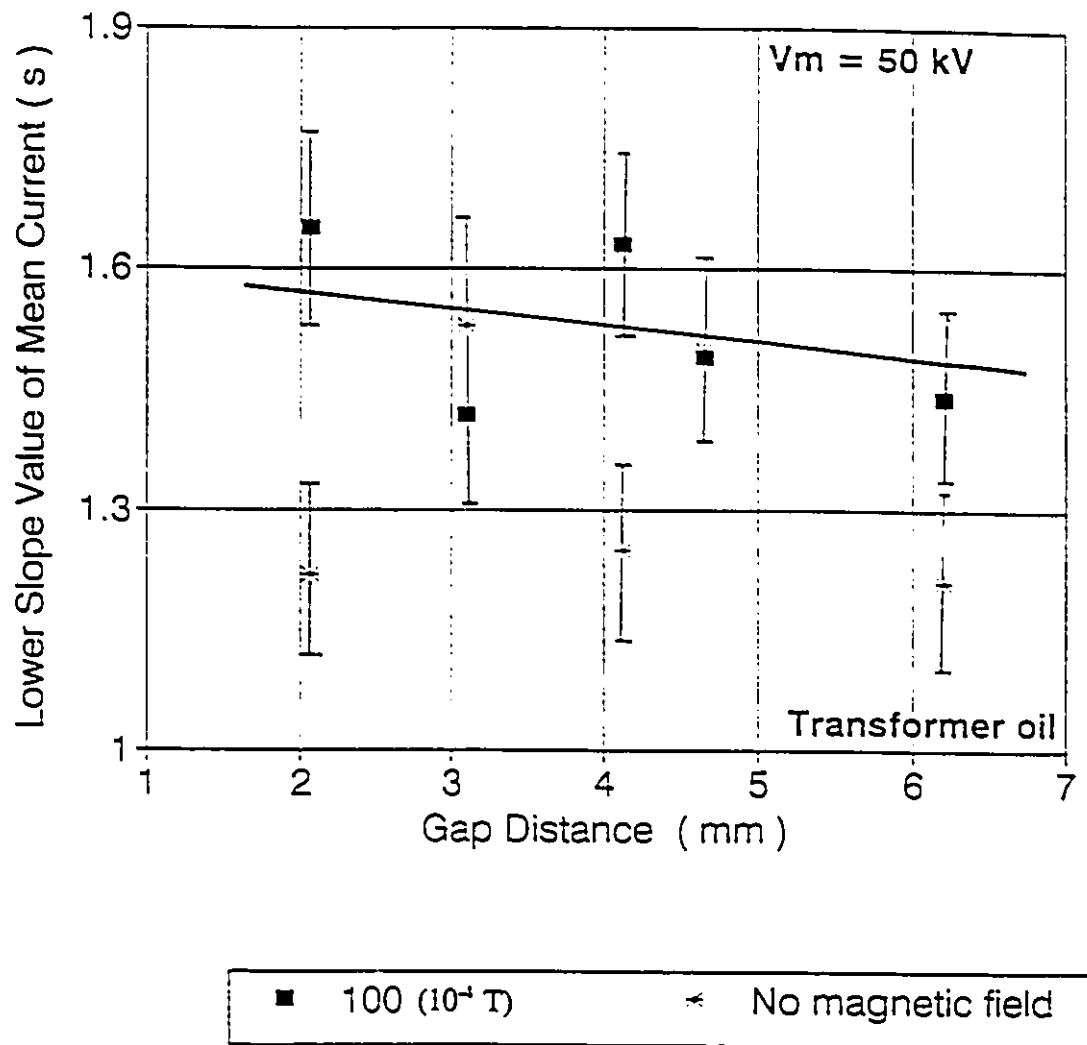


Figure 4.60 The lower slope value of mean current with/without magnetic field in transformer oil at 50 kV

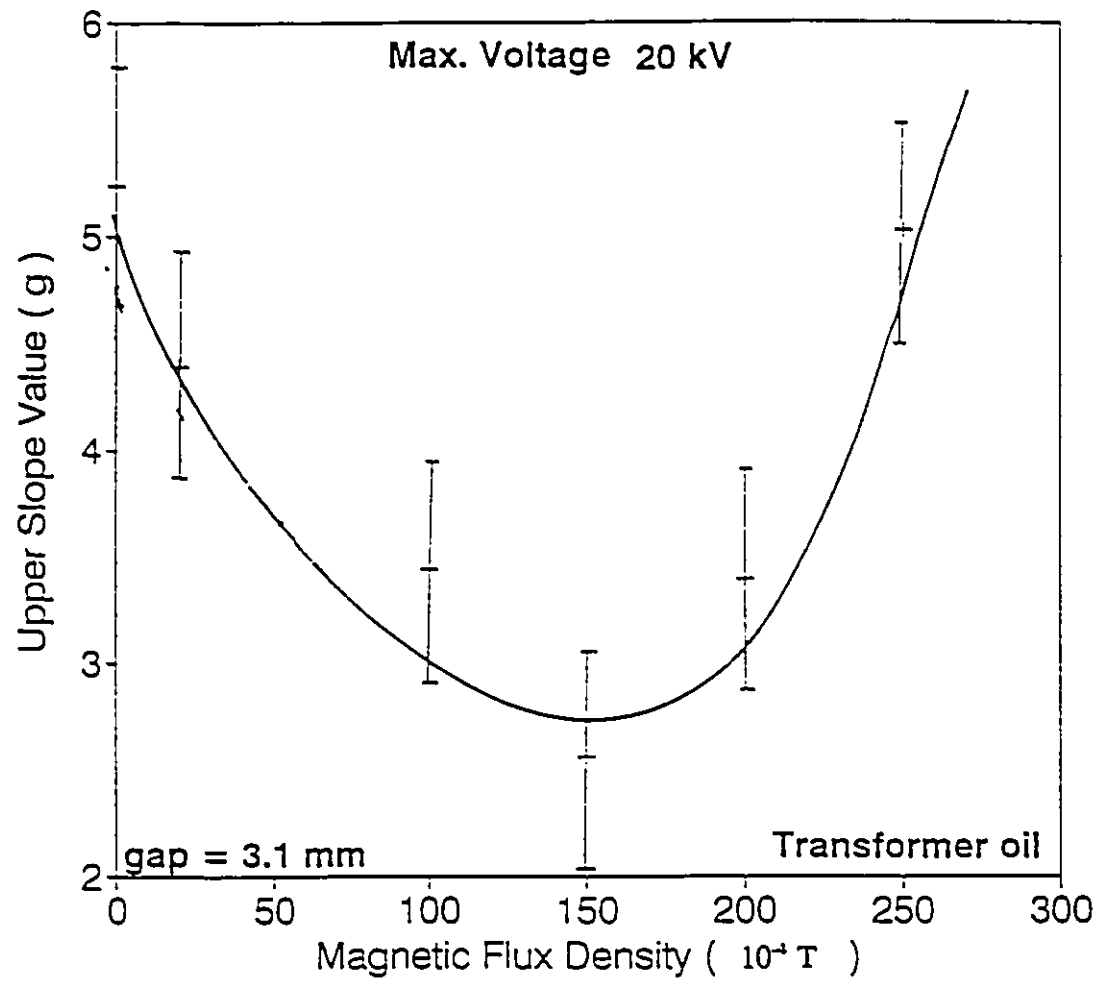


Figure 4.61 The upper slope value of displacement current with differing magnetic fields in transformer oil

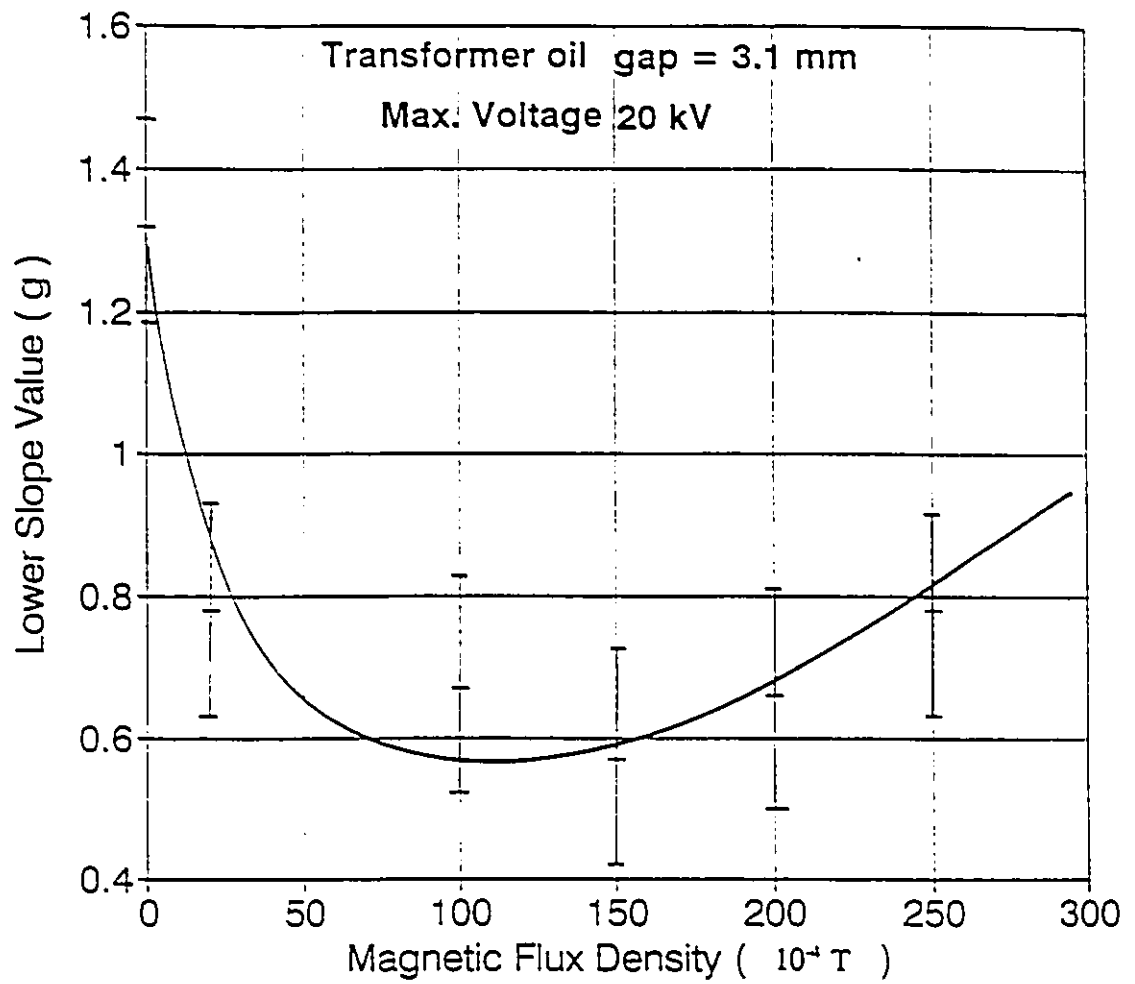


Figure 4.62 The lower slope value of displacement current with differing magnetic fields in transformer oil

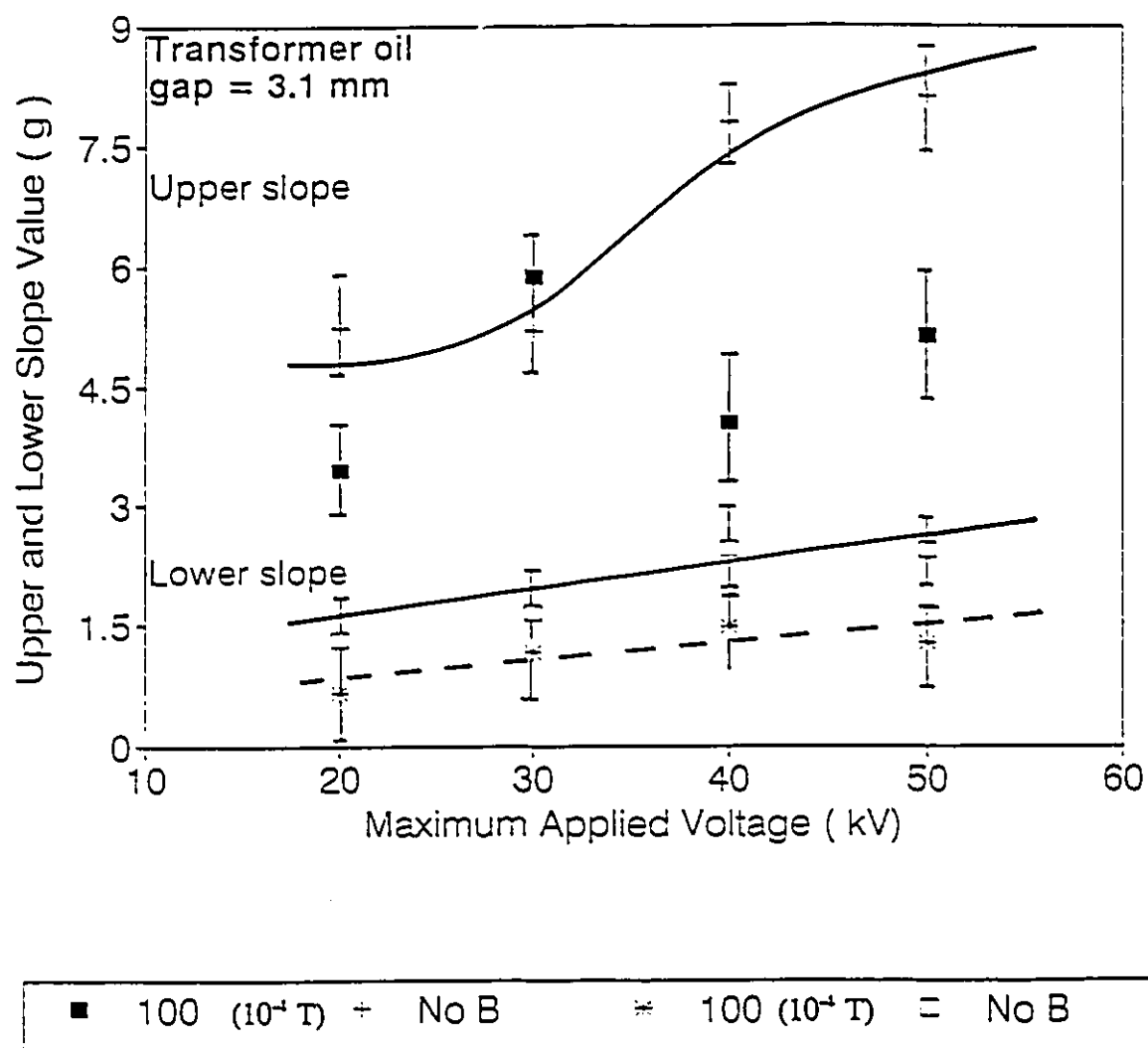


Figure 4.63 The upper slope and lower slope values of displacement current as a function of maximum applied voltage with/without magnetic field in transformer oil

4.3 DI-ISO-OCTYL-PHTHALATE (ESTER OIL)

The di-iso-octyl phthalate liquid (ester oil) is one of the organic esters, with the chemical formula $(C_8H_{17}COO)_2C_6H_4$. This kind of ester oil has a very high viscosity and water solubility. The ester oil in its clean and dry condition will possess an electric strength in the region of 20 kV/mm and volume resistivities of the order of 1 - 100 GΩm and 20 GΩm at 20 °C and 90 °C respectively (see Table 3.1). In its dry form, the conductivity is no greater than that of the hydrocarbon liquids.

The electrical properties of di-iso-octyl phthalate are very dependent upon the final manufacturing treatment. As they are relatively new materials to the electrical industry, their electrical properties have not been fully investigated [15,71,72]. So far in the purest form (free from moisture, polar contaminants and acids), the organic ester liquids have been used in power cables and high frequency capacitors [73]. As the solubility of water in ester oil is much higher than it is for transformer and silicone oils (Table 3.1), water absorption from humid atmospheres is therefore greater even in a relatively dry condition.

For a better comparison between the oils, all the experiments have been carried out under the same test conditions. An example of the experimental results for ester oil is given in Figure 4.64. It shows the waveforms of the applied voltage and its response current as a function of the time. It is clear that the response current waveform is very

similar to that of the applied triangular ramped voltage. The value of the response current is most likely to be in proportion to that of the applied voltage. Thus, this appears to be typically related to it linearly in an almost ohmic relationship except at the peak value of applied voltage as is evident from Figure 4.65. Moreover, unlike silicone oil shown in Figure 3.6, the response current for the ester oil always remains positive. The residual voltage is the same as the silicone oil while the residual current is different. It is understood that the residual voltage is dependent only upon the power supply system and the residual current is related to the oil sample (Chapter III). The conduction current in ester oil is so large such that the capacitor current is almost neglected when compared to the conduction current. The residual current response is positive instead of negative. Figure 4.65 gives the relationship between the applied voltage and its response current. It should be noted that the direction of traversal of the voltage-current loop is reversed when compared to previous work with silicone oil or transformer oil. By this, it is meant that at the same voltage level, the current with an increasing voltage is smaller than that for a decreasing voltage. This current turnover phenomenon was only recorded occasionally in transformer oil at a very high electric stress level. It also has been observed in silicone oil during experiments, but was too feeble to measure or record.

By setting the electrodes at a gap spacing of 3.1 mm for example, the experiment has been carried out with different maximum applied voltage values. The effect of the maximum applied voltage with its average response current upon the log-log characteristics is shown in Figure 4.66. As a result, instead of two sharply divided linear

portions which were obtained for transformer oil and silicone oil, only one linear portion was found in the high stress region for the ester oil throughout the entire experiment. The value of the upper slope is the same as the value of the lower one for the average current characteristics. Thus, $s_u = s_l = s$. Moreover the slope (s) of that portion was always the same value in the high field regime even while varying the maximum applied voltage. Since only one slope exists in the high field region on the $\log I$ - $\log V$ scale, there is no threshold point for the ester oil analysis shown in Figure 4.66. Similar experimental results were also obtained by changing the gap spacing from 0.8 to 6.2 mm respectively [74].

Figure 4.67 shows the experimental results of the mean current vs. the applied voltage for the different gap spacings when the maximum applied voltage is fixed at 20 kV. It appears that the slope values s for each of the different electrode spacings are almost identical at 1.04 ± 0.035 . When the electrode gap distance is changed under the same applied voltage, according to the Ohm's law, the response current will change too. Figure 4.67 shows the difference between $\log I$ vs $\log V$ of each curve for the different gap dimensions.

Figures 4.66 and 4.67 show that the slope value for the ester oil is very significant. The slope value for ester oil does not change with different maximum applied voltages or with the electrode spacing as was observed with both transformer oil and silicone oil. Under these test conditions, the s value is equal to 1.040 ± 0.035 , very

close to unity.

Since the slope value is very close to one, the ratio (R) between the applied voltage to its mean response current could also be called the corresponding resistance. Thus R can be simply approximated by using $R = V^*/I \approx V/I$, the resistance values for each electrode spacing, which was tested at the maximum applied voltage value of 20 kV. Figure 4.68 gives the value of corresponding resistances R of the ester oil as a function of gap spacing. It is shown that the resistance R directly increases with the space spacing within the limits of error of the experiment. The resistance R could be written as

$$R \approx 13 + 3d \quad (4.10)$$

where d is a gap distance in mm, R is in $G\Omega$.

To examine the accuracy of Equation 4.10, a uniform field system is used in this calculation. The resistance of the oil thus would be expected to be proportional to the gap spacing and inversely proportional to the cross sectional area of the discharge path simultaneously. The resistivity for the ester oil is $1 G\Omega m$ as shown in Table 3.1, thus following Equation 3.11,

$$\rho \frac{d}{A} = R, \quad A = \frac{\rho d}{R} \quad (4.11)$$

$$r = \left(\frac{A}{\pi} \right)^{1/2} = \sqrt{\frac{\rho d}{\pi R}}$$

where the cross sectional area is assumed to be perfectly circular and r is the radius of the cross sectional area. Let the gap distance, d , be 3.1 mm, therefore by using Equation 4.11, the calculated result of r is about 6.5 mm. The electrode ratio used at the tip is 6.2 mm, this value is very close to that given by the above calculation. It is clear that the calculated result could differ slightly from the actual value, as a result of the non-uniform field effect.

It should be noted in Figure 4.64, that the current waveform is nearly identical in shape to the applied voltage waveform while it is increasing or decreasing as a function of time. Moreover, $V(t)$ at $t < 5$ is equal to $V(t+5)$ at $t > 5$. Thus, $I_{up} \propto I_{down}$, and then this also could be written as $I_{down} \approx I_{up} + \Delta I$, where ΔI is a constant with a value greater than zero. As was mentioned previously, I_{up} is smaller than I_{down} , so the displacement current I_d is negative in polarity as a result. Moreover, I_d could be simply written as,

$$I_d = (I_{up} - I_{down})/2 \approx \frac{I_{up} - (I_{up} + \Delta I)}{2} \approx -\frac{\Delta I}{2} < 0 \quad (4.12)$$

Thus, the displacement current will be very nearly a constant as well, with a value of $-\Delta I/2$. Again, because ΔI is unchanged by the applied voltage, so only one linear portion

will also appear from the displacement current versus its applied voltage for the ester oil except near the peak value of applied voltage. This is not true around the peak value of the applied voltage. At either the peak point or the lowest point of applied voltage, there is a transient current passing through the circuit. Otherwise similar to the mean current, the slope value for displacement current $g = g_u = g_i$ is shown in Figure 4.69. Obviously, the displacement current in this case is negative when compared with that of silicone oil. This is a totally different result from those for both transformer oil and silicone oil. It is noticed from Figure 4.65 that at approximately 2~3 kV from the maximum applied voltage level, the displacement current changes abruptly. Again, Figure 4.69 also shows that with a $\log V - \log I$ plot the current decreases dramatically with the applied voltage at the maximum voltage level.

The so called current turnover phenomenon had been first found in transformer oil at very high electric field levels. Those current reversals only occurred above a certain potential level (V_t) shown in Figure 4.28. This I vs V figure is a double loop, a slanted "figure 8" form. Examining the result from the ester oil tests shown in Figure 4.67 indicates that there appears to be a total current reversal. Thus, one may be interested to see the behaviour of the current loop when the maximum applied voltage levels are very much lower than those used in the original tests. Figure 4.70 shows the experimental result for the ester oil tests at relatively low maximum applied voltage levels. These maximum applied voltage levels ranged from 3 kV to 10 kV respectively with a gap separation of 3.1 mm. Maximum applied voltage levels below 3 kV are

beyond the range of the existing experimental equipment. The result shows that there is no difference between the I versus V characteristic curves when compared with the results from previous tests (Figure 4.65). The current turnover phenomenon is found from the lowest level of applied voltage without a double loop even at 3 kV. Thus, the current reversals were present throughout the entire experiment for ester oil. No experiments were performed with ester oil using a maximum applied voltage less than 3 kV.

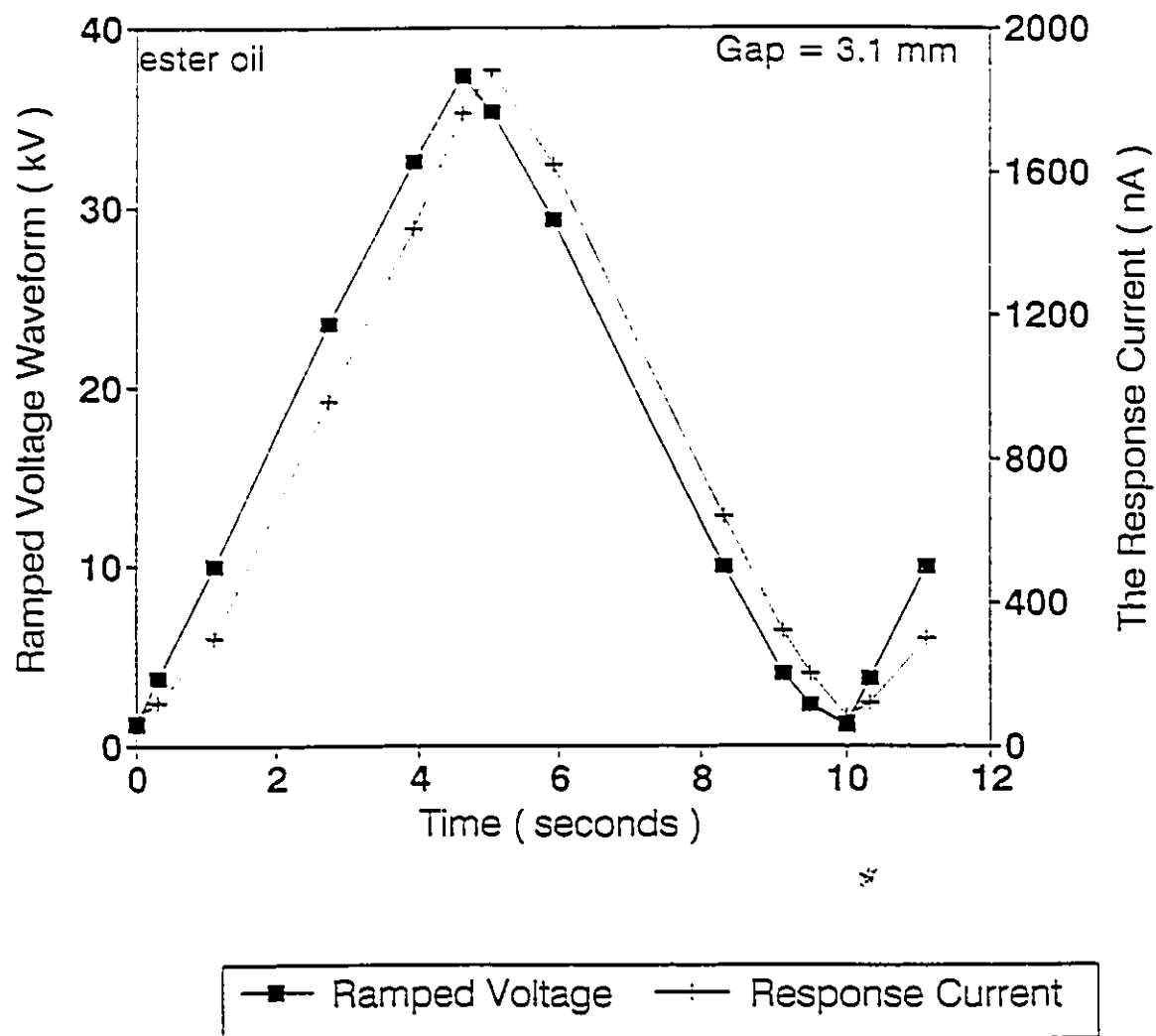


Figure 4.64 The waveform of voltage and current response as a function of time in ester oil

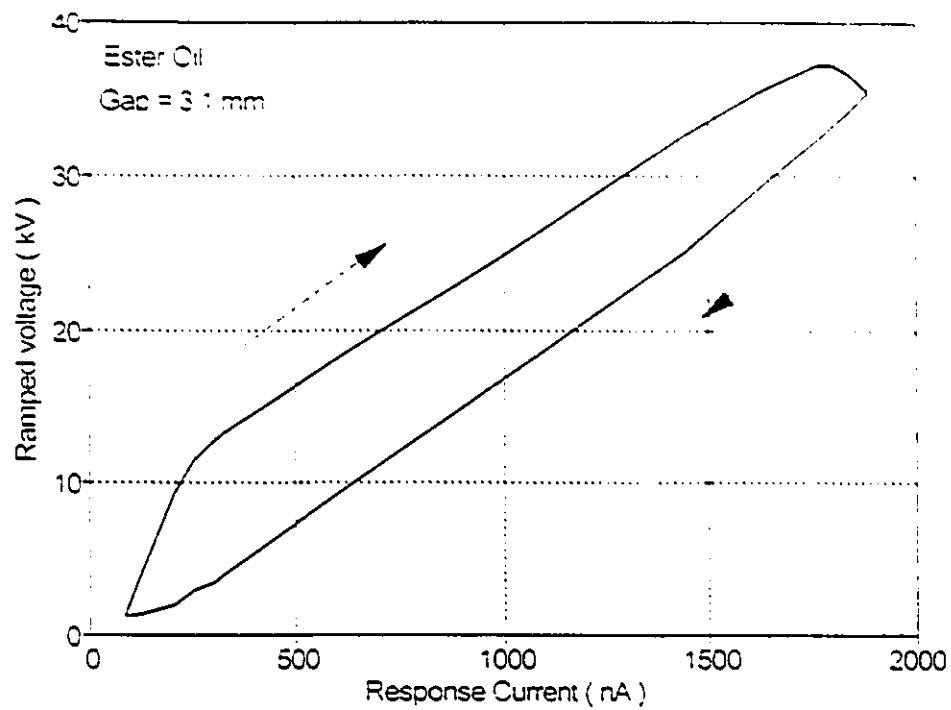


Figure 4.65 The current response loop with the ramped applied voltage in ester oil

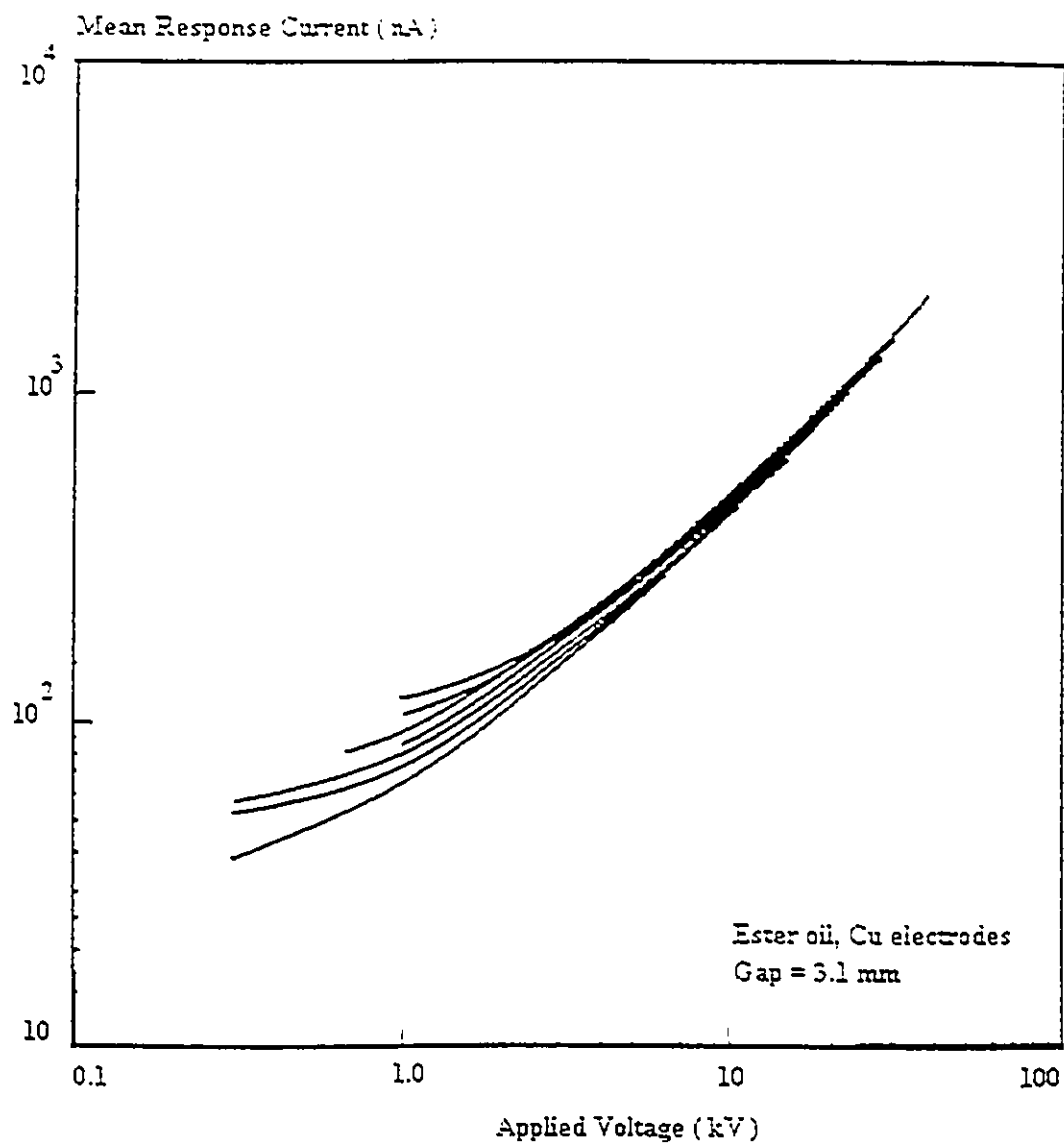


Figure 4.66 Log V-log I of mean current characteristics
with maximum applied voltage in ester oil

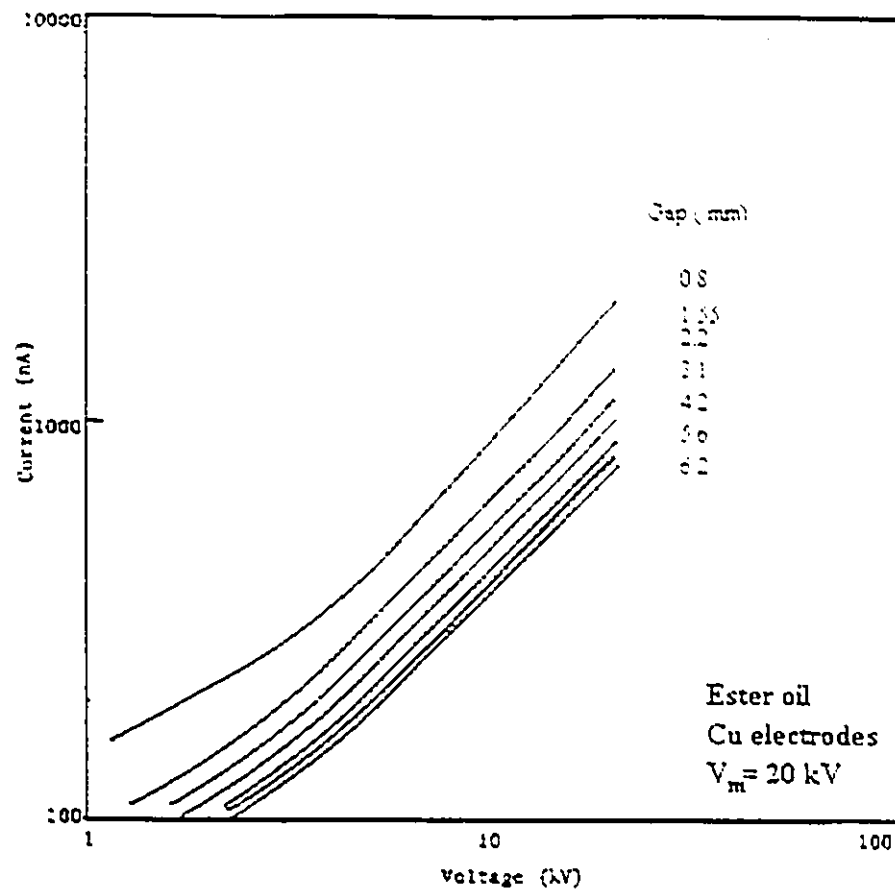


Figure 4.67 Log V-log I of mean current characteristics with gap spacings in ester oil

Figure 4.67 Log V-log I of mean current characteristics in ester oil

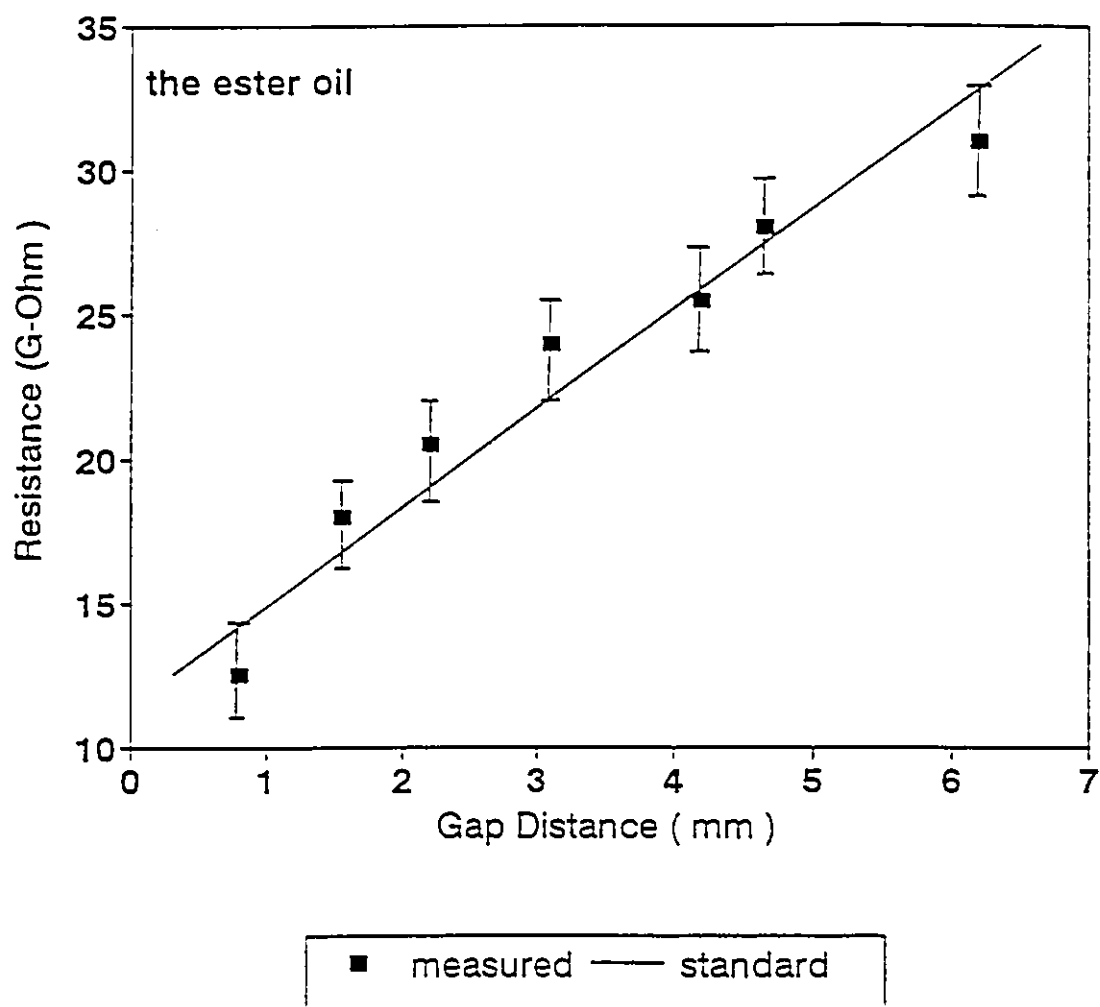


Figure 4.68 The resistance R of the ester oil as a function of gap spacing

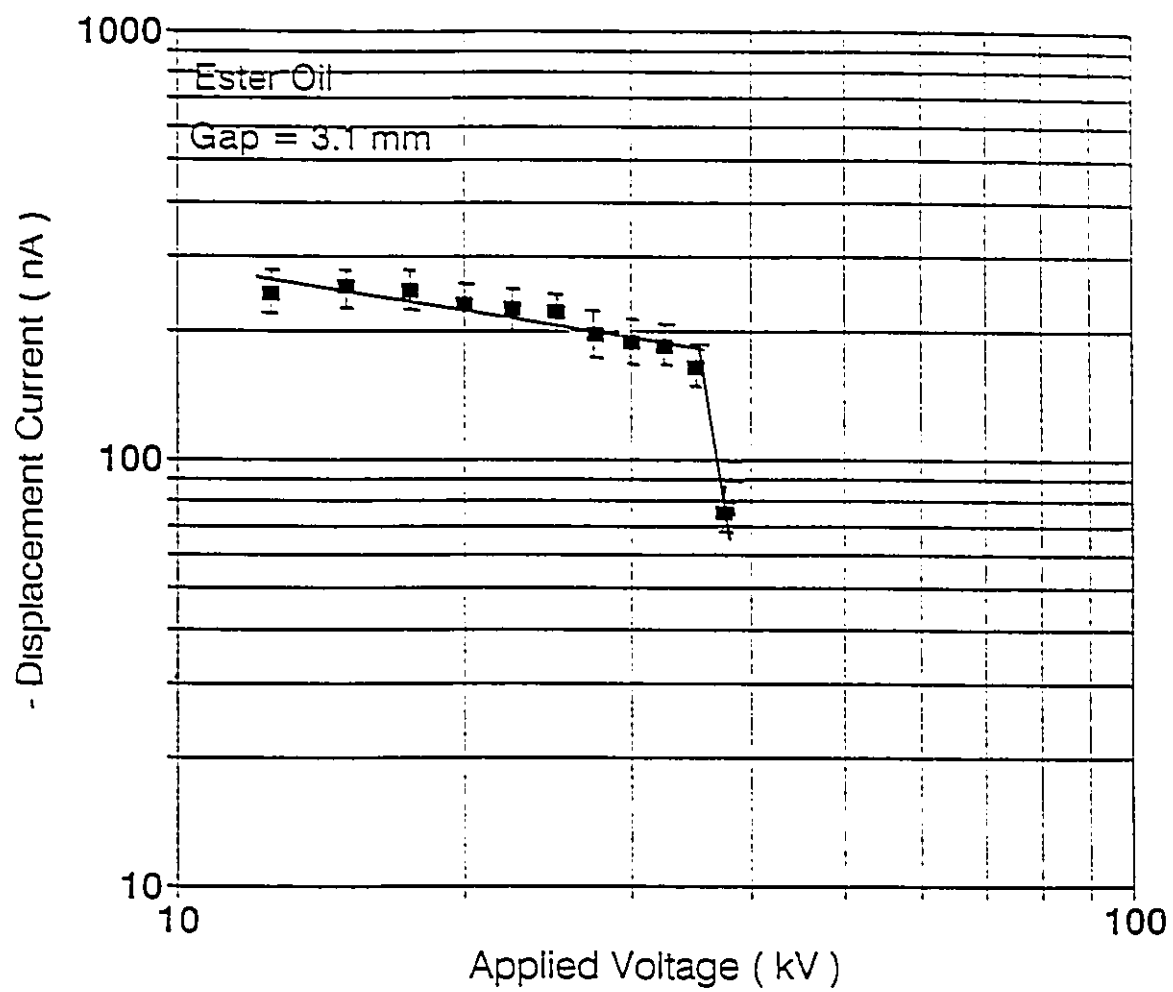


Figure 4.69 The displacement current as a function of applied voltage in ester oil

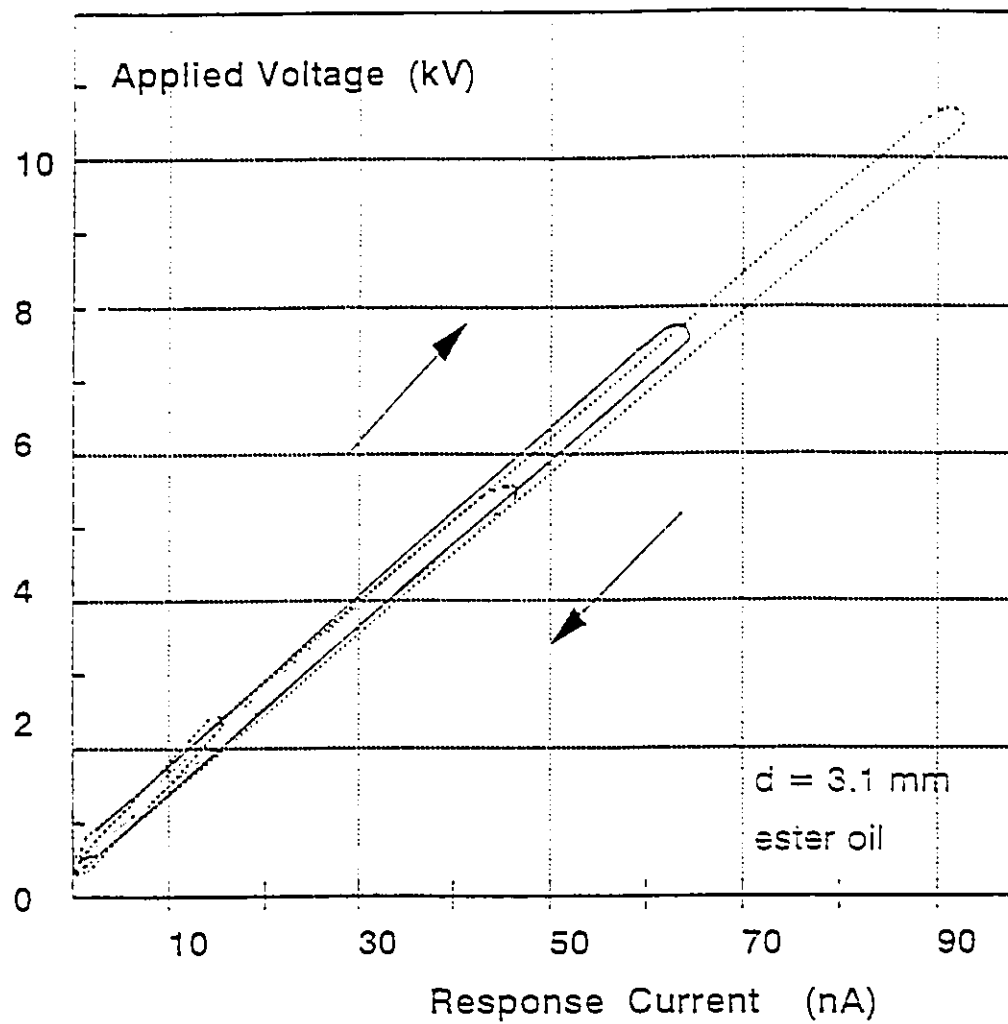


Figure 4.70 The current response loop with the ramped applied voltage in ester oil at lower field stress

4.4 CASTOR OIL, POLYBUTENE AND DODECYLBENZENE LIQUIDS

4.4.1 CASTOR OIL

As mentioned in Chapter III, castor oil is not commonly used in the electrical industry due to its higher dielectric losses and poor frequency response characteristics. Castor oil is considered to be one type of insulating liquid. Thus, castor oil is tested here to be used as a reference to which other insulating liquids are to be compared. A determination of the V-I characteristics of the castor oil and the V-I characteristic curve slope value for various maximum applied voltages are the main goals for the castor oil investigation. The test is made with a 3.1 mm electrode gap separation with a maximum applied voltage ranging from 25 kV to 55 kV respectively. Copper electrodes are used as the cathode as well as the anode. Figure 4.71 gives the V-I loop of the castor oil with a maximum applied voltage at around 40 kV. It shows that the V-I characteristics of castor oil are similar to those of both silicone oil and transformer oil. For the same applied voltage level, the corresponding value of current with the voltage increasing is larger than that for when the voltage is decreasing. More precisely, the V-I loop for castor oil closely resembles that of transformer oil. Although the response current value for castor oil is larger than that of silicone oil and transformer oil, no current turnover phenomenon is observed in castor oil.

Figure 4.72 shows the upper and lower slope values of mean current response as

a function of the maximum applied voltage. The upper slope value seems to change slightly with the maximum applied voltage. The lower slopes are almost constant regardless of the value of the maximum applied voltage. The average value of the lower V-I slope value is approximately $3/2$. This result is very similar to that of silicone oil as well as transformer oil. This is true, even though the response current value for castor oil is much larger than those of the other two oils.

The slope value of the graph of the displacement current as a function of maximum applied voltage is also shown in Figure 4.73. For the displacement current, the lower slope value changes slightly with an increase in maximum applied voltage, while the upper slope value increases sharply under the same conditions.

4.4.2 POLYBUTENE LIQUID

For the same purpose as castor oil, polybutene liquid is also tested as a reference by using the same conditions as used for castor oil. Figure 4.74 shows the V-I characteristic loops with different maximum applied voltages. Polybutene liquid appears to have the typical silicone oil V-I characteristic as shown in Figure 3.6. For silicone oil, as the voltage increases, ie. $dV/dt > 0$, the response current is positive, when the applied voltage decreases, the response current becomes negative. It is interesting to note that for polybutene liquid, the absolute value of the response current as the applied voltage increases is smaller than that for when the applied voltage is decreasing. Thus,

$|I_{up}| < |I_{down}|$ for the same applied voltage level. In contrast to the preceding analysis (see section 3.6), the response loop is shifted to the left (negatively). If that is so, then the displacement current is expected to be negative. First, this result is different from previously tested oils such as transformer oil and silicone oil. Normally, $|I_{up}| > |I_{down}|$ for silicone oil, transformer oil and castor oil. It is suspected that in addition to the response current from the liquid sample, a displacement current is involved in the test circuit. Secondly, the behaviour is also different from that of ester oil or transformer oil after the current turnover phenomenon occurs. As the current turns over, I_{up} is smaller than I_{down} with the same level of applied voltage, both currents are positive as shown Figure 4.65. Thus a positive conduction current still flows through the circuit. In this case, a negative current is assumed to be involved in the test circuit. The corresponding ratio for the residual voltage versus its current is $140 \text{ G}\Omega$, the same level as that for the silicone oil tested.

Figure 4.75 gives the relationship between the slope values of the mean current and the maximum applied voltage. The upper slope value varies a little as the maximum applied voltage is increased while the lower slope value does not change much with the applied voltage. The average value of lower slope value is around 0.8, clearly, it is smaller than that of silicone oil and transformer oil tested previously which has a lower slope value close to 1.5.

The slope values from the graph of the displacement current as a function of the

maximum applied voltage is shown in Figure 4.76. Again, the lower slope value does not vary much with the maximum applied voltage, but the upper slope value clearly increases with an increase in the maximum applied voltage. These results are in agreement with those for the transformer oil (Figure 4.47) tested.

4.4.3 DODECYLBENZENE LIQUID

Like castor oil and polybutene liquid, dodecylbenzene liquid (DDB) was also tested under the same conditions as were the previously described liquids. Figure 4.77 shows the V-I characteristics of DDB for different maximum applied voltages. The value of response current for DDB is double that of castor oil and is over ten times larger than that of polybutene for the same applied voltage level. The V-I loop graph of DDB is very different from those of the other tested liquids as well. The shape of the loops looks similar to that of ester oil, but with a reversed direction of tracing. Thus, like silicone oil, for the same applied voltage level, the current with the voltage increasing is still larger than the current when the applied voltage decreases.

The most unusual characteristic for DDB liquid is that the value of I_{up} is relatively close to the value of I_{down} for the same applied voltage. If the maximum applied voltage is low, I_{up} is nearly equal to I_{down} . Even when the maximum applied voltage was increased to a higher level, a comparison of the mean current i.e. $(I_{up} + I_{down})/2$, to the displacement current, $(I_{up} - I_{down})/2$, shows that the displacement current is almost

negligibly small. This means that the conduction current is the dominant component of the total response current for the high voltage tests for DDB liquid. Moreover, one would expect that the ratio of the applied voltage to the mean current is a constant value. Figure 4.78 shows the mean current versus applied voltage using a log-log scale for DDB liquid for different maximum applied voltages. When the maximum applied voltage level is low such as 30 kV or 40 kV, two divided linear regimes appear in the graph. When the maximum applied voltage increases to 50 kV or 60 kV, only one linear region is observed in the high field portion. Under these conditions, the value of the upper slope is equal to that of the lower slope, thus $s_u = s_l = s = 1.5$. Other than DDB, this phenomenon was only seen in the ester oil experiment. The numeric value for the slope determined from Figure 4.78 was not equal to unity, as would be the case from an almost ohmic response for ester oil.

The relationship between the slope value and the maximum applied voltage is shown in Figure 4.79. It shows very clearly that the values of upper and lower slopes are getting closer to each other as the maximum applied voltage increases. These two slope values are gradually merging to become one as the maximum applied voltage approaches 49 kV. This phenomenon is very important to the insulating liquid investigation. This merging slope value process confirms the hypothesis suggested previously for silicone oil and transformer oil behaviour. Even though the magnitude of response current for DDB is about double that of transformer oil, the merged slope value approaches $3/2$, which is the observed value for transformer oil.

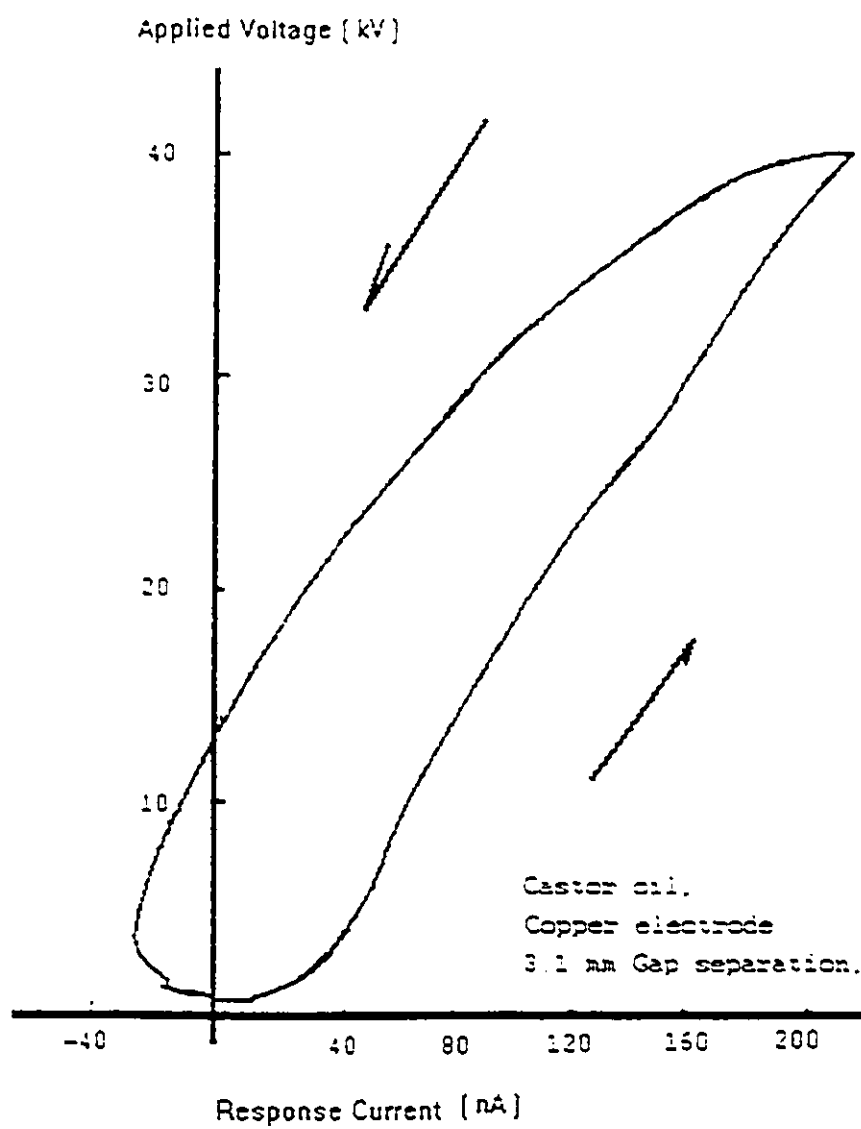


Figure 4.71 The current response loop with the ramped applied voltage in castor oil

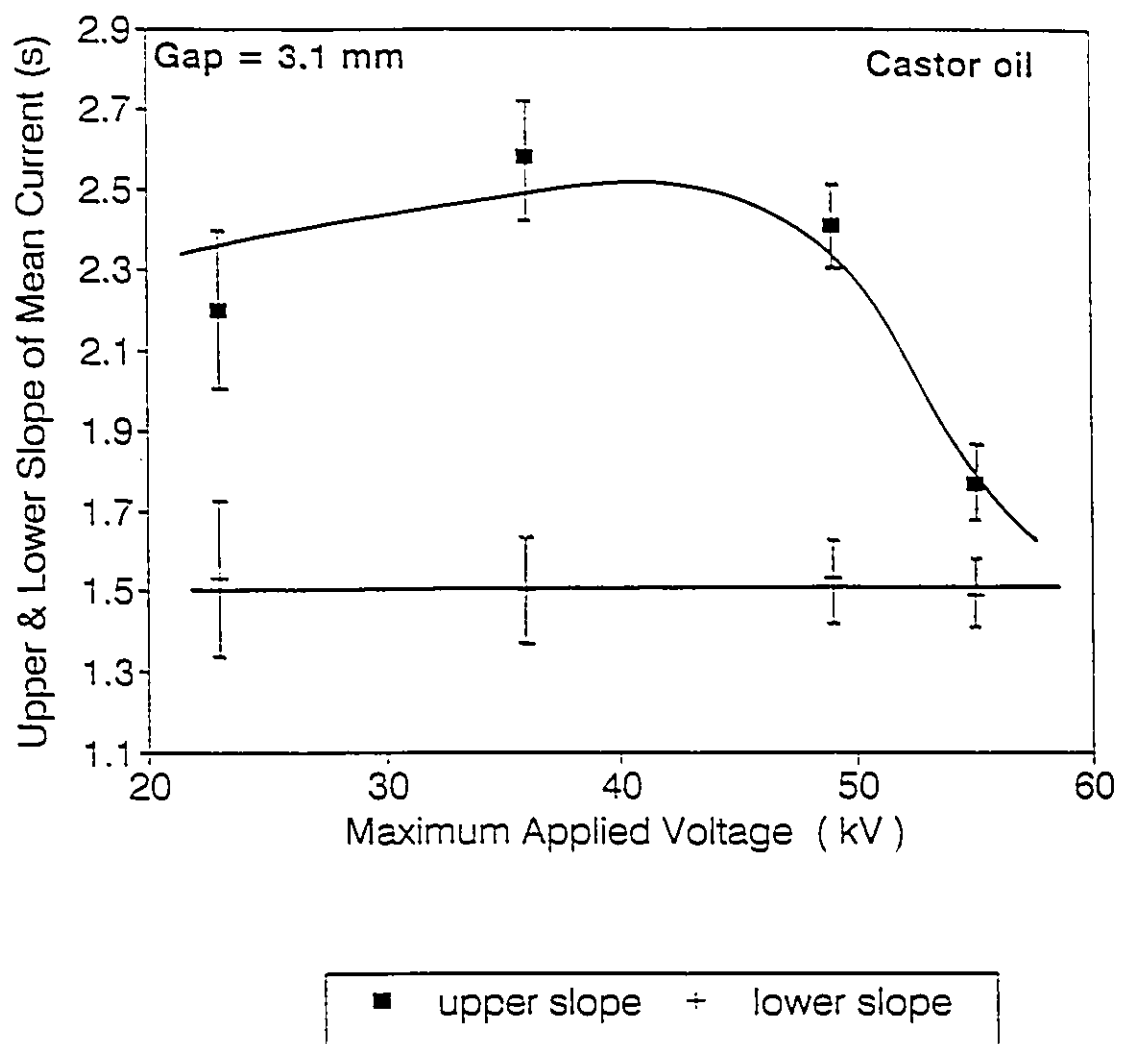


Figure 4.72 Upper and lower slope values of mean current as a function of maximum applied voltages in castor oil

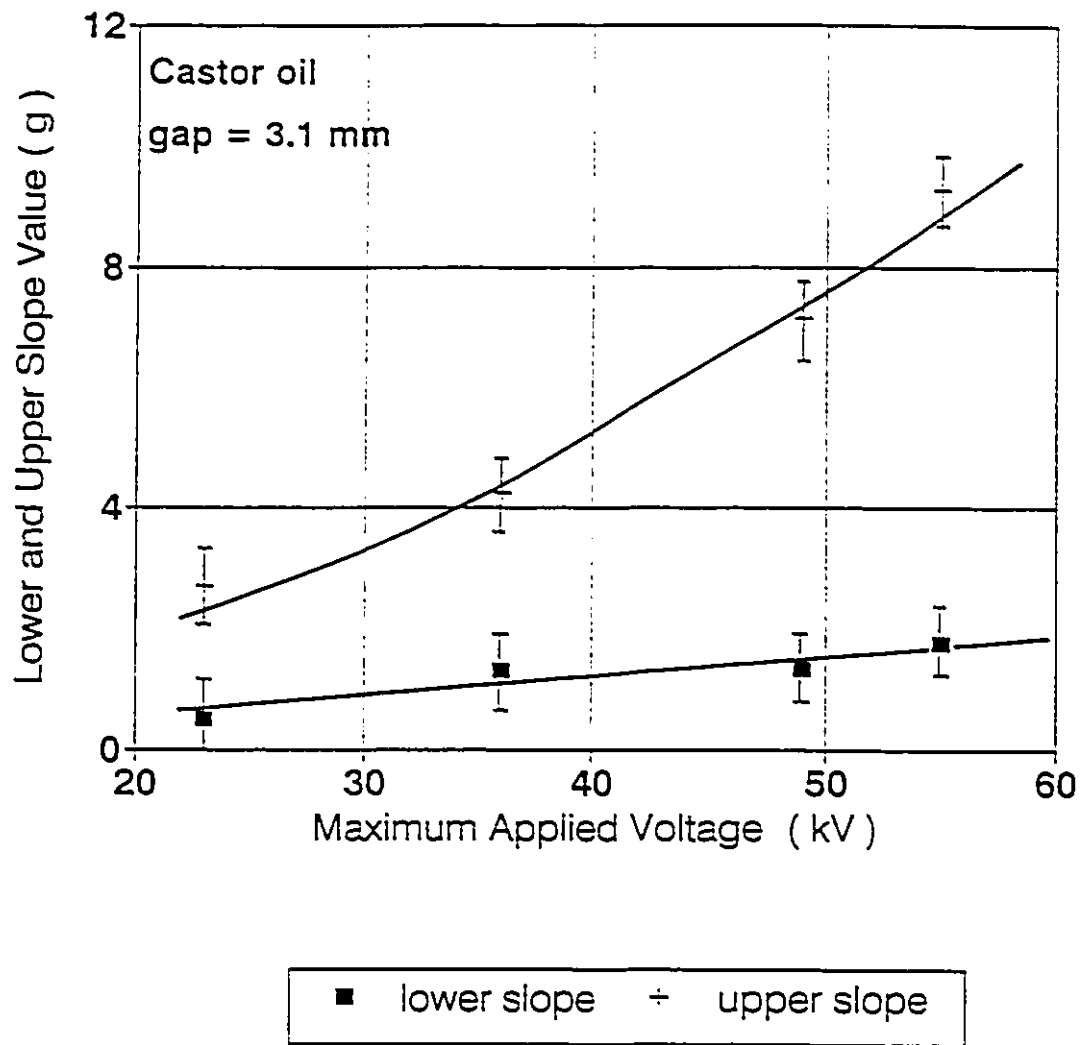
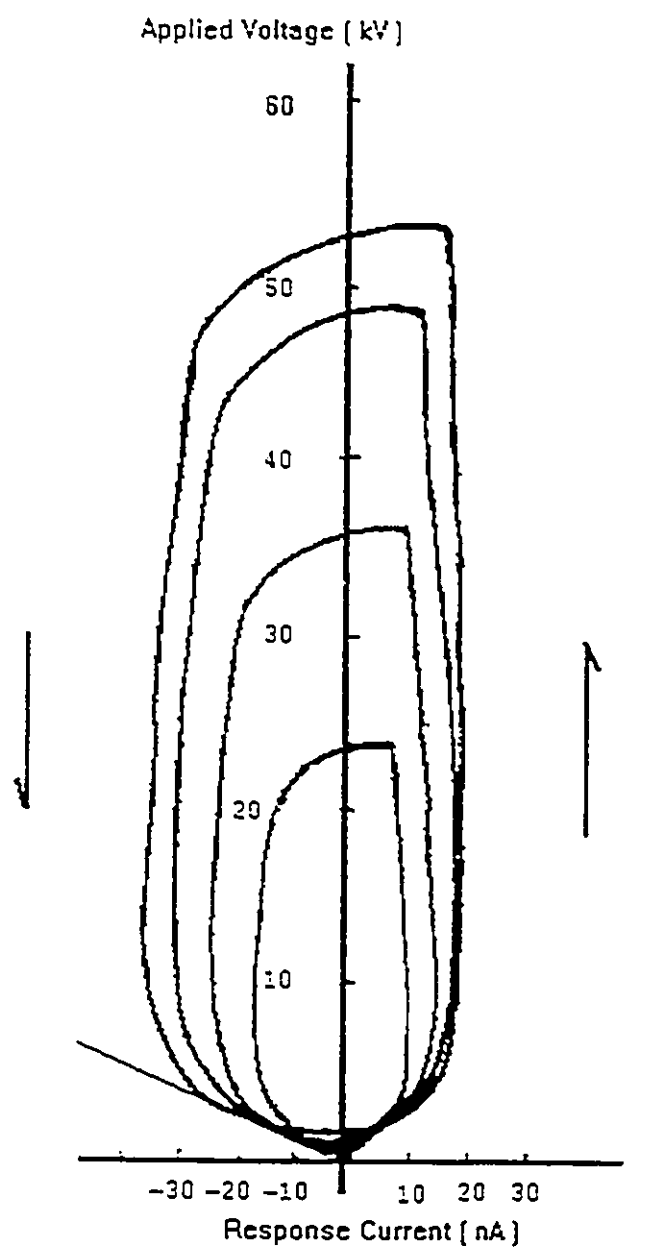


Figure 4.73 Upper and lower slope values of displacement current as a function of maximum applied voltages in castor oil



PolyButene Liquid Copper electrode
 $d = 3.1 \text{ mm}$ gap separation

Figure 4.74 The current response loop with the ramped applied voltage in Polybutene liquid

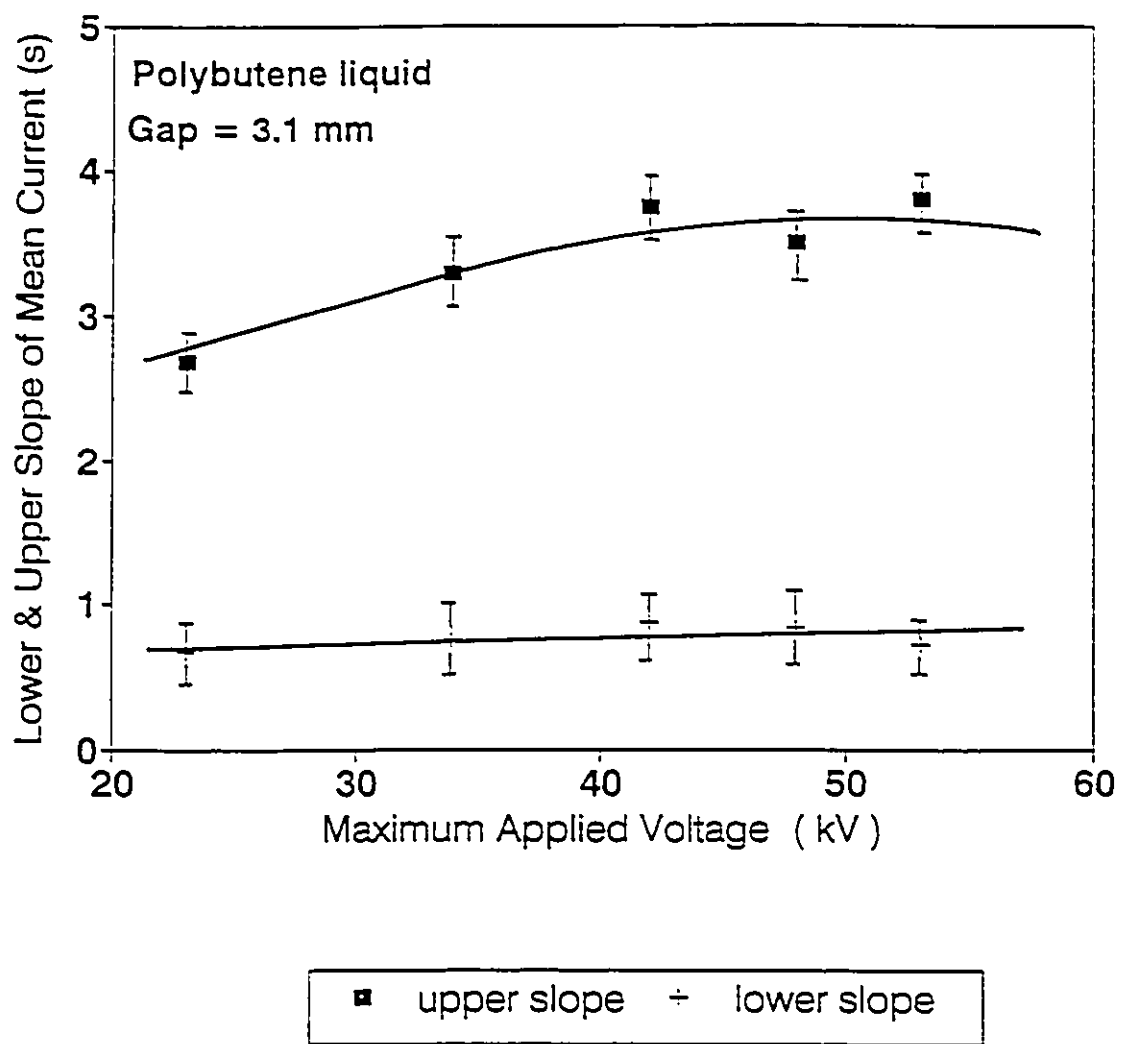


Figure 4.75 Upper and lower slope values of mean current as a function of maximum applied voltage in Polybutene liquid

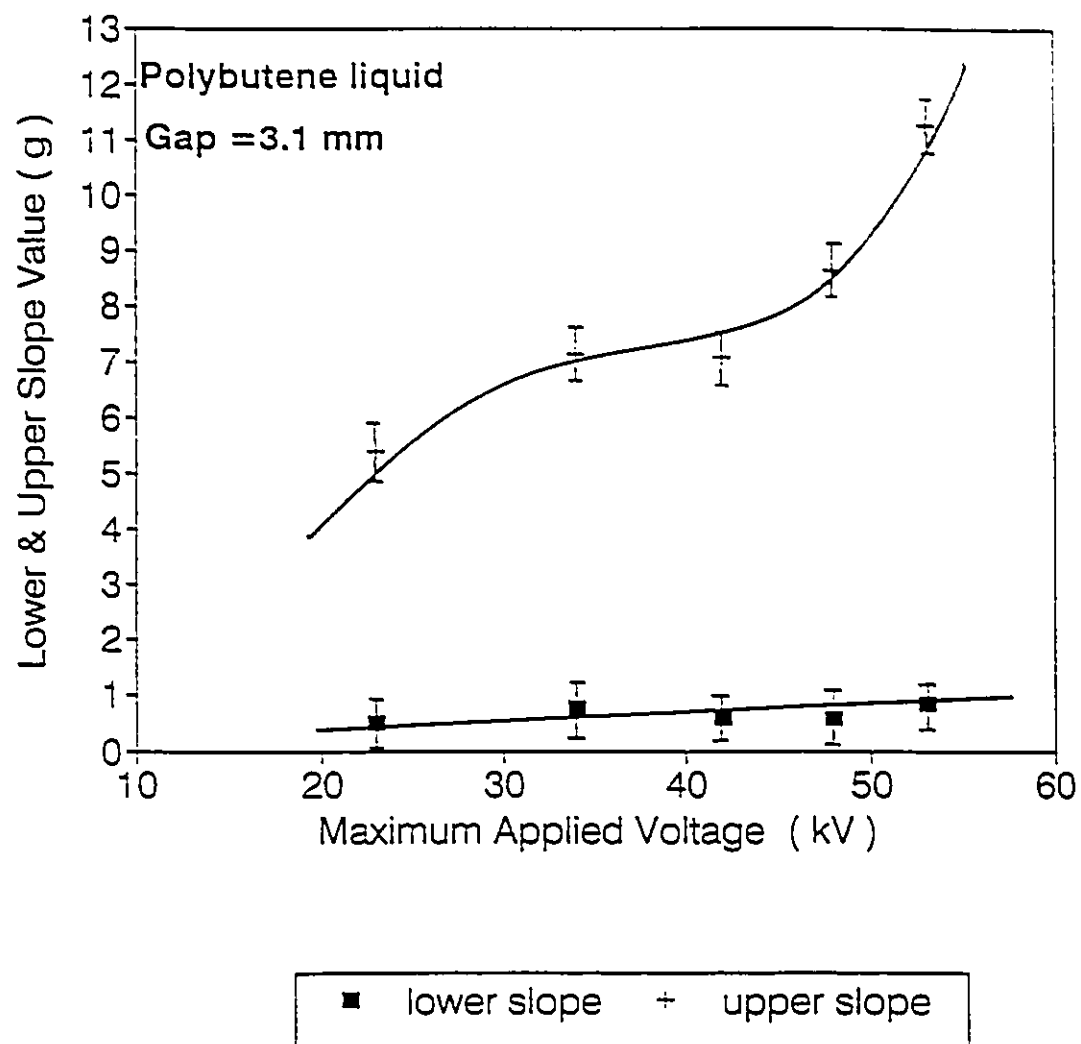


Figure 4.76 Upper and lower slope values of displacement current as a function of maximum applied voltages in polybutene liquid

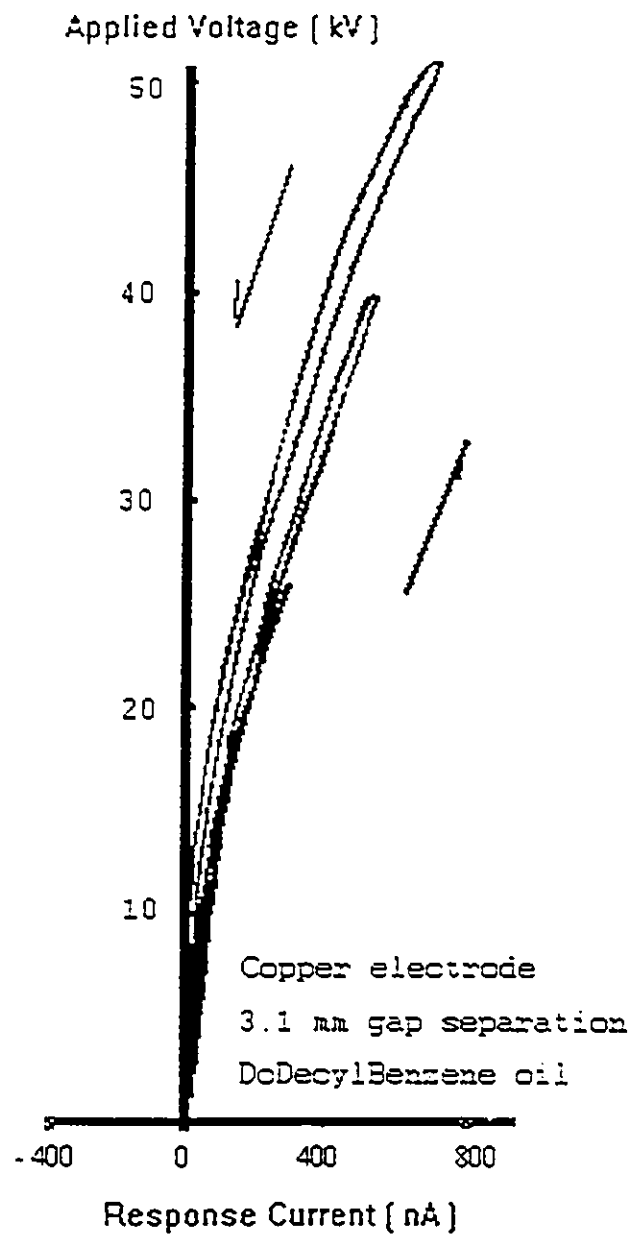


Figure 4.77 The current response loop with differing ramped applied voltages in DoDecylBenzene liquid

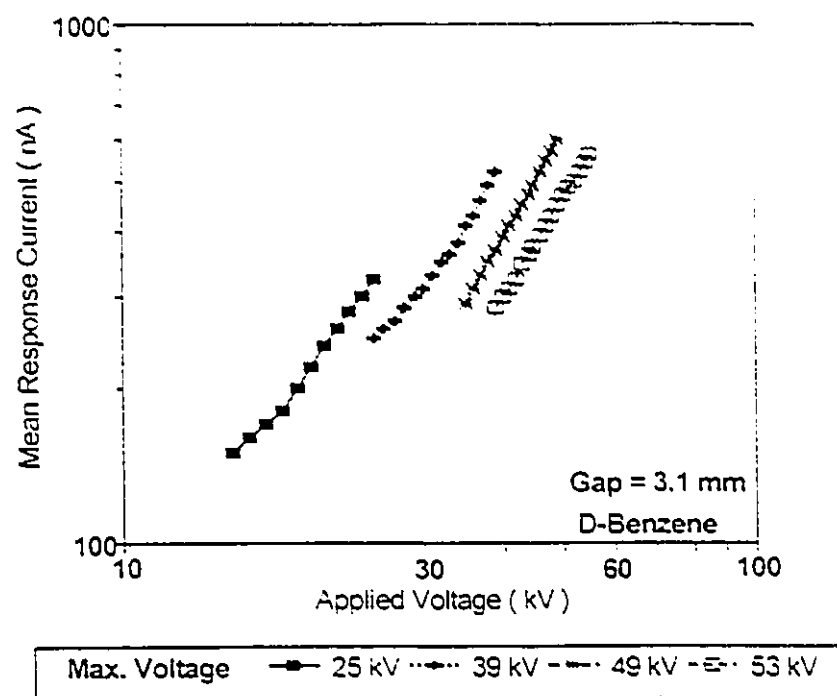


Figure 4.78 Log V-log I of mean current characteristics with different maximum applied voltage in DoDecylBenzene liquid

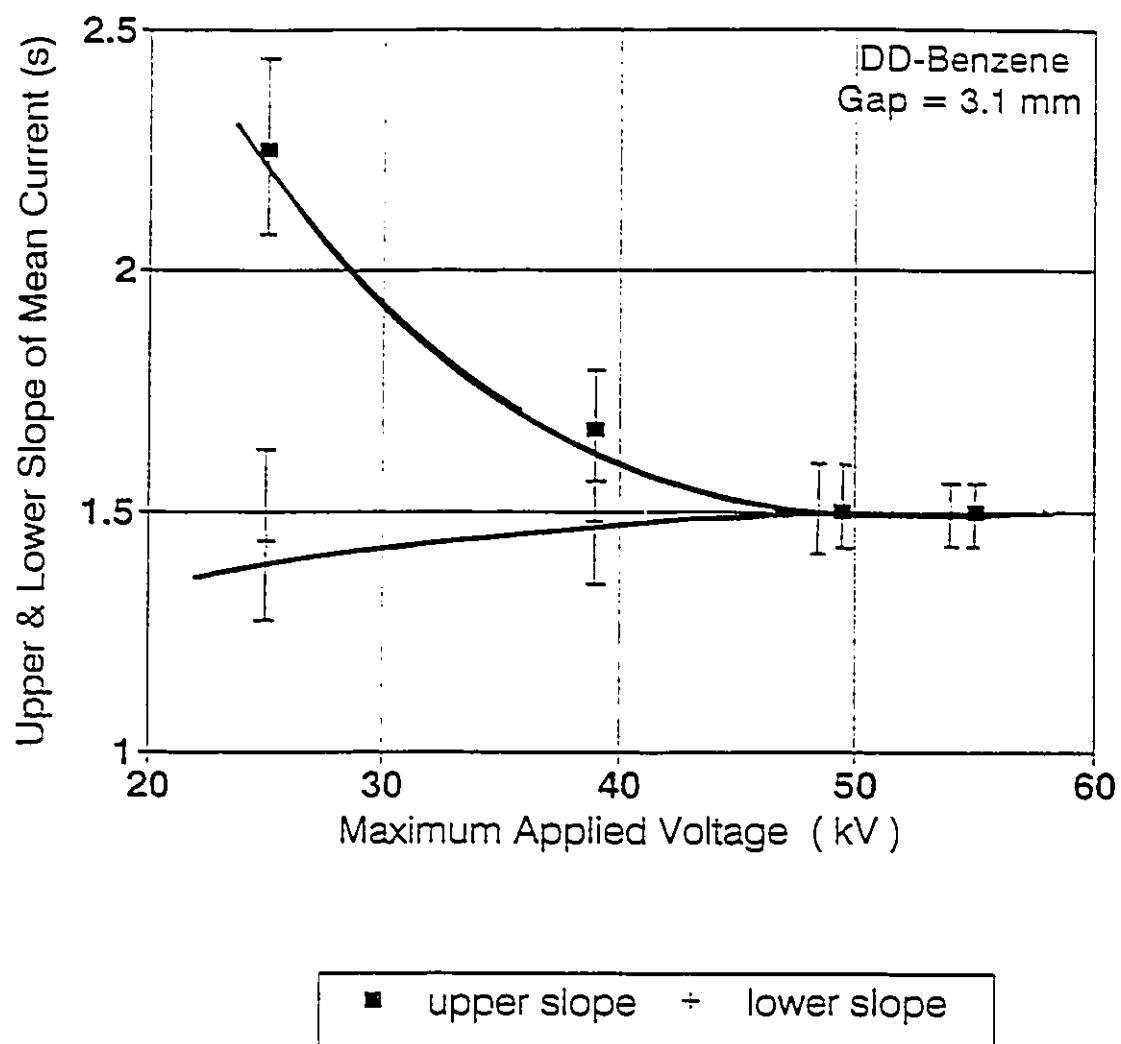


Figure 4.79 Upper and lower slope values of mean current as a function maximum applied voltage in DoDecylBenzene liquid

4.5 SUMMARY AND DISCUSSION OF RESULTS

Dielectric liquids are by no means ohmic conductors. Whenever the applied field exceeds a certain critical value, usually in the range 10 to 100 kV/cm, conductivity rises very quickly with a further increase in voltage. The dependence is sometimes exponential; in other cases, one has rather a law suggesting a space charge limited current. This phenomenon is truly universal, as pointed out by Nikuradse half a century ago [28]. Its mechanism is still controversial, and may well be not at all the same over the entire range of dielectric constants. This has also been proved by the previous experimental results described in this chapter. Thus, the conduction current and space charge current will be considered individually. It should be noted that the conduction and space charge current are not exactly equal to the mean current and the displacement current which are used throughout all the experimental analysis. The value of mean current is the combination of conduction and convection currents. Similarly, the value of displacement current consists primarily of space charge which has been displaced within the fluid as well as at the electrodes. In addition, moreover, there is a voltage variable capacitive current due to electrochemical surface effects. Thus, the mean and displacement current will be used for the analysis of the conduction and the space charge current.

4.5.1 CONDUCTION CURRENT

All of these tests featured a current measuring technique using ramped voltage applied up to a high prebreakdown electrical stress. Most significantly, it has been observed that the maximum excursion of the voltage applied to dielectric oils in a ramp with a fixed rise time plays an important role in determining its current response. The applied voltage and its response current characteristic loops for all six liquids could be sorted in two categories: the clock-wise and counter-clockwise loop, based on the direction of current. The so called clock wise loop occurs when at the same voltage level the current with the applied voltage increasing is smaller than when the applied voltage level is decreasing, such as is the case for ester oil (showing in Figure 4.65). The current-voltage loop is in the clockwise direction. The counter-clockwise loop is the opposite case, in which the current with the applied voltage increasing is larger than that for when the applied voltage is decreasing. These types of oils include silicone oil, castor oil, polybutene and DDB (Figure 3.9 as an example). Transformer oil has a different behaviour when compared with the other liquids tested. It mainly presents the counter-clockwise loop as silicone oil does. Under certain conditions, transformer oil would some times switch from a counter-clockwise to a clockwise loop type at higher electric field levels, this is refereed to as the current turnover phenomenon. In other words, the V-I characteristic for transformer oil has shown both clockwise and counter-clockwise loops at the same time (see Figure 4.28).

Figure 4.80 shows the $\log V - \log I$ plot of mean current versus the applied voltage for all six liquids tested. The response current value of the ester oil is about two orders of magnitude larger than that of the transformer or silicone oil and polybutene liquid, and about one order of magnitude larger than that of dodecylbenzene (DDB) liquid and castor oil under the same test conditions. Even through the V-I characteristics of those six oils have two categories, they have so far still obeyed the equation $I \propto V^n$ at intermediate and high electric fields. The one belonging to the clockwise loop group has one slope value, thus the upper and lower slope values for ester oil are a constant, $s_u = s_l = s$ and has the value 1.040 ± 0.035 through all the experimental conditions.

For the counter-clockwise loop case, the situation is more complicated. Basically both the upper and lower slope values, including transformer oil, change when the maximum applied voltage and gap separation are varied. For silicone oil and transformer oil, the lower slope value slightly increases with an increase in the maximum applied voltage and is close to the value of $3/2$ (shown Figures 4.2 and 4.47,). For castor oil and DDB liquid, the lower slope value is almost constant, with a value of approximately $3/2$, as shown in Figures 4.72 and 4.79. For polybutene liquid, the lower slope value also presents a constant value as the maximum applied voltage is increased but that value is approximately 0.9.

The upper slope value for silicone oil, transformer oil and DDB liquid decreases as the maximum applied voltage is increased (shown in Figures 4.1, 4.34 and 4.79).

More specifically, the upper slope value for transformer oil and DDB approaches $3/2$ as the maximum applied voltage is increased. The upper slope values for polybutene liquid increase slightly with the maximum applied voltage (see Figure 4.75). For castor oil, the upper slope value as shown in Figure 4.72 increases, first when the voltage increases then begins to decrease as the applied voltage is increased further.

It is clear that for both transformer oil and DDB liquid at lower voltage excursions, the $\log V - \log I$ curves show distinctly separate linear regimes. However their slopes vary in an opposite sense as the maximum voltage excursion is increased. The exponents in the two power laws, $I \propto V^n$, are thus functions of the maximum voltage excursion and, ultimately, they blend together at high maximum excursion to exhibit a single slope of $3/2$.

Generally the relationship between the conduction current and the electric field stress for liquid dielectrics in uniform fields is shown in Figure 4.81 [41]. It can be divided into three distinct regions: the low stress region A, in which the current begins to increase linearly with voltage as an approximately "ohmic" type of response. As the field is increased, it comes to the intermediate field region B, and a saturation current will set in. The field level at which this occurs will depend on the ion production rate. The last region is the high field region C. In region C there would then be a more or less exponential form of increase in current with an increasing field, as new sources of charge carriers are introduced.

The main current characteristic of silicone oil (dimethyl siloxane) is recognizably similar to the regions A, B and C. Figure 4.31 is a typical example of the applied voltage and its response current waveforms for silicone oil. It shows that the current does not go too far into the region C before breakdown. The value of the current as well as the breakdown voltage in silicone oil is lower than that of transformer oil. The current turnover phenomenon also appeared in silicone oil, but it was not stable, defined or reproducible. The turnover of the loop was either conditioned out, with the characteristic reverting to the original form after several cycles, or it expanded out of control upon recycling, ending with electrical breakdown at the chosen maximum voltage level.

The slope values for mixed and matched electrode experiments with silicone oil showed no reproducible trend and indeed lead to a suspicion that the process of selecting the value of s may be chaotic. More experiments and detailed analysis will be described in the following chapter.

Transformer oil has a similar V-I characteristic to that of silicone oil in the low voltage regime as shown in Figure 4.31. When raising the maximum applied voltage, the corresponding current sharply increased. The response current will traverse all the regions (A, B, C) of the electrical field. A good example of this current behaviour is given in Figure 4.32. Among the five liquids tested, transformer oil has the highest breakdown voltage value, therefore it can be stressed much further into the high stress regime than can silicone oil. To summarize the gap distance effect as seen in Figure

4.42-4.45, the s_0 increases with an increase in the electrode gap distance while s_1 value decreases at a smaller rate. Similar to silicone oil, the slope values for mixed and matched electrode experiments showed no reproducible trend. Moreover, the turnover phenomenon of transformer oil represents a transition from a single to a double loop response. It indicates, paradoxically, that the displacement current component has reversed. The turnover phenomenon occurring above the threshold coordinate has been found in all four of Cu, Al Mg and Zn electrodes. When the $\log V - \log I$ characteristic is plotted, its slope is undisturbed by the turnover phenomenon.

The current characteristic is very different for the ester oil. As shown in Figure 4.66, the relationship between the current and voltage does not exhibit the regions B and C and hence there is no current saturation. The conduction current for the ester oil increased linearly with the applied voltage from the lowest voltage until almost breakdown. For this reason there is no threshold point in the $\log V - \log I$ characteristic of the ester oil as shown in Figures 4.66 and 4.67. Both slope values remain constant regardless of the electrode gap distance. For ester oil however, the current and voltage waveforms are almost identical and current is clearly seen to lag the voltage. Thus the time varying current and voltage in Figure 4.64 can be expressed by,

$$I(t) = \frac{V_m}{5R}(t - \tau), \quad (t > \tau) \quad (4.13)$$

where V_m is a maximum applied voltage value, t is a time in seconds and τ is the time lag and R is the equivalent resistance. When the gap separation is 3.1 mm, τ is given

by 0.35 ± 0.05 s and R is about 22 G Ω . Paradoxically, the current response in this case lags the voltage and thus the system behaves as though it were an inductor.

The current characteristics of castor oil are very similar to those of silicone oil as shown in Figure 4.71. In comparison to Figure 4.81, castor oil does not have a clear saturation region B at the intermediate field region. Instead, the mean current continually increases with the applied voltage as in region A. It is understood that the ion production rate in the liquid is high enough to show the changes indicated as described in reference [6]. Since the C region which under the high electric field exists only when a new charge source is developed and is compatible with the original current. The current characteristics of castor oil shows a small C region at higher field levels. The new charge source mentioned above is not large enough to account for the ion production required for a significant increase in the original current level.

The voltage - current loop of polybutene liquid, shown in Figure 4.72, also has the same pattern as that of silicone oil. The log V -log I curve of mean current of polybutene is located very close the magnitude to those of silicone oil and transformer oil as shown in Figure 4.81. The three regions, especially the regions B and C for polybutene liquid are very clearly presented in Figure 4.81. The flattened curve is almost a straight line. Thus, it is the most flattened V -I curve of all of the six liquids tested. One could state that polybutene liquid is a good insulation material at medium electric field levels, based on the previously mentioned information. The ion production

rate for polybutene liquid in region B is very low. Thus, when the electric field increases to the levels found in region C, the conduction current increases sharply which indicates a new charge source is involved.

When comparing dodecylbenzene (DDB) liquid to the other liquids previously mentioned, it has the second largest conduction current level of all, just below that of ester oil. DDB liquid has only one slope value existing in the intermediate and higher field region when the maximum applied voltage is high at 40 kV or 50 kV. Thus, there is no saturation region B nor a high field region C for DDB when compared to the general field and the conduction current patterns. It is understood that when subjected to an electric field, the DDB liquid can produce enough ions to keep the conduction current continuously increasing with an increase in the applied voltage.

4.5.2 DISPLACEMENT CURRENT

As an electrical analog to any dielectric liquid, the electrical behaviour in the most general case can be compared to that of a capacitor and resistor connected in parallel. This circuit, consisting of electrical components, models the electrical behaviour of a dielectric material. This method has already been used to analyze the experimental conditions described in Chapter III, section 3.7, as shown in Figure 3.15. In general, the resistor, R , contributes to the conduction current, the capacitor, C , whose value relates to the space charge and electrode condition, provides the displacement current.

The resistor and capacitor are such that electric potential across them is dependent on the electric stress, especially when the applied voltage is very high, close to the liquid breakdown level.

However, the total capacitance, C , is dependent on two separate capacitors which are connected in series, is given by Equation 4.14:

$$\frac{1}{C} = \frac{1}{C_H} + \frac{1}{C_D} \quad (4.14)$$

C_H is the capacitance from the stored charges in the region between the metal and the first layer of the double layer (Helmholtz layer). C_D , results from the diffuse charge layer [32]. The value for C_D is dependent upon the charge source in the dielectric liquid. The value for C_H has a close relationship with the electrode material and inner layer condition. The capacitance C_H is highly dependent upon the amount of charge on the electrode (q_M) in the inner Helmholtz layer, and the amount of contact-adsorbed ionic charge (q_{CA}) in the Helmholtz outer layer. The general expression for the interface capacitance for a Helmholtz layer is as follows in Equation 4.15 [32],

$$\frac{1}{C_H} \propto \frac{dq_{CA}}{dq_M} \quad (4.15)$$

The capacitor, C_H , is constant when $dq_{CA}/dq_M = 0$, that is when there is no change in the number of contact-adsorbed ionic charges (q_{CA}) with a change in the charge on the

electrode (q_M).

The variation in capacitance with the potential difference across the interface is the macroscopic expression of the variation of the molecular structure of the interface. It must be understood that the capacitance is dependent on the rate of growth of the number of contact-adsorbed ions and its change with the excess electric charge on the metal (described in section 3.2.1). Double layer theory for two simple parallel layers permits the description of the structure of the interface in terms of the two regions described above. The inner Helmholtz plane (IHP) region, has a low dielectric constant corresponding to almost fully oriented water. This water concentration is very important because water molecules which are highly polar are drawn to the electrodes surfaces and form double layers there. The outer Helmholtz plane (OHP) region, has a high dielectric constant corresponding to partially oriented water. The migration of an ion through the double layer involved chemical interaction, interaction with the electrical field arising from the electrode charge, and lateral interaction with an already settled population of contact-adsorbed ions. Thus, the number of contact-adsorbed ionic charges (q_{CA}) in the OHP is, as a matter of fact, related to the charge on the electrode (q_M) in the IHP. The relationship between contact-adsorbed ionic charges, q_{CA} , and the charge on the electrode q_M can be written as:

$$\ln q_{CA} \propto k_2 q_M - k_3 q_{CA}^{3/2} \quad (4.16)$$

where k_2 and k_3 are constants.

When a voltage is applied, the simple two capacitor model indicates the nature of the associated disturbance. In response to this disturbance the additional electrode charge accumulates first. Ions then start to adsorb on contact with the electrode and populate the inner Helmholtz layer (IHP). The charge q_{CA} grows as the electrode charge becomes more positive. As q_{CA} increases further, the lateral repulsion term from Equation 4.15 increases in significance. It reduces the slope dq_{CA}/dq_M in Equation 4.15, thus, it slows down the rate of growth of the population of contact-adsorbed ions. The electrode charge encourages the growth of the population of contact-adsorbed ions, but this growth sets up and accentuates the lateral repulsion forces which try to inhibit further growth as shown in Figure 4.82. The electrical forces of attraction give rise to lateral repulsion forces which in turn produce the capacitance versus applied voltage characteristic curve appearing in Figure 4.82. Figure 4.82 also indicates that as the potential increases even further, eventually the capacitance value will become a constant again.

The particular value observed for the total capacitance C , therefore, predominantly depends upon the electrode surface material, (a semiconductor in this case, as described in Chapter III), the electrode interface condition, the ionic concentration in the liquid, and the applied voltage value. When the ion concentration in the liquid is large, the value of C_D becomes large, while the value C_H does not change significantly. From Equation 4.14, the second term, hence, becomes small when compared with the first, and thus:

$$C \approx C_H \quad (4.17)$$

the capacitance C is effectively equal to the capacitance in the Helmholtz region (layer). This means that most of the charge is squeezed on to the Helmholtz layer and very little charge is scattered diffusely into the solution in the diffusion layer.

When the value of C_H is such that it dominates the total capacitance, one would expect that the water molecules are in contact with the charged electrode. It is assumed that a certain number of water dipoles are adsorbed on the electrode. There are two limiting conditions on the relation between the charge on the electrode and the orientation of the dipoles relative to the surface of the metal. One condition arises on an electrode which has a high positive charge, for example when charging the dielectric liquid in this case. The electric-field vector is pointed away from the metal into the solution. In the presence of an external electrical field, dipoles reduce their potential energy by aligning themselves so that the dipole vector becomes parallel to the field. In other words, the water dipoles flip up so that the oxygen atoms are in contact with the electrode and the hydrogen end of the water molecule points into the solution as shown in Figure 4.83.

The other limiting condition occurs when electrons are pumped into the electrode to make it very negatively charged which appears like discharging in this case. The flipped-up dipoles will turn around and flip down. In the flip-down state, the hydrogen atoms are facing the electrode and the oxygen atom is toward the solution as shown in

Figure 4.84. This phenomenon in which the water molecules flip-up and flip-down is the so called flip-flop model. This flip-flop model for water turns out to be of consequence at the electric interface [32].

Contrary to the flip-flop models at sufficiently low ion concentrations in such a dielectric liquid, C_D is much smaller and $1/C_D \gg 1/C_H$, thus:

$$C \approx C_D \quad (4.18)$$

This means that more charges are driven from the Helmholtz layer into the diffusion layer, and fewer charges remain in the Helmholtz layer. The electrified interface has become in effect a diffusion layer in structure with the space charge density smeared out into the bulk fluid. When C_D and C_H are comparable, the full double layer structure is necessary to describe these phenomena.

The space charge and space charge effect in dielectric materials has also been reviewed in Chapter II section 2.3. To explain the formation of space charges at the electrodes, it is assumed that each of the positive and negative ions in the liquid is surrounded by a cloud of molecular dipoles. These dipole clouds prevent the ions from approaching the electrodes sufficiently close enough to be immediately neutralised. The resulting accumulation of charges considerably enhances the field in the vicinity of the electrodes, thus increasing the neutralisation probability from field injected electrons. A dynamic equilibrium is reached when the rate of arrival of ions is equal to their rate of neutralisation.

It is possible to divide insulating liquids into two groups. One is heterocharge liquids for which the charges formed in the vicinity of each electrode are opposite in sign to the charge of the electrode. As a result, the electric field is enhanced at both electrodes and depressed in the central region between the electrodes [32]. Another group is the homocharge liquids for which the charge has the same sign as those of the electrodes. The electric field is reduced at both electrodes and enhanced in the central region. Previously reported experimental results have led to the following classification [41]. The heterocharge liquids are most likely to be formed in general, as dry liquids with low viscosity. The homocharge liquids are found among the high viscosity dried oils. When heterocharge liquids are moist, homocharges as well as heterocharges appear. In other words, both heterocharge and homocharge may appear under certain conditions.

The displacement current for silicone oil has been studied extensively by Esendal and Watson [6,9]. Silicone oil is considered to be a very good insulating liquid. The ionic concentration in the liquid is sufficiently low that the diffuse-charge region capacitance C_D is smaller than that of the capacitance of the Helmholtz region, C_H . Hence, at low or intermediate field levels, the value of $1/C_D$ is larger in comparison to the value of $1/C_H$ and $C \approx C_D$. This indicates that the effects of the ions in the liquid will be dominant over the other effects. In Chapter III it has been shown that for silicone oil, the experimental results are different depending on whether the tested liquid was filtered or not. The vacuum filtration processes necessarily involves some partial removal of impure water molecules and thus imparts to the dielectric liquid a low

impurity ion level. As the applied voltage rises higher, more charges will appear in the interface region, i.e. the electrode charge is the main charge source for silicone oil. Even though C_D is also expected to vary, the change is small. In other words, the impurity and ionic charges control the response current in silicone oil. If this is true, the electrode material should not have much effect upon the displacement current. The experimental results agree with this assumption. To summarize as shown in Figure 4.5-4.7, the inverse lower slope value increases slightly as the electrode gap distance increasing while the upper one as being nearly constant. The effect of the electrode material on both slope value is not quite clear at this moment.

Both slope value decrease with an increasing in the electrode gap distance. As the applied voltage increases, in transformer oil C_D increases continuously due to the ionic double layer composed of impurity water molecules in the liquid. Assuming that the value for C_H does not change as much as the value of C_D does, it follows that C_H begins to be comparable in magnitude to C_D under those conditions. The total capacitance C is then considered C_H and C_D in a series connection. The response current of transformer oil begins to show some difference from that of silicone oil. How the value of C_H changes will depend upon the charges in the Helmholtz layer, especially to the number of impurity (water) and water dipoles in the flip-flop state. When C_H is large enough to influence C significantly, the condition of water molecular orientation in the double layer becomes important. The current turnover phenomenon is a typical example of such a situation. Under the conditions when a certain number of water dipoles in the

transformer oil are absorbed on the charged electrode, the water dipoles will be in the flip-up state (Figure 4.83). This could be treated as a homocharge condition in the dielectric liquid (Figure 2.6), in which the electric field is reduced at the electrode as a result. After the applied voltage reaches same characteristically high value, the water dipoles flip-down. According to the flip-flop model [32] this would turn the water dipoles from being in a homocharge situation to assuming a heterocharge condition where the electric field is enhanced at the electrode. As a result, more charges are produced as the voltage decreases than when the voltage increases at the same potential level. Thus, this is the reason for the turnover phenomenon occurring.

The oxide layer covering the cathode surface becomes charged when in contact with a double layer as described above. In this case the associated space charge capacitance dominates the electrical properties of the double layer system. Figure 4.86a is drawn representing the effective capacitance as a function of applied voltage and is obtained from Figure 4.46 by calculating the value of C (the effective capacitance) from the displacement current by division by dV/dt . This now closely resembles the functional form given by Bockris and Reddy [32] (Figure 4.86b). Their graph however gives the semiconductor-capacitance, C_{sc} , as a function of potential drop across the semiconducting layer. This implies that there is an electronic cloud analogous to the ionic cloud adjacent to an electrode in solution with respect to the space charge and the potential drop inside the semiconductor. There is a difference however between such examples and the graphed data of Figure 4.86a. In the present case capacitance beyond the turnover point

is effectively negative. Below turnover the capacitance is positive and displacement current arises from electron injection which annihilates a homocharge polarization (shown in Figure 4.83). Such polar orientation of impurity water molecules at the interface is unstable in a sufficiently strong electric field and will flip-flop as explained above, changing the whole electrical structure of the region as is evident at the turnover point. This implies that there is an electronic cloud analogous to the negative charge cloud adjacent to an electrode in solution. Thus the curve of Figure 4.86b which is concave to the abscissa will be transformed into one which is convex to the abscissa (Figure 4.86a).

Figure 4.86a shows the functional form of the variation of system capacitance with the applied voltage. This is very similar to that given by Bockris and Reddy [32] shown in Figure 4.86b indicating the variation of capacitance per unit area of cathode surface with potential drop across the semiconducting film and double layer. Compatibility between these curves is possible by assuming a value for the area of cross section of current injection together with a relationship between double layer potential and the applied voltage in the present situation. This however depends upon the assumption of the same value of semiconductor intrinsic carrier density (i.e. 10^{13} - $10^{16}/\text{cm}^3$). The electrodes used here are of copper and the oxide layers of such have been investigated in vacuum [47], the result being $2.54 \times 10^{13}/\text{cm}^3$, thus justifying this assumption. Thus scaling the applied voltage in Figure 4.86a to conform with the micropotential scale of Figure 4.86b the factor dividing the macro scale will be around 3×10^4 . Thus dV/dt for the micro capacitor C will be reduced by this factor and $C =$

3×10^4 . Thus dV/dt for the micro capacitor C will be reduced by this factor and $C = I/(dV/dt)$ will be multiplied by 3×10^4 . Thus in comparing the system capacitance with the value given by Bockris and Reddy the value obtained from experiment will be in the 10^{-8} F range, comparing closely with C_{∞}/cm^2 if the injection area of cross section is 1.2 cm^2 . This result is also compatible with the corresponding value of cross section area obtained for Di-iso-octyl-phthalate liquid (ester oil) analysis (section 4.3).

For ester oil, the response current value is the highest among the results of all six tested liquids. The waveform of the current is similar to that of transformer oil after the current turnover. The ester oil was tested without being vacuum filtered and ester oil has a high water absorption level. All of this indicates that there is a strong water dipole flip-flop model phenomenon on the electrodes with ester oil. In other words, the number of water dipoles adsorbed on the electrode dominates the total response current and its characteristics. This is considered to be the reason for the abrupt change in the $\log V$ versus $\log I$ characteristic.

The analytical interpretation of the behaviour of castor oil is very simple as it has the same V-I characteristic as silicone oil. Impurities therefore in the castor oil dominate the total response current. Polybutene liquid also has a similar V-I characteristic to that of silicone oil. Figure 4.74 shows that Polybutene liquid is almost a perfect dielectric material, yielding capacitors having almost zero losses. With the same voltage value, the charging current (the current when voltage is increasing) is very close to that for

when the voltage is decreasing (discharging) with an opposite polarity.

An interesting characteristic of Polybutene liquid is that the absolute value of the discharging current is larger than that of the charging current. So far this phenomenon has not been fully understood. One possibility is that the charge and discharge circuits for the capacitor (dielectric liquid) are different. Assume that the capacitor is C, the capacitance of the dielectric liquid with no electric losses, R represents a leakage resistor connected in parallel with C, r is a resistance connected in series with the power supply which represents the internal resistance for a non-ideal power supply and the protection resistance for the circuit. Figure 4.85 illustrates this simplified RC circuit diagram, where switch positions 1 and 2 show the circuit in the charge or discharge condition respectively. When charging the capacitor, the current i_2 which passes through the capacitor is written as:

$$rRC \frac{di_2}{dt} + (R+r) i_2 = 0 \quad (4.19)$$

Let R_t be the value of R and r connected in parallel, $\tau = R_t C$, thus i_2 is

$$\text{Charge condition:} \quad i_2 = \frac{E}{r} e^{-t/\tau} \quad (4.20)$$

As switching to the position 2 for discharge of the capacitor, i_2 then is expressed as:

$$\text{Discharge condition : } i_2 = - \frac{E}{R_t} e^{-t/\tau} \quad (4.21)$$

The difference between the charge and discharge current of capacitor is the difference between r and R_t for charging and discharging respectively. Since $R_t = R \parallel r$, therefore, $R_t < r$ and the value of charging current is smaller than that of the discharging current. It is also suspected that there are some negative ions in the liquid which behave like bipolar heterocharges involved in the circuit as seen in Figure 2.6 in Chapter II.

Dodecylbenzene (DDB) liquid is different from other oils mentioned above. The V-I characteristic loop looks like that of ester oil but it is traced out in the same direction as for silicone or transformer oil (count clockwise). Figure 4.77 shows that the current when the applied voltage is increasing is almost equal to the current when the applied voltage is decreasing. The conduction current is much larger than the displacement current. As the displacement current is negligible, the equivalent (total) capacitance is no longer important in this case. Thus, the voltage-current relationship is considered as a non linear resistance due to the fact that the slope value, s , is 1.5 instead of unity.

The characteristics of those four out of the six tested oils have so far obeyed the equation $I \propto V^s$. As with the mean current, the upper and lower slope values of displacement current exponent g for transformer oil, silicone oil, castor liquid and

Polybutene liquid change when the maximum applied voltage and gap separation are varied. The displacement current for ester oil is opposite in sign in comparison to the others. The displacement current has a linear relationship with applied voltage. The slope value for ester oil therefore, is a constant under all the experimental conditions and has a value close to unity. The displacement current for DDB is so small that it is negligible when compared to its conduction current. If there is any displacement current, the slope values for DDB should be similar to that of the ester oil except positive in sign.

4.5.3 MAGNETIC FIELD EFFECTS

It is clearly indicated that there is a magnetic field effect for both the upper and lower slope values in transformer oil. This agrees with the results of previous work with silicone oil [5.8] using the same experimental technique. The characteristics of transformer oil exposed to a transverse magnetic field also obeyed the equation $I \propto V^s$. Moreover, the upper and lower slope values of s for transformer oil change when the maximum applied voltage and gap separation are varied. As the magnetic flux density increases both the upper and the lower slope values increase up to a magnetic flux density at about 150×10^{-4} T then decrease as the magnetic flux density increases further (figure 4.53). The slope value yields a loop which is concave to the abscissa when plotted as a function of magnetic flux density. Moreover, the upper slope value also clearly shows a similar curve as the electrode gap distance increases with a 20 kV maximum applied voltage level. The slope value plot becomes less curved and more

straightened as the maximum applied voltage increases as shown in Figure 4.54. At the 50 kV voltage level, the upper slope values increase steadily as the electrode gap distance increases. The lower slope values exhibit a similar relationship with gap separation but smaller in magnitude when compared with the upper slope value. The lower slope values decrease slightly at the 20 kV, 40 kV and 50 kV voltage levels instead of increasing as in the upper slope case except for the 30 kV range (Figure 4.56).

In comparison with the results from the silicone oil experiment (350×10^{-6} m²/s) [5] as shown in Figure 4.86 with a magnetic flux density of 200×10^{-4} T, the upper slope value is smaller for silicone oil, and the shape of the graph plot is also different. It has been reported that the magnetic field effect could cause either an increase or decrease in the current due to the variation in the collision frequency between mobile charges and the liquid molecules [44]. According to the power law in Equation 4.1, at the same applied voltage level the current will be increased if the s value is increasing. The prebreakdown experimental results therefore, for transformer oil agree with a similar phenomenon that Secker and Hilton [46] reported for hexane from their breakdown tests results. The results from transformer oil at 3.1 mm gap, 50 kV range for example, show that s_u and s_l increased 12-17% and 16-20% respectively as magnetic flux density varied from 20 to 150×10^{-4} T but 12-17% and 27-33% decrease between 150 to 250×10^{-4} T.

There is no previous report of the magnetic field influence on displacement current. Clearly, results from transformer oil tests indicate that the magnetic field effect

influences the slope value of the displacement current more directly than that of the conduction current especially for the upper slope value g_u . The g_u and g_l of displacement current for an applied voltage of 20 kV decreased 25-52% and 35-63% respectively as the magnetic flux density increased to 150×10^{-4} T, then had a 30-60% and 15-30% increase between 150 to 250×10^{-4} T. Both the upper slope g_u and lower slope g_l curves are convex to the abscissa when plotted as a function of magnetic field density which is just the opposite result from that of the s_u and s_l results which show curves concave to the same axis. Thus the result of adding the magnetic flux density is a substantial increase in conduction current and at the same time results in a decrease in the displacement current in the liquid for magnetic flux density less than 150×10^{-4} T. At magnetic flux density levels greater than 150×10^{-4} T, the conduction current begins to decrease while the displacement current starts to increase with an increase in the magnetic flux density.

Since conduction current arises from the motion of injected charges while displacement current is due to annihilation of double layer polarization at the electrode, it is not surprising to see that the impact on both of these currents as a result of the presence of a magnetic field is different. The results can be interpreted as follows. According to Watson [90] it happens that

$$g-s = \sqrt{U^2-1} \quad (4.22)$$

where $U \propto (T^*/T)^{1/2}$, this being the temperature of energetic free electrons normalized

with respect to the ambient temperature.

It is quite conceivable that U may be strongly dependent on magnetic flux density B . Watson showed that U can be very large or quite small [90]. If then B affects a large U strongly then $g-s$ from Equation 4.22 shows that U and g may then strongly vary with B while s would be much less so. On the other hand, if B influences a small U then $g-s$ is almost zero and $g+s$ will exhibit the magnetic effect almost equally, hence $g+s$ would be almost independent of magnetic flux density. Previous workers [44] measured total current under d.c conditions in which case the current component (in the present case, the displacement current) from double layer polarization annihilation would appear as part of the sum of conduction current and displacement current. If then $g+s$ were to be almost independent of magnetic flux density then such total currents as were observed would now be unlikely to show much effect. It is significant that polar fluids will produce double layers and thus demonstrate magnetic field effects as has been reported in reference [44].

Magnetic effects such as have been observed here are most likely to arise from some kind of Hall effect influencing free electrons during their short period (about 100 ns [89]) at liberty before being retrapped. The cyclotron frequency is about 2.8×10^8 Hz if choosing $e = 1.6 \times 10^{-19}$, $m = 9.1 \times 10^{-31}$ kg and $B = 100 \times 10^{-4}$ T. The remarks above, however, suggest that flux density may also influence the temperature of this population. A detailed theory of this has yet to be developed.

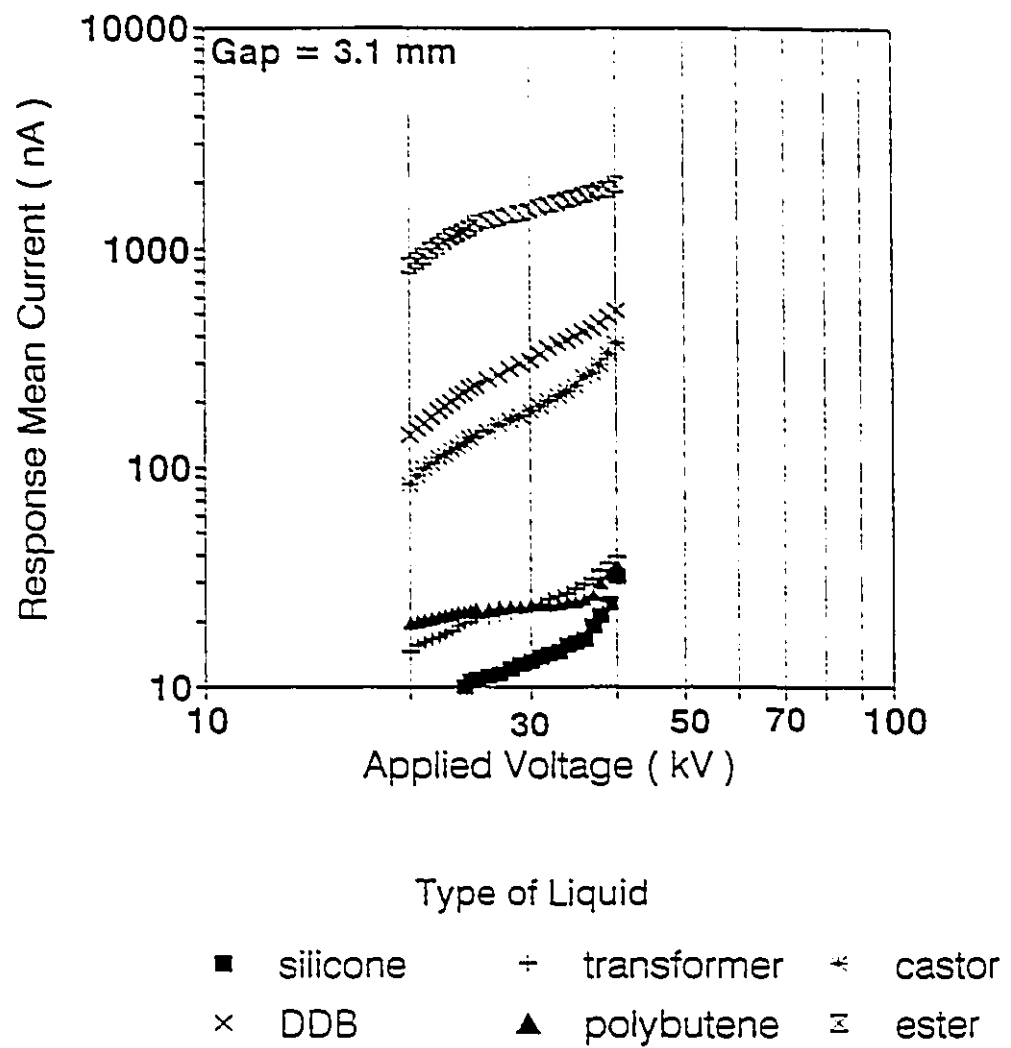


Figure 4.80 The upper slope values of mean current with maximum applied voltage in six dielectric liquids

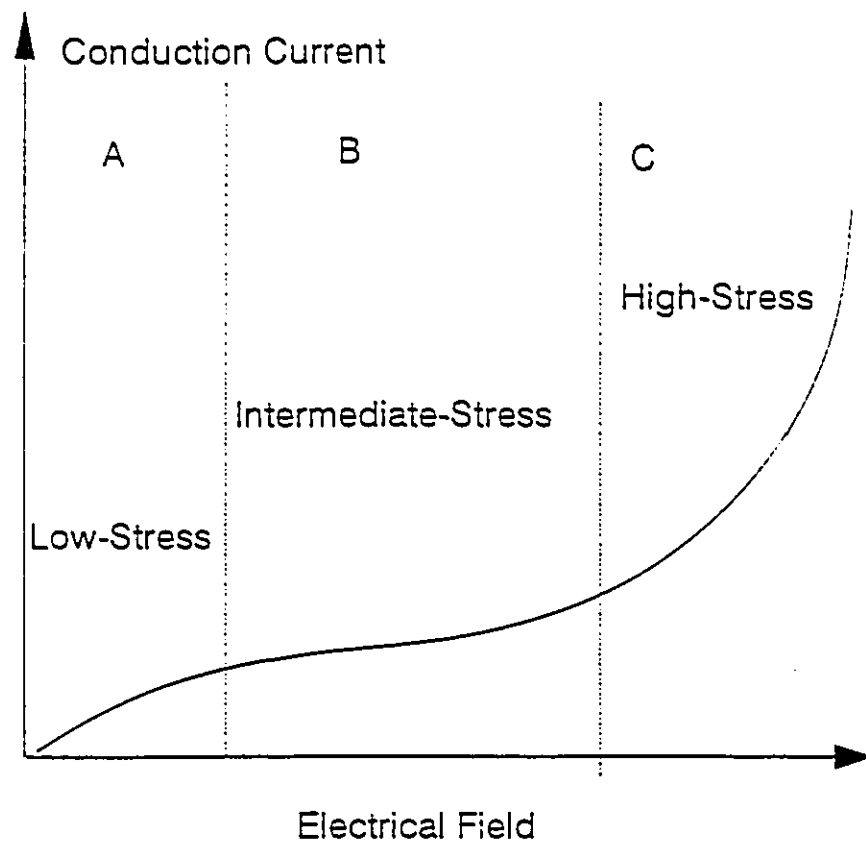


Figure 4.81 General relationship between current and field strength for liquid dielectrics

Differential Capacitance

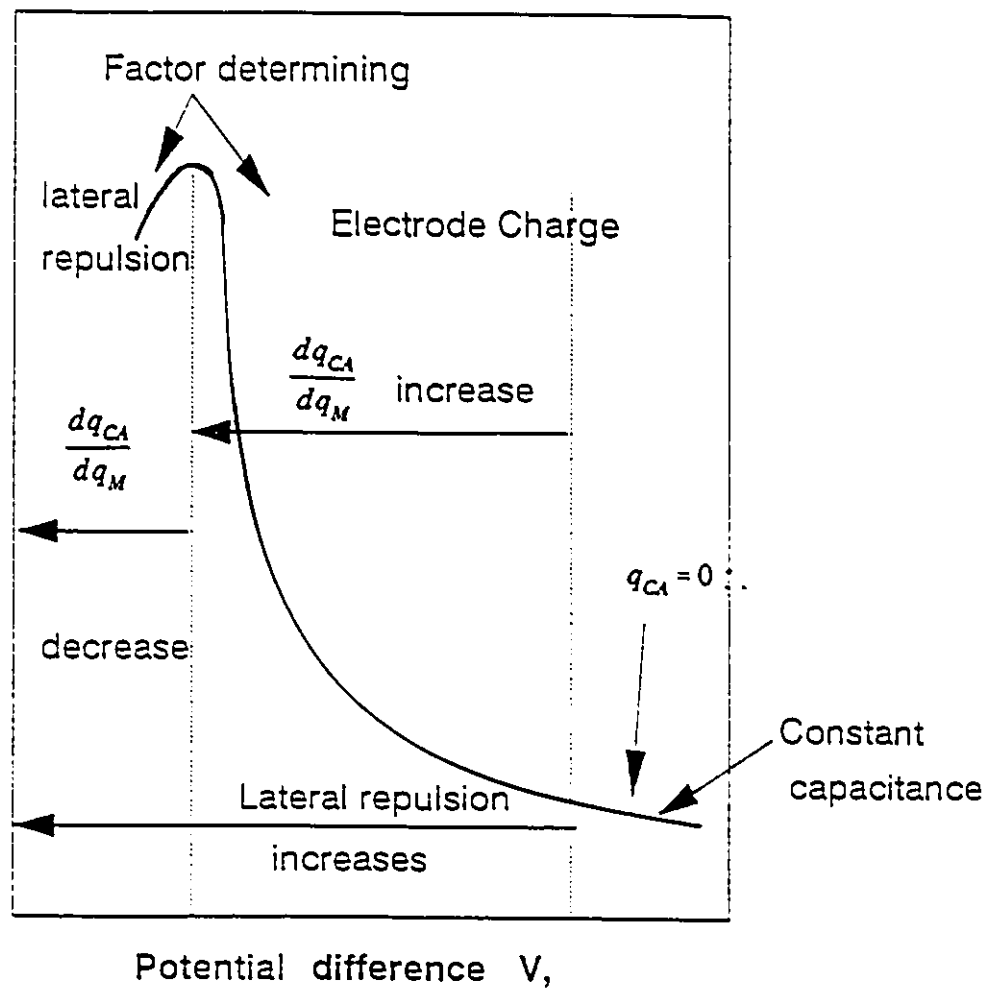


Figure 4.82 The lateral-repulsion model for the capacitance-potential curve

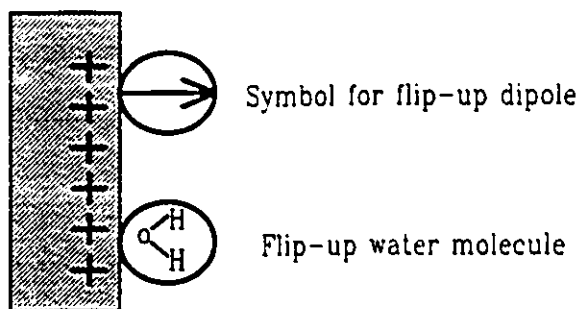


Figure 4.83 The flip-up orientation of a water molecule on an electrode

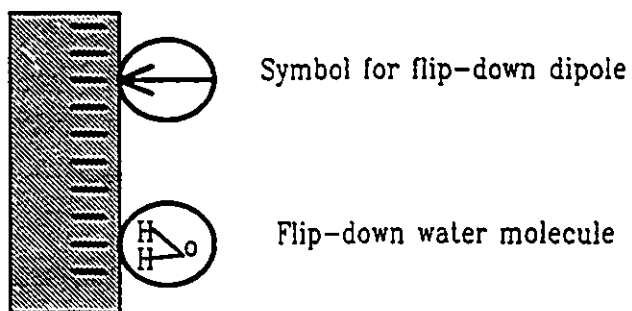


Figure 4.84 The flip-down orientation of a water molecule on an electrode

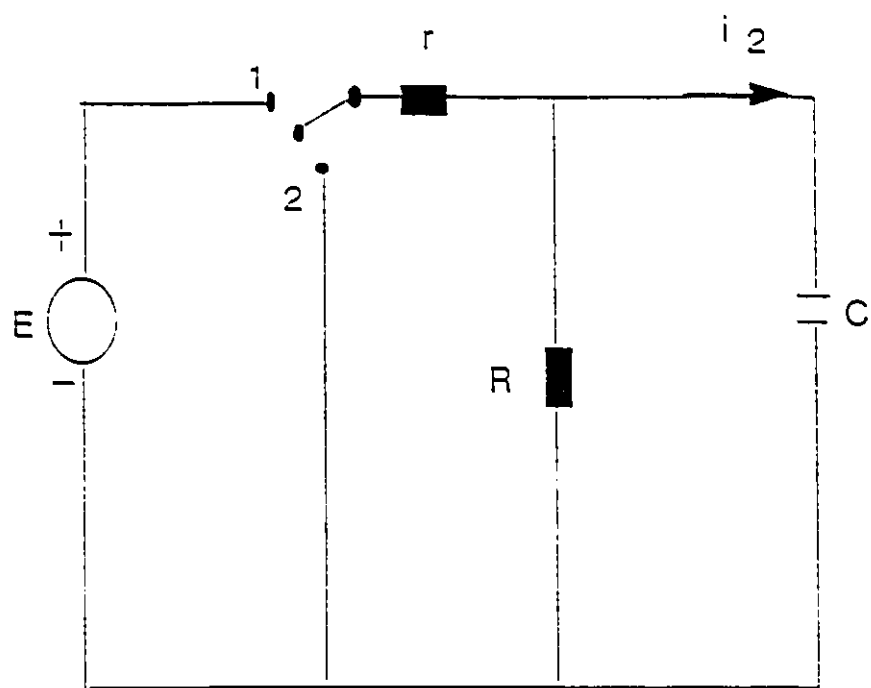


Figure 4.85 The RC charging and discharging circuit

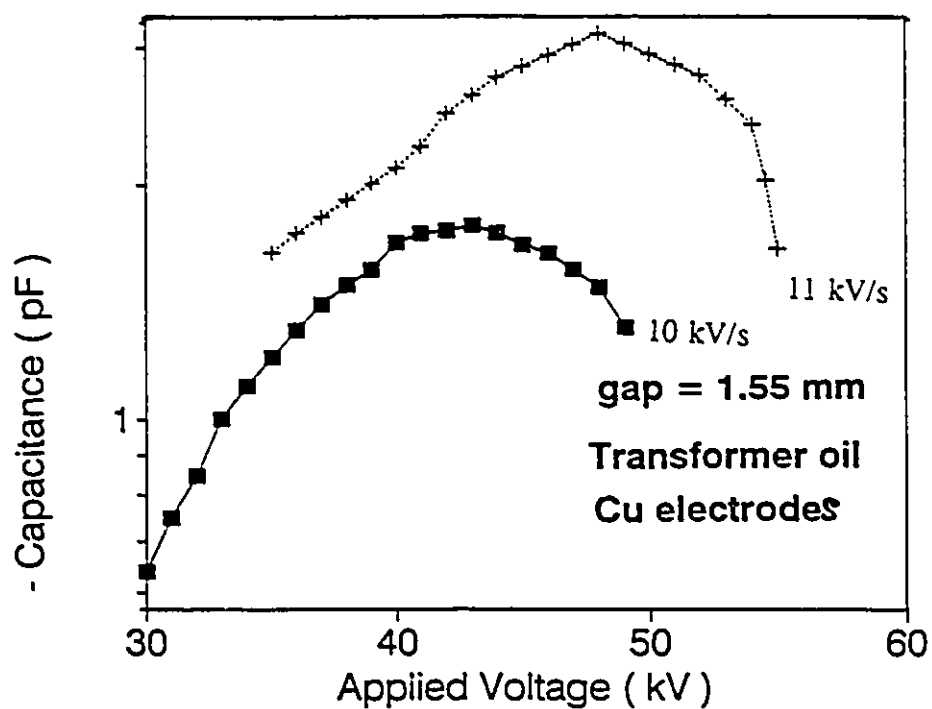


Figure 4.86a Effective capacitance as a function of cathode to anode gap voltage

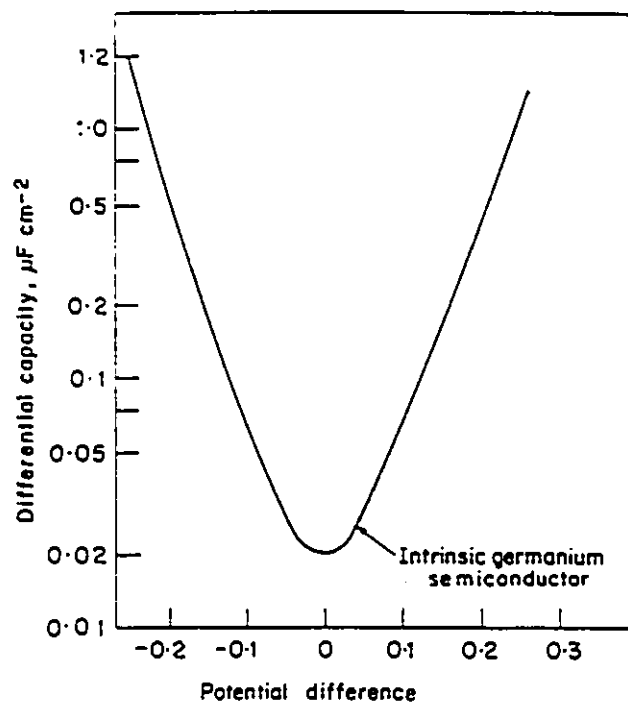


Figure 4.86b The capacitance of a semiconductor-electrolyte interface as a function of the potential

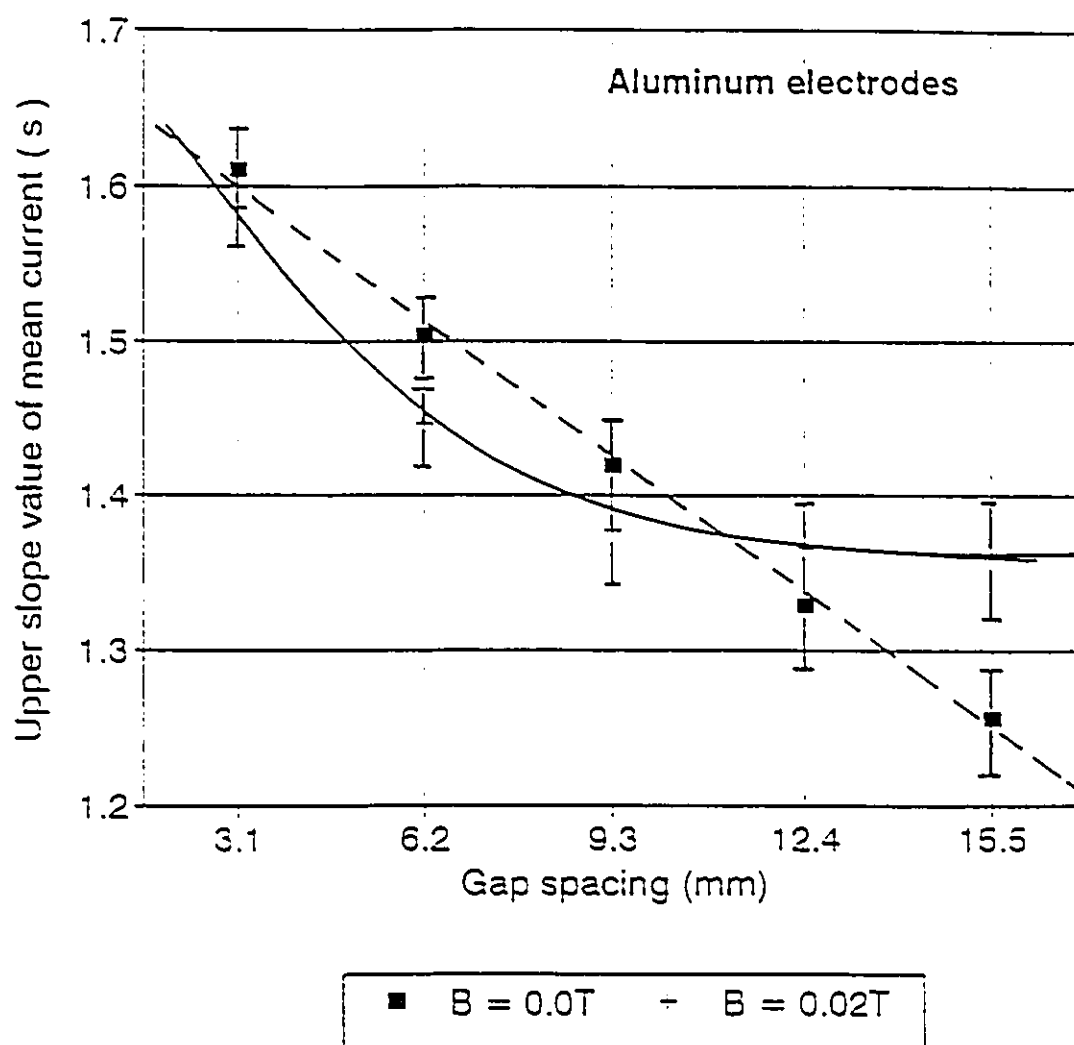


Figure 4.87 The upper slope of mean current as a function of gap spacings with/without magnetic flux density in silicone oil

CHAPTER V

AN ELECTROHYDRODYNAMIC (EHD) MODEL FOR HIGH STRESS CONDUCTION IN DIELECTRIC LIQUID

5.1 INTRODUCTION

According to the theory of charge transport in dielectric liquids [75], it is proposed that under slow triangular voltage waveform application the upper slope of the Ostroumov plot may be effected by the cathode material in the highest field region. The lower slope in the intermediate field strength regime has not so far been investigated closely, except that the lower slope represents the current characteristic in the lower (intermediate) field region. The lower slope may, however, be explained by taking into account the charge injection from both cathode and anode or may be related to current produced by charge dissociation in bulk. The dominating process is dependent on the properties and the condition of liquids, and also the electrode materials as well. Thus there is strong evidence [20] that a portion of the current at low fields (< 100 kV/cm) is due to the presence of ions produced by dissociation of the oil itself or its impurities. In the present circumstance, however, Esendal and Watson [6] have introduced evidence that indicates the smallness of the contribution of ionic conduction.

Under high electric field stress, if the liquid field-enhanced dissociation is more

apparent than that of injection, the conducted current will be less dependent on the electrode surface and its materials, otherwise the electrode material will affect its current characteristics. If so various kinds of charge injection could be obtained by carefully choosing the electrodes. Thus, the present experiments will focus on the probable contribution of the cathode and anode materials.

All the experimental results were obtained by using the same geometry of electrodes [66]. The measurements were made over a range of gap separations from 2.07 to 7.75 mm. In this investigation the same techniques were used as those developed previously [6] (refer to section 3.6). The data reduction method used here was also the same as in this previous work for obtaining the average current values up to the maximum applied voltage values ranging from 20, 30 and 40 kV respectively. The tests shown below were carried out on silicone oil with a viscosity of 5×10^{-6} m²/s and a resistivity of 1000 TΩ-m, after filtering through a 2-2.5 μm filter before starting. In order to verify the intended proposition that cathode or anode material will influence the magnitudes of s_u and s_i , a series of tests have been carried out using Al, Cu, Mg, and Zn electrodes in which these materials were alternately mixed or matched.

5.2 EXPERIMENTAL RESULTS AND DISCUSSION

The experimental results for the cases where the maximum applied voltage was 20 kV and 30 kV have almost no correlation between s_u or s_i and electrode materials over

a range of voltage and gap separations. In the 20 kV range, even the two formerly sharp divisions between the high and intermediate field regions are especially difficult to attain clearly. Instead, three divisions in the Ostroumov plot are sometimes present in one case, or there is only one slope, the lower slope is present in another case. Under these circumstances the slope values in the 20 kV and 30 kV maximum applied voltage tests are not really suitable for further analysis. The maximum applied voltage of 40 kV gives better experimental results, consequently high stress testing seems to be more reliable for this purpose than others [83].

The curves in Figures 5.1 and 5.2 give the relationship between the inverse value of upper slope (s_u) and the gap separation for four different pairs of identical electrode materials. The measurements were made for maximum applied voltages of 40 kV and 30 kV respectively. It will be seen that the curves of s_u^{-1} vs. gap separation have the general form of straight lines and $1/s_u$ value increase slightly with gap separation, except for copper electrodes in the 30 kV case. It could be speculated that as the gap distance increases, the field stress will decrease for the same potential level, thus reducing the current amplitude, and hence causing the value of s_u^{-1} to increase. Although all of these four different electrodes were tested alternately mixed or matched, there were no clear results to confirm the proposition that s_u is associated with the cathode electrode. In the 40 kV range, the experimental results from the combinations of Cu with Zn and Zn with Mg materials seem to show agreement with the proposition. It is also found that when the Zn electrode is used as the anode, the slopes from the other four cathode materials

show that they are dependent on the cathode as shown on Figure 5.3. Consequently, when the Mg electrode is used as the cathode, the slopes seem to be dependent upon the anode materials (Figure 5.4). For the maximum applied voltage in the 30 kV range, only Zn with Mg from the above group gave a similar agreement when compared with the 40 kV range test. Moreover, by using the same partners as shown in Figure 5.3, such as the use of Zn as the anode material, the results of the slopes with four different materials are different from those obtained in the 40 kV range, shown in Figure 5.5. Figure 5.6 represents the results from similar combinations to those of Figure 5.4 but at a maximum applied voltage of 30 kV. Figure 5.7 shows, for example, the value at 40 kV of s_i^{-1} as a function of gap separation for the combinations, Zn(+)-Zn(-): Zn cathode, Zn anode; Zn(+)-Mg(-): Zn cathode, Mg anode; Mg(+)-Mg(-): Mg cathode, Mg anode; Mg(+)-Zn(-): Mg cathode, Zn anode.

Figures 5.8, 5.9 and 5.10 show the slopes of the lower linear region (s_i^{-1}) as a function of gap distance, in which four different materials are used also as mixed and matched pairs with the maximum applied voltage at 40 kV, 30 kV and 20 kV respectively. Again the 40 kV range gives better experimental results from the viewpoint of confirming the proposition stated above. Aluminum differs strongly from other materials, in that s_i^{-1} increases with the gap distance where others are negatively or only slightly changed. This phenomenon appears in both the 40 kV and 30 kV tests. In the 20 kV range shown in Figure 5.10 the lower slope of aluminum shows the same results when compared to the 40 kV and 30 kV tests except that Zn also has a positive

relationship with the gap separation. The lower slope in each case is very strongly dependent on the electric field for aluminum electrode material. In the 40 kV range, some of the experimental results, such as those from Cu with Mg, and Al with Zn pairs of electrodes show that the lower slopes were associated with anode materials, while in one case only (Mg with Al) it was correlated with the cathode material. There is therefore no reliable correlation with either anode or cathode material. It is similarly so for the upper slope, only the Cu with Mg electrode pair gives a similar agreement in the maximum applied voltage range of 30 kV. Figure 5.11 presents similar results to those of Figure 5.7 but in this case for s_i rather than s_u .

With a maximum voltage excursion of 40 kV it was confirmed for some of the possible electrode material combinations that the cathode determined the upper slope value, s_u . A confirmation that either the anode or cathode material determined the lower slope was not however clearly obtained at all. These levels of confirmation of the proposition were considerably reduced with a 30 kV value of maximum voltage excursion. The results are random or become chaotic with a maximum applied voltage of 20 kV. For the maximum applied voltage in the 20 and 30 kV range, there is some difficulty in obtaining reproducible values of s_u and s_i . As the electrode effect is strongly field dependent, high stress testing seems to be more reliable for charge injection and yields better experimental results. Thus these effects on the slope value are strongly field dependent.

If the electrode effects were to be less field dependent, charge dissociation could play a important role. Generally the relationship between the conduction current and the electrical field can be roughly divided into the three regions as seen in Figure 4.81. In the low field region A, the current appears to rise linearly with the field, and to obey Ohm's law. As the field is increased, it comes to the intermediate field region B, a saturation current will be seen, the field at which this occurs will depend on the ion production rate [41]. In the high field region C, there would then be a more or less exponential form of increase in current with the increasing field. For a continuous current to flow in any of the regions, there must be a source of charge. Several agents could contribute to the current in the A and/or B regions. Amongst those agents there is natural radiation, dissociation of ionic impurities, and solid impurity particles. Those impurities are the most likely source of charge at intermediate fields, as it is extremely difficult to remove all such traces [23]. With a small field applied to the electrode-liquid system, the dissociated negative and positive ions, which escape recombination, will drift to the electrodes and give rise to a flow of current. At high fields the ions may be removed to the electrodes at a rate faster than the generation rate in the bulk of the liquid. The current is then determined by the generation rate, and also by the rate of ion neutralization at the electrode. The combined effects of bulk generation and electrode neutralization can then produce a situation where the current tends to saturation. At even higher field stresses, for a continuous current in the external measuring circuit, negative charge must be injected at the cathode and absorbed at the anode. It is reasonable to expect that this would lead to a rapid increase in current levels with an increase in the

applied field.

In most cases, the lower slope of the Ostroumov plot actually can be seen to represent the current variation with respect to the electric field in transition from region B to region C (see figure 4.81). This is the region which is between the intermediate field and high field regions. It could be explained that the lower slope is less field stress dependent during applications of high field stress, except for the Al. electrode material. Another possibility lies in the ability of oxide layers on either electrode to block the neutralization of ions at their surfaces, hence contributing to the overall electric field distribution. In all cases, the role of neither the cathode nor the anode could fully explain these effects upon the two slopes, nor how these two slopes are related to each other.

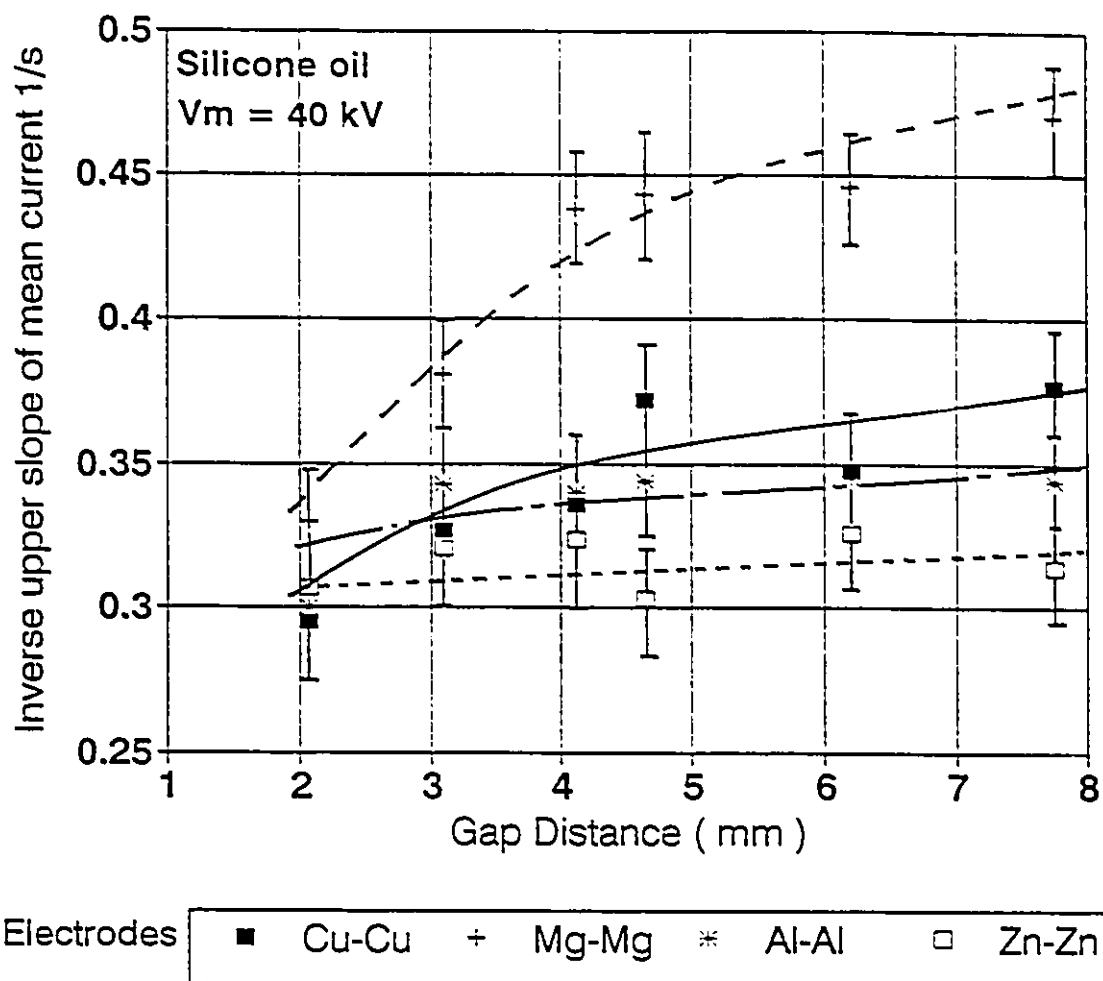


Figure 5.1 Inverse upper slope value of mean current as a function of gap spacings at 40 kV

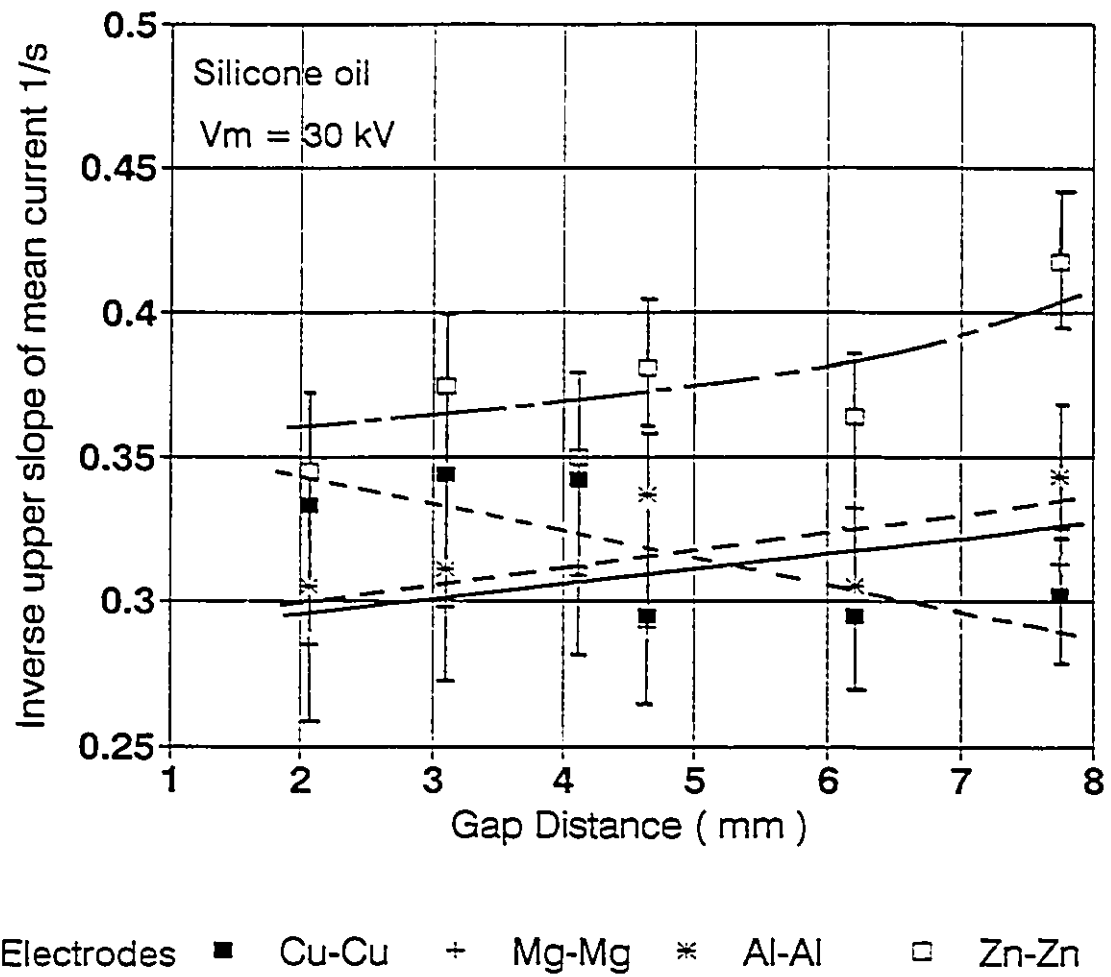


Figure 5.2 Inverse upper slope value of mean current as a function of gap spacings at 30 kV

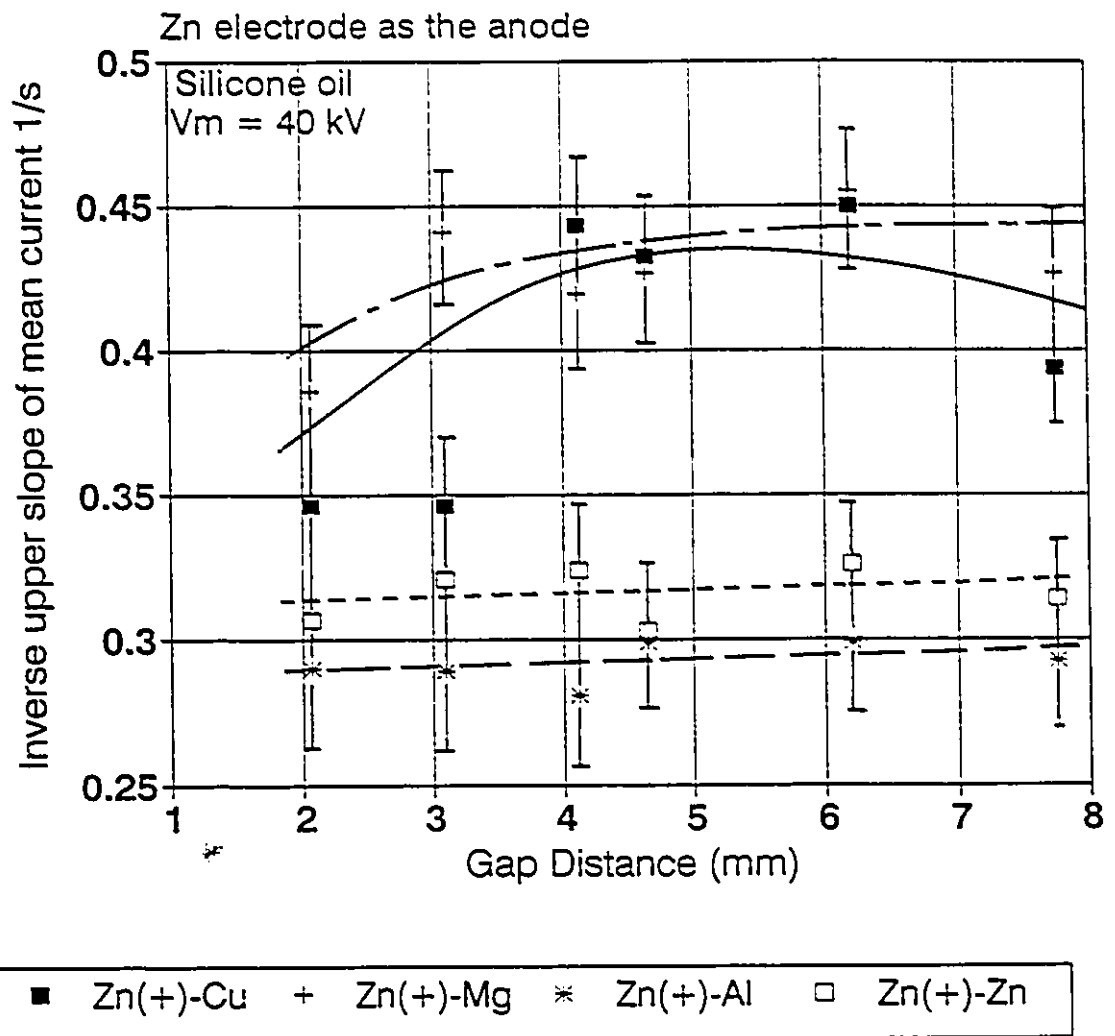


Figure 5.3 Inverse upper slope value of mean current as a function of gap spacings at 40 kV using the same anode material

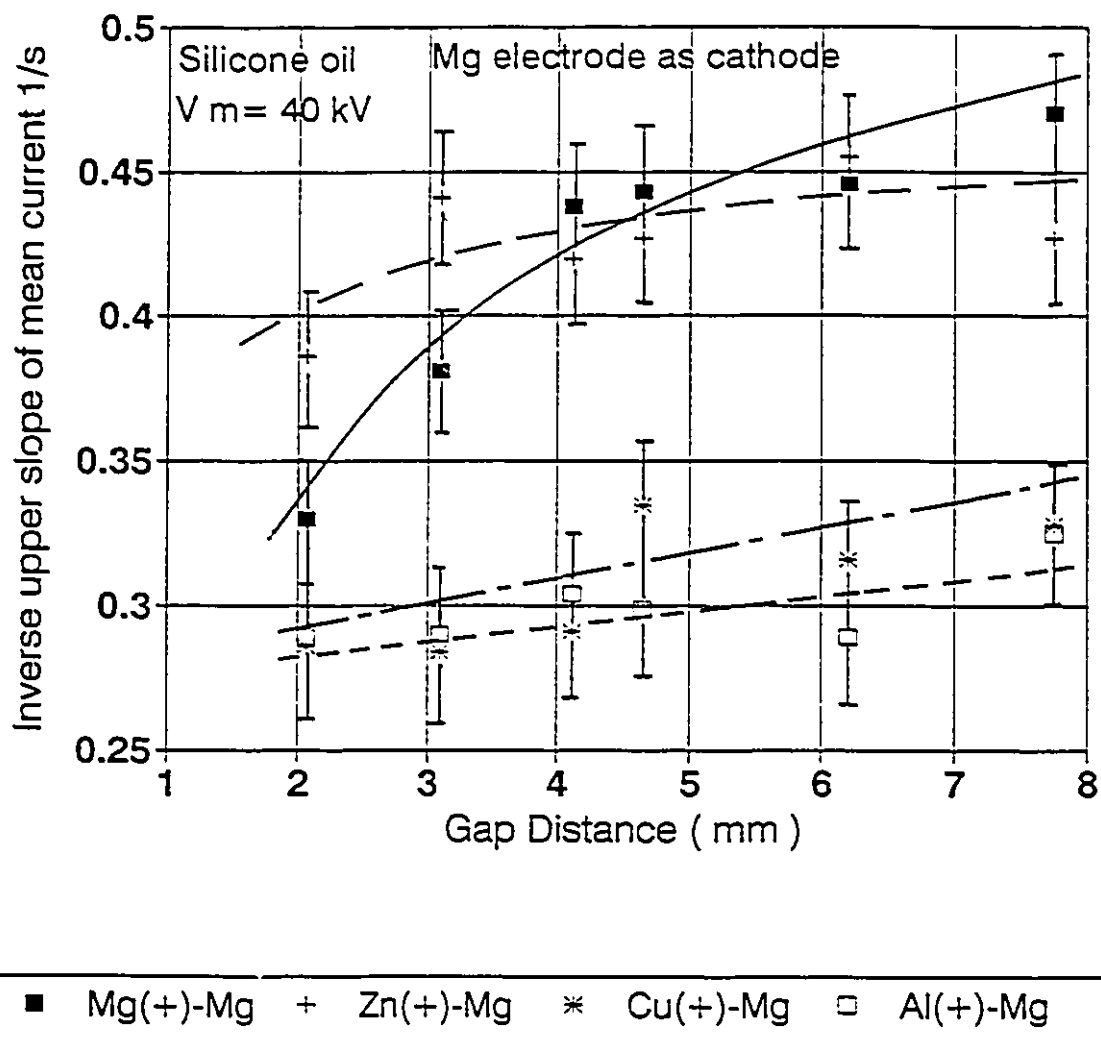


Figure 5.4 Inverse upper slope value of mean current as a function of gap spacings at 40 kV using the same cathode material

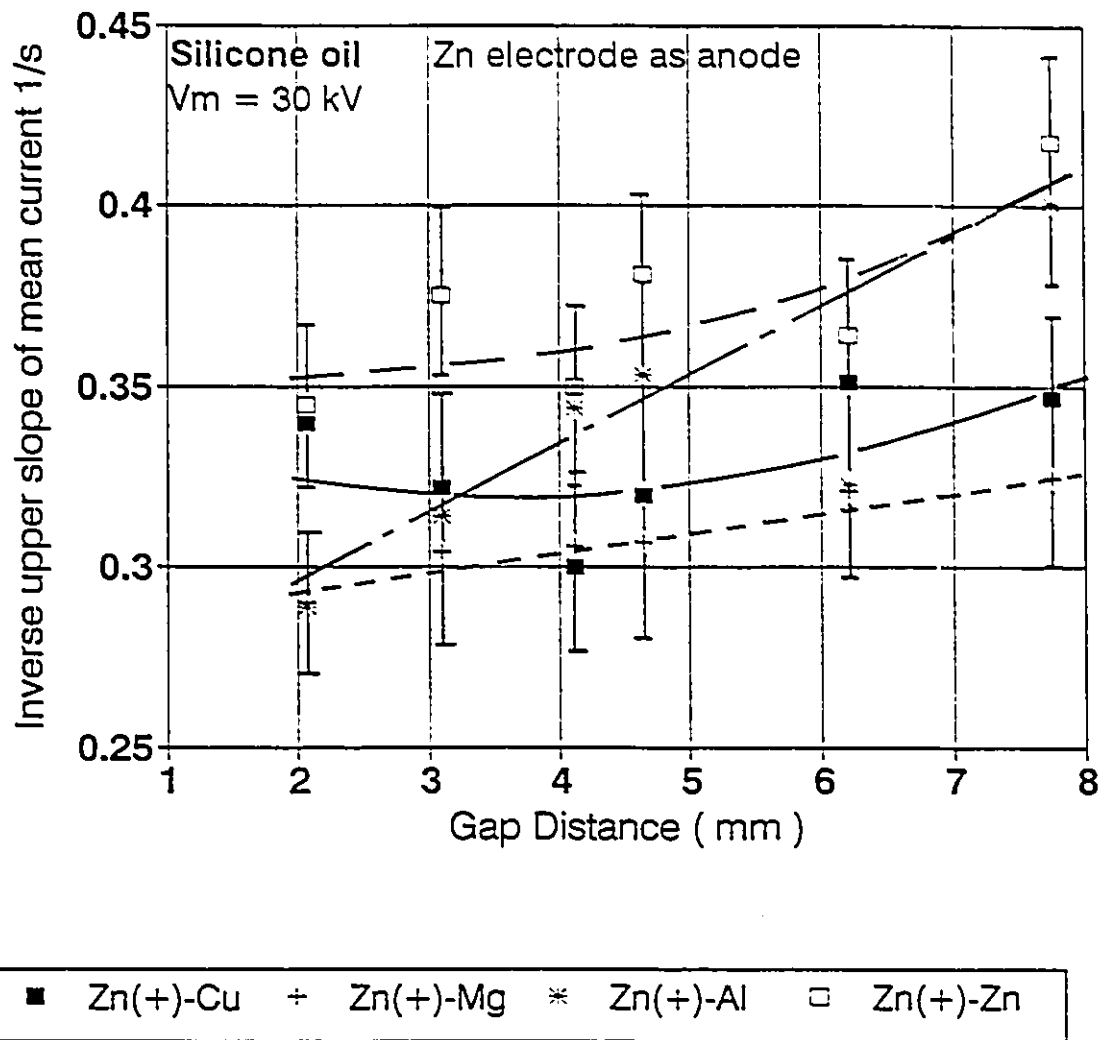


Figure 5.5 Inverse upper slope value of mean current as a function of gap spacings at 30 kV using the same anode material

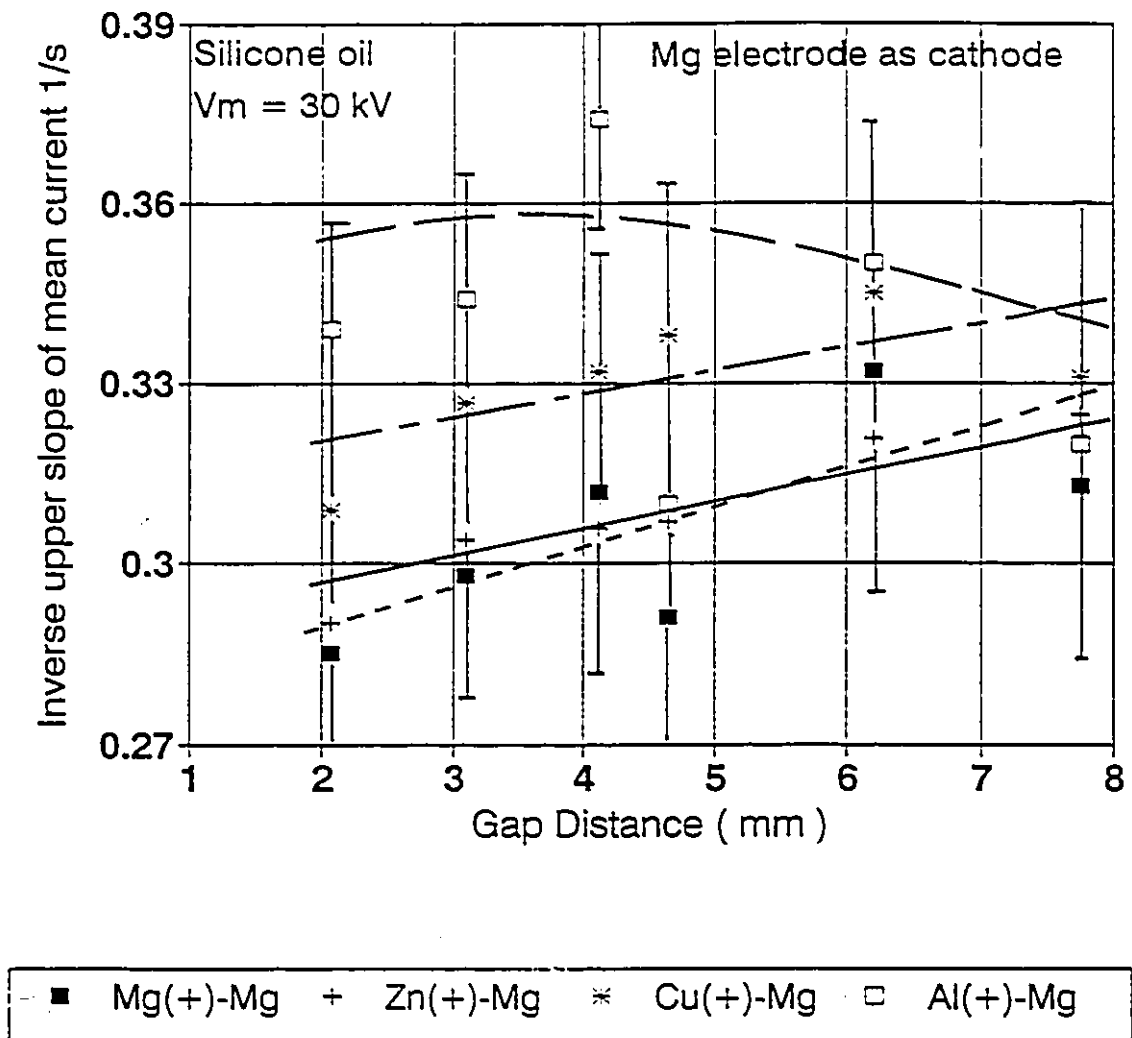


Figure 5.6 Inverse upper slope value of mean current as a function of gap spacings at 30 kV using the same cathode material

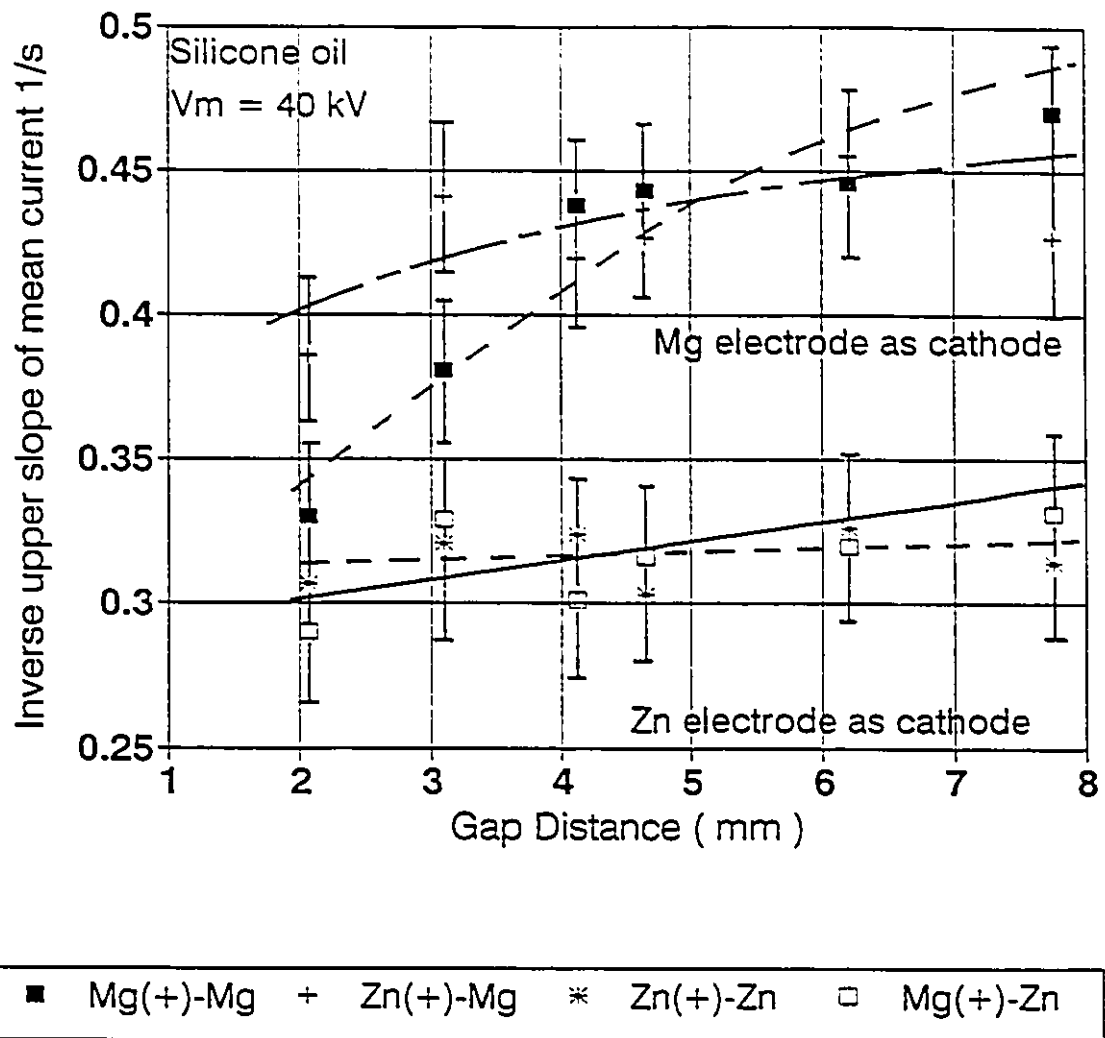


Figure 5.7 Inverse upper slope value of mean current as a function of gap spacings at 40 kV with differing cathode materials

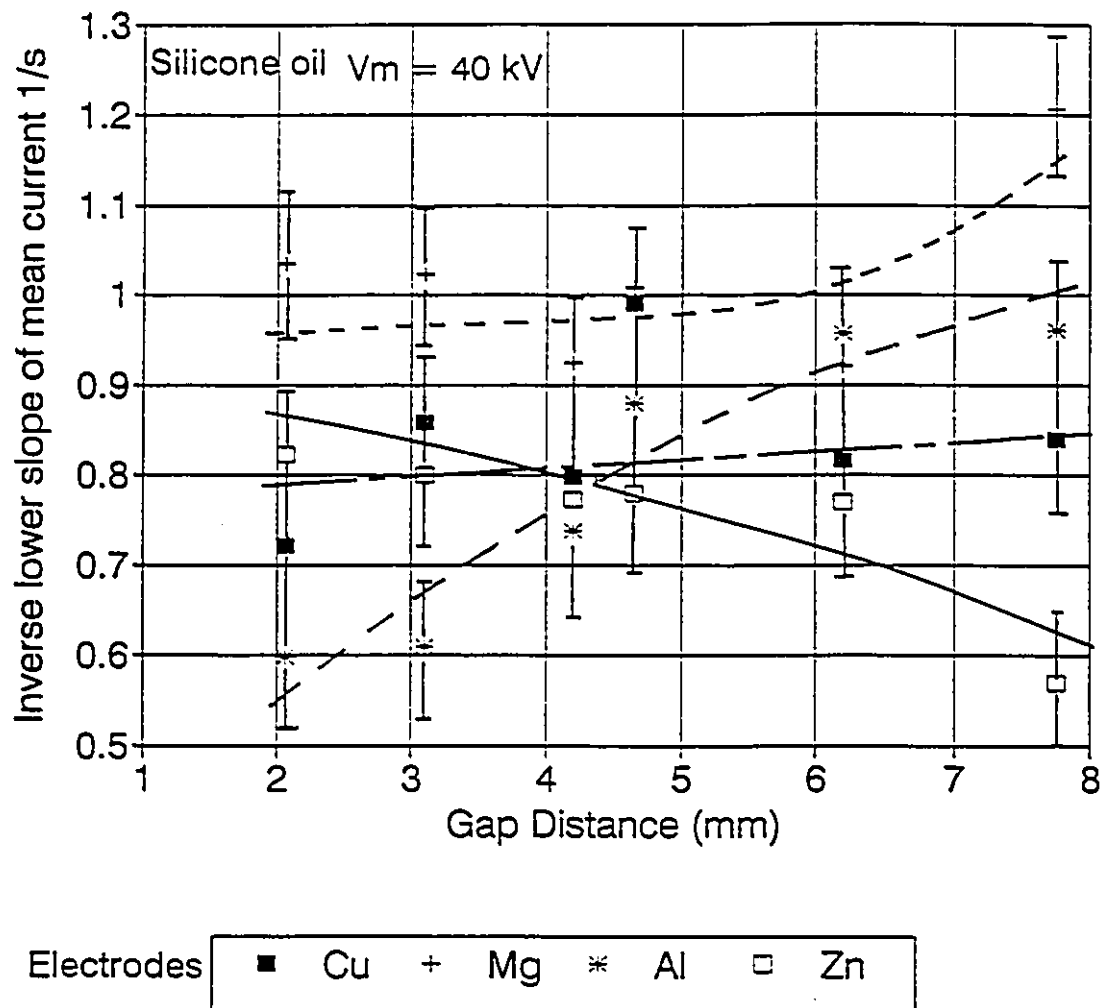


Figure 5.8 Inverse lower slope value of mean current as a function of gap spacings at 40 kV

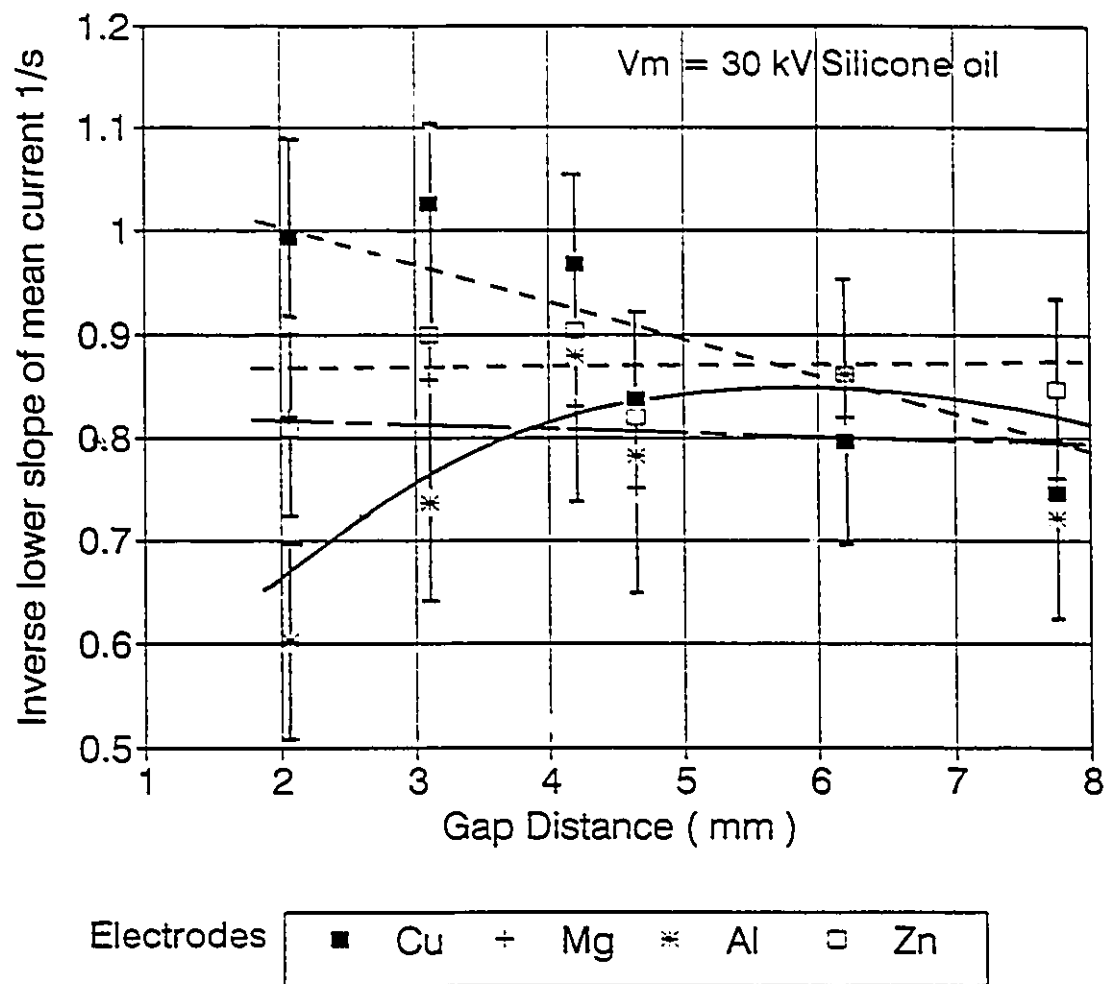


Figure 5.9 Inverse lower slope value of mean current as a function of gap spacings at 30 kV

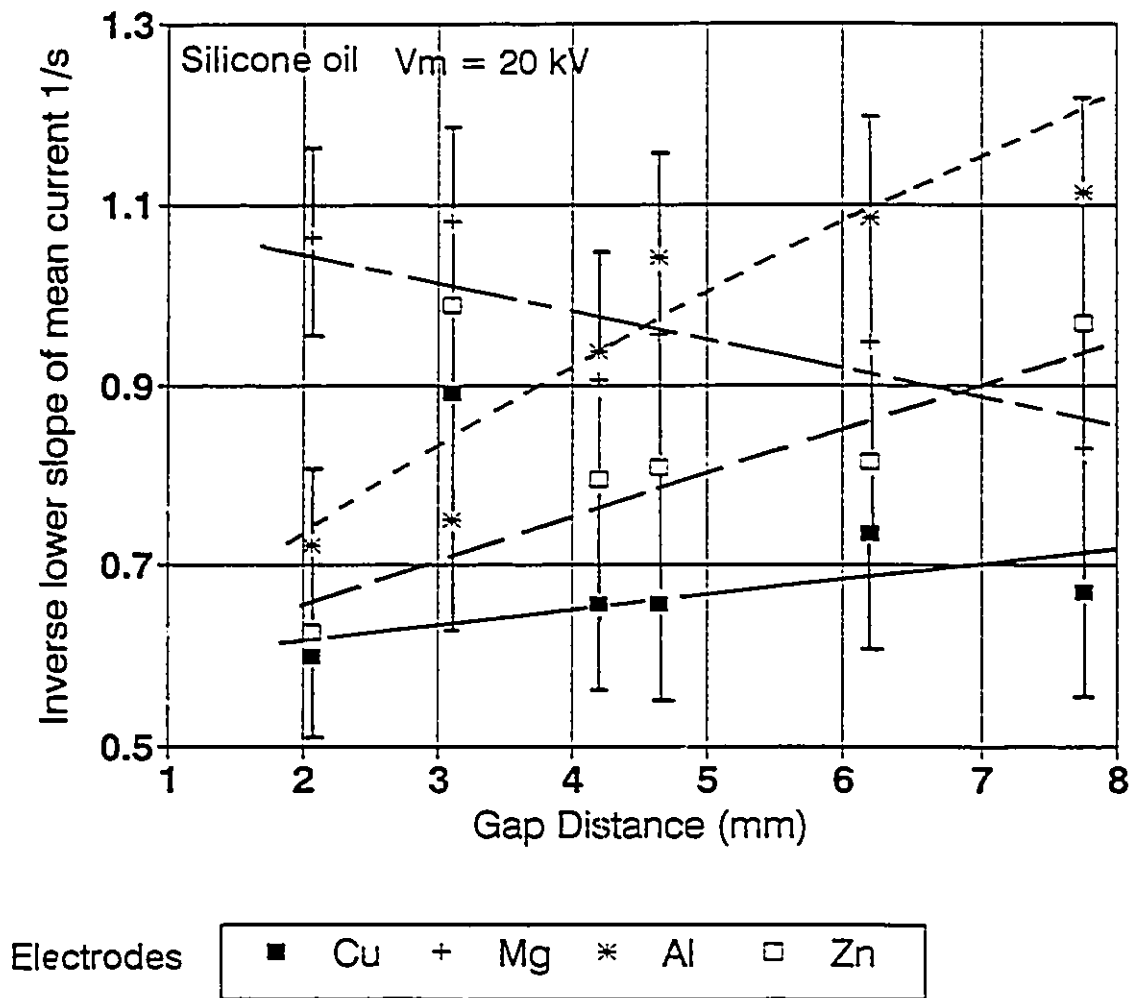


Figure 5.10 Inverse lower slope value of mean current as a function of gap spacings at 20 kV

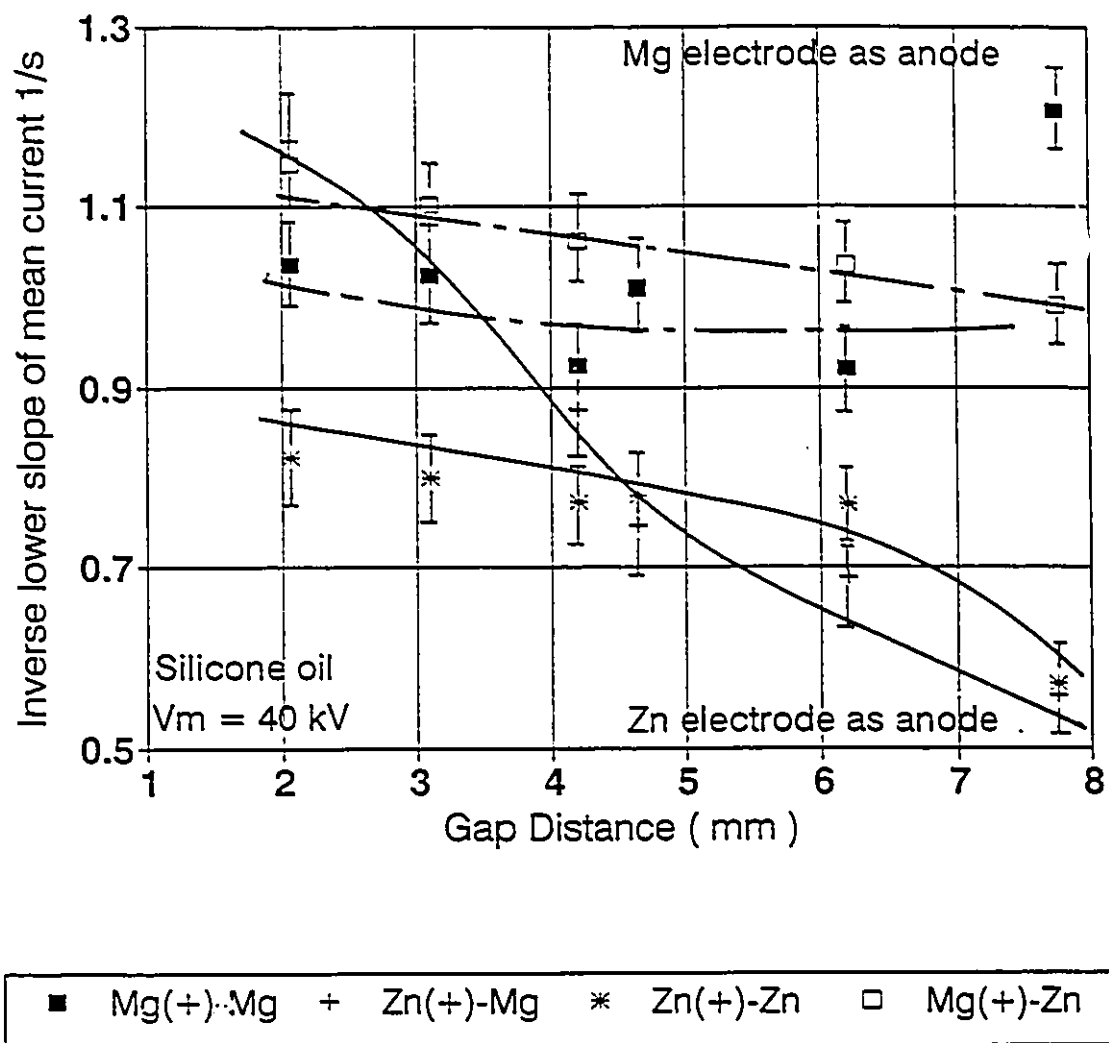


Figure 5.11 Inverse upper slope value of mean current at 40 kV with differing cathode materials

5.3 EHD THEORETICAL MODEL

5.3.1 INTRODUCTION

As mentioned before, the two slopes s_0 and s_1 originate from a threshold point. When the maximum applied voltage is at 20 kV the number of distinctly linear sections of the Ostroumov plot may sometimes appear as three instead of two. With an increase in the maximum applied voltage and therefore the maximum applied field, the values of the slopes (s) vary as well as their number (refer to the experimental results from Chapter IV). This phenomenon has not had much attention paid to it in previous studies. When the maximum electric field increases, the magnitude of the two slopes become closer in value to each other as shown in Figure 4.34. As the maximum voltage excursion is raised the two exponents merge into a single slope with the value of $3/2$. It is also found that at lower field stress levels, it is difficult to obtain a stable slope value. Hence this could be considered as being between a chaotic and an ordered system. Since the original concept of the cathode and anode effect was not fully confirmed by experimental results, a new theoretical approach was developed by considering electrodynamic as well as electrostatic phenomena in the system. This is a nonlinear iterative system model complementing the original theoretical mathematical model [76].

Although a great deal is known of the behaviour of the exponents s_0 and s_1 for

the upper and lower regimes nothing until now has been uncovered about how the specific slope values arise. Recently Watson developed a new ElectroHyroDynamic (EHD) model [76]. By using this model the experimental results could be satisfactorily explained. The complementary model to be described is based upon the formation of electric fields in the medium in which gradients of electronic space charge density arise. Symmetrical gradients of trapped electron density appear by field assisted detrapping followed by diffusion and retrapping at a remote location. Such gradients can act as positive charges screening the uniform component of trapped charge. The theory, however, indicates that the trapped charge density becomes a function of itself and can only be computed by mathematical iteration. In a similar manner the slope factor s itself is found to be arrived at similarly. Hence, since this factor defines the convection current density (an EHD variable) as being proportional to the appropriate power of the applied potential, then the electrohydrodynamics of the system are similarly defined.

The theoretical work and the computational technique for the EHD model are very closely related since they were developed simultaneously and supported each other in a complementary fashion from time to time. Thus, as a result, the experimental results could be simulated by computer as well as the simulation function could be derived from the corresponding new theoretical approach. Therefore it is necessary to introduce this EHD model briefly, and the iterative evaluation program will be described later on.

Theoretically the transport is seen to result from the formation and movement of

a group of trapped charges bounded in tiny cells enclosing Beltrami Flow Fields [75]. Such flow cells do not interact with the fluid and can accelerate therefore as free particles for a finite time period. These can react with both the electrostatic field as well as with an electrodynamic component introduced by detrapping of electrons and subsequent diffusion and retrapping on adjacent field lines, causing rotation of the fluid and mechanical acceleration $\omega \times u$. This introduces a fluid dynamic analogue of the usual electrodynamic body force, $J \times B$ (see Appendix E). Since vorticity is generated thus it is manifested as an effective reduction of the fluid viscosity [82].

5.3.2 BASIC EHD MODEL THEORY

From an earlier study, the average current response to rising and falling voltage appears on a log-log scale with two linear portions which are divided at high field levels [6]. Both of these two portions obey the equation

$$I \propto V^s \quad (5.1)$$

in which s is referred to as either the upper slope or lower slope. Now considering the flow of an electrically charged viscous dielectric liquid as incompressible, the electrical body force will drive the fluid into motion. Under electrodynamic conditions, the

electric field strength E' can be defined [12] as ¹,

$$E' \equiv - \frac{1}{\rho_e} \nabla(\rho_e V) \equiv - \nabla V - \frac{V \nabla \rho_e}{\rho_e} \quad (5.2)$$

Where the terms, ∇V and $V \nabla \rho_e / \rho_e$, represent the electrostatic and electrodynamic field portions respectively. V in this case is an applied linearly ramped voltage and ρ_e represents the electrostatic charge density in the fluid.

According to Beltrami force-free flow theory, the vorticity ω and velocity u vectors obeys the Vector Helmholtz Equation [VHE], and the potential is associated with the Scalar Helmholtz Equation [SHE] [Appendix C]. Using Equation A.5 and Poisson's equation $\nabla^2 V = -\rho_e/\epsilon$, it is shown that ρ_e and V are directly proportional so that,

$$V = \frac{\rho_e \lambda^2}{\epsilon} \quad (5.3)$$

¹ From the energy differential equation $dA = \mathbf{f} \cdot d\mathbf{l} = q\mathbf{E} \cdot d\mathbf{l}$, so the total energy $A = q \int \mathbf{E} \cdot d\mathbf{l}$, and then the potential $V = A/q = 1/q \int q\mathbf{E} \cdot d\mathbf{l}$, rearranging the equation $qV = \int q\mathbf{E} \cdot d\mathbf{l}$. Finally differentiating it $\nabla(qV) = q\mathbf{E}$, so $\mathbf{E} = \nabla(qV)/q$, by using the charge density ρ_e , $\mathbf{E} = \nabla(\rho_e V)/\rho_e$.

Rewriting Equation 5.1 (see Appendix C) as,

$$\begin{aligned} \therefore \mathbf{u} &= -\nabla\psi = \nabla(-bV) & -J &= \rho_e \mathbf{u} = -\rho_e b \nabla V \\ J &= \rho_e b s V^{s-1} = \frac{bs\epsilon}{\lambda^2} V^s & \therefore J &= k' V^s \end{aligned} \quad (5.4)$$

where k' is constant, ψ is a velocity potential. Since \mathbf{E} could be given as $\mathbf{E} = -\nabla V = \pm jV/\lambda$ [Appendix E], so $E/E_c = V/V_c$ and Equation 5.4 could change to

$$J = -k' V^s \propto -\rho_e b \frac{V}{\lambda} \quad (5.5)$$

$$\therefore \rho_e = k_1 V^{s-1} \propto k' V^{s-1}$$

where k_1 is constant. Introducing this into Poisson's equation $\nabla \cdot \mathbf{E} = \rho_e/\epsilon$ with the Laplacian given as

$$\begin{aligned} \nabla \cdot \mathbf{E} &= \frac{\rho_e}{\epsilon} = \frac{k_1}{\epsilon} V^{s-1} \\ &= \frac{d\mathbf{E}}{dV} \cdot \frac{dV}{dx} = -\frac{d\mathbf{E}}{dV} \cdot \mathbf{E} = -\frac{1}{2} \frac{dE^2}{dV} \end{aligned} \quad (5.6)$$

Assuming that this can be integrated to give

$$\begin{aligned} -\int d\left(\frac{1}{2}\epsilon E^2\right) &= \int k_1 V^{s-1} dV = \frac{k_1}{s} V^s \\ -\frac{1}{2} \epsilon E^2 &= \rho_e \frac{V}{s} \end{aligned} \quad (5.7)$$

Now by considering the field strength, the substitution of Equation 5.5 into Equation 5.2 results in the relationships,

$$\begin{aligned} E' &= -\frac{1}{\rho_e} \nabla(k_1 V^{s-1} V) \\ &= -\frac{k_1}{\rho_e} \nabla(V^s) = -s \nabla V \end{aligned} \quad (5.8)$$

$$\text{since } E = -\nabla V, \quad s E = -s \nabla V = E'$$

and since $\nabla \cdot E = \rho_e/\epsilon$ a new charge density ρ_e' can be defined by $\nabla \cdot E' = \rho_e'/\epsilon = s \nabla \cdot E = s \rho_e/\epsilon$, where $\rho_e' = s \rho_e$ represents the density of electrodynamic charge coexisting with ρ_e but not as a function of the electrostatic potential V . Using the same method as in Equation 5.6, the integration of Poisson's equation above reduces to $\epsilon E'^2/2 = -\rho_e' V$.

Now if E' and ρ_e' follow Poisson's equation, then $d(\epsilon E'^2/2) / dV' = \rho_e'$. Now let $E' = -\nabla V'$ here, where a composite potential $V' = V + \xi$ exists as the sum of the electrostatic potential and independent dynamic potential. Assuming therefore that ξ is independent of V , it follows that $d(\epsilon E'^2/2) / dV' = \rho_e'$ represents a Poisson equation in a new system of primed field. Thus the charge density ρ_e' is independent of the potential V' . Furthermore Poisson's equation can be written for ρ_e' which is independent of V while simultaneously $\rho_e = \rho_e(V)$ as defined in Equation 5.5. Thus two charge density components can be distinguished according to whether or not they are functions of the electrostatic potential V .

The normal electrostatic body force, $\rho_e E$, leads to translational motion at velocity, u , but in addition there is rotation with vorticity, ω , brought about by an electric moment wherever $\nabla \rho_e$ is crossed with ∇V (or u) (meaning $\nabla \rho_e \times \nabla V \neq 0$), which is to say whenever electronic space charge density is not a function of the static potential, V . Now it becomes possible to write E' in the form,

$$E' = -\nabla V - \frac{\partial \alpha}{\partial t} \quad (5.9)$$

where $\alpha = \rho u / \rho_e$ is a fluid dynamic vector potential similar to that arising in conventional electromagnetic theory [77].

The two categories of electronic charge arise from their redistribution in an electric field by field stimulated detrapping, diffusion and retrapping at remote locations which may or may not lie on the same original field line. Thus the apparent convection velocity is

$$u' = u + bE \quad (5.10)$$

where bE is a drift velocity which is superimposed upon the true convection velocity, u . Since $b = \rho_e \tau_v / \rho$, this can be rearranged to give

$$\alpha' = \alpha - \tau_v \nabla V \quad (5.11)$$

where α' is defined as $\alpha' = \rho \mathbf{u}'/\rho_0$ which is a new vector potential and τ_v is a characteristic time. In the presence of a rising voltage therefore the potential everywhere at every instant in time can be written as,

$$V' = V + \tau_v \frac{\partial V}{\partial t} \quad (5.12)$$

Equation 5.11 with Equation 5.12 constitute a pair of gauge transformations [Appendix D]. This transformation pair will assure the invariance of E' as given in Equation 5.9 when replacing α and V by α' and V' respectively. There is thus a complete analogy with the corresponding equations of magnetic electrodynamics as opposed to this form of fluid electrodynamics [77]. Detrapping and diffusion therefore, as described by Equation 5.11, are readily incorporated into such a dynamic model.

A new concept introduced here is that of the "beltramion" which plays the role of a quasiparticle in the high field conduction process. The basic properties of Beltrami flow fields are presented for convenience in Appendix C. For a Beltrami flow field, there is in addition to the Vector Helmholtz equation (VHE) in \mathbf{u} , $\nabla^2 \mathbf{u} + \mathbf{u}/\lambda^2 = 0$ [Equation C.3] another similar equation in ω ,

$$\nabla^2 \omega + \frac{\omega}{\lambda^2} = 0 \quad (5.13)$$

Moreover there is a second SHE in ρ_e arising from $\mathbf{u}_2 = \nabla \times (c\psi)$ where c is a fixed vector (Equation C.5), hence,

$$\nabla^2 V + \frac{V}{\lambda^2} = \nabla^2 \rho_e + \frac{\rho_e}{\lambda^2} = 0 \quad (5.14)$$

Equation 5.13 has the physical significance of describing the diffusion of vorticity with an effective dynamic viscosity, ν^* . Using the equations A.1 and A.7, there is a rate of change, $\partial\omega/\partial t = -\omega/\tau_v$ [Appendix C], where $\nu^*\tau_v = \lambda^2$. Equation 5.14 similarly describes the diffusion of electrons with coefficient, D, as they detrap and relocate in remote traps. With $\partial\rho_e/\partial t = -\rho_e/\tau_v$, this indicates that $D\tau_v = \lambda^2$ and so $\nu^* = D$ is necessary for Equations 5.13 and 5.14 to be compatible. This means in fact that the values of λ^2 in those equations must also be compatible.

5.3.3 THE SOLITARY WAVE²

When the applied voltage is raised a solitary wave is launched from the cathode by field stimulated injection of electrons [76]. As the applied potential is raised the previously injected and trapped electrons move away with the flow and at the higher stress a greater concentration is injected adjacent to the cathode so a gradient of electron density is created pointing to the cathode [75]. The gradients of the terms of Equation 5.12 can be compared, term by term with their counterparts in Equation 5.2. The final terms indicate that

² A wave which can pass through one another and emerge from encounter with no change in profile

$$V \nabla \rho_e / \rho_e = (\lambda^2 / \epsilon) \nabla \rho_e = (D \tau_v / \epsilon) \nabla \rho_e = \tau_v \nabla \left(\frac{\partial V}{\partial t} \right) \quad (5.15)$$

$$-\nabla V' = -\nabla V + \tau_v \nabla \left(\frac{\partial V}{\partial t} \right) \equiv -\nabla V + \nabla \left(\frac{\lambda^2}{\epsilon} \nabla \rho_e \right)$$

and thus in the Beltrami field, the displacement current is maintained by charge diffusion which causes $\nabla \rho_e$, then

$$\frac{d\mathbf{E}'}{dt} \equiv \frac{\partial \mathbf{E}'}{\partial t} + \mathbf{u}' \cdot \nabla \mathbf{E}' + \nabla \times (\mathbf{E}' \times \mathbf{u}') = 0 \quad (5.16)$$

If \mathbf{E}' is steady in the moving reference frame of the wave, and

$$\frac{dV'}{dt} \equiv \frac{\partial V'}{\partial t} + \mathbf{u} \cdot \nabla V' = 0$$

therefore,

$$\frac{\partial^2 V'}{\partial t^2} + u^2 \nabla^2 V' + \mathbf{u} \cdot [\nabla \times (\mathbf{E}' \times \mathbf{u})] = 0$$

Moreover, if

$$\nabla \times (\mathbf{E}' \times \mathbf{u}) = \mathbf{E}' \times \mathbf{u} / \lambda$$

$$\text{then} \quad \mathbf{u} \cdot \nabla \times (\mathbf{E}' \times \mathbf{u}) = 0$$

thus:

$$\frac{\partial^2 V'}{\partial t^2} + u^2 \nabla^2 V' = 0$$

By considering the scalar product of a velocity, \mathbf{u} , with the terms of Equation 5.2

it follows that the mobile time derivative of V' will be zero provided that,

$$\tau_v \frac{\partial V'}{\partial t} = \tau_v \frac{\partial(V + \tau_v \frac{\partial V}{\partial t})}{\partial t} = \tau_v \frac{\partial V}{\partial t} + \tau_v^2 \frac{\partial^2 V}{\partial t^2} \quad (5.17)$$

If $V = \tau_v^{-2} \partial^2 V / \partial t^2$ that Equation 5.17 could be given as

$$\tau_v \frac{\partial V'}{\partial t} = \tau_v \frac{\partial V}{\partial t} + V = V' \quad (5.18)$$

$$\text{Thus} \quad \partial(\tau_v^2 \frac{\partial V'}{\partial t}) / \partial t = \tau_v^2 \frac{\partial^2 V'}{\partial t^2} = \tau_v \frac{\partial V'}{\partial t} = V'$$

indicates that if V' also satisfies the SHE, thereby implying that V' follows a diffusion equation, then it also must satisfy the homogeneous wave equation with the velocity $\partial x / \partial t \equiv u = \lambda / \tau_v$. Hence from Equation 5.17,

$$\begin{aligned} \nabla^2 V' + \frac{V'}{\lambda^2} &= \nabla^2 V' - \frac{1}{u^2} \frac{\partial^2 V'}{\partial t^2} = 0 \\ &= \nabla^2 (V + \tau_v \frac{\partial V}{\partial t}) - \frac{1}{u^2} \frac{\partial^2 (V + \tau_v \frac{\partial V}{\partial t})}{\partial t^2} = 0 \end{aligned} \quad (5.19)$$

Rearranging Equation 5.18, the final equation could be written as

$$\nabla^2 V - \frac{1}{u^2} \frac{\partial^2 V}{\partial t^2} = -\tau_v \frac{\partial}{\partial t} (\nabla^2 V - \frac{1}{u^2} \frac{\partial^2 V}{\partial t^2}) \quad (5.20)$$

The driving term, in Equation 5.19 represents $\nabla \cdot \mathbf{E}'$ with which it is seen as being similar to the more familiar inhomogeneous wave equation of electromagnetic theory. Now by writing

$$\begin{aligned}\nabla \cdot \mathbf{E}' &= \frac{d\mathbf{E}'}{dV} \left(\frac{dV}{dx} \right) = -E \cdot \frac{d\mathbf{E}'}{dV} \\ &= -\frac{d}{dV} \left(\frac{1}{2} E E' \cos\theta \right) = -\frac{d}{d(V/V_c)} \left(\frac{1}{2V_c} E E' \cos\theta \right)\end{aligned}\quad (5.21)$$

a new variable θ is introduced which is the angular separation between \mathbf{E}' and \mathbf{E} where V_c is characteristic potential. From the preceding argument, since $\nabla \cdot \mathbf{E}' = \rho'_c/\epsilon$ is not a function of V , the expression above is modified by writing,

$$\begin{aligned}\theta &\equiv V/V_c = eV/kT^* \\ \text{Thus: } \nabla \cdot \mathbf{E}' &= -\frac{d}{d\theta} \left(\frac{1}{2V_c} E E' \cos\theta \right) = \frac{1}{2V_c} E E' \sin\theta\end{aligned}\quad (5.22)$$

where T^* is a renormalized temperature. Thus Equation 5.19 is reduced to the Sine-Gordon equation form [78], with instead the left hand side using θ and the right hand side given by $(EE'/2V_c)\sin\theta$, and thus ³

$$\nabla^2\theta - \frac{1}{u^2} \partial^2\theta/\partial\tau^2 = (E E'/2V_c^2)\sin\theta \quad (5.23)$$

Now, equating the driving term of Equation 5.23 with the time derivative term in Equation 5.20 it follows that

$$\nabla^2 V - \frac{1}{u^2} \frac{\partial^2 V}{\partial t^2} = (E E'/2V_c^2) \cos(V/V_c) \tau_v \frac{\partial V}{\partial t} \quad (5.24)$$

³ In Sine-Gordon wave theory [78] θ is actually $\theta/4$ which enables $\tan\theta$ to cover the range from zero to ∞ while θ goes from zero to $\pi/2$.

and this is consistent with Equation 5.22 only if,

$$\frac{\tau_v}{V_c} \frac{\partial V}{\partial t} = \tan \theta \quad (5.25)$$

A comparison now of this with standard solutions of the Sine-Gordon equation gives,

$$\frac{\tau_v}{V_c} \frac{\partial V}{\partial t} = e^{\left(\frac{x/\lambda - t/\tau_v}{\sqrt{1-U^2}} \right)} \quad (5.26)$$

Where U is a normalized wave velocity [78]. Since V' also satisfies the SHE, the imaginary velocity of Equation 5.17 assures that the exponential function $V' = V_c \exp \Psi$ of the variable, where $\Psi = j(x/\lambda - t/\tau_v)$, will satisfy the diffusion equation in V' which reverts to the SHE when Equation 5.14 is also satisfied. It will be noted that by comparison with $V'/V_c = \exp \Psi$ only the nature of the phase Ψ of the wave function θ is altered in changing from the static to the dynamic potential functions. This again is similar to the role played by the wave function in a Gauge transformation [Appendix D] of the first kind in electromagnetic theory [79].

Integration of Equation 5.25 in time yields a value of V given by $-\tau_v(\partial V/\partial t)(1-U^2)^{1/2}$ which corresponds to the maximum value attained and the corresponding gradient is the maximum electrostatic field strength, E_c . It readily follows that E_c could be written as $-\nabla V$, in this way when $E/E_c = (x/\lambda - t/\tau_v)/(1-U^2)^{1/2}$ and hence

$$\frac{\tau_v}{V_c} \frac{\partial V}{\partial t} = e^{(E/E_c)} \quad (5.27)$$

where E is the electric field variable and E_c is the maximum value with which it is normalized.

The previously concealed variable, θ thus appears in order to describe the interaction of a Beltrami field with a Sine-Gordon solitary wave. In this interaction $\nabla \cdot \mathbf{E}'$ is a function of θ which is a normalized potential. Furthermore, θ is undetermined with respect to V/V_c by any multiple of 2π , the addition of which to θ would leave Equation 5.22 invariant. Such quantized changes in V/V_c correspond to the transition in which electrons are detrapped, diffuse away with the renormalized temperature T^* , and trapped again with the added electric field from non-electrostatic terms.

5.4 COMPUTER SIMULATION

5.4.1 THE ITERATION EQUATION OF THE THEORETICAL MODEL

Electrons are detrapped from individual locations and remain free for a very short time during which they diffuse uniformly in all directions to remote sites and retrap again. A density gradient is thus created with a deficit of electronic charge nearer to the origin and the electrostatic field is screened. There is a thermal equilibrium between the trapped electrons and the positive charge representing this deficit so the reorganized

potential distribution is satisfied by a Poisson-Boltzmann equation.

$$V = \frac{q}{4\pi\epsilon_0 r} e^{(-r/\lambda)}, \quad V = \frac{V_0}{r} e^{(-r/\lambda)} \quad (5.28)$$

where V_0 is a constant value. This thermal displacement of charges however takes place by free electron motion at the free electron temperature T^* . Equation 5.27 should also satisfy the Poisson-Boltzmann Differential Equation (PBDE) $\nabla^2 V - V/\lambda^2 = 0$. The Boltzmann special equation moreover indicates that,

$$\rho_e = \rho_e' e^{(-e(V - \tau_v \partial V/\partial t)/kT)} \quad (5.29)$$

Where ρ_e' and ρ_e are in thermal equilibrium at the temperature T . The exponent above the term $e\tau_v(\partial V/\partial t)/kT$ could be replaced by $e\tau_v uE/kT$ to indicate that V is stationary in the frame of the wave moving at the speed $u = \lambda/\tau_v$. There are however three possible values for the characteristic length whose relationships follow from the energy balance equation. In the transition from the electrostatic to the electrodynamic state the potential V is shifted to $V + 3kT^*/2e$. It follows directly moreover from the SHE that $\rho_e V = -\epsilon E^2$ and upon shifting the potential V as indicated above, the result of new energy balance is then

$$\rho_e V + \frac{3}{2} n_e^* kT^* = -\epsilon E^2 \quad (5.30)$$

where $n_e^* = \rho_e^*/e$ is the density of the briefly liberated electrons. After normalizing

with respect to $n_e^* T^*$ and by giving $n_e^* T^* = n_e T$, the equation above reduces to,

$$(\lambda_o / \lambda_D)^2 + \frac{3}{2} = (\lambda / \lambda_D)^2 \quad (5.31)$$

where $\lambda_o^2 = \epsilon V / \rho_e$, and $\lambda^2 = -(E / \nabla \bullet E)^2 = -(V / \nabla V)^2 = \epsilon V / \rho_e'$ is defined by the Poisson equation and SHE $\nabla^2 V + V / \lambda^2 = 0$ (Equation C.6). $\lambda_D^2 = \epsilon kT / \rho_e e$ is defined as the Debye length. Now normalizing with respect to λ_D^2 to provide a second relationship between $(\lambda_o / \lambda_D)^2$ and $(\lambda / \lambda_D)^2$, Equation 5.31 could also be rewritten as,

$$(\lambda / \lambda_D)^2 = \frac{3}{2} + (\lambda / \lambda_D)^2 \frac{\rho_e'}{\rho_e} \quad (5.32)$$

Hence by defining $\rho_e' / \rho_e = \theta = V / V_c$ and with the aid of Equations 5.27 and 5.28 and this expression validates the SHE. Now ρ_e' and ρ_e in Equation 5.28 can be given in terms of λ^2 and λ_o^2 by using the results from Equation 5.31,

$$(\lambda / \lambda_D)^2 = \frac{3}{2} + (\lambda / \lambda_D)^2 e^{(\epsilon(V + \tau_v \partial V / \partial x) / kT)} \quad (5.33)$$

Moreover $eV / kT = E_c / E$ follows from the SHE as follows. The PBDE applies to large numbers of point charges in thermal equilibrium but in our case it concerns the equivalent of similar numbers of dipoles superposed upon a uniform negative charge density. A potential distribution for any dipole can be obtained by transforming the gradient of V from that with respect to the field point to that with respect to the source

point [77]. The field strength and consequently its divergence then reverses sign but remains the same in magnitude. Thus the PBDE changes to the SHE which can be written as $\nabla \cdot (\nabla \nabla V) = 0$ and ∇E is consequently constant because $\text{curl}(\nabla \nabla V) = 0$ too. The final equation is

$$(\lambda/\lambda_D)^2 = 3/2 + (\lambda/\lambda_D)^2 e^{(\frac{E_c}{E} - \frac{E}{E_c}(\lambda/\lambda_D))} \quad (5.34)$$

Equation 5.33 shows $(\lambda/\lambda_D)^2$ to be a function of itself and so must be treated as an iteration algorithm. The potential V shifts in quanta of $3n_e kT/2$ as indicated in Equation 5.29 and since V is proportional to ρ_e for a scalar Helmholtz field then ρ_e and thus λ_D^2 will change, hence further perturbing V .

5.4.2 COMPUTER-GRAPHICAL METHODS

In the past ten years, a new branch of mathematical method was developed which is called "experimental mathematics" or computer-graphical methods. This new branch deals with all the theory of complex dynamic systems, such as the chaotic motion of a fluid which is one of the typical examples. The "experimental" here refers primarily to computers and computer graphics. Computer graphics allows the viewing of dynamical processes as they evolve [82]. Dynamic systems usually can be described through three factors: (a) it is subject to lasting changes of the system; (b) their complexity, i.e.,

dependence upon many parameters; (c) their iterative nature, the laws that govern their behaviour being described by feedback. The general feedback scheme form is shown in Figure 5.12.

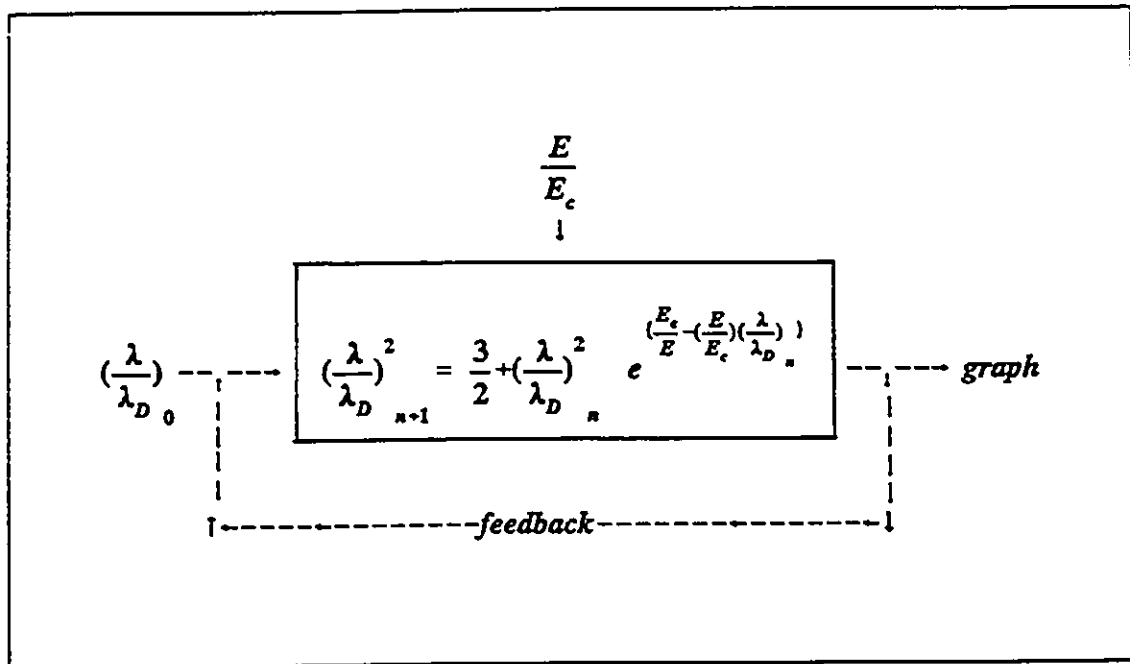


Figure 5.12 The theoretical model of the iteration scheme for the EHD model

Theoretical and experimental studies of dynamical systems show that for many nonlinear systems the time history is sensitive to initial conditions and that a precise knowledge of future behaviour is consequently not possible. If the system can vary thus in unpredictable ways, there is no stability or order which is detectable in such behaviour, it apparently is in disorder or in "chaos". In many cases the dynamic system can depend on several parameters. The behaviour of the dynamic system which is dependent on the so called bifurcation parameter is of great interest for our own mathematical model. In particular with our case, the routes to the chaos situation are

controlled by changing the bifurcation parameters [82].

For computer simulation purposes, Equation 5.33 can be rewritten according to the computer algorithm given in Figure 5.13

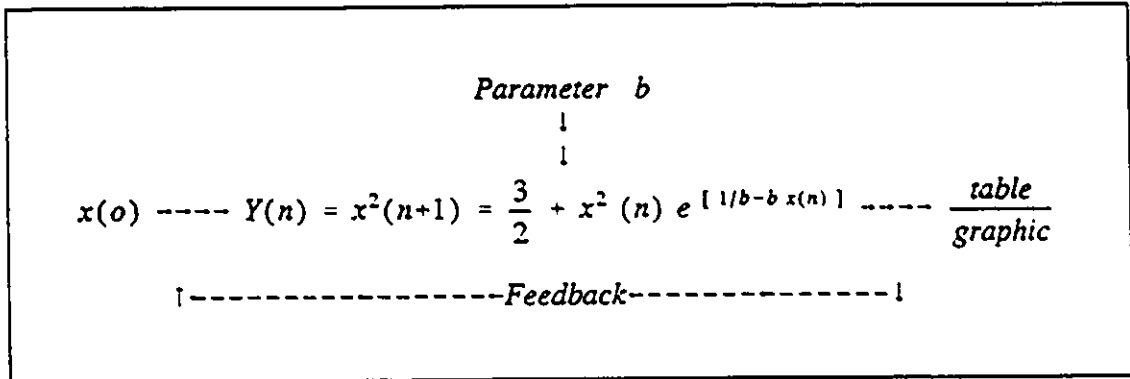


Figure 5.13 The calculation of the iteration scheme for the EHD model

where $b = E/E_c$ is a normalized electrical field, $x = (\lambda/\lambda_D)$ is defined as a normalized scale length and $Y = f(x) = x^2$. For any particular fixed value of b , the value of Y can be calculated ⁴ from an arbitrary starting value x_0 , and using Figure 5.13, a new x_1 is found. The result x_1 becomes the initial value for the next stage and x_2 will be calculated and so the process repeats itself. Table 5.1 shows the calculation from x_1 to x_5 and Y_1 to Y_5 by using six given b values in the range from 0.17 to 0.27 with $x_0 = 5.0$.

⁴ Except $X_0 \leq 0$ or X_0 out of the curve length, in either case, Y value will be trapped in an endless loop

Plotting Table 5.1 results in Figure 5.14 which shows that for each b value ($b = 0.17, 0.19, 0.21, 0.23, 0.25, 0.27$), it may have one or several different corresponding Y values. To gain an understanding of this dynamic system, carrying out the feedback process for just six b -values is not sufficient. In other words, when the simulation is computed using only six b -values, there is no regularity to be seen on the graph (Figure 5.15), the Y values appear to be more or less disordered.

Now by increasing the b value from 6 to 70 points in the same range, and at same time increasing the number of iterations to 40 instead of 5 in computing the Figure 5.13, the simulation result is shown in Figure 5.15 with Y as a function of b . It can be seen that the curve tends towards a single value or many such values as the iteration number increases. From Figure 5.15, it may also be noticed in this case that when b is greater than 0.2 the lines get closer and closer together, as the number of iterations increased. This means that after a sufficient number of iterations the system will settle to one value of Y when $b \geq 0.25$, but this may be achieved after only a few or many such iterations, depending on the value of x_0 chosen at the start. Moving further down the b parameter scale to 0.24 two such values of Y (states) are shown to result from the iterative process and the solution jumps back and forth between them if there are enough iterations carried out. This is known as the bifurcation phenomenon. Further down the b scale at 0.2 there are four such states and again the system will jump between them for a sufficiently large number of iterations (" sufficient" being determined by the starting value x_0). By consideration of Figure 5.15 for progressively lower values of $b = E/E_c$,

this process of division into more and more states for any one b value continues. Very quickly however a value of $b < 0.175$ will be reached below which each state is indistinguishable from its neighbours. Since the solution jumps from one to another this appears as a chaotic process.

It is understood that as the electric field level is very high, there is only one value for $(\lambda/\lambda_D)^2$ (or the slope s). If the field stress value decreases to a certain level, $(\lambda/\lambda_D)^2$ there will be two final slope values, it bifurcates. The results show further bifurcations as the electric field further decreases and finally it goes to chaos. Figure 5.16 is the computation result of carrying out the iteration procedure for 40 iterations without drawing points, followed by another 30 iterations while plotting the resulting points.

To get a better idea of how each singular Y result is determined for any particular parameter value, a computer graphics program gives a very clear explanation. It can be seen that Figure 5.13 is the equation of a curve which is concave to the abscissa with its vertex determined for different values of b . This is hence analogous to the situation described by the logistic equation which has been extensively studied iteratively [84].

Another method to study the "feedback effect" in this equation is by using a graphical iteration technique which develops a visual sense for the process of iterating Y . The graphical iteration takes place in the following way [84] seen in Figure 5.17: beginning with setting an x -value x_0 , a vertical line at x_0 will hit the curve at height Y_0 .

$= f(x_0)$ by using the Equation 5.33. To iterate Y , a new vertical line must be drawn and located at the new x -value x_1 equal to the square root of Y -value, ie. $x_1 = \sqrt{Y_0}$. This is where the line $Y = x^2$ becomes involved. Now staying at Y_0 point, simply by moving it over horizontally until it hits the $Y = x^2$ line, a new x -value x_1 is found. By drawing a second vertical line a Y_1 value will be found at the intersection point between the second vertical line and the curve, and so on. This is the initial value for the next stage of the feedback. This process can go from tens to hundreds of iterations and in this case $n = 40$ is used.

Table 5.1 The Data for 5 Iterations in EHD Modelling

	n *	1	2	3	4	5
b= 0.17	x(n)	5	61.92	6.19	69.31	3.83
	y(n)	3833.83	38.39	4803.69	14.57	2743.6
b= 0.19	x(n)	5	43.26	9.97	63.48	4.69
	y(n)	1868.4	99.33	2888.53	21.99	1743.6
b=0.21	x(n)	5	32.01	12.07	36.775	8.46
	y(n)	1024.79	145.75	1352.4	71.52	1417.97
b=0.23	x(n)	5	24.77	12.67	25.97	11.59
	y(n)	613.48	160.71	674.46	134.26	723.9
b=0.25	x(n)	5	19.81	12.36	19.52	12.63
	y(n)	392.57	152.82	380.96	159.57	371.83
b=0.27	x(n)	5	16.27	11.59	15.49	12.25
	y(n)	264.61	134.44	239.96	150.64	224.42

* n is the number of iterations.

This procedure will be explained further with four distinct results in the following four figures. Figure 5.17 shows Y as a function of x in curve at $b = 0.26$ and $Y = x^2$ as the feedback function. After 40 iterations the final value with a spiral track shown in Figure 5.17 approached to one point at $Y = 220$. In all the cases the horizontal and vertical lines tend towards segments of the original curve which correspond to limiting x -values. Clearly the two final vertical lines shown in Figure 5.18 represent two different Y -values as well as x -values when b is increased to $b = 0.2$. This indicated the results of bifurcating to two values. When comparing this result with Figure 5.15 it shows that, as $b = 0.2$ and 0.26 , these corresponding Y values have either one or two solutions. In other words, Figures 5.17 and 5.18 give the computer simulation results as plots made possible by the use of a the computer graphics program.

Figure 5.19 and 5.20 show what will happen in the computer simulation after the results are further bifurcated when $b = 0.19$ and 0.17 . Figure 5.19 shows that four final Y values appear on the curve which means there are four stable solutions under $b = 0.19$. The sequence of these four solution values appear in a form such that they cycle to and from four separate points as shown in Figure 5.19. Figure 5.20 shows the result after further bifurcation, the typical chaotic example as $b = 0.17$ in this case. For each iteration, a new y value is obtained which is different from the previous one. As a result, there are not any final stable solutions to be found, regardless of the number of iterations. In fact, the solution values will cover all of the parabola shown in Figure 5.20. When compared to Figure 5.16 at $b = 0.17$, the resultant Y values cover the

entire range of possibilities.

5.4.3 COMPARISON WITH EXPERIMENTAL RESULTS

Equation 5.33 shows the iterative algorithm followed in maintaining such a field. A graph of (λ/λ_D) as a function of E/E_c has been presented in Figure 5.16. Furthermore Figure 5.16 has been replotted in Figure 5.21 with the ordinate and abscissa modified according to Equations 5.29 and 5.32. In order to make a valid comparison with the experimental results, a proper scaling factor has been chosen to fit with the experimental data as indicated. On the basis of this, $(\lambda/\lambda_D)^2$ in Figure 5.16 can be converted to s in Figure 5.21 by using the renormalized factor $f^2 = T^*/T$, and $(\lambda/\lambda_D)^2 = 2\pi f^2 s$ [83]. Thus, choosing $f^2 = 618.8$ in order to fit data closely. The convention between V_m show in Figure 4.34 and E/E_c in Figure 5.16, the following expression is used $V_m = \exp \{200 E/E_c - 36\}$. As a result, therefore, the two dotted lines in Figure 5.21 are the results from the computer simulation of Equations 5.29, 5.32 and 5.33 and the data points are presented along with the experimental results. Figure 5.21 shows the upper slope s_u and lower slope s_l as a function of maximum applied voltage V_m , the high field slope values s_u , are observed to vary much more strongly with the applied voltage than the lower are. Aluminum and copper electrodes show the same phenomena. Both upper and lower slopes merge into a single power law tending to the value $3/2$ as the maximum applied voltage becomes very large. This had been mentioned earlier in Chapter 4 and can be seen in Figure 4.34.

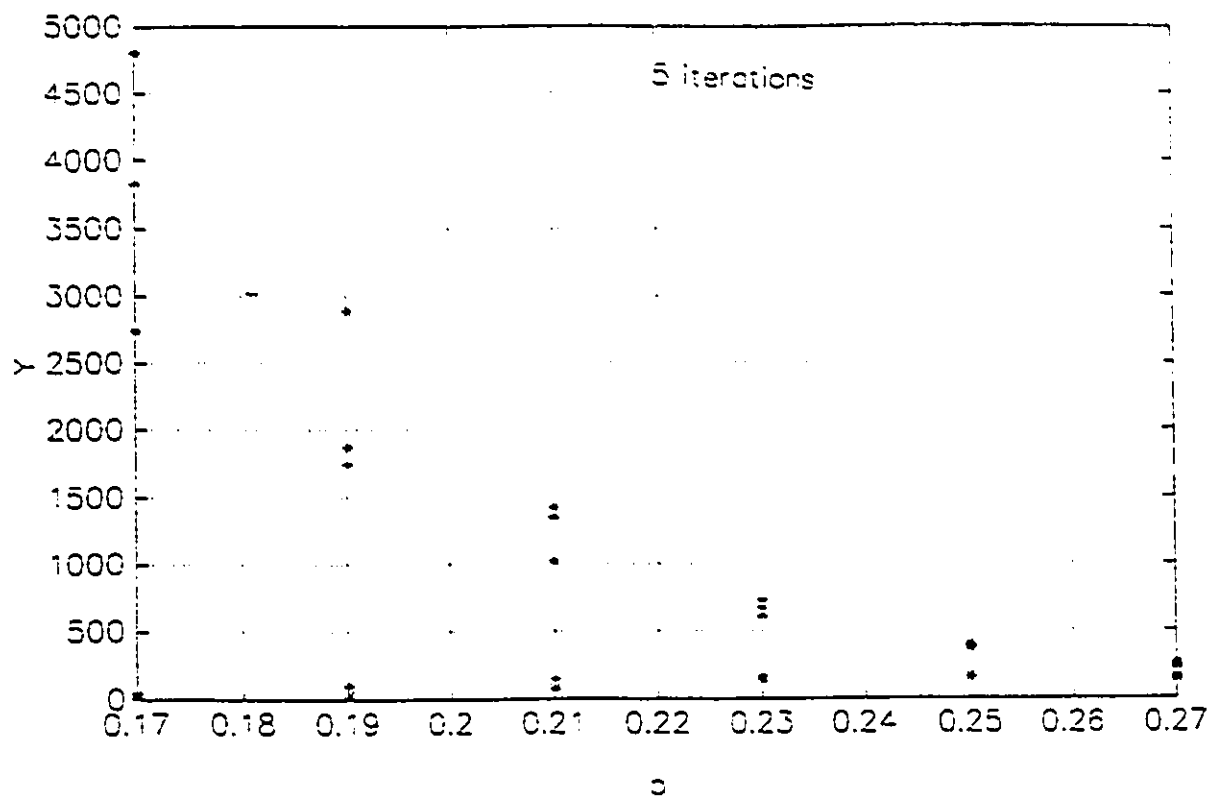


Figure 5.14 Simulation results for Y as a function of b , after 5 iterations

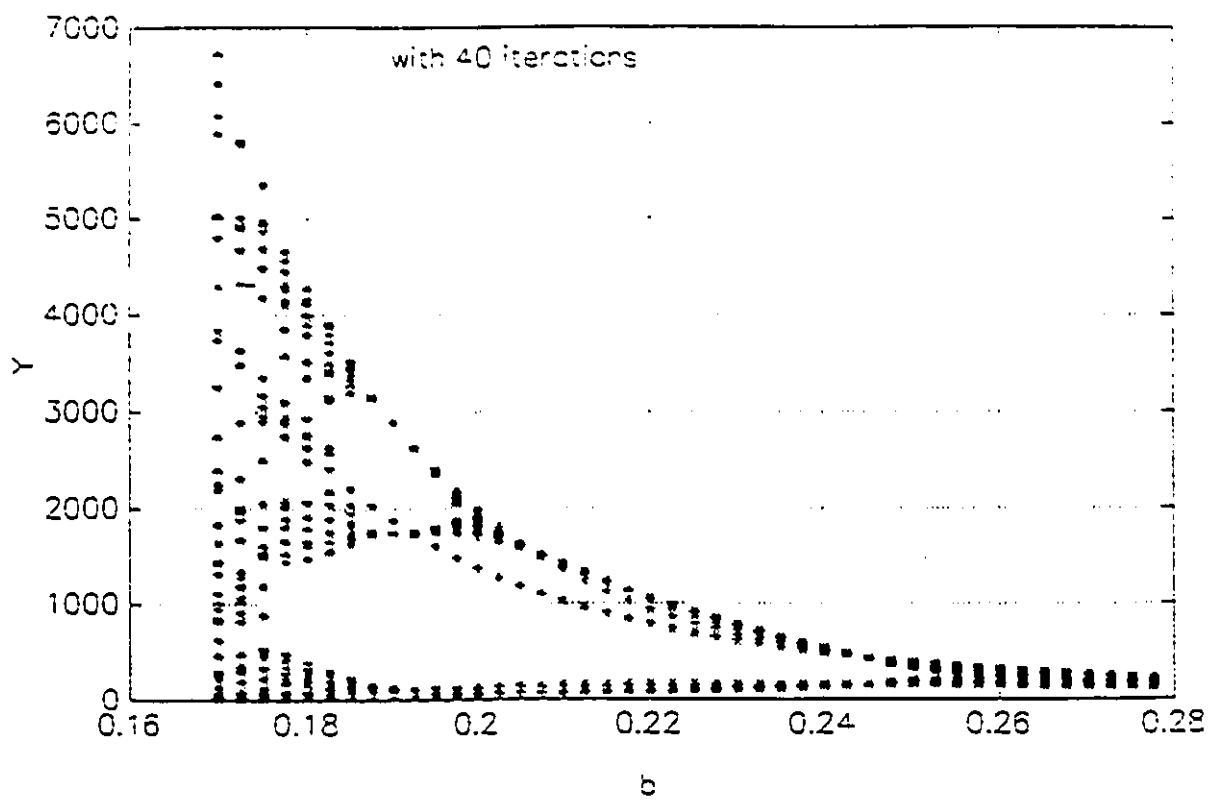


Figure 5.15 Simulation result for Y as a function of b , after 40 iterations

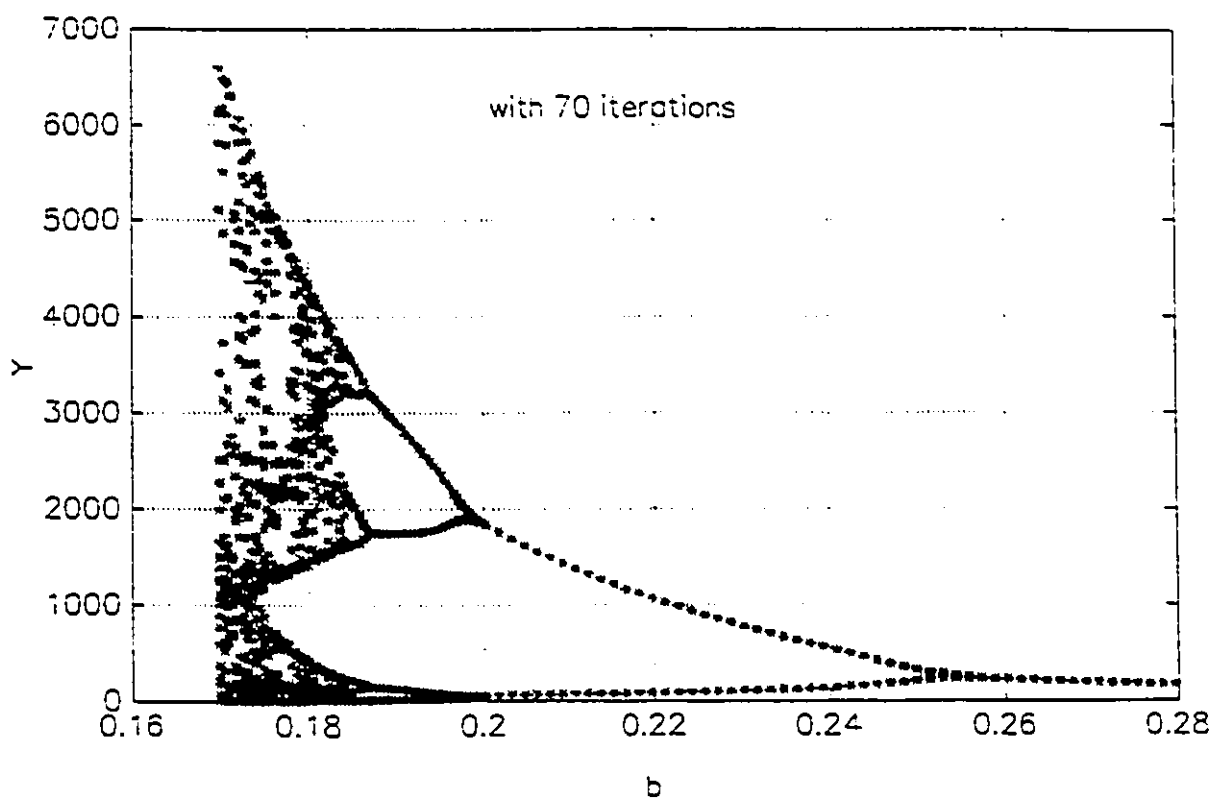


Figure 5.16 Simulation result of Y as a function of b , after 70 iterations

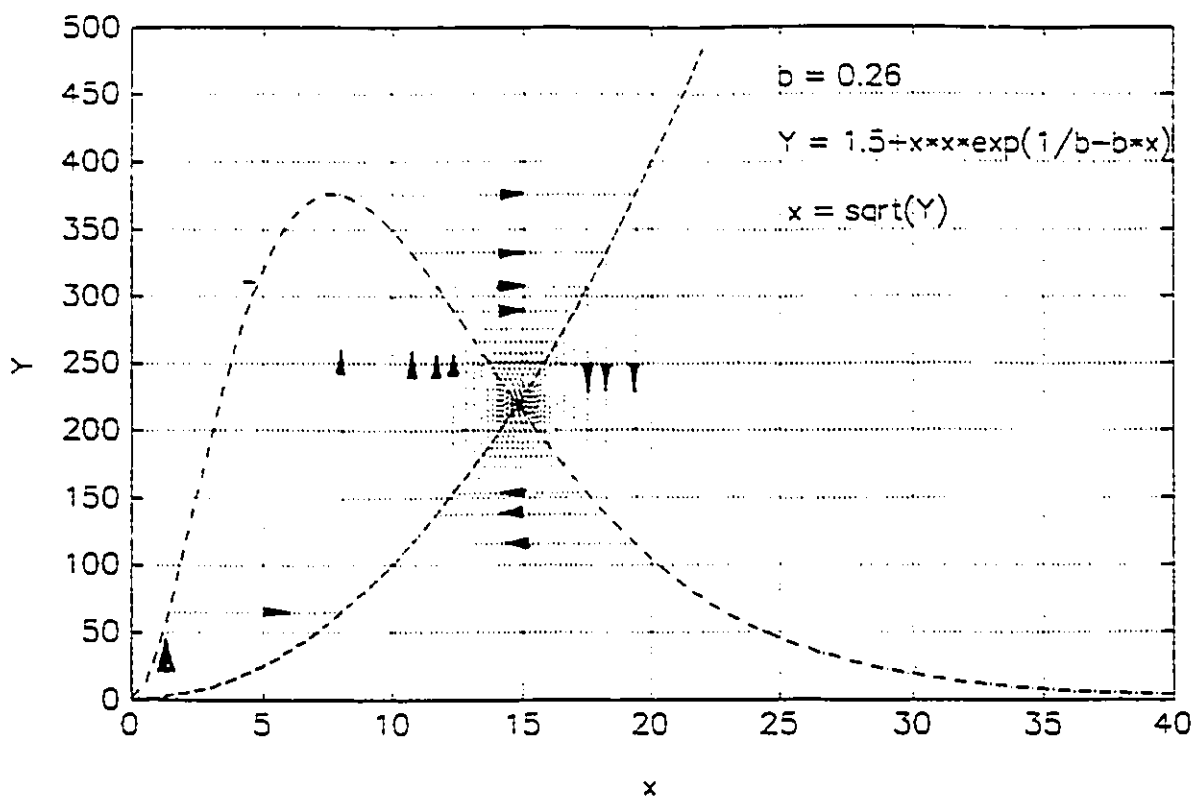


Figure 5.17 Iteration process for Y as a function of x

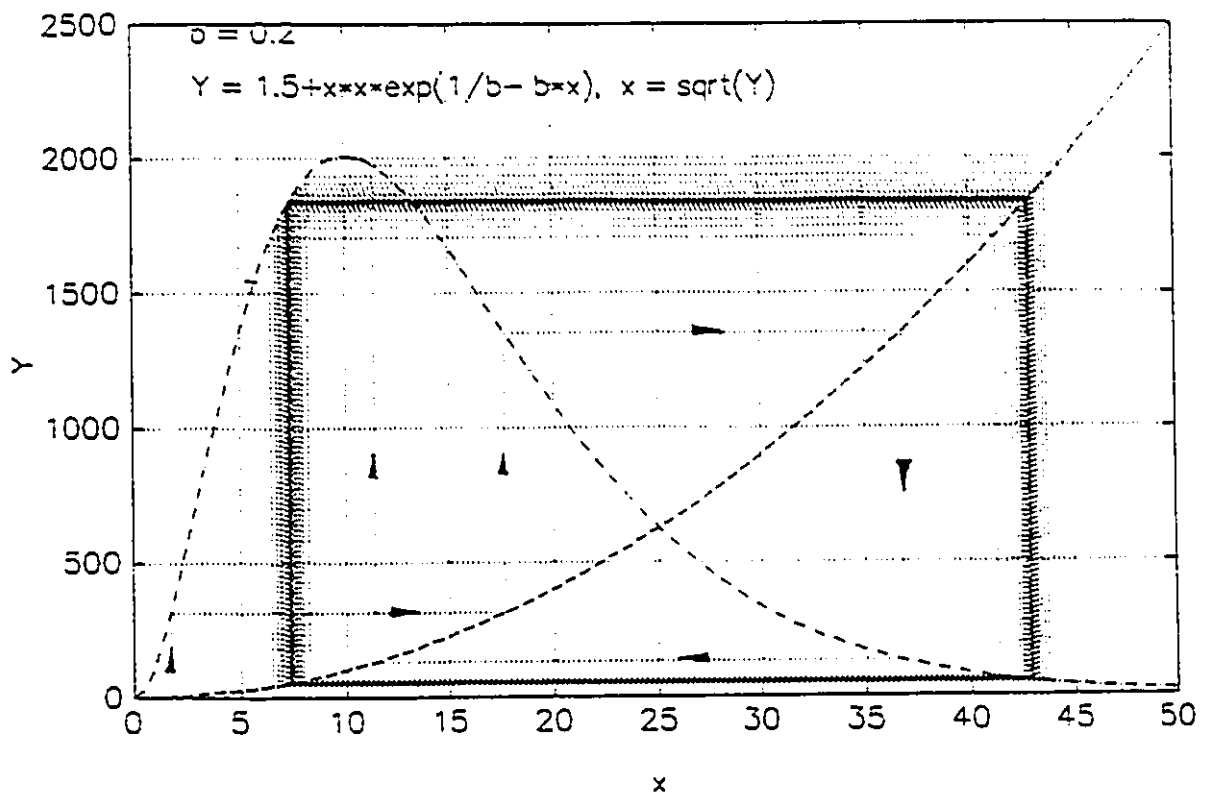


Figure 5.18 Iteration process for Y as a function of x , exhibiting single bifurcation

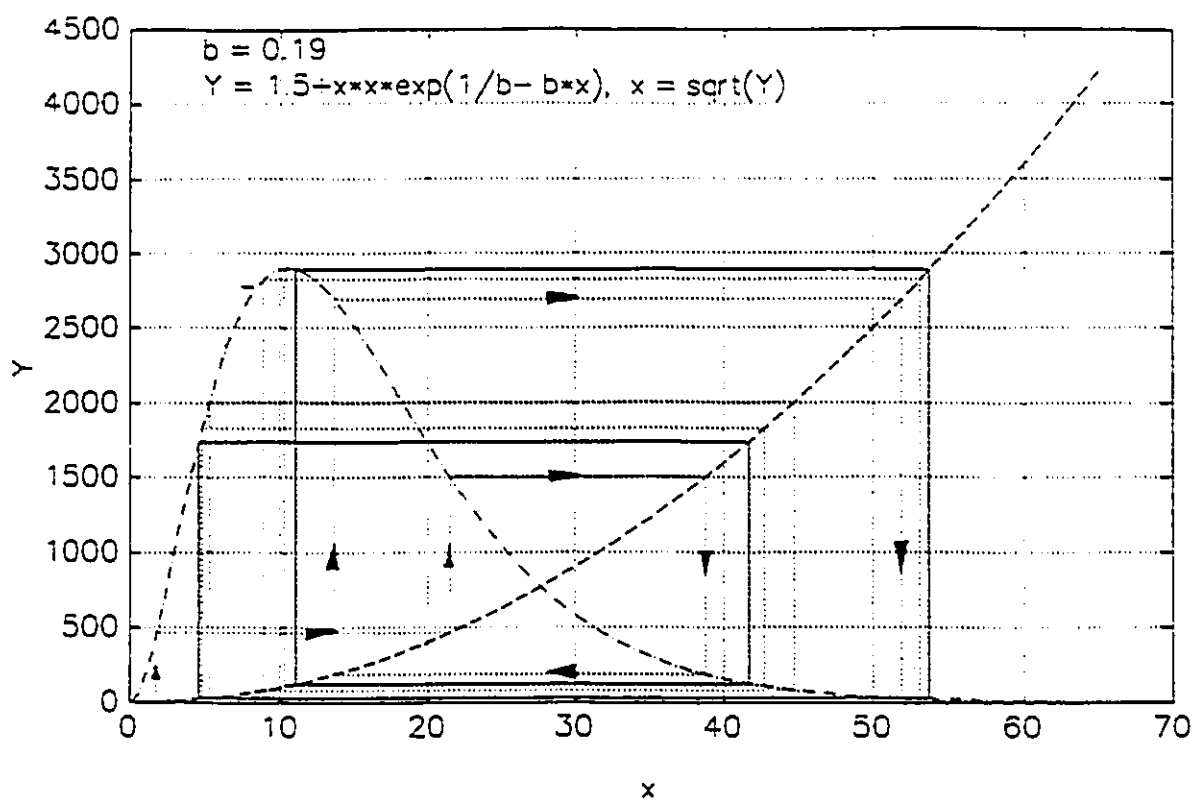


Figure 5.19 Iteration process for Y as a function of x, exhibiting multiple bifurcation

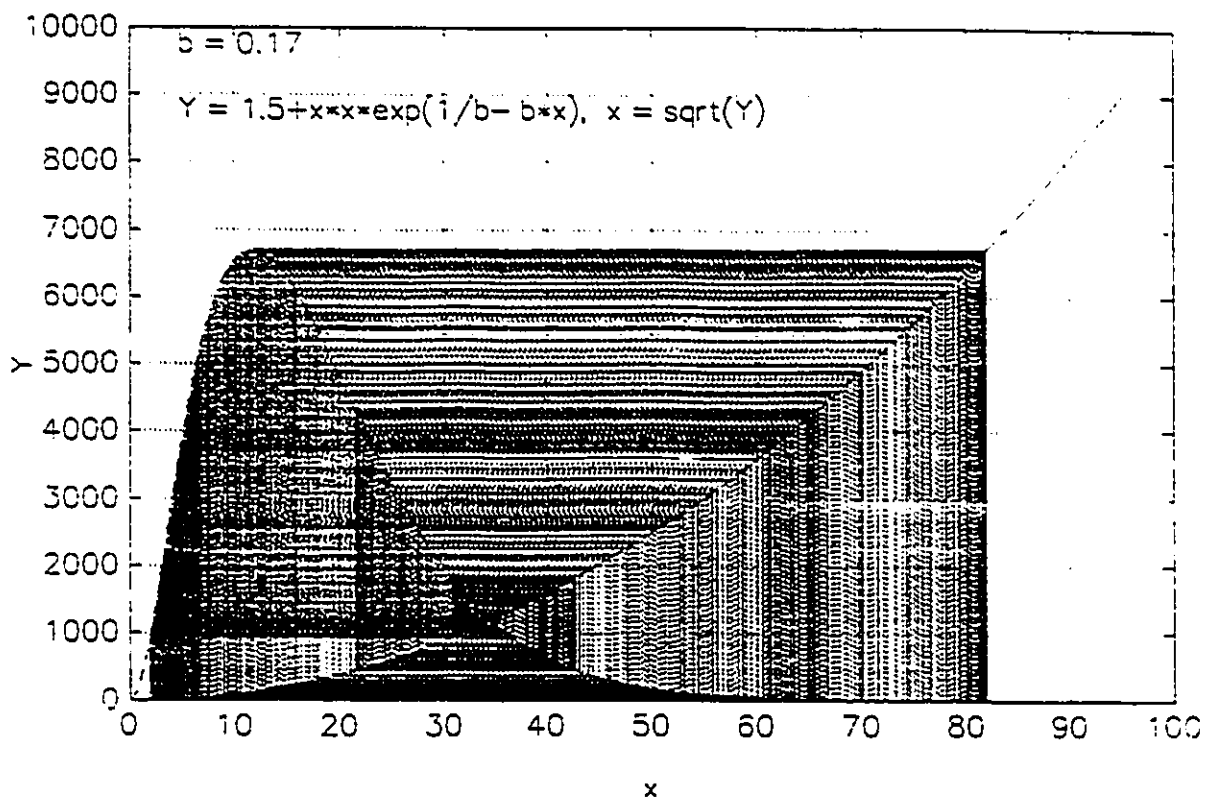


Figure 5.20 Iteration process for Y as a function of x , exhibiting chaotic case

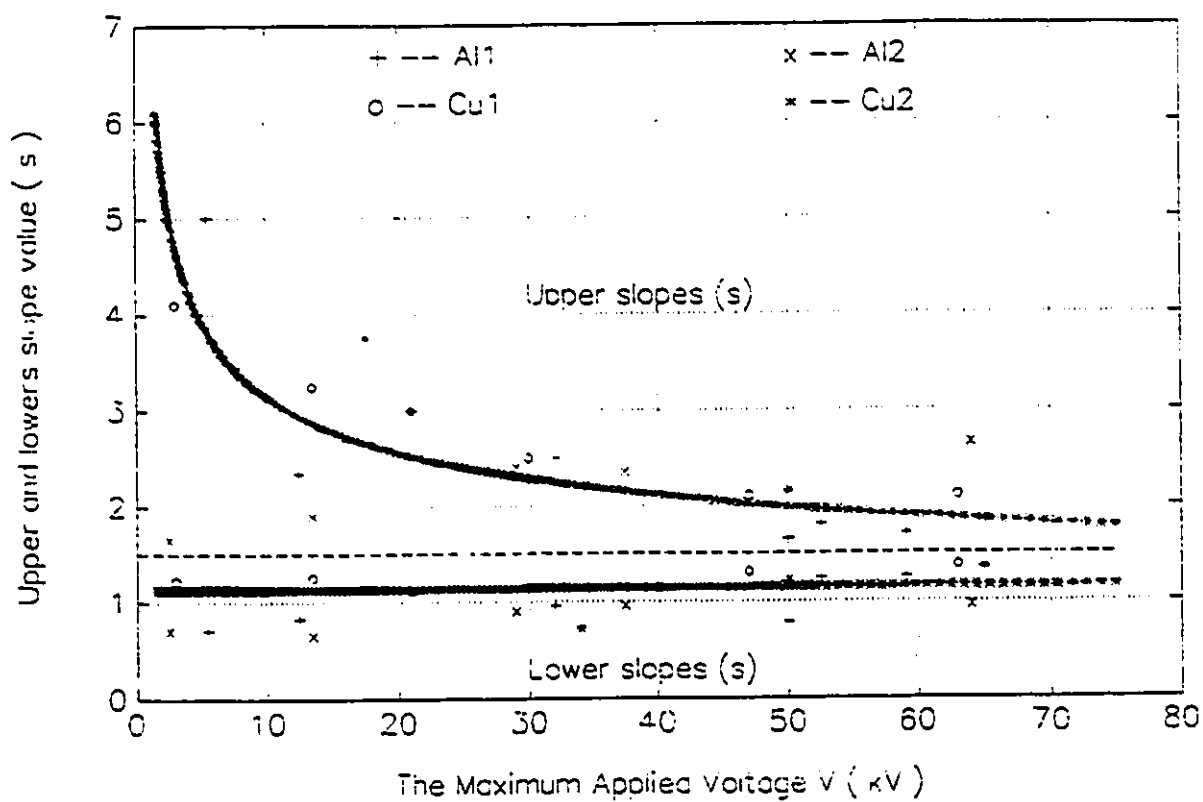


Figure 5.21 The slope value as a function of maximum applied voltage from both experimental data and computer simulation results

5.5 EHD TURBULENCE AND THE α -EFFECT

5.5.1 EXPERIMENTAL RESULTS

It is known that EHD movement is involved when a dielectric liquid is subjected to high electric field stress [51]. Recently, Watson and Chang developed a new concept pertaining to dielectric liquid EHD theory, involving EHD turbulence and the so called α -effect [89]. It has also been reported that any particles which may be present in the liquid and which are lighter than the fluid, travel with the surrounding fluid. These particles eventually migrate to the centres of the convection cells in the turbulent state where the fluid velocity diminishes to zero [93]. If these statements are accepted as being true, then the presence and movement of a bubble in a liquid can be used to indicate the existence of EHD turbulence. A thirty minute long video tape was made of the experiment while it was being conducted. Several bubbles injected into the dielectric liquid in the course of filling the test cell before the test was started remained throughout the experiment as indicators of the turbulent state.

The experimental conditions were the same as those of the previously described (Chapter 3) investigations. When the maximum applied voltage was relatively low, such as 10 kV and 20 kV with a 3.1 mm electrode gap distance, there was no sign of bubble movement. As the maximum applied voltage was increased from 30 kV to 55 kV, turbulent movement of the bubbles in the liquid showed clearly in the video taped record

of the experiment. The majority of the bubbles moved randomly about the liquid. Figure 5.22, shows a typical example of this behaviour. This figure contains a series of consecutive photographs taken from a two second long portion of the video taped record in the case of the 55 kV applied voltage. In these photographs a bubble is seen in the inter electrode gap to the right of the electrode centre line (see arrow). Through the series of consecutive photographs the indicated bubble is seen to travel in a clockwise circular path. The bubble completes two circular orbits before being ejected from the interelectrode region by extreme fluid turbulence. Given the electrode gap dimension and the time between consecutive photographs, the velocity of the indicated bubble is estimated in this case to be around 3 – 30 mm/sec. It should be noted that the dielectric liquid turbulence eventually grew to fill the entire test cell.

5.5.2 THEORETICAL CONSIDERATIONS [94]

When beltramions [82] are influenced by an applied electric field electrons are temporarily liberated and before translating to another trap they possess a velocity, u_e , which is superimposed upon the local Beltrami flow velocity, u . In general u_e is not parallel or antiparallel with u and so $(u_e + u) \times \omega \neq 0$. The Navier-Stokes equation can be written in $u \rightarrow u_e + u$ as the fluid velocity variable. Thus,

$$\frac{\partial u}{\partial t} + \omega \times u = -\nabla \left(\frac{p}{\rho} + \frac{u^2}{2} + \rho_e \frac{V}{\rho} \right) - \nu \nabla \times \omega \quad (5.35)$$

When $u_e = 0$ then

$$v \nabla \times \omega = -\frac{\partial u}{\partial t} = \frac{u}{\tau_v} \quad (5.36)$$

leads to the Vector Helmholtz equation defining Beltrami flow and $\omega \times u = 0$. The treatment of the case in which u_e is not equal to zero will be postponed until later. Thus

$$\nabla \left(\frac{p}{\rho} + \frac{u^2}{2} + \rho_e \frac{V}{\rho} \right) = 0 \quad (5.37)$$

or

$$\rho_e \frac{E'}{\rho} = -\nabla \left(\frac{p}{\rho} + \frac{u^2}{2} \right) \quad (5.38)$$

Since

$$\nabla \left(\frac{u^2}{2} \right) \equiv u \times \omega + (u \cdot \nabla) u \quad (5.39)$$

then, if $p/\rho = \text{constant}$, it follows that,

$$\rho_e \frac{E'}{\rho} = \omega \times u - (u \cdot \nabla) u \quad (5.40)$$

Now, considering the quasiparticle to be situated in an applied poloidal field with

potential V , the local potential will be the sum of this and the internal potential which is negative (binding potential field). Thus Equation 5.40 above will undergo a change in sign of E' due to this arising from the binding potential field. In addition there will be an additional term $\rho_e E/\rho$ from the applied field. Hence

$$\rho_e \frac{E'}{\rho} - \rho_e \frac{E}{\rho} = \omega \times u - (u \cdot \nabla) u \quad (5.41)$$

This can now be partitioned into

$$\rho_e \frac{E'}{\rho} = \omega \times u, \quad \rho_e \frac{E}{\rho} = (u \cdot \nabla) u \quad (5.42)$$

and in the frame of reference in which

$$\frac{du}{dt} \equiv \frac{\partial u}{\partial t} + (u \cdot \nabla) u = 0 \quad (5.43)$$

then,

$$\rho_e \frac{E}{\rho} = -\partial u / \partial t \quad (5.44)$$

Now, returning to the Navier-Stokes equation, this partitioning leads to the conclusion that,

$$\omega \times u = -\nabla \left(\frac{p}{\rho} + \frac{u^2}{2} \right) - \frac{V \nabla \rho_e}{\rho} - \nu \nabla \times \omega \quad (5.45)$$

and thus if,

$$\frac{V \nabla p_e}{\rho} = -v \nabla \times \omega \quad (5.46)$$

then

$$\nabla \left(\frac{p}{\rho} \right) + (\mathbf{u} \cdot \nabla) \mathbf{u} = 0 \quad (5.47)$$

or, from Equation 5.43, when $p/\rho = \text{constant}$, then

$$\frac{\partial \mathbf{u}}{\partial t} = 0 \quad (5.48)$$

Thus the significance of Equation 5.46 can be that it guarantees a steady flow solution as defined by Equation 5.48.

According to Equation 5.44 however $\partial \mathbf{u} / \partial t \neq 0$ and so $\nabla(p/\rho)$ can no longer be considered as being zero, Instead, we have,

$$\nabla \left(\frac{p}{\rho} \right) = \rho_e \frac{E}{\rho} \quad (5.49)$$

or,

$$\nabla p = \rho_e E \quad (5.50)$$

Thus Equation 5.46 is now seen as the necessary consequence when an electrostatic

pressure balance is achieved inside the beltramion. Equation 5.46 can now be written in terms of the virtual polarization

$$P_v \equiv \epsilon V \nabla \rho_e / \rho_e \quad (5.51)$$

Thus,

$$P_v = -\rho \frac{\epsilon}{\rho_e} v \nabla \times \omega \quad (5.52)$$

and if the mobility of charges, b , is written as,

$$b \equiv \rho_e \frac{\tau_v}{\rho} \quad (5.53)$$

then

$$P_v = -\frac{\epsilon \tau_v v}{b} \nabla \times \omega = -\frac{\epsilon \lambda^2}{b} \nabla \times \omega \quad (5.54)$$

It is clear now from this expression that,

$$\nabla \cdot P_v = 0 \quad (5.55)$$

and, according to the equation

$$\begin{aligned} \nabla \times \omega &= \omega / \lambda \\ \text{then } P_v &= -\frac{\epsilon \lambda}{b} \omega \end{aligned} \quad (5.56)$$

Also, by virtue of the Einstein relation,

$$v \equiv b \frac{kT}{e} \quad (5.57)$$

then

$$\mathbf{P}_v = -\frac{ekT}{e} \tau_v \nabla \times \boldsymbol{\omega} \quad (5.58)$$

The significance of these expressions lies in the condition that \mathbf{P}_v will be represented in the moving reference frame by,

$$\frac{D\mathbf{P}_v}{Dt} \equiv \frac{\partial \mathbf{P}_v}{\partial t} + \mathbf{u} \cdot \nabla \mathbf{P}_v + \nabla \times (\mathbf{P}_v \times \mathbf{u}) \quad (5.59)$$

Hence, according to Equation 5.55 then

$$\frac{\partial \mathbf{P}_v}{\partial t} + \nabla \times (\mathbf{P}_v \times \mathbf{u}) = \frac{D\mathbf{P}_v}{Dt} = v \nabla^2 \mathbf{P}_v \quad (5.60)$$

where \mathbf{P}_v is considered to diffuse across the boundary of the moving Beltrami flow cell.

Moreover, Equation 5.56 leads to the conclusion that Equation 5.60 can also be written in $\boldsymbol{\omega}$ as the vector variable since it is directly proportional to \mathbf{P}_v . Hence

$$\frac{\partial \omega}{\partial t} + \nabla \times (\omega \times u) = \nu \nabla^2 \omega \quad (5.61)$$

This can be obtained also by taking the divergence of the Navier-Stokes equation, Equation 5.35, and so it validates Equation 5.56 as well as the assumption that P_v diffuses across the boundary.

Since there is diffusive transfer of P_v across the quasiparticle boundary the process can also be visualized as an expansion of the boundary into the surrounding fluid. The boundary is defined by the characteristic Debye length, λ , where,

$$\lambda^2 \equiv \frac{\epsilon k T}{\rho_e e} \quad (5.62)$$

and ρ_e , being a variable in the Beltrami flow field, is necessarily decaying according to $\exp \{-t/\tau_v\}$. Hence this implies that λ^2 must grow exponentially at the rate $\exp \{-t/\tau_v\}$, thus accounting for the above mentioned expansion of the flow field. The agent of this expansion moreover is the pressure, p , which is in equilibrium with the gradient of electrostatic force as given in Equation 5.50. As ρ_e decays it follows that ∇p (which acts inwardly to bind the particle together) will also decay so that expansion will result. It may also be noted that by substitution of $\omega \times u$ in Equation 5.61 using Equation 5.42 and noting that,

$$\mathbf{E}' \equiv -\frac{1}{\rho_e} \nabla(\rho_e V) \quad (5.63)$$

it follows that

$$\partial \omega / \partial t = \nu \nabla^2 \omega \quad (5.64)$$

from which the Vector Helmholtz Equation is recovered using $d\omega/dt = -\omega/\tau_v$ and $\lambda^2 = \nu \tau_v$.

The importance of Equation 5.60 lies in it being an exact analogue of the equivalent expression in MHD, in which the flux density, \mathbf{B} , is the variable, while

$$\nabla \cdot \mathbf{B} = 0 \quad (5.65)$$

is an additional condition corresponding to Equation 5.55 in \mathbf{P}_v . It was shown initially by Steenbeck, et al [95] that for pairs of expressions such as Equation 5.65 and Equation 5.60 (in \mathbf{B} as the variable) the development of helical disturbances could be amplified into large scale instabilities. By considering \mathbf{B} and \mathbf{u} to be the sums of steady values \mathbf{B}_0 and \mathbf{u}_0 with fluctuating terms \mathbf{b} and \mathbf{u} they were able to show that an expression,

$$\partial \mathbf{B} / \partial t = \nabla \times (\mathbf{u} \times \mathbf{B}) + \eta^2 \nabla^2 \mathbf{B} \quad (5.66)$$

would become,

$$\partial B_o / \partial t = \nabla \times (u_o \times B_o) + \alpha \nabla \times B_o + (\eta + \beta) \nabla^2 B_o \quad (5.67)$$

where η is the magnetic viscosity and is an eddy viscosity while α (unrelated to the usage of α in the present theory) is a term which is non-zero only when the turbulence lacks reflectional symmetry i.e. it will be helical in either the left or right handed sense. Equation 5.67 is known to admit unstable solutions for many geometrical configurations and choices of u_o as a flow field [96].

In the present use an electrohydrodynamic model has been proposed in which electrodynamic body forces act analogously to those in MHD. Thus P_{v0} and u_o will have perturbations P_v and u superimposed and since P_v and ω are proportional this will result in the development of a "vortex dynamo" [97].

The influence of adding the velocity u_e to u in the Navier-Stokes equation is to reduce dramatically the value of the dynamic viscosity, ν , to the level of the electron diffusion coefficient D_e . Electrons diffuse according to,

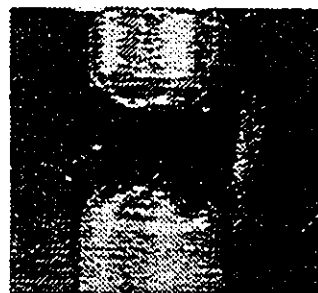
$$D_e \nabla^2 \rho_e = \partial \rho_e / \partial t = -\rho_e / \tau_v \quad (5.68)$$

and thus the scalar Helmholtz equation in ρ_e is obtained with $\lambda^2 = D_e \tau_v$. By taking the gradient of each side of Equation 5.68 the vector Helmholtz equation in P_v is readily obtained with $\lambda^2 = D_e \tau_v$. Since P_v and ω are directly related according to Equation 5.56 then the vector Helmholtz equation in ω is obtained with the same expression for λ^2 .

This equation however is none other than Equation 5.64 for which $\lambda^2 = \nu \tau_v$. It follows therefore that $\nu = D_e$. This is achieved physically by the diffusion of liberated electrons transverse to the flow velocity vector, \mathbf{u} . After retrapping, an electric field, \mathbf{E} , is created and free electrons with velocity $\mathbf{u}_e = b\mathbf{E}$ add an extra velocity component to the motion of charge. Moreover $(\mathbf{u}_e + \mathbf{u})^2 = u_e^2 + u^2$ and the kinetic energy density of the fluid appears to have been increased although in actual fact this is not the case. Likewise the fluid appears to have acquired momentum which is not so. During this diffusion of free electrons with rapid expansion and slower recovery to thermodynamic equilibrium there is brought into operation a mechanism involving a "second viscosity" such as is described by Landau and Lifshitz [98]. The details are given in Appendix F and the effect is incorporated into the incompressible fluid model by introducing a new dynamic viscosity, $\nu^* \ll \nu$.



(a) $t = 0.0$ seconds



(b) $t = 0.06$ seconds



(c) $t = 0.16$ seconds



(d) $t = 0.98$ seconds



(e) $t = 1.11$ seconds



(f) $t = 2.08$ seconds

Figure 5.22 Photographs of bubble movement in castor oil at 55 kV maximum applied voltage

CHAPTER VI

CONCLUSION AND FUTURE WORK

The objective of the present study has been to confirm or at least to define the limits of the theory of current response to the application of ramped high voltage in dielectric liquids. This theory was developed by Watson [89] and proposes the transport of charge through such liquids by means of tiny cells enclosing Beltrami flow fields. Such fields correspond to the force-free fields occurring in magnetohydrodynamic (MHD) systems. Indeed the EHD model underlying this theory is quite analogous to an MHD system. One feature in particular is common and essential to these systems which is the fact that the vector variables decay exponentially in time and the Beltrami flows cells (beltramions) likewise decay. This has the important result that the Debye length, λ , specifying the boundary of such cells, will expand at an exponential rate. The bulk liquid must therefore exhibit instability leading to EHD turbulence. Such turbulence has been studied by Kikuchi [97] and MHD turbulence has been the subject of many investigations following the pioneering work [95]. It was discovered by Steenbeck et al, that helical disturbances in MHD could be amplified by energy input to the fluid, leading to large scale instabilities. This phenomenon is commonly encountered also in meteorology in the form of typhoons as well as in planetary atmospheres. It is known as the α -effect and has been shown to be possible in EHD systems [97]. The experimental observation of bulk liquid instability therefore constitutes evidence of the validity of the model assumed.

It must not be overlooked however that in some cases such as with iso-octyl phthalate liquid (ester oil), the double layers adjacent to the electrodes lead to homocharge layers at these interfaces and this appears to be unsuited for the launching of a Sine-Gordon soliton into the gap which is important for the production of beltramions in its steep electric field wave front [99]. There should be no surprise therefore that this liquid behaves differently from the others investigated. This kind of phenomenon indeed occurs also in transformer oil when it is stressed beyond the turnover point. Thus the limits of application of the EHD theory depend strongly upon the kind of double layer at the electrodes i.e homocharge or heterocharge.

The turnover phenomenon moreover and the V-I characteristic beyond it has led to the discovery of behaviour which is well known in the physical chemistry of other types of dielectric liquid. Thus the capacitance of a semiconducting surface oxide layer has found application here in accounting for the turnover phenomenon [32].

Transverse magnetic fields have been shown previously moreover to influence the V-I characteristic of silicone oil but many earlier studies with other liquids, including transformer oil, have been inconclusive. The present study, by means of the application of a dynamic time varying voltage, has led to the definite observation for the first time of a magnetic influence upon the displacement current. This indicated that the process by which double layer polarization is annihilated at the cathode by electron injection must be strongly dependent upon transverse magnetic fields. Two processes therefore occur

which are influenced by transverse magnetic fields. On the one hand conduction current is influenced slightly in the case of transformer oil, probably by the operation of a kind of Hall effect on free electrons while they are at liberty prior to retrapping. On the other hand displacement current is strongly influenced in such cases but the mechanism is taking place in the double layer region and is left unspecified.

Finally, and most important, was the experimental discovery that the slopes of conduction current s_u and s_l on the Ostroumov plot depended upon the value of the maximum excursion of the applied voltage. The values of s_u fell as the maximum applied voltage increased, reaching asymptotically the value $3/2$ to which the values of s_l also reached from below at a much smaller rate. No method could be found by which to estimate or predict any value of s . A theoretical idea was proposed and tested by a computer simulation of the expected iterative process by which the value of λ was attained. The result showed dramatically that the upper and lower limits of the bifurcation diagram followed precisely the kind of behaviour seen in the experiment. This phenomenon arose from dielectric considerations alone and the influence of electrodes in its behaviour seemed to be minimal at least.

The future work should be focused on understanding the magnetic field influence on dielectric liquids in general. A study of strongly non-uniform electric fields (e.g. needle to plane) effects should be undertaken. Moreover, the mechanism for the effects of the electrode materials on the prebreakdown current should be investigated further.

APPENDIX A

RESIDUAL VOLTAGE AND ITS RESPONSE CURRENT

In the Figure A.1, the test cell portion, including the electrodes, the test cell and the test oil sample, is represented by a capacitor C_t and a resistor R_t , where C_t could be calculated from the standard formula of rod-rod geometry as [70]:

$$C_t = \frac{\pi \epsilon l}{\ln \left(\frac{l}{r} \sqrt{\frac{4d+l}{4d+3l}} \right)} \quad (\text{A.1})$$

where d is the gap distance of 2-7 mm, l is the length of rod, approximately 20 mm, r is the radius of the rod tip, 6.2 mm in this case. From Equation A.1, $C_t = 10\text{-}30$ pF. Choosing silicone oil as an example, ρ for silicone oil is 1000 GΩm (Table 3.1), the R_t is approximately at 80 to 300 GΩ. C will represent the remaining additional capacitance in the power supply system, normally in the μF range. R_1 is the limiting resistor of the high voltage power supply output, it is 100 kΩ. R_2 is a resistor of 120 MΩ used for absorbing the extra leakage current from the system⁵. R_3 is the resistive voltage divider of 80 MΩ. V_s is a triangular waveform voltage source as:

⁵It had been noticed after the fact that it is not necessary to have the resistor, R_2 , in the system from high power system point of view. Unfortunately, it had been in place for all of the experiments and it was also included in all of the previous work.

$$V_s = \begin{cases} V_o t/5 & 5 \geq t \geq 0 \\ V_o (10-t)/5 & 10 \geq t \geq 5 \end{cases} \quad (\text{A.2})$$

where V_o is the peak value, in this case being the maximum applied voltage value, and t is the time in seconds.

Calculating the total equivalent resistance R_{eq} and total equivalent capacitance C_{eq} values from Figure A.1 yield the following:

$$\begin{aligned} R_{eq} &= R_1 + R_2 \parallel R_t \parallel (R_3 + R_4) \\ C_{eq} &= C + C_t \end{aligned} \quad (\text{A.3})$$

The test cell resistance is much larger than that of the total system equivalent resistance. The total equivalent resistance therefore of the entire circuit arrangement is approximately the same as that of the resistor R_1 . On the contrary, the capacitance of the test cell is much smaller than the system capacitance C , therefore the combined parallel capacitance is essentially that of the system itself. As a result the equivalent circuit could be reduced to a single RC circuit in which the input V_s represents the power supply triangular voltage waveform. The output voltage, V_2 , is the voltage across the test cell as shown in Figure A.2. $R_1 \ll R_2, R_3$ or R_t , so $R_{eq} = R_1$, and as $C \gg C_t$, thus $C_{eq} = C + C_t = C$. Thus from the equivalent RC circuit shown in Figure A.2, the voltage across the capacitor could be written as

$$V_s = i R_1 + V_2$$

$$i = C \frac{dV_2}{dt}$$
(A.4)

and to accomplish this, writing its differential equation where $p = 1/(R_1 C)$:

$$\frac{dV_2}{dt} + p V_2 = p V_s$$
(A.5)

As the Fourier series equation is defined as follows [91]:

$$f(t) = a_0 + a_1 \cos t + a_2 \cos(2t) + \dots a_n \cos(nt) \dots$$

$$+ b_1 \sin t + b_2 \sin(2t) + \dots b_n \sin(nt) \dots$$
(A.6)

Where

$$a_0 = \frac{1}{2\pi} \int_n^{n+2\pi} f(t) dt$$

$$a_n = \frac{1}{\pi} \int_n^{n+2\pi} f(t) \cos(nt) dt$$

and

$$b_n = \frac{1}{\pi} \int_n^{n+2\pi} f(t) \sin(nt) dt$$

Thus, by using Equation A.6, the triangular waveform V_s in Equation A.2 is derived as follows:

$$V_s = \frac{1}{2} V_o - \frac{4}{\pi^2} V_o \sum \frac{1}{(2n-1)^2} \cos (2n-1) \frac{\pi}{5} t$$
(A.7)

Using Equation A.7, the solution to the differential Equation A.5 for the voltage V_2 across the capacitor is:

$$V_2 = V_o \left[\left(\frac{1}{2} - \frac{4}{\pi^2} b p \right) + \left(\frac{4}{\pi^2} a p^2 - \frac{1}{2} \right) e^{-p t} \right] \quad (\text{A.8})$$

where

$$a = \sum \frac{1}{(2n-1)^2} \frac{1}{p^2 + \left[(2n-1) \frac{\pi}{5} \right]^2}$$

$$b = \sum \frac{1}{(2n-1)^2} \frac{p \cos\left[(2n-1)\frac{\pi}{5}t\right] + (2n-1)\frac{\pi}{5} \sin\left[(2n-1)\frac{\pi}{5}t\right]}{p^2 + \left[(2n-1) \frac{\pi}{5} \right]^2}$$

The initial voltage conditions give $V_1(0) = 0$ and $V_2(0) = 0$. Now, by using $R_1 = 100$ k Ω , $C = 2.85$ μ F and $V_o = 40$ kV, thus $p = 1/R_1C = 3.5$, the solution for V_1 and V_2 from Equation A.8 is shown in Figure A.3 as $V(1)$ and $V(2)$ respectively.

It has been noticed in Figure A.3 that, V_2 has a ΔV difference of approximately 1.5 kV at both the maximum value and the minimum value points. The so called the residual voltage is the voltage between the minimum voltage value and zero coordinate. Besides containing the residual voltage, this waveform is also found to have a time delay from the original voltage waveform, the ΔT is 0.20 seconds, meaning that the V_2 waveform will appear later than the original waveform by 0.20 seconds. The most important characteristic of the voltage ΔV is that its value is not dependent on the

parameters of the test cell (R_t and C_t), it is only dependent on the power system setup. Thus the residual voltage value is unaffected by the presence or absence of the test cell. This has been observed from the experimental result as seen in Figure 3.18, a graph of the residual voltage ΔV versus the maximum applied voltage.

If one chooses the t value to be very large, then $e^{-\pi^2} \rightarrow 0$; thus Equation A.8 could be simplified to the following equation:

$$V_2 \approx V_o \left(\frac{1}{2} - \frac{4b}{\pi^2 R_t C} \right) \quad (\text{A.9})$$

Considering the circuit in Figure A.1, as the applied voltage is increased, the capacitor C_t is in a charging condition. The charging current will flow into C_t . If there is an ammeter connected as shown in Figure A.1, the meter connections are made in such a way that the ammeter indicates a positive current. As the applied voltage ramp rate reverses, C_t starts to discharge and the current now is flowing in the opposite direction, and the ammeter will indicate a negative current value as shown in Figure A.4. There is a large transient current during the voltage ramp rate reversal. Since the voltage V_2 applied to the test cell is lagging, the test cell capacitance, modelled by C_t , is still discharging when the voltage source V_2 is at its minimum value and its ramp rate reverses. The response current of the test cell I_t could be calculated by using the following equation

$$I_t = I_{C_t} + I_{R_t} = C_t \frac{dV_2}{dt} + \frac{V_2}{R_t} \quad (\text{A.10})$$

By using the result from Equation A.9 and substituting the component values into the expression, I_t could be written as:

$$I_t = \frac{V_0}{2 \times 10^{11}} - \frac{4p}{\pi^2 10^{11}} \cdot V_0 K \quad (\text{A.11})$$

$$K = \sum a \left\{ \left[p + \left[(2n-1) \frac{\pi}{5} \right]^2 \right] \cos \left[(2n-1) \frac{\pi}{5} t \right] - \right.$$

$$\left. \left[(2n-1) \frac{\pi}{5} \right] (p-1) \sin \left[(2n-1) \frac{\pi}{5} t \right] \right\}$$

For example, at $t = 20$ seconds, the response current will very quickly change from a negative value to a positive value (since the experiment runs at 10 seconds per cycle).

The calculated results of the applied voltage and corresponding response current are shown in the Table A.1. Thus there is a positive residual voltage value from the supply voltage waveform and a negative corresponding current passing through the test cell at the same time. At $t = 20.20$ second, the corresponding response current reaches its lowest value. In other words, the current has a 0.2 second lag with respect to the applied voltage.

TABLE A.1 The Calculated Results of the Applied Voltage and Corresponding Response Current in the Test Sample

t (seconds)	V ₁ (kV)	V ₂ (kV)	I _t (nA)
19.95	0.506	2.736	-387.7
20.0	0.178	2.366	-388.2
20.05	0.36	2.016	-285.4
20.10	0.76	1.782	-174.8
20.15	1.16	1.683	-87.54
20.20	1.56	1.595	-2.118
20.25	1.96	1.689	51.75
20.30	2.36	1.787	105.0
20.35	2.76	1.885	158.3
20.40	3.16	1.999	208.7
20.45	3.56	2.26	233.7

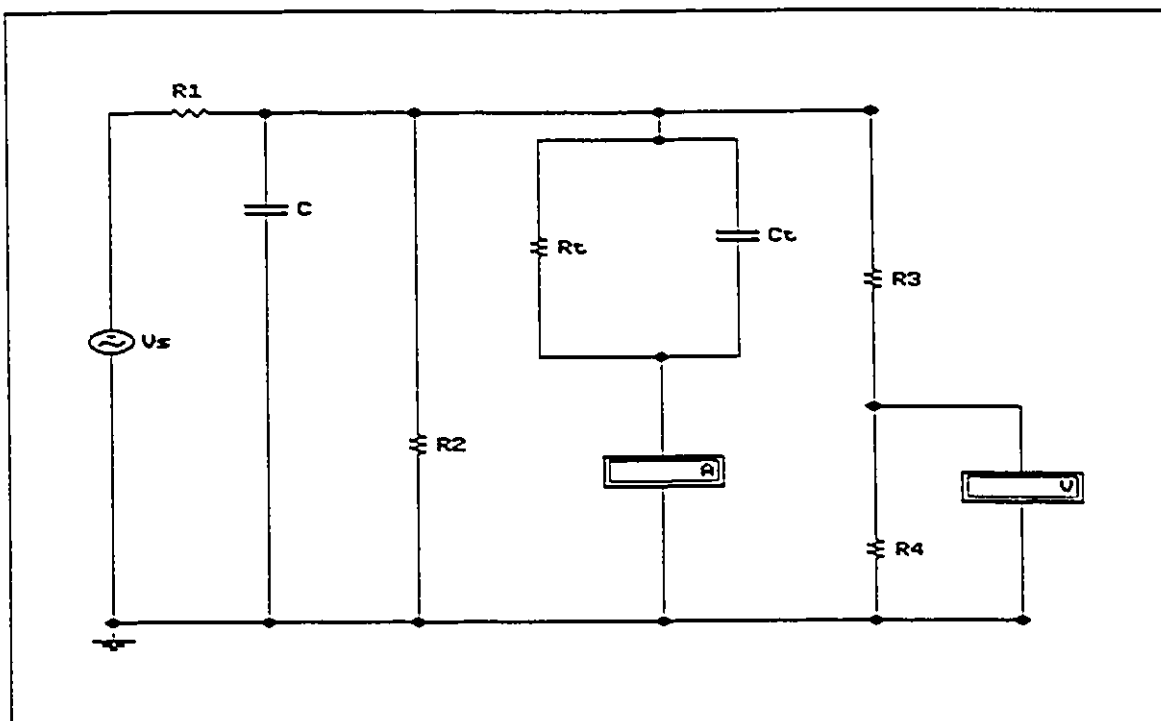


Figure A.1 The equivalent circuit of high voltage power supply system

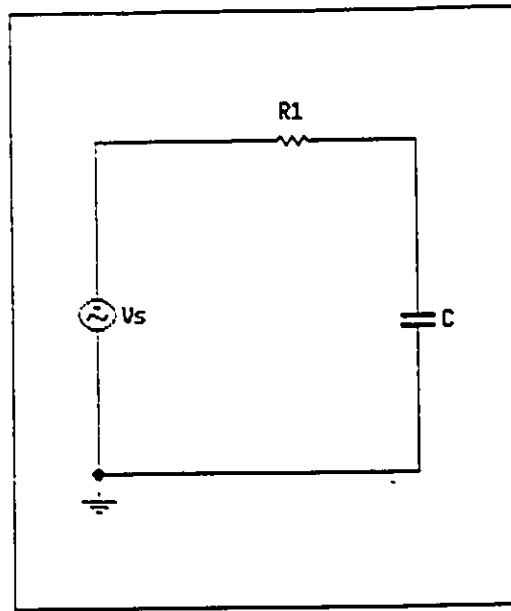


Figure A.2 The simplified RC circuit from Figure A.1

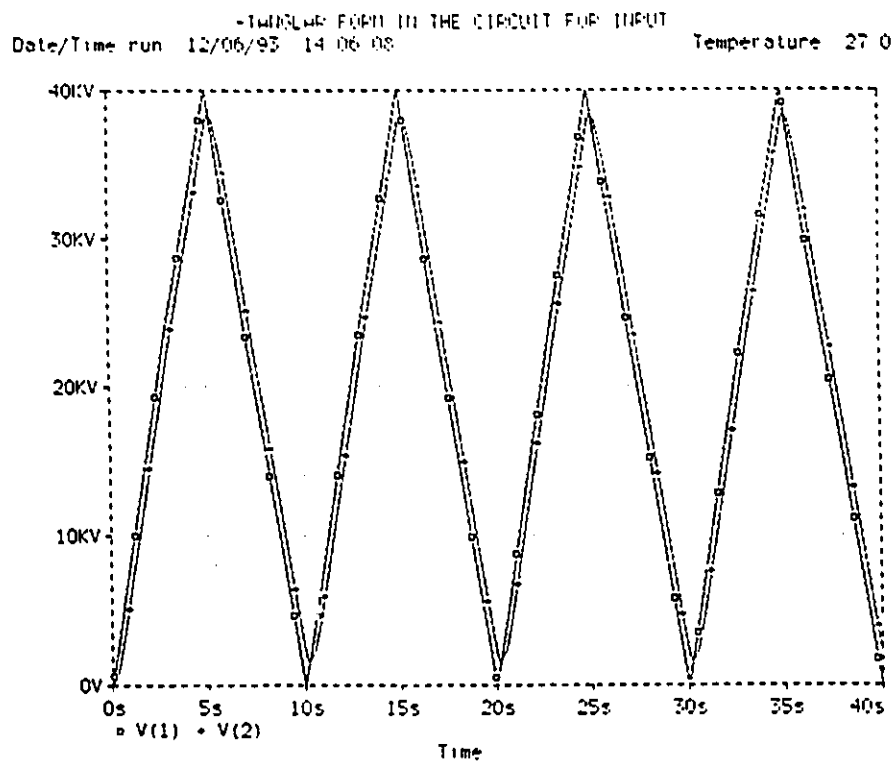


Figure A.3 The calculated results of input and output voltage from the RC circuit

*TANGLAR FORM IN THE CIRCUIT FOR INPUT
 Date/Time run 12/06/93 14 06 08 Temperature 27.0

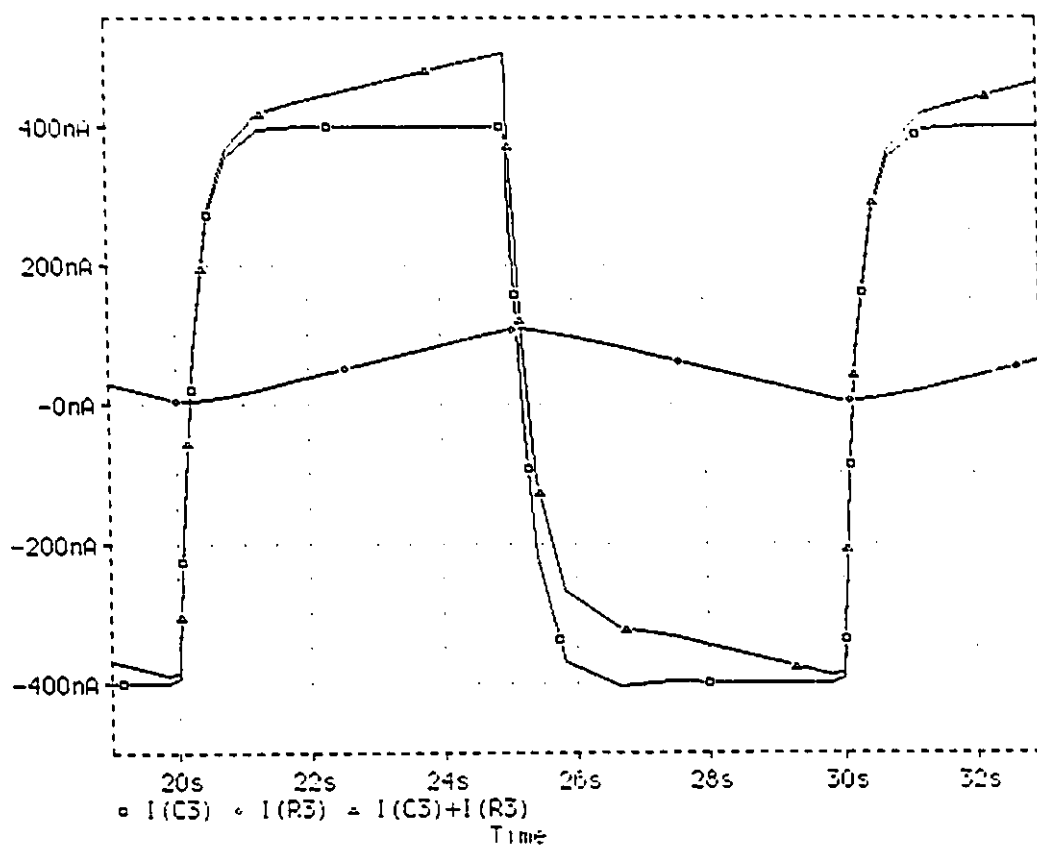


Figure A.4 The calculated result of response current from the RC circuit

APPENDIX B

THE FIELD DISTRIBUTION OF THE TEST CELL AND NEAR A GAS/LIQUID SURFACE WITH /WITHOUT MENISCUS PHENOMENON

B.1 COMPUTATIONAL METHOD AND MODELLING

The calculation of electric fields for this geometry requires the solution of Laplace's equation with boundary conditions satisfied. The charge simulation technique presented in the literature is static in the sense that it represents the system under conditions of fixed voltage and boundary values. In our particular application however, the interface boundary locations are varying with time due to the time variation of the externally applied voltage. The voltage applied here is a triangular waveform at 0.1 Hz, and the ramp rates varying from 6.0 to 14.0 kV/s up to a peak voltage of 70 kV [66]. Since the frequency is much lower than the power frequency (60 Hz), the electric field stress and the voltage (potential) can be defined as a quasistatic field case and treated as D.C. quantities.

The dielectric boundary conditions present a more complex problem than that of the triangular supply voltage waveforms. It has been observed in the experiment that at high electric stress, the liquid surface was disturbed and partly drawn up the shaft of the upper electrode as a meniscus on the free surface by electro-capillary force. Figure B.1

shows typical examples of experiment results of the oil surface changing under different maximum applied voltages. The meniscus values measured could rise as high as 1.3 cm under an applied maximum voltage of 59 kV. This phenomenon must be due to the electric force at this two-dielectric interface [85], and related to the oil dynamic flow properties under electro-capillarity (electrostriction) conditions [86]. Another fact which also should be taken into account is that part of the liquid in the system is in electrohydrodynamic (EHD) motion.

From an electrically stressed liquid duct experiment [87], it has been shown that the equipotential surfaces are more densely spaced than would be the case for a charge-free field close to the anode, indicating a higher electric field due to the presence of space charge in this gap. In that particular case of a uniform field region, the field close to the anode was found to be 25% greater than the corresponding Laplacian field. Since the CSMCAD package was only capable of producing solutions to Laplace's equation, the space charge effect could not be included in the CSMCAD model at that time. As a result the calculated electric field strength would be slightly different than its actual value.

It is important to know the field distribution near the gas/liquid surface when the electrical meniscus occurs, to determine how the field distribution will change in that section and how it will effect the near area field. A literature survey of this problem indicated that very little is published about the properties of gas/liquid two-dielectric

material systems in non-uniform fields, or concerning composite liquid dielectric arrangements. Thus more general results on the field behaviour near the high voltage electrode as well as near the electrode contact point at the gas/liquid surface will be described.

B.2 CALCULATIONS AND COMPARISON

The charge simulation method basically consists of replacing the surface charges of each electrode by a discrete set of inner charge distributions, whose positions and types are predetermined, but whose magnitudes are unknown [88]. In the computation package only a two dielectric system modelling capability is available. Therefore the original experimental system has to be simulated approximately using a two dielectric modelling system rather than a more appropriate three dielectric material modelling system. In a two dielectric arrangement, the system of equations required for determination of the simulated charge can be formulated and written in a matrix form as shown in Figure B.2. Thus in the matrix form, the row number corresponds to the number of the contour point and the column number corresponds to the number of the charge.

Six different geometries have been numerically modeled here in order to compare the field behaviour and other effects produced by different boundary configurations.

These are shown from Figure B.3(a) through B.3(f). Figures B.3(a,b) are used to analyze the test cell effect; Figures B.3(c,d) are used to analyze the electric meniscus effect; Figures B.3(e,f) are used in analyzing the effect of edge conditions. In Figure B.3(e,f), the gas and liquid were assumed to have a fixed "sharp" shape at the boundary. All the arrangements have rotational symmetry, for which ring charge modelling has been found to provide the most accurate solutions. The upper electrode in Figure B.3 represents a charged conductor at potential V of 1 Volt above the lower electrode representing a grounded level of 0 Volts. The maximum percentage potential and field errors in all the calculation conditions are less than 0.12% and 0.55% respectively. It is found that the location and the value of the maximum potential and field error are slightly different in the one and two dielectric material systems. For example, the maximum potential and field errors in the Figure B.3(a) geometry are 0.1% and 0.06% at point E along the upper electrode surface, and in the Figure B.3(c) geometry, the maximum errors increased slightly at point E' to 0.08% and 0.56% respectively.

Figure B.4 is the equipotential field distribution in the test cell and Figure B.5 is the electric field distribution along the axis between the two electrodes from cathode to anode. Examination of the field in Figure B.5 shows that the maximum electric field strength is at the tip of the upper hemispheric electrode. The maximum electric field was found to have the same value in all six models. The non uniform field coefficient $E_{\max}d/V$ of this modelling geometry is 1.17 (where d is the gap distance) - i.e., the maximum field stress is 17% greater than the corresponding uniform field. It should be

emphasized that when all of the field problems are solved by using solutions to the Laplace equation, the space charge effect is not included. If the space charge effect were to be added to the model, the resulting maximum field strength would be higher. It is also shown that the electric field in the centre part of the gap is quite low. As a result of trials involving modifying the boundary condition such as by changing the edge parameter, the meniscus, or by including the second dielectric region, the electric field and potential distribution were observed not to change significantly near the high voltage electrode region.

On the upper electrode surface, the electric field distribution on the hemispherical section was found not to be affected by varying the container and other boundary condition details. However, such changes do have an affect on the electric field distribution along the cylindrical section of the electrode. Comparing the two dielectric system to the single dielectric system as Figure B.3 shows, the maximum increase in the magnitude of electric field strength in this region is about 10%, observed in Figure B.6, the field distribution along the upper electrode.

In the interface area, the voltage drops by 75% of the original from the high voltage electrode surface to the container, and the field stress is also decreased by 95% from the maximum value. It is clear that the test cell should have little effect on the field distribution since both potential and field stress drop to very low values at points close to the container wall. Considering the two dielectric material systems, there is no

appreciable change in the potential distribution except that the maximum field value at the electrode surface increased by 10% and then decreases quickly with distance to its normal value close to the container. The meniscus phenomenon does not affect the field values and the field distribution in the liquid except near the meniscus itself, because of the variation of the dielectric constant in that region.

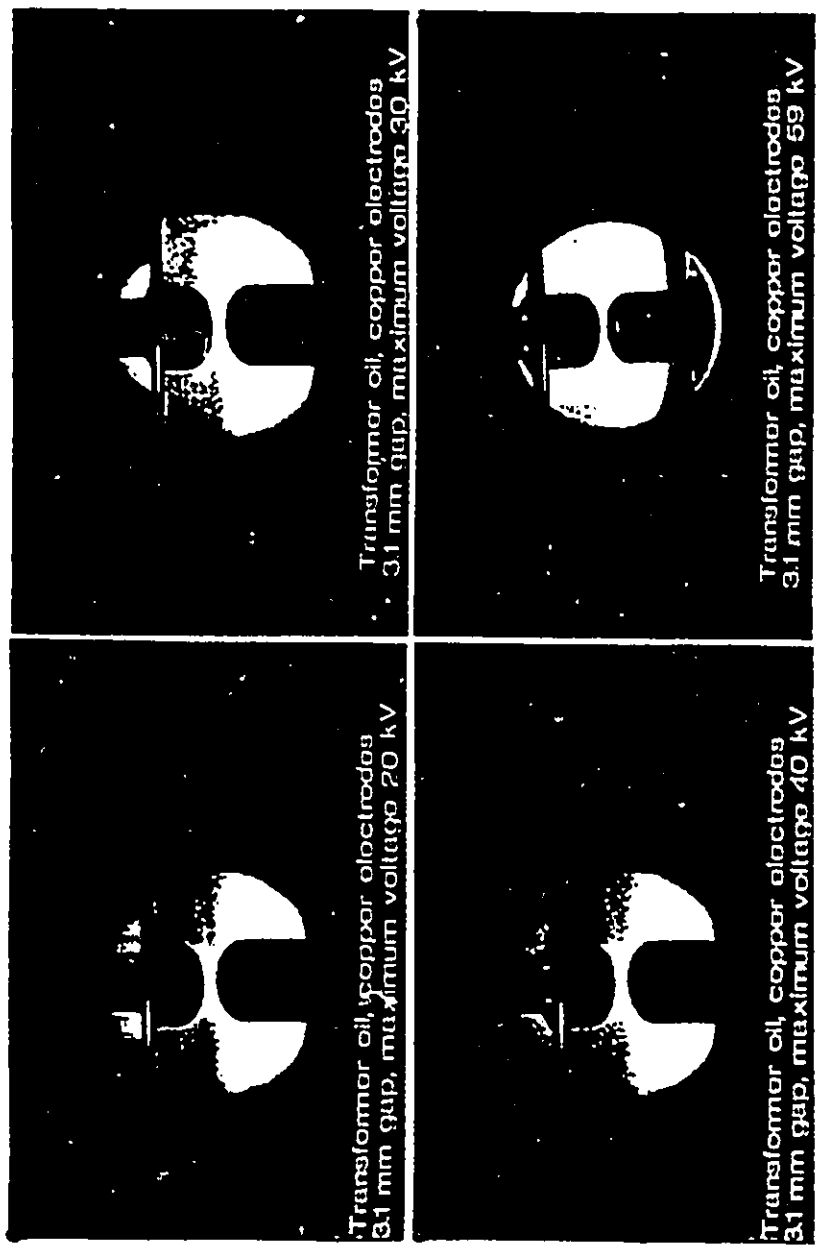


Figure B.1 Typical examples of the oil surface changing under the different maximum applied voltage

P_{ij}	P_{ij}	0	V	potential on conductor boundary points adjacent to solid dielectric
P_{ij}	0	P_{ij}	V	potential on conductor boundary points adjacent to air dielectric
0	P_{ij}	$-P_{ij}$	0	potential matching at two dielectric surface
$(\epsilon_r - 1)F_{ij}$	$\epsilon_r F_{ij}$	$-F_{ij}$	0	normal flux density matching at surface

$$= X Q_j$$

\uparrow
 conductor side charge coefficients

\uparrow
 air side charge coefficients

\uparrow
 dielectric side charge coefficients

Figure B.2 Matrix representation of equations for application to two dielectric system

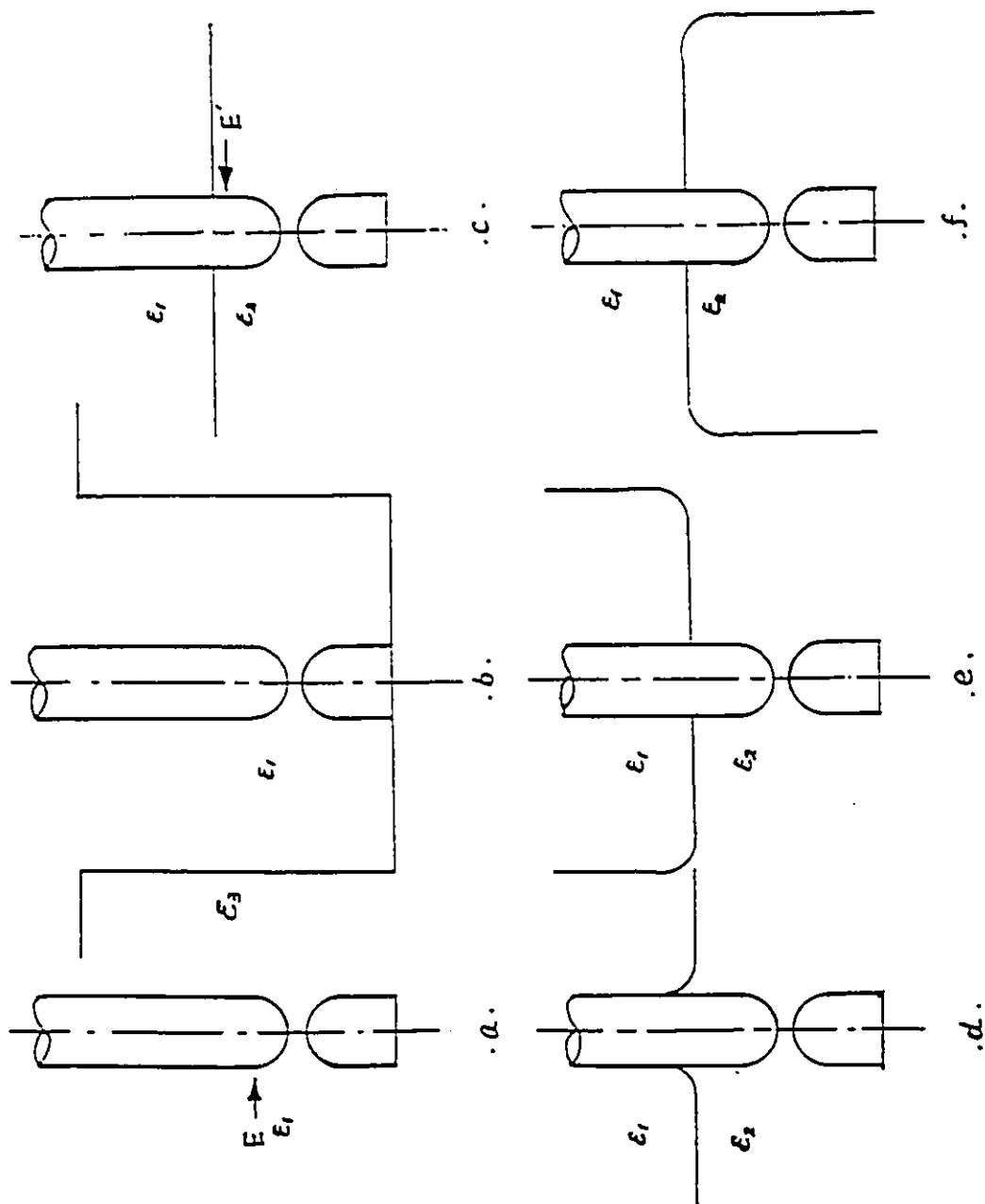


Figure B.3 The arrangement of the boundary condition

EQUIPOTENTIAL FIELD LINES

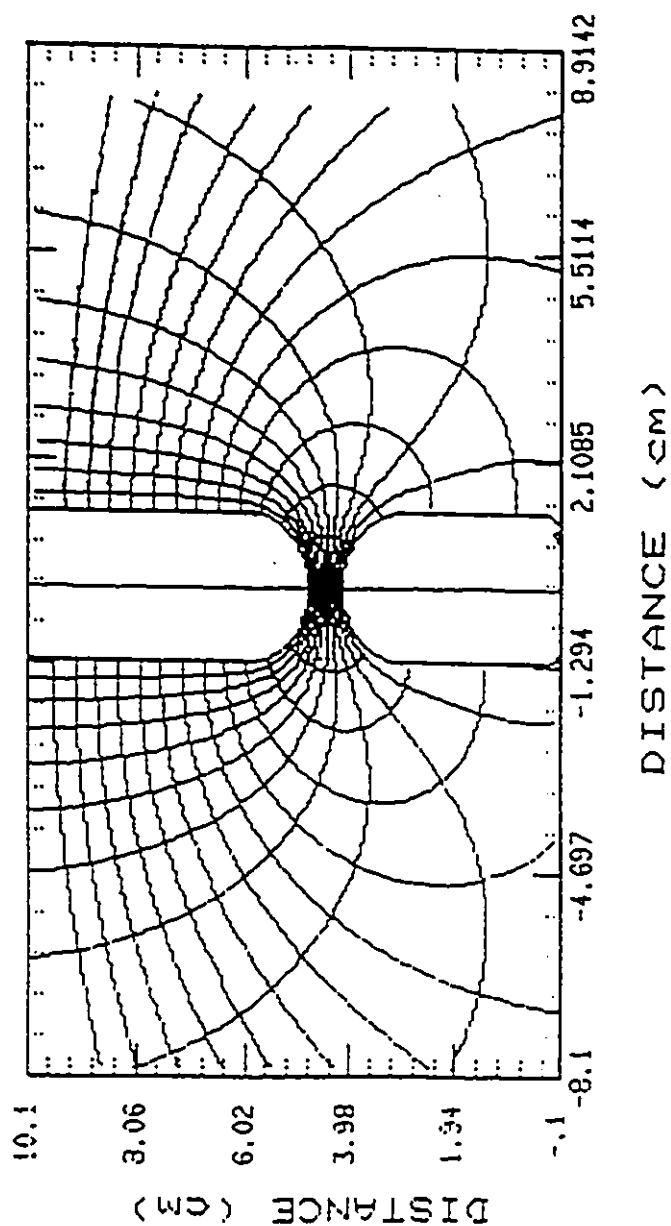


Figure B.4 The two-dimensional equipotential field plot

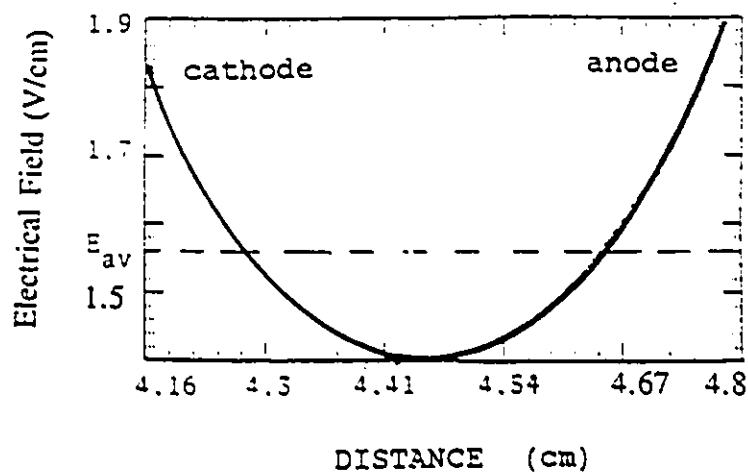


Figure B.5 The field distribution between the electrodes

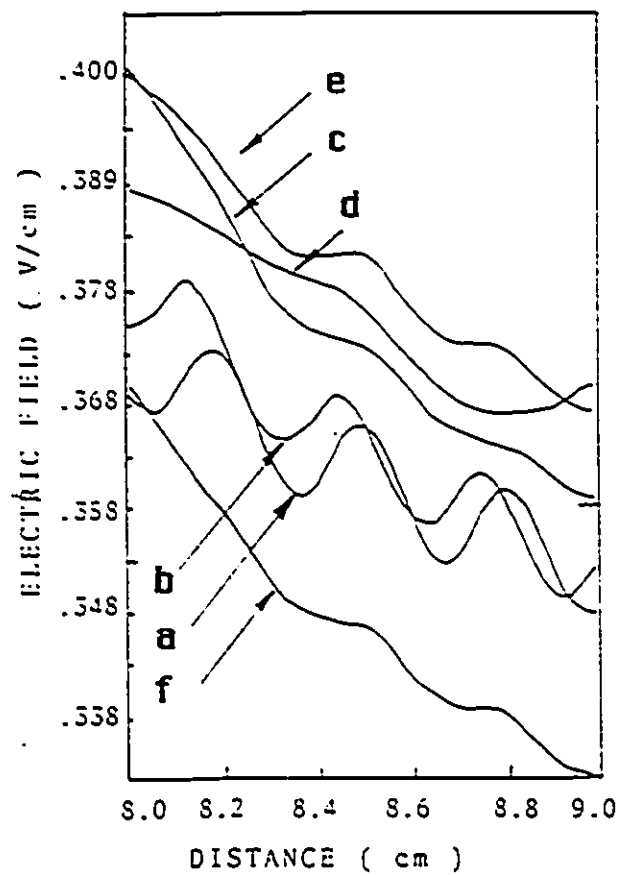


Figure B.6 The field distribution along the upper electrode with different boundary condition shown in Figure B.3

APPENDIX C

THE PROPERTIES OF FORCE-FREE BELTRAMI FLOW FIELDS

Beltrami flow fields are characterized by having the vorticity ω and velocity u vectors lying parallel everywhere so that inertial body force, $\rho\omega \times u$, is identically zero and hence,

$$\omega = \frac{u}{\lambda} \quad (C.1)$$

can be written and this obeys the Vector Helmholtz Equation (VHE):

$$\nabla^2 \times u = \lambda^2 u \quad (C.2)$$

and under a certain condition such as u is incompressible, thus [92]:

$$\begin{aligned} \nabla \cdot u &= 0 \\ \text{hence:} \quad \nabla^2 u + \frac{u}{\lambda^2} &= 0 \end{aligned} \quad (C.3)$$

with a specific characteristic length, λ . These fields are mathematically identical to the force-free fields of magnetohydrodynamics, the properties of which have been well defined [81]. Every solution of Equation C.3 is not necessarily a solution of Equation C.1, although the converse is true [81]. A most important fact to appreciate is that not all solutions of the VHE will specify Beltrami flows but only those associated with a corresponding Scalar Helmholtz Equation (SHE),

$$\nabla^2 \psi + \frac{\psi}{\lambda^2} = 0 \quad (\text{C.4})$$

Three types of solution are specified by,

$$\begin{aligned} u_1 &= \nabla \psi \\ u_2 &= \nabla \times (c \psi) \\ u_3 &= \frac{1}{c} \nabla \times u_2 \end{aligned} \quad (\text{C.5})$$

where c is a fixed vector. Since $u = \nabla(b_o V)$, where b_o represents a mobility and V is a potential, then $\Psi = b_o V$. so the SHE could be also written as

$$\nabla^2 V + \frac{V}{\lambda^2} = 0 \quad (\text{C.6})$$

Thus, this will assure from Equation C.6 that there is equipartition of kinetic energy $\epsilon E^2 = \rho u^2$ and electrostatic energy $-\epsilon E^2 = \rho_e V$ densities. Moreover Equation C.6 has the solution

$$\begin{aligned} V &= V_o e^{(\pm j \frac{z}{\lambda})} \\ \therefore \nabla V &= \pm j \frac{V}{\lambda} = -E \end{aligned} \quad (\text{C.7})$$

It is also a fundamental property of Beltrami flows that they are always bounded

within a specific region of either two or three dimensional space within which they are defined. In this case the region is a sphere defined in size by the Debye length since it is only within such a volume that significant electric fields and forces can exist by comparison to thermal body forces.

It is always the case that the vector variable, u in this case, will decay freely.

The equation is then:

$$\frac{\partial u}{\partial t} = -k_2 \nabla^2 u = -(k_2/\lambda^2)u \quad (C.8)$$

where k_2 is a constant. Using equation C.3, the solution of which is

$$u = u_0 e^{-(k_2/\lambda^2)t} = u_0 e^{-t/\tau_v} \quad (C.9)$$

where u_0 is any solution of equation C.1 which is not time-dependent, τ_v is a characteristic time constant.

APPENDIX D

GAUGE TRANSFORMATION

In a conventional electromagnetic field, a moving charged particle involves the vector and scalar potentials A and ϕ of the field explicitly. The physical effects of the electromagnetic field depend only on the electric field E and the magnetic field B given by

$$B = \nabla \times A, \quad E = -\nabla \phi - \frac{\partial A}{\partial t} \quad (D.1)$$

If A and ϕ are replaced by A' and ϕ' that

$$\begin{aligned} A &\rightarrow A' = A + \nabla \chi, \\ \phi &\rightarrow \phi' = \phi - \frac{\partial \chi}{\partial t} \end{aligned} \quad (D.2)$$

where χ is any function of space and time. All physical quantities must be invariant under this gauge transformation (Equation D.2) [79]. According to this, the argument can be applied to the field strengths such as B and E and they are unchanged by switching A and ϕ to A' and ϕ' respectively, thus:

$$\begin{aligned} \nabla \times A' &= \nabla \times (A + \nabla \chi) = \nabla \times A + \nabla \times (\nabla \chi) = \nabla \times A = B \\ -\nabla \phi' - \frac{\partial A'}{\partial t} &= \nabla \left(\phi - \frac{\partial \chi}{\partial t} \right) - \frac{\partial (A + \nabla \chi)}{\partial t} \\ &= -\nabla \phi + \nabla \left(\frac{\partial \chi}{\partial t} \right) - \frac{\partial A}{\partial t} - \frac{\partial (\nabla \chi)}{\partial t} = -\nabla \phi - \frac{\partial A}{\partial t} = E \end{aligned} \quad (D.3)$$

where

$$\begin{aligned}\nabla \times (\nabla \chi) &= 0 \\ \nabla \left(\frac{\partial \chi}{\partial t} \right) &= \frac{\partial (\nabla \chi)}{\partial t}\end{aligned}\tag{D.4}$$

Another kind of transformation under quantum mechanics theory is a so called gauge transformation of the first kind [79]. Thus when a complicated function of the coordinate $\psi(x,t)$ switches to $\psi'(x,t)$, the physical quantities only change by a common phase factor of the wave function such as:

$$\psi(x, t) \rightarrow \psi'(x, t) = \psi(x, t) \exp [i e \chi(x, t) / \hbar c] \tag{D.5}$$

where x is a space and t is a time. For example, the Schrodinger equation is affected by the gauge transformation (Equation D.5), in that $p-(e/c)A$ is replaced by $p-(e/c)(A + \nabla \chi)$ and E is replaced by $E + (e/c)\partial \chi / \partial t$. Thus

$$\begin{aligned}(p - \frac{e}{c} A') \psi' &= [-i\hbar \nabla - \frac{e}{c} A - \frac{e}{c} (\nabla \chi)] \psi \exp^{[\frac{i e \chi}{\hbar c}]} \\ &= \exp^{[\frac{i e \chi}{\hbar c}]} [-i\hbar \nabla - \frac{e}{c} A] \psi\end{aligned}\tag{D.6}$$

and

$$\begin{aligned}(E - e\phi') \psi' &= [i\hbar \frac{\partial}{\partial t} - e\phi + \frac{e}{c} (\frac{\partial \chi}{\partial t})] \psi \exp^{[\frac{i e \chi}{\hbar c}]} \\ &= \exp^{[\frac{i e \chi}{\hbar c}]} (i\hbar \frac{\partial}{\partial t} - e\phi) \psi\end{aligned}\tag{D.7}$$

The only change is the common phase factor.

Since this gauge transformation theory of the second kind appears correct in EHD [82], then gauge transformation theory of the first kind must also exist in the EHD system compared with the quantum mechanical system. In the EHD system V' is a composite dynamic potential function and V_c is a static potential function. Thus Equation D.8 shows:

$$\frac{V'}{V_c} = e^{j(\mathcal{A}\lambda - \mathcal{A}\tau_v)} = e^{\Psi} \quad (\text{D.8})$$

the nature of the phase Ψ is the only difference from switching the static to the dynamic potential function. This is true that the equation is affected by the gauge transformation of the first kind only in that it accounts for a change in phase of the wave function.

APPENDIX E

THE DERIVATION OF AN ANALOGUE TO THE ELECTRODYNAMIC BODY FORCE

The magnetic force F_m is given in the case of a truly electromagnetic situation as

$$F_m = J \times B = \mu_o J \times H \quad (E.1)$$

where $\mu_o = 1/(\epsilon c^2)$ which becomes $1/(\epsilon u_w^2)$ in the EHD case being considered here, and u_w is a wave velocity, while $J = -\rho_e u$. Maxwell's equations for moving media [77] indicates that H can be replaced by $P_v \times u$, where in this case P_v is a virtual polarization (given in Equation E.3). In the full expression of Ampere's Law, several components of current density are considered but the "true" as well as the convected current density are obviously too small to create significant $J \times B$ forces in this case. Similar body forces in the fluid can however arise due to the existence of a vector field which is analogous to H . This field is $P_v \times u$, the curl of which is one component in Ampere's Law. Now by using Equation 5.3 in Chapter V,

$$V = \frac{\rho_e \lambda^2}{\epsilon} \quad (E.2)$$

and introducing this into the following equation for E' which is derived in Equation 5.2 of Chapter V, thus

$$E' = -\nabla V - \frac{\lambda^2 \nabla \rho_e}{\epsilon} \quad (\text{E.3})$$

$$\epsilon E' = -\epsilon \nabla V - \lambda^2 \nabla \rho_e \rightarrow \epsilon E - P_v$$

where $P_v = \lambda^2 \nabla \rho_e$ according to the direction of the density gradient. Hence H can be written as,

$$H = P_v \times u \equiv \lambda^2 \nabla \rho_e \times u \quad (\text{E.4})$$

Now introducing $\mu_0 = 1/(\epsilon u_w^2)$, $J = -\rho_e u$ and the above expression for H into Equation E.1, the equation for $J \times B$ can be rewritten as

$$\begin{aligned} J \times B &= \frac{1}{\epsilon u_w^2} [-\rho_e u \times (\lambda^2 \nabla \rho_e \times u)] \\ &= -\frac{\lambda^2 \rho_e^2}{\epsilon u_w^2} u \times \left(\frac{\nabla \rho_e \times u}{\rho_e} \right) \end{aligned} \quad (\text{E.5})$$

Furthermore, by using Equation E.3, it follows that Equation E.5 can also be rewritten in the form

$$J \times B = \frac{1}{\epsilon u_w^2} [-\rho_e u \times (P_v \times u)] = \frac{1}{\epsilon u_w^2} [-\rho_e u^2 P_v] \quad (\text{E.6})$$

assuming that u is perpendicular to $P_v \times u$, and finally,

$$\mathbf{F}_m = \mathbf{J} \times \mathbf{B} = \left(\frac{u}{u_w}\right)^2 \left(-\frac{P_e}{\epsilon}\right) \mathbf{P}_v = \left(\frac{u}{u_w}\right)^2 (V \nabla \rho_e) \quad (\text{E.7})$$

This force operates when electrons diffuse, and then are detrapped and consequently displaced. Thus \mathbf{F}_m is in the negative \mathbf{P}_v direction and so energy is expended (or gained) in creating either a positive or negative $\nabla \rho_e$ gradient. Hence the detrapping and relocation involve an expansion and so a change in energy. This energy is the binding energy (source of binding potential). Thus Equation E.7 can then be rearranged as,

$$\frac{(\mathbf{J} \times \mathbf{B})}{\rho_e} = \frac{\text{body force}}{\text{charge density}} \equiv \frac{\text{force}}{\text{charge}} = \text{field} \quad (\text{E.8})$$

$$\text{thus } \frac{(\mathbf{J} \times \mathbf{B})}{\rho_e} = - \left(\frac{u}{u_w}\right)^2 \frac{P_v}{\epsilon}$$

Now the Shafranov Theorem [92] states that the magnetizing force \mathbf{H} and the current density \mathbf{J} in an equilibrium configuration are analogous to the linear velocity \mathbf{u} and the vorticity vector $\boldsymbol{\omega}$ in an incompressible fluid (in the system in which the vortex is at rest). This is ascertained by a comparison between the following sets of equations:

Steady Vorticity Flow	Equilibrium Magnetic Field	
$\nabla \cdot \mathbf{u} = 0$	$\nabla \cdot \mathbf{H} = 0$	
$\nabla \times \mathbf{u} = \boldsymbol{\omega}$	$\nabla \times \mathbf{H} = \mathbf{J}$	(E.9)
$\nabla(\mathbf{u} \times \boldsymbol{\omega}) = 0$	$\nabla(\mathbf{H} \times \mathbf{J}) = 0$	

A comparison between these equations, permits the following to be deduced:

$$\begin{aligned} H &\propto u, & J &\propto \omega \\ \text{so } J \times B &\propto \omega \times u \end{aligned} \quad (\text{E.10})$$

As a Beltramion moves into virgin fluid, its own internal field can stimulate more detrapping and expansion so $J \times B = F_m \neq 0$, in which case the Beltramion is in an interactive (or formative) mode. By the Shafranov Theorem therefore $\omega \times u \neq 0$. Now since the total time derivative of ω is zero, thus:

$$\begin{aligned} \therefore d\omega/dt &\equiv \partial\omega/\partial t + \nabla \times (\omega \times u) = 0 \\ \therefore \partial\omega/\partial t &= -\nabla \times (\omega \times u) \end{aligned} \quad (\text{E.11})$$

Moreover $\nabla \times F_m$ from Equation E.7 is given as:

$$\begin{aligned} \nabla \times (J \times B) &= (u/u_w)^2 \nabla \times (V \nabla \rho_e) = (u/u_w)^2 (\nabla V \times \nabla \rho_e) \\ &= (u/u_w)^2 (\nabla \times E') = -(u/u_w)^2 \frac{\rho}{\rho_e} \frac{\partial \omega}{\partial t} = -\frac{V}{u_w^2} \frac{\partial \omega}{\partial t} \end{aligned} \quad (\text{E.12})$$

where E' is given from Equation E.3 and from the SHE and $u^2 \rho = \epsilon E^2$, it follows that $\rho u^2 / \rho_e = -V$. Combining Equations E.11 and E.12,

$$\nabla \times (J \times B) = -\frac{1}{u_w^2} V \frac{\partial \omega}{\partial t} = \frac{1}{u_w^2} V \nabla \times (\omega \times u) \quad (\text{E.13})$$

The result from Equation E.13 is therefore consistent with the Shafranov Theorem. If the following condition

$$\nabla V \times (\omega \times u) = 0 \quad (\text{E.14})$$

exists. Equation E.13 is thus expressed as

$$\nabla \times (J \times B) = \frac{1}{u_w^2} \nabla \times (V \omega \times u) \quad (\text{E.15})$$

The Equation E.13 can be finally derived as

$$J \times B = \frac{V}{u_w^2} \omega \times u \quad (\text{E.16})$$

then $J \times B \propto \omega \times u$

thus, the Shafranov theorem therefore is satisfied.

Now, Combining Equations E.12 and E.15, Equation E.14 which validates this is consistent with

$$(u/u_w)^2 E' = (V/u_w^2) \omega \times u \quad (\text{E.17})$$

$$\frac{u^2}{V} E' = -\frac{\rho_e}{\rho} \nabla V = \omega \times u$$

and $\omega \times u$ is now a vector which has been derived from the variable V in the SHE just

as \mathbf{u} was similarly described in Appendix C. Thus $\omega \times \mathbf{u}$ would then satisfy a VHE. Since moreover $\rho u^2 / \rho_e = -V$ Equation E.17 can be crossed with \mathbf{u} to obtain

$$(\omega \times \mathbf{u}) \times \mathbf{u} = \omega u^2 = \frac{u_2}{V} \nabla V \times \mathbf{u} \quad (\text{E.18})$$

$$\therefore \quad \omega = \frac{\nabla V \times \mathbf{u}}{V} = j \frac{\mathbf{a} \times \mathbf{u}}{\lambda}$$

where \mathbf{a} is the unit vector in the field direction. In order to satisfy a VHE in ω , Equation E.18 would need to be supplemented by,

$$\nabla \times \omega = j \frac{\mathbf{a} \times \omega}{\lambda} \quad (\text{E.19})$$

Equations E.18 and E.19 together now constitute a separate solution of the VHE of the kind described by \mathbf{u}_2 and \mathbf{u}_3 in Equation C.5. In this case $\omega \times \mathbf{u} \neq 0$ and the solution is interactive with the fluid. Thus a Beltramion can accelerate in the \mathbf{u}_1 mode (Equation C.5) without disturbing the fluid. At a certain point in its motion the electric field can detrap electrons and initiate the $\mathbf{J} \times \mathbf{B}$ force described above. There will be a transition to the interactive mode. This is the fundamental mechanism underlying the development of EHD instability by the α -effect described in section 5.5.

APPENDIX F

FIRST AND SECOND VISCOSITIES [99]

Consider electrons to be briefly detrapped and assume a high velocity by conduction in the electric field. This velocity, u_e adds to the fluid velocity, u . Thus

$$u' = u + u_e = u + bE = u + (\rho_e \frac{\tau_v}{\rho})E \quad (F.1)$$

Now

$$\nabla \times u' \equiv \omega' = \omega + \nabla \times (bE) \quad (F.2)$$

and

$$\begin{aligned} \nabla \times (bE) &\equiv \nabla \times (\rho_e \frac{\tau_v}{\rho} E) \\ &= \frac{\tau_v}{\rho} \nabla \rho_e \times E = \tau_v \left(\frac{\nabla \nabla \times \nabla \rho_e}{\rho} \right) \end{aligned}$$

But from Equation 5.46

$$\frac{\nabla \nabla \rho_e}{\rho} = -v \nabla \times \omega$$

and so

$$\begin{aligned} \nabla \times (bE) &\equiv \nabla \times u_e = -\tau_v v \nabla \times \nabla \times \omega \\ \text{so} \quad \nabla \times (bE) &= \nabla \times u_e = \tau_v \partial \omega / \partial t \end{aligned} \quad (F.3)$$

Thus

$$\omega' = \omega + \tau_v \partial \omega / \partial t = \nabla \times (u + bE) \quad (\text{F.4})$$

Now, writing the incompressible Navier-Stokes equation in u' it takes the form

$$\begin{aligned} & \frac{\partial u}{\partial t} + \frac{\partial u_e}{\partial t} + (\omega + \tau_v \frac{\partial \omega}{\partial t}) \times (u + u_e) \\ &= -\nabla \left(\frac{p}{\rho} + \frac{u^2}{2} + u \cdot u_e + \frac{u_e^2}{2} + \rho_e \frac{V}{\rho} \right) - \nu \nabla \times (\omega + \tau_v \frac{\partial \omega}{\partial t}) \end{aligned} \quad (\text{F.5})$$

Now consider the voltage to be rising at a rate $\partial V / \partial t$ and in the moving reference frame

$dV/dt = \partial V / \partial t - u \cdot E = 0$. Hence since $u_e = bE$, then

$$u \cdot u_e = u \cdot bE = \frac{\rho_e \tau_v}{\rho} \frac{\partial V}{\partial t} \quad (\text{F.6})$$

Hence Equation F.5 will become

$$\begin{aligned} & \frac{\partial u}{\partial t} + \frac{\partial u_e}{\partial t} + (\omega \times u + \tau_v \frac{\partial \omega}{\partial t}) \times u + \omega \times u_e + \tau_v \frac{\partial \omega}{\partial t} \times u_e \\ &= -\nabla \left[\frac{p}{\rho} + \frac{u^2}{2} + \frac{u_e^2}{2} + \frac{\rho_e}{\rho} (V \tau_v \frac{\partial V}{\partial t}) \right] - \nu \nabla \times \omega - \nu \nabla \times (\tau_v \frac{\partial \omega}{\partial t}) \end{aligned} \quad (\text{F.7})$$

The simple incompressible Navier-Stokes equation is,

$$\begin{aligned}
& \frac{\partial \mathbf{u}}{\partial t} + \boldsymbol{\omega} \times \mathbf{u} \\
& = -\nabla \left(\frac{p}{\rho} + \frac{u^2}{2} + \rho_e \frac{V}{\rho} \right) - \mathbf{v} \nabla \times \boldsymbol{\omega}
\end{aligned} \tag{F.8}$$

and subtraction of this from Equation F.7 gives

$$\begin{aligned}
& \frac{\partial \mathbf{u}}{\partial t} + \left(\tau_v \frac{\partial \boldsymbol{\omega}}{\partial t} \times \mathbf{u} + \boldsymbol{\omega} \times \mathbf{u}_e + \tau_v \frac{\partial \boldsymbol{\omega}}{\partial t} \times \mathbf{u}_e \right) \\
& = -\nabla \left(\frac{u_e^2}{2} + \rho_e \frac{\tau_v}{\rho} \frac{\partial V}{\partial t} \right) - \mathbf{v} \nabla \times \left(\tau_v \frac{\partial \boldsymbol{\omega}}{\partial t} \right)
\end{aligned} \tag{F.9}$$

Expansion of $\nabla(u_e^2/2)$ gives

$$\begin{aligned}
-\nabla(u_e^2/2) &= (\nabla \times \mathbf{u}_e) \times \mathbf{u}_e - (\mathbf{u}_e \cdot \nabla) \mathbf{u}_e \\
&= \left(\tau_v \frac{\partial \boldsymbol{\omega}}{\partial t} \right) \times \mathbf{u}_e - (\mathbf{u}_e \cdot \nabla) \mathbf{u}_e
\end{aligned} \tag{F.10}$$

Entering this in Equation F.9 and considering

$$(\mathbf{u}_e \cdot \nabla) \mathbf{u}_e = 0 \tag{F.11}$$

the result is

$$\begin{aligned}
& \frac{\partial \mathbf{u}_e}{\partial t} + (\tau_V \frac{\partial \boldsymbol{\omega}}{\partial t} \times \mathbf{u} + \boldsymbol{\omega} \times \mathbf{u}_e) \\
& = -\nabla \left(\frac{\rho_e}{\rho} \tau_V \frac{\partial V}{\partial t} \right) - \nu \nabla \times (\tau_V \frac{\partial \boldsymbol{\omega}}{\partial t})
\end{aligned} \tag{F.12}$$

Now partitioning this into two separate equations will give,

$$\frac{\partial \mathbf{u}_e}{\partial t} + \boldsymbol{\omega} \times \mathbf{u}_e = -\nu \nabla \times (\tau_V \frac{\partial \boldsymbol{\omega}}{\partial t}) = -\nu \nabla \times \nabla \times \mathbf{u}_e = \nu \nabla^2 \mathbf{u}_e \tag{F.13}$$

and ,

$$\tau_V \frac{\partial \boldsymbol{\omega}}{\partial t} \times \mathbf{u} = -\nabla \left(\frac{\rho_e}{\rho} \tau_V \frac{\partial V}{\partial t} \right) \tag{F.14}$$

Equation F.13 can be studied from the viewpoint of the compressibility of the free electron gas. Thus, since $\mathbf{u}_e = b\mathbf{E}$, then,

$$\nabla \cdot \mathbf{u}_e = \nabla \cdot \left(\rho_e \frac{\tau_V}{\rho} \mathbf{E} \right) = \rho_e \frac{\tau_V}{\rho} \nabla \cdot \mathbf{E} + \frac{\tau_V}{\rho} \nabla \rho_e \cdot \mathbf{E}$$

If now $\nabla \rho_e$ is transverse to \mathbf{E} this will express the idea that the diffusion current density

$\mathbf{J}_d = D_e \nabla \rho_e$ dissipates no electric power in the process. Hence

$$\nabla \cdot \mathbf{u}_e = \frac{\rho_e^2 \tau_V}{\rho \epsilon} = \frac{1}{\tau_V} = \frac{\rho_e}{\sqrt{\rho \epsilon}} \tag{F.15}$$

Now, by forming the divergence of every term in Equation F.13 and after replacing $\nabla \cdot \mathbf{u}_e$ using Equation F.15 noting that ρ_e obeys the scalar Helmholtz Equation

$$\nabla^2 \rho_e + \rho_e / \lambda^2 = 0 \quad (\text{F.16})$$

it follows that,

$$\nabla(\omega \times \mathbf{u}_e) \equiv \mathbf{u}_e \cdot \nabla \times \omega - \omega \cdot \tau_v \frac{\partial \omega}{\partial t} = 0 \quad (\text{F.17})$$

Since moreover $\nabla \times \omega = \mathbf{u} / \lambda^2$ by the vector Helmholtz equation then,

$$\frac{\mathbf{u}_e \cdot \mathbf{u}}{\lambda^2 \tau_v} = \omega \cdot \frac{\partial \omega}{\partial t} \quad (\text{F.18})$$

and thus

$$\frac{b\mathbf{E} \cdot \mathbf{u}}{\lambda^2 \tau_v} = \frac{\rho_e}{\rho \lambda^2} \frac{\partial V}{\partial t} = \omega \cdot \frac{\partial \omega}{\partial t}$$

and with $\lambda^2 = \epsilon kT / \rho_e e$. It follows that

$$\tau_v \frac{\partial V}{\partial t} = \left(\frac{kT}{e} \right) \tau_v^3 \frac{\partial}{\partial t} (\omega^2 / 2) \quad (\text{F.19})$$

elimination of $\tau_v \partial V / \partial t$ between this and Equation F.14 now yields,

$$\begin{aligned} (\tau_v \frac{\partial \omega}{\partial t}) \times \mathbf{u} &= -\nabla [\lambda^2 \omega \cdot (\tau_v \frac{\partial \omega}{\partial t})] \\ (\nabla \times \mathbf{u}_e) \times \mathbf{u} &= -\nabla [\lambda^2 \omega \cdot (\nabla \times \mathbf{u}_e)] - \nabla \{ \lambda^2 [\nabla(\mathbf{u}_e \times \omega) + \mathbf{u}_e \cdot \nabla \times \omega] \} \end{aligned} \quad (\text{F.20})$$

and from Equation F.17 then,

$$(\nabla \times \mathbf{u}_e) \times \boldsymbol{\omega} = -\nabla(\mathbf{u}_e \cdot \mathbf{u}) \equiv -[\mathbf{u}_e \times (\nabla \times \mathbf{u}) + \mathbf{u} \times \nabla \times \mathbf{u}_e + (\mathbf{u} \cdot \nabla) \mathbf{u}_e + (\mathbf{u}_e \cdot \nabla) \mathbf{u}]$$

Thus when no spatial variation of either \mathbf{u}_e or \mathbf{u} takes place along their vector directions i.e along stream lines, there will be pure velocity shear and the final two terms above disappear. Thus

$$\mathbf{u}_e \times (\nabla \times \mathbf{u}) \equiv \mathbf{u}_e \times \boldsymbol{\omega} = 0 \quad (\text{F.21})$$

and this is consistent with Equation F.17, this being the condition underlying the partitioning of Equation F.12 into Equations F.13 and F.14. Moreover, by applying Equation F.21 directly to Equation F.13 , it follows that,

$$\nu \nabla^2 \mathbf{u}_e = \frac{\partial \mathbf{u}_e}{\partial t} \quad (\text{F.22})$$

Thus

$$-\nu(\nabla \times \nabla \times \mathbf{u}_e - \nabla \nabla \cdot \mathbf{u}_e) = \partial \mathbf{u}_e / \partial t \quad (\text{F.23})$$

shows that in addition to the viscous dissipation by shearing of \mathbf{u}_e there is another term, $\nu \nabla \nabla \cdot \mathbf{u}_e$, present which accounts for a component of $\partial \mathbf{u}_e / \partial t$ resulting from finite compressibility. This is the so called "second viscosity" mechanism described by Landau and Lifshitz [98] which results from a slow relaxation back towards thermodynamic

equilibrium after a rapid compression or expansion. The two terms on the left of Equation F.23 are almost equal and can be incorporated into an incompressible model such as that proposed here by modifying ν to the value $\nu^* \ll \nu$ and eliminating the compressibility term. Thus

$$-\nu^* \nabla \times \nabla \times \mathbf{u}_e = \partial \mathbf{u}_e / \partial t \quad (\text{F.24})$$

BIBLIOGRAPHY

- [1] E.O. Forster, "Progress in the Field of Electric Properties of Dielectric Liquids", IEEE Trans. Electr. Insul., Vol. EI-25, No. 1, February 1990, pp. 45-53.
- [2] J.E. Brignell, "Automatic Measurement of the Electric Strength of Liquid Dielectrics", J. Sci. Instrum., 1963, Vol.40. pp. 576-578.
- [3] A. Denat, N. Felici and J.P. Gosse, "Strong Current Injection into Insulating Hydrocarbons under High Electric Fields", Proc. of 7th. Inter. Conf. on Conduction and Breakdown in Dielectric Liquids, Berlin. W.G., 1981. pp.279-283.
- [4] G.A. Ostroumov, "Results of Measurement of the Electrical Conductivity of Insulating Liquid", Soviet Physics, JETP. Vol.14, No.2. 1962, pp.317-319.
- [5] A. Watson and S.S. Girgis, "The Influence of Electrode Separation, Geometry and an Applied Magnetic Field Upon Current Conduction in Silicone Oil", Journal of Electrostatics, 2. 1976, pp. 175-186.
- [6] S. Esendal and A. Watson, "Threshold for Initiation of a Power Law Current Response to Ramped High Voltage in Silicone Oil", Annual Report of CEIDP, 1982, pp. 473-479.
- [7] M.A. Abiri, "The Influence of Electrode Material, Viscosity, and Magnetic Field upon Prebreakdown Current in Dielectric Oil", M. Sc. Thesis, University of Windsor, 1980.
- [8] S.S. Girgis, "The Influence of a Magnetic Field upon the Prebreakdown Current in Silicone Oil", M. Sc. Thesis, University of Western Ontario, 1974.
- [9] S. Esendal, "Thresholds for Initiation of a Power Law Current Response to Ramped High Voltage in Silicone Oil and Oil/ Film Dielectrics", M. Sc. Thesis, University of Windsor, 1982.
- [10] M.A. Abiri, A. Watson and M.R. Raghuveer, "The Influence of Electrode Material Upon Pre-Breakdown Current in Viscous Silicone Oil", Annual Report of CEIDP, pp. 477-483 (1980).
- [11] A. Watson, "A Quantum Electrodynamic Analogue Model Applied to the Analysis of High Field Conduction in Dielectric Fluid", Conf. Record of the 6th Intern. Symp. on High Voltage Engineering, New Orleans, LA., 33.03, 1989.

- [12] A. Watson, "Force-Free Flow Involvement in Charge Transport Through Dielectric Fluids under Time Varying Applied Stress", CEIDP Annual Report, 1985, pp. 116 - 122.
- [13] R.W. Sillars, "Electrical Insulating Materials and Their Application", Peter Peregrinus Ltd. 1973.
- [14] H.R. Sheppard, "A Century of Progress in Electrical Insulation 1886-1986", IEEE Electrical Insulation Magazine, Sept. 1986 Vol.2, No. 5. pp. 20-30.
- [15] A.C.M. Wilson, "Insulating Liquids: Their Uses, Manufacture and Properties", Peter Peregrinus Ltd. 1980.
- [16] H.R. Sheppard, "PCB Replacement in Transformers", Proceedings of the American Power Conference, 1977. Vol.39, pp. 1062-1068.
- [17] C.C. Claiborne and H.A. Pearce, "Transformer Fluids", IEEE Electrical Insulation Magazine, July/August 1989 vol.5, No.4. pp. 16-19.
- [18] K.R. Linsley, "Nonflammable Small Power Transformers", Proceedings of the American Power Conference, 1981. Vol.43, pp. 715-720.
- [19] D.W. Goodwin and K.A. Macfadyen, "Electrical Conduction and Breakdown in Liquid Dielectrics", Proc. Phys. Soc. B, 1953. 66, pp. 85-96.
- [20] T.J. Lewis, "The Electric Strength and High Field Conductivity of Dielectric Liquid", Prog. in Dielectrics, Vol. 1, 1959, pp. 97-140.
- [21] A.H. Sharbaugh and P.K. Watson, "Conduction and Breakdown in Liquid" Progress in Dielectrics, Volume 4. New York, 1962, pp. 199-248.
- [22] N.J. Felici, "DC Conduction in Liquid Dielectrics (part I), A survey of Recent Progress," Direct Current, Vol. 2, No. 3. 1971. pp. 90-99.
- [23] T.J. Gallagher, "Simple Dielectric Liquids", Clarendon Press. Oxford, 1975.
- [24] I. Adamczewski, "Ionization, Conductivity and Breakdown in Dielectric Liquids," Taylor and Francis, London, 1969.
- [25] E.O. Forster, "Progress in the Field of Electrical Breakdown in Dielectric Fluids", 1985 International Conference on Properties and Applications of Dielectric Materials, Xian, China, 1985, pp. 13-16.
- [26] T.J. Lewis, "An Overview of Electrical Processes Leading to Dielectric

Breakdown of Liquids", The Liquid State and Its Electrical Properties, Plenum Press, 1987, pp. 431-501.

- [27] W.F. Schmidt, "Electronic Conduction Processes in Dielectric Liquids", IEEE Trans. Electr. Insul. Vol. EI-19, No.5, October 1984, pp. 389-417.
- [28] N.J. Felici, " A Tentative Explanation of the Voltage Current Characteristic of Dielectric Liquid," Proc. 7th Inter. Conf. on Conduction and Breakdown in Dielectric Liquids, Berlin, 1981. pp. 110-114.
- [29] R. Tobazeon, " The Liquid State and Its Electrical Properties, Plenum Press, 1987, pp. 465-501.
- [30] J.O'M. Bockris, B.E. Conway and Ralph E. White, "Modern Aspects of Electrochemistry," Vol. 17, Chapter 2. Plenum Press. 1986
- [31] B.E. Conway and M. Salomon, "Electrochemistry: Its Role in Teaching Physical Chemistry", Journal of Chemical Education, Vol.44, No.10, 1967, pp. 554-563.
- [32] J.O'M. Bockris and A.K.N. Reddy, "Modern Electrochemistry", Plenum Press. New York, 1970, Chapter 7.
- [33] T. Mechlia, B. Gosse, A. Denat and J.P. Gosse, "Electrophoretic Determination of the Charge at the Liquid-Solid Interface: Relation with Conduction Phenomena", IEEE Trans. Electr. Insul., Vol. EI-20, No. 2, April 1985, pp. 365-370.
- [34] A. Denat, B.Gosse and J.P. Gosse, "Ion Injections in Hydrocarbons", Journal of Electrostatics, Vol. 7, 1979, pp. 205-225.
- [35] A. Alj, A. Denat, J.P. Gosse, and B. Gosse, "Creation of Charge Carriers in Non-Polar Liquids", IEEE Trans. Electr. Insul., Vol. EI-20, No. 2, April 1985, pp. 221-231.
- [36] R. Tobazeon, M. Haidara and P. Atten, "Ion Injection and Kerr Plots in Liquids with Blade-Plane Electrodes", J. Phys. D: Appl. Phys., 17, 1984, pp. 1293-1301.
- [37] R.V. Latham, "The Origin of Prebreakdown Electron Emission from Vacuum Insulated High Voltage Electrodes", Vacuum, 1982, Vol.32, pp. 137-140
- [38] A. Watson, "High Voltage static Breakdown in Vacuum", Can. J. Phys. Vol. 54, 1976, pp. 142-157.
- [39] T.J. Lewis, "Electronic Processes in Dielectric Liquids Under Incipient

- Breakdown Stress", IEEE Trans. EI. Vol-20, No.2, April 1985, pp.123-132.
- [40] Z. Croitoru, "Space Charges in Dielectrics", Progress in Dielectrics, Vol.6, Editor J.B. Birks, Academic Press., 1965, pp.105-146.
 - [41] A.A. Zaky and R. Hawley, "Conduction and Breakdown in Mineral Oil", Peter Peregrinus Ltd., 1973.
 - [42] M. Zahn, "Space Charge Effects in Dielectric Liquids", The Liquid State and Its Electrical Properties, Plenum Press, Series B: Phy. vol.193, 1987, pp. 367-430.
 - [43] A.H. Sharbaugh, J.C. Devins and S.J. Rzaad, "Progress in the Field of Electric Breakdown in Dielectric Liquids, " IEEE Trans. Electr. Insul., Vol. EI-13, No. 4, August 1978, pp. 249-276.
 - [44] L. Savenu and D. Mondescu, "Aspects of the Influence of a Magnetic Field on the Electrical Conductivity of Dielectric Liquids", Conference on Conduction and Breakdown in Dielectric Liquids, Grenoble. 1968, pp. 385-397.
 - [45] T.J. Gallagher, "The Influence of a Magnetic Field on the Breakdown of a Liquid", Proc. 4th Int. Conf. on Conduction and Breakdown in Dielectric Liquids, Dublin, 1972, pp. 210-213.
 - [46] P.E. Secker and K.J. Hilton, "Measurement of Breakdown Stress in Hexane Subjected to a Transverse Magnetic Field", Proc. 4th Int. Conf. on Conduction and Breakdown in Dielectric Liquids, Dublin, 1972, pp. 206-209.
 - [47] A. Watson, " Perturbation of the Static Voltage Breakdown Mechanism in Vacuum by a Weak Magnetic Field," Canadian Journal of Physics, Vol. 54, 1976, pp. 2403-2417.
 - [48] H. Krompholz, R. Korzekwa, M. Lehr and K. Kristiansen, " Magnetic Insulation for the Space Environment", Space Structures, Power, and Power Conditioning, Vol. 871, 1988, pp. 341-347.
 - [49] M. Lehr, R. Korzekwa, H. Krompholz and M. Kristiansen, " Magnetic Field Effects on Dielectric Surface Flashover", Proc. Inter. Symp. on Discharges and Electrical Insulation in Vacuum. 1990,
 - [50] M. Ohki and S. Saito, " Effect of a Magnetic Field on Low-Pressure Gaseous Breakdown Along the Surface of a Solid Insulator", IEE Proc. A. vol. 138, No.6, 1991, pp. 300 -312.
 - [51] N.J. Felici, "DC Conduction in Liquid Dielectrics (part II) Electrohydrodynamic

Phenomena," Direct Current, Vol. 2, No. 4. 1971 pp. 147-165.

- [52] N.J. Felici and J.C. Lacroix, J. Electrostatics, Vol.5 1978, pp. 135-144.
- [53] J. Cross, "Breakdown Across a Dielectric Spacer in Insulating Oil and the Role of Electrohydrodynamics in Liquid Breakdown," IEEE Trans. Electr. Insul., Vol. EI-17, 1982, pp. 493-498.
- [54] W.F. Schmidt, "Elementary Processes in the Development of the Electrical Breakdown of Liquids", IEEE Trans. Electr. Insul., Vol. EI-17, No. 6, December 1982, pp. 478-483.
- [55] P.P. Wong and E.O. Forster, "The Dynamics of Electrical Breakdown," IEEE Trans. EI-17, 1982, pp. 203-220.
- [56] N.J. Felici, "Blazing a Fiery Trail with the Hounds", IEEE Trans. Electr. Insul., Vol. EI-23, No. 4, August 1988, pp. 479-503.
- [57] N.J. Felici, "Bubbles, Partial Discharges and Liquid Breakdown", Inst. Phys. Conf. Ser. No. 48. 1979, pp. 181-190.
- [58] P.K. Watson, " Electrostatic and Hydrodynamic Effects in the Electrical Breakdown of Liquid Dielectrics", IEEE Trans. Electr. Insul., Vol. EI-20, No. 2, April 1985, pp. 395-399.
- [59] E.O Forster and G.J. FitzPatrick, "Electric Breakdown in Dielectric Liquids", Phys. Technol. 16 (1985), pp. 282-287.
- [60] F. Spitzer, "Prebreakdown and Breakdown Measurements on Transformer Oil", Conference on Dielectric Materials, Measurements and Applications, 1970, pp. 333-339.
- [61] P.E. Secker and K.J. Hilton, " Measurement of Breakdown Stress in Hexane Subjected to a Transverse Magnetic Field", Proc. of 4th Inter. Conf. on Conduction and Breakdown in Dielectric Liquids, Dublin, 1972, pp. 206-209.
- [62] H.N. Venkoba Rao, S. Birlasekaran and Y. Mahadevan, "A Programmable Voltage Scan Generator", Transactions of the SAEST, Vol.15, No 2, 1980, pp. 173-177.
- [63] " Operating Instruction Manual", Del Electronics Corp. Mt. Vernon, N.Y.
- [64] H.O. Finklea, West Virginia University, private communication.

- [65] " Technical Information, Alpha II series", Brandenburg Limited, 939, Surrey, England, 1976
- [66] D.H. Ren and A. Watson, "Ramped Voltage Testing of Transformer Oil", Annual Report of CEIDP, pp. 363-368, 1989.
- [67] D.H. Ren, P.H. Alexander and A. Watson, "The Field Distribution Near a Gas/Liquid Surface by Using a Developed Charge Simulation Method", 21th Annual Pittsburgh Conference on Modelling and Simulation, USA. pp.2371-2375, 1990.
- [68] H.M. Ismail, "Charge Simulation Based Computer-Aided Design Implementation of High Voltage Systems Modelling", Ph.D. Dissertation, University of Windsor, 1989.
- [69] D.H. Ren and A. Watson, "Characteristics of the Threshold Coordinated for High Stress Conduction in Transformer Fluid", 10th Intern. Conf. on Conduction and Breakdown in Dielectric Liquids. Grenoble, France, Sep. 10-14, 1990.
- [70] "Handbook of Electrical Engineering", Vol. 3. High Voltage Technology, Industrial Press, Beijing. 1980.
- [71] A. Bradwell, "Electrical Insulation", Peter Peregrinus Ltd., U.K. 1983.
- [72] H.L. Saums, "Materials for Electrical Insulation and Dielectric Functions", Hayden Book Company, INC, Rochelle Park, New Jersey, 1973.
- [73] Y. Kamata, "New Liquid Insulating Materials", IEEE Trans. Electr. Insul., Vol.EI-21 No.6, pp. 929-931, 1986.
- [74] D.H. Ren and A. Watson, "Prebreakdown Phenomena in Organic Ester Transformer Fluid", Intern. Symp. on Electrical Insulation. Toronto, Canada, June 3-6, 1990.
- [75] A. Watson and D. H. Ren, "High Stress Space Charge Limited Current Flow in Dielectric Oil Under Ramped Voltage Application", Annual Report of CEIDP, pp. 648-653. 1990.
- [76] A. Watson, "High Field Conduction in Dielectric Liquid with Ramped Voltage Application: A Theory of the Mechanism", 10th International Conf. on Conduction and Breakdown in Dielectric Liquids, France, Sept. 1990, pp. 156 - 160.
- [77] W. K. Panofsky and M. Phillips, "Classical Electricity and Magnetism",

Addison-Wesley, 1962.

- [78] G.B. Whitham, "Linear and Non Linear Waves", New York, Wiley. 1974.
- [79] P. Stehle, "Quantum Mechanics", San Francisco, Holden-Day Press, 1966.
- [80] K-H. Becker and M. Dorfler, "Dynamical Systems and Fractals", Cambridge University Press, 1989.
- [81] S. Chandrasekhar and P.C. Kendall, "On Force-Free Magnetic Fields", Ap. J., 126, pp.457-460, 1957.
- [82] A. Watson and D.H. Ren, "High Stress Aggregation and Transport of Electrons in Dielectric Oil", CEIDP Annual Report, 1993. pp. 281-286
- [83] D. H. Ren and A. Watson, "Charge Injection into Dielectric Oil From the Anode or Cathode under Ramped Voltage Application," CEIDP Annual Report. pp 532-537. 1991.
- [84] D. R. Hofstadter, "Metamagical Themas", Basic Books, Inc., Publishers, New York. pp 364-359. 1985.
- [85] R. Plonsey and R. Collin, "Principles and Applications of Electromagnetic Fields", McGraw-Hill, New York, 1961.
- [86] W. R. Smythe, "Static and Dynamic Electricity", McGraw-Hill, New York, 1950.
- [87] G. Tehodossiou, J. Nelson and G. Odell, "A Computer Simulation of Transient Electrohydrodynamic Motion in Stressed Dielectric Liquids", J. Phys. D:Appl. Phys., 19. pp. 1643-1656, 1986.
- [88] H. Singer, H. Steinbigler and P. Weiss, "A Charge Simulation Method for the Calculation of High Voltage Fields", IEEE Trans. on Power Apparatus and Systems, Vol. Pas-93, pp. 1660-1668, 1974.
- [89] J. Chang and A. Watson, "Electromagnetic Hydrodynamics", IEEE Trans. Electr. Insul., Vol.1 No.5, pp. 871-895, 1994.
- [90] A. Watson, "The Displacement Current from Ramped Voltage Application to Dielectric Liquids", Annual Report of CEIDP, pp. 935-941, 1994.
- [91] W. Blakeley, "Calculus for Engineering Technology", Chapter 19, John Wiley & Sons, New York, 1968.

- [92] D. Samaras, "The Theory of Ion Flow Dynamics", Dover, 1962
- [93] A. Crisanti, et al, "Motion of Passively Advected Impurities in Two-Dimensional Flows: Chaos, Structures and Diffusion", in "Nonlinear Dynamics of Structures", World Scientific, 1990, pp. 44-70.
- [94] This section was contributed by A. Watson.
- [95] M. Steenbeck, F. Krause and K-H. Rädler, " A Calculation of Mean Electromotive Force in an Electrically Conducting Fluid in Turbulent Motion, under the Influence of Coriolis Forces." Z. Naturforsch, Vol. 21a, pp.369, 1966.
- [96] H.K. Moffatt, "Some Developments in the Theory of Turbulence" J. Fluid Mech. Vol 106, pp 27-47, 1981
- [97] H. Kikuchi, "EHD Vortex in the Atmosphere with Helical Turbulence in Electric and Space - Charge Fields" in " Nonlinear Dynamics of Structures", World Scientific, pp. 261-272, 1990.
- [98] L.D. Landau and E.M. Lifshitz, " Fluid Mechanics" 2nd Edition, Vol. 6. Pergamon Press, Oxford, 1987.
- [99] A. Watson, private communication.

VITA AUCTORIS

NAME: Diana Hua Ren

PLACE OF BIRTH: Beijing, China

YEAR OF BIRTH: 1961

EDUCATION: Xi-An JaoTong University, ShanXi, China
1978-1982 B.Sc.

Electric Power Research Institute, Beijing, China
1982-1984 M.Sc.

University of Windsor, Ontario, Canada
1989-1995 Ph.D. (candidate)